Doctoral Dissertation
Doctoral Program in Energy Engineering (35th Cycle)

Polyelectrolyte complexes embedding reduced graphite oxide

From aqueous dispersion toward multifunctional polyelectrolytes composites

By

Tianhui Jiang

******

Supervisor(s):
Prof. Alberto Fina, Supervisor
Prof. Federico Carosio , Co-Supervisor

Doctoral Examination Committee:
Prof. Jaime Grunlan, Referee, Texas A&M University
Prof. Sebastien Pruvost, Referee, Institut National des Sciences Appliquées Lyon
Prof. Rossella Arrigo, Referee, Politecnico di Torino
Prof. Monica Boffito, Referee, Politecnico di Torino
Dr. Gennaro Gentile, Referee, Institute for Polymers Composites and Biomaterials

Politecnico di Torino
2023

Declaration

I hereby declare that, the contents and organization of this dissertation constitute my own original work and does not compromise in any way the rights of third parties, including those relating to the security of personal data. Part of the work reported in this Dissertation was published in the co-authored paper [1], while other parts are under consideration for publication in scientific journals.

Tianhui Jiang

2023

* This dissertation is presented in partial fulfillment of the requirements for **Ph.D. degree** in the Graduate School of Politecnico di Torino (ScuDo).

Acknowledgment

When I write this line at this moment, it reminds me that my doctoral study and research have come to an end period. This three-year study in Politecnico di Torino and life in Italy is quite special experience for me, I would like to express my appreciation in these short pages.

An enormous thank you to my supervisor Alberto Fina and Co-supervisor Federico Carosio, for their patience and support, their valuable advice and guidance throughout my study. Thank you two for all the efforts you paid for the completion of this thesis. Thank you Alberto, your patience, carefulness and rigorous attitude toward academic study are also my role model. Thank you Federico for keeping me motivated in the study due to your creativity, humor and constant encouragement. I consider myself extremely lucky to have two supervisors with different personalities but are both kind, accommodating and passionate about academics. This work is supported by Chinese Scholarship Council (CSC), thanks to Chinese government and the staff member for their availability and helps through my PhD period.

I have to thank of course, all the colleagues in the laboratory, both former and present. Thanks to Daniele Battegazzore for this help in teaching me the usage of different instruments. Thanks to Fausto Franchini for his kindness and availability in electrical conductivity measurements despite his busy schedule. Thanks to Dario Pezzini for the help in SEM. Dario, thank you for your helpful assistance and thank you for bearing my poor italiano during the test. Thanks to Giuseppina Lacono for helping me with TGA tests. Thanks to Lorenza Maddalena, thank you for your help in starting my experiments and my endless Raman test. Chiara Paravidino, thank you very much for dissolving instruments problems. You are super nice. Massimo Marcioni, a pastry expert and craftsman in LbL, is also a real engineer. I believe your Italian dessert will also conquer the stomach of your new colleagues and all the best to you. Francesco Cantamezza, a Chinese food lover and a coriander alliance memberthe. If you go to China in future, I can introduce you to the eight major cuisines. Fang Ding, we tried all the bars on the way to University and did the breakfast ranking of Alessandria. Our outlook of life and values is so similar, and it's quite comfortable to stay with you. Letiza Maria Aghemo, although for one

year you stayed here, you are the most energetic person I have met, I wish you much success and happiness. I could make a personalized dedication for all of them, but then I would need another thesis for that, so thanks to Sergio, Ewa, Marta, Gulia, Fulvia, Emir, Elissa, Samuele, Diego, and Valentina and to whom I forget. I wish you all the best.

I would also like to especially thank those people who made me feel at home during my trips, Yufan Ding, Yichen Wang and Yang Lin. Thank you for everything.

Carrying out a thesis at a foreign country especially at a special time with pandemic has not been an easy task, although I was lucky to have so many nice people around me, there are also hard experienced and not so pleasant moments, the support of my family has always been a pillar in my life. Your unconditional support that I have is my parachute for venturing into new experience. I love my family!

Lastly, I would like to end this with a Chinese ancient poem and express my good wishes to you all.

青山一道同云雨，明月何曾是两乡。

Abstract

The aqueous dispersion of polyelectrolyte (PE)-based graphene-related materials (GRMs) represents an interesting intermediate in the development of advanced materials through sustainable processes. There is a lack of prominent work systematically studying the effects of typical parameters of PEs structure, molecular weight and charge density on the dispersion and stabilization of polyelectrolyte grafted reduced graphite oxide (rGO) in water. One of the main goals of this project is to reveal the interaction between PEs and rGO, and explore the balance of adsorption of polymers and the anti-aggregation ability of PE-rGO assembles. Four PEs were evaluated, including polyacrylic acid (PAA), branched poly(ethylenimine) (BPEI), sodium carboxymethyl cellulose (CMC), and poly(sodium 4- styrenesulfonic acid) (PSS). The charge density plays a critical role in weak PEs (PAA and BPEI) in dispersing rGO, both of them revealed optimum performance at mild charge density where good adsorption and repulsive charges of polymers onto rGO were reserved. BPEI has been found to induce good dispersibility of rGO in water, also depending on polymer chain length. The negatively charged strong PEs (PSS and CMC) were inferior due to the high surface tensions and limited adsorption onto rGO. Therefore, the suitable PEs and dissociation conditions used for rGO dispersion were obtained.

On the other hand, the good dispersion of rGO in aqueous PE solutions offers the opportunity to further preparation of uniformly distributed rGO in polymeric composites via liquid-phase mixing. The graphene and GRMs reinforced polymer composites have been investigated in the last decade by researchers and used in batteries, sensors, biomedical and other fields. Using autonomous complexation of oppositely charged PEs eliminates the use of organic solvents and endows composites manufacture from thin layers to bulk materials. In this work, PAA and poly(diallyldimethylammonium chloride) (PDAC) were used to fabricate a polyelectrolyte complex (PEC). Based on the fundamental properties of polymeric matrix and incorporation of rGO in PECs, I focused on the mechanical properties of rGO incorporated polyelectrolyte complexes (rGO-PECs) under different salt

content and humidity conditions. The addition of a small amount of rGO could greatly improve the mechanical properties of composites under ambient condition, and for the salt-plasticized samples, the addition of graphene is also beneficial to inhibit the polymer chains' mobility, thus improving the strength and reducing the deformation. At a high moisture environment, the polymer matrix tended to be ductile with extremely high deformation and low tensile strength owing to its humidity sensitivity, and the strong mismatch of soft matrix and hard rGO led to limited reinforcement. In this case, the salt impacts the mechanical properties even with a tiny amount in PECs.

To further promote the applications of rGO-PEC composites in electronic components, the rGO content and dispersion in PECs are particularly important. The PAA has been proven to have good compatibility with rGO and was used in rGO dispersion, while there is no study focused on hybrid dispersing systems consisting of oppositely charged PEs and high concentration of salt. The hybrid system contained all components in the final-prepared composite, which increased rGO content in rGO-PEC composites. Therefore, this work compared different dispersion methods on rGO content, rGO dispersion in PECs and the composites' mechanical, thermal and electrical properties. The PAA single-phase approach had the advantage in terms of the rGO dispersion, requiring a short sonication time to achieve separation and dispersion of rGO, instead, the hybrid-phases approach showed much higher rGO content in the composite and fast transformation from dispersion condition into complexation condition. The mechanical property, thermal and electrical conductivities, as well as stability in water were compared in rGO-PECs prepared in two methods. To optimize desired properties, the effects of PAA:rGO and sonication time on the physical properties of rGO-PECs were further studied. In the single phase dispersion method, the low PAA:rGO ratio was critical to achieving the improvement of electrical conductivity but also brought a much higher salt fraction in PECs, which is unfavourable in terms of its mechanical strength and stability in water. On the other hand, the mechanical property, thermal and electrical conductivities of rGO-PECs fabricated by multiphase approach were dependent on the combined effects of rGO aggregates and the dispersed rGO size/defectiveness, which was dominated by sonication time. Indeed, longer sonication time led to a better dispersion of rGO in PECs, improved mechanical properties, and good stability in water, while also causing a slight decrease in thermal and electrical conductivity.

Contents

1. Literature review 1

1.1 Liquid phase dispersion of graphene and graphene related materials (GRMs) 1

1.1.1 Graphene and GRMs: definitions, properties and applications 1

1.1.2 What makes a good liquid dispersion of graphene and GRMs 4

1.1.3 Types of GRMs used in liquid phase dispersions 8

1.1.4 Covalent functionalization for GRMs dispersions 11

1.1.5 Non-covalent functionalization for GRMs dispersions 17

1.2 Polyelectrolyte (PE) and PE functionalized GRMs dispersions 20

1.2.1 Polyelectrolytes 20

1.2.2 PE-functionalized GRMs for aqueous dispersion 21

1.3 Polyelectrolyte complexes (PECs) 23

1.3.1 Polyelectrolytes complexes and polyelectrolyte multilayers 23

1.3.2 Parameters affecting the formation and properties of PEC 27

1.4 Incorporation of organic and in-organic particles into PECs 30

1.4.1 Incorporation of proteins, drugs and bioactive molecules 31

1.4.2 Incorporation of metal nanoparticles 32

1.4.3 Incorporation with silica, carbon nanotubes, GRMs and other inorganic particles 32

1.5 Aim of research 37

2. Materials and Methods 39

2.1 Materials and sample preparation 39

2.1.1 Preparation of polyelectrolyte/rGO dispersions 41

2.1.2 Preparation of rGO and/or salt incorporated PAA/PDAC composite 42
2.1.3 Preparation of PAA/PDAC composites incorporating high rGO concentration 44
2.2 Characterization methods 45
2.2.1 Contact angle of polyelectrolyte on rGO film 45
2.2.2 Dispersion stability and rGO concentration from UV-vis spectroscopy (Ultraviolet-visible spectroscopy) 45
2.2.3 Size measurement by dynamic light scattering (DLS) 47
2.2.4 Raman spectroscopy 47
2.2.5 Phase quantification and thermal properties of PECs 47
2.2.6 Fourier transformed infrared-Attenuated total reflection (FTIR-ATR) 49
2.2.7 Scanning electron micrographs (SEM) and energy dispersive X-ray spectroscopy (EDS) 49
2.2.8 Mechanical properties 49
2.2.9 Healing properties 50
2.2.10 Electrical conductivity 50
2.2.11 Thermal conductivity 51
2.2.12 Stability in water 51
3. PE-enabled rGO water dispersions: effects of PE structure, molecular weight and charge density 52
3.1 Introduction 52
3.2 Result and discussion 53
3.2.1 Visual observation and surface tension 53
3.2.2 UV-vis analysis 59
3.2.3 Quantification of polyelectrolyte adsorbed to rGO 62
3.2.4 Size and defectiveness of suspended rGO 64
3.2.5 Interaction between polyelectrolyte and rGO 67
3.3 Conclusions 70
4. PAA/PDAC complexes incorporating rGO 72

4.1 Introduction 72
4.2 Result and discussion 74
4.2.1 Selection of PAA/PDAC complexation conditions 74
4.2.2 FTIR-ATR analysis 74
4.2.3 Thermal stability, morphology and mechanical properties 81
4.2.4 Effect of rGO concentration in PECs 89
4.2.5 Humidity sensitive mechanical property 93
4.2.6 Water triggered self-healing property 95
4.3 Conclusions 97
5. PAA/PDAC complexes incorporating high rGO concentrations 99
5.1 Introduction 99
5.2 Result and discussion 101
5.2.1 Visual observation 101
5.2.2 General characterization 104
5.2.3 Morphology characterization 106
5.2.4 Morphology characterization 108
5.2.5 Effect of sonication time: rGO distribution and mechanical variation 109
5.2.6 PAA/G//PDAC-S with different PAA: rGO ratio 113
5.2.7 Swelling and stability in water 115
5.2.8 Thermal conductivity (TC) and electrical conductivity (EC) 119
5.3 Conclusions 125
6. General conclusions 127
7. References 132

Index

BPEI	Branched poly(ethylenimine)
CMC	Sodium carboxymethyl cellulose
CoPEC	Compacted polyelectrolyte complexes
CTAB	Cationic cetyltrimethylammonium bromide
CVD	Chemical vapour deposition
DLS	Dynamic light scattering
DMSO	Dimethyl sulfoxide
DMTA	Dynamic Mechanical Thermal Analysis
E’	Storage modulus
E’’	Loss modulus
EC	Electrical conductivity
EDS	Energy dispersive X-ray spectroscopy
FLG	Several-layer graphene
FTIR-ATR	Fourier transformed infrared-Attenuated total reflection
GNP	Graphite nanoparticles
GO	Graphene oxide
GRMs	Graphene related materials
LbL	Layer-by-layer
MLG	Multilayer graphene
NaCl	Sodium chloride
NMP	N-methyl-pyrrolidone
PAA	Polyacrylic acid
PAH	Poly(allyl amine hydrochloride)
PANa	Sodium polyacrylate
PDAC	Poly(diallyldimethylammonium chloride)
PDMAEMA	Poly(N,N-dimethylaminoethyl methacrylate)
PE	Polyelectrolyte
PECs	Polyelectrolyte complexes
PEG	Polyethylene glycol
PEMs	Polyelectrolyte multilayers
PLGA	Poly-l-glutamic acid
PLL	Poly(L-lysine)
PMAA	Poly-(methacrylic acid)

POMs	Polyoxometalates
PPC	Protein-polyelectrolyte complex
PSS	Poly(sodium 4- styrenesulfonic acid)
PVA	Polyvinyl alcohol
rGO	Reduced graphite oxide
RH	Relative humidity
SDBS	Sodium dodecylbenzen sulfonate
SEM	Scanning electron micrographs
TC	Thermal conductivity
TGA	Thermogravimetric analysis
THF	Tetrahydrofuran
UV-vis	Ultraviolet-visible spectroscopy
A_G	Absorption intensity of UV-vis at 600 nm
$A_{G,\,i}$	Initial absorption intensity of UV-vis at 600 nm
c	Concentration
C_s^{cr}	Critical salt concentration
I_D/I_G	Intensity ratio of D band to G band
l	distance between the electrodes
L	Path length
m_0	Mass of filter membrane
m_1	Mass of filter membrane together with deposited material
M	Residual weight proportion of deposited PE/rGO
M_{PE}	Residual weight proportion of PE
M_G	Residual weight proportion of rGO
$M_{G@P/P}{}^R$	Residual weight proportion of PEC^R
$M_{P/P}{}^R$	Residual weight proportion of $(PAA/PDAC)^R$
Mw	Molecular weight
p_c	percolation threshold
P	Laplace pressure
R	Resistance
S	surface area
$S_{l/g}$	Spreading coefficient
$t^{1/2}$	Square root of sonication time
Tg	Glass transition temperature
V	Volume of dispersion for filtration
W_G	Weight fraction of rGO in PEC^R
w_G	Weight fraction of rGO in deposited PE/rGO

α	Absorption coefficient
β	Constant coefficient related to specific solid surface
γ	Interfacial tension, it also refers to surface tension of liquid phase (interfacial of liquid phase and air)
δ_D	dispersion cohesion parameter
δ_H	hydrogen bonding cohesion parameter
δ_P	polarity cohesion parameter
δ_T	Hildebrand solubility parameter
θ	contact angle
ρ	Electrical resistivity
σ	Electrical conductivity
φ	salt doping level
Γ_G	Full width at half maximum of G

List of Figures

Figure 1.1 Schematic diagram of the GO reduction procedure and electrical characterization of the products. Reprinted by permission from Springer Nature Customer Service Centre GmbH: [Springer Nature] [Nature Chemistry] [14] Copyright 2009. 3

Figure 1.2 Structure of graphene (G), graphene oxide (GO) and reduced graphene oxide (rGO). Reprinted from Ref. [80].....11

Figure 1.3 Main information of covalent functionalization of graphene sheets, including functional groups used in chemical reactions, grafting molecules and methods.....12

Figure 1.4 Schematic diagram of grafting-from and grafting-to methods to functionalized graphene with polymers. Reprinted from Ref [8]. 13

Figure 1.5 Photographs of polystyrene and poly(ethylene glycol) functionalized graphene nanosheets (G-N-PS and G-N-PEG1900) in various solvents. Reproduced with permission from [89]. Copyright 2010, American Chemical Society. 14

Figure 1.6 Synthesis of Alkyne-functionalized graphene (Alkyne-FG) and CTAs-functionalized graphene (CTAs-FG) (a), RAFT polymerization of vinyl monomers with CTAs-FG using 'Grafting from' method (b), RAFT polymerization of vinyl monomers with Azido-CTAs (CTAs-N3) (c), Click Reaction of polymer-N3 to Alkyne-FG using 'Grafting to' method (d). Reproduced with permission from [96]. Copyright 2010, American Chemical Society. 16

Figure 1.7 PMMA-g/t-FG samples (green) from left to right have molecular weight of PMMA-N_3 ~2 500, ~5 000, ~10 000 and ~20 000 g· mol^{-1}. PMMA-g/f-FG (blue) from left to right have weight ratios of the monomer MMA and initiator (2, 2′ -azobis-(2-methylpropionitrile, AIBN) [M]/[I] 2700, 1350 and 650. Reproduced with permission from [96]. Copyright 2010, American Chemical Society. 16

Figure 1.8 Structure of confined PAA on a nanoparticle surface. R is the radius of a polystyrene nanoparticle, D is the average distance between two PAA chains, and L is the thickness of PAA layer attached on the nanoparticle. Reprinted by permission from Springer Nature Customer Service Centre GmbH: [Springer Nature] [Colloid and Polymer Science] [126] Copyright 2019 21

Figure 1.9 The formation of PEC in solution with counterions release (a) and PEM fabrication via LbL (b).....24

Figure 1.10 The processes occurring during mixing of PE solutions and formation of PEC particles [155]. Copyright 2012, American Chemical Society. 25

Figure 1.11 Representation of intrinsic and extrinsic compensation in PEC [160] 26

Figure 1.12 Schematic diagram of formation of polyanion-decorated PEC-silica particles (a) and the charge change on particles with varying pH (b). Reprinted from [206], Copyright (2015), with permission from Elsevier. 33

Figure 1.13 Schematic diagram of the carbon nanotube noncovalent modification in LbL electrostatic self-assembly. Reproduced with permission from [216]. Copyright 2012, American Chemical Society. 34

Figure 1.14 Fabrication of GO incorporated PEI/PAA nanohybrid membranes. Reprinted from [217], Copyright (2012), with permission from Elsevier. 35

Figure 2.1 XRD pattern recorded (a) and SEM images (b) (c) for pristine rGO. ..40

Figure 2.2 Illustration of fabrication process 41

Figure 2.3 Schematic representation of the fabrication process used to create PAA/G//PDAC films 42

Figure 2.4 Schematic representation of the two different methods for fabricating rGO decorated PAA/PDAC 44

Figure 2.5 Absorption coefficient (α) of RGO dispersions with different PEs. 46

Figure 3.1 rGO inclusion in water and polyelectrolytes. 54

Figure 3.2 rGO inclusion in polyelectrolyte solutions over 1 night 55

Figure 3.3 The liquid contact angel images of water, BPEI25, PAA100, PSS70 and CMC90 droplets on the surface of rGO with time.....57

Figure 3.4 rGO inclusion in PAA solutions at different pH 58

Figure 3.5 Photographs of rGO dispersed in different polyelectrolytes solutions before (a) and after four-week of aging in static conditions (b) 59

Figure 3.6 UV-vis spectra of of PEs with 0.1 wt%, inset: absorption spectra for BPEI25, BPEI270, PSS70 and PSS200 with 0.01wt% (a), PE/rGO dispersions (b), concentration of rGO in PE/rGO dispersions (c), the amount of remaining rGO in dispersions after 0 to 4 weeks, expressed as percentage of original absorptions (original concentration), $A/A_{G,i}$ (d).....61

Figure 3.7 The TGA curves of PE/rGO after aging 4 weeks. 63

Figure 3.8 Average size of suspended rGO with different aging time 65

Figure 3.9 Raman spectra of rGO with PEs, pristine rGO and rGO_s after sonication in water. 66

Figure 3.10 Photographs and UV-vis spectra of PAA100/rGO with different pH.68

Figure 3.11 Photographs and UV-vis spectra of BPEI25/rGO with different pH..69

Figure 4.1 PAA and PDAC mixing at different pH and salt NaCl concentration .74

Figure 4.2 FTIR (a) and ATR-FTIR (b) spectra of pristine PAA and PAA at pH 7, FTIR (c) and ATR-FTIR spectra (d) of PDAC.....76

Figure 4.3 ATR-FTIR spectra of PAA, PDAC at pH 7 and the PECs, rinsed $PECs^R$ in wide range of 4000-400 cm^{-1} (a), (c) and specific range of 1800-1200 cm^{-1} (b), (d).....78

Figure 4.4 Salt and moisture contents in all samples (a), TGA curves of PECs (at air) (b) and $PECs^R$ (c) for measuring salt content.....79

Figure 4.5 TGA and DTG of pure components (a), PECs (b) and $PECs^R$ (c) at N_2 atmosphere 82

Figure 4.6 Cross-section images of un-pressed PAA/G//PDAC (a) and (b), PAA/G//PDAC (c), and (d), PAA/G//PDAC-s (e) and (f). The (d) and (f) are the regions marked by yellow dotted boxes in (c) and (e) respectively. White arrows: defects in un-pressed PAA/G//PDAC, red arrows: the direction of G, yellow arrows: the G at fracture boundary, dashed curve, the fracture boundary.....85

Figure 4.7 The stress-strain curve of PECs with the inset of enlargement at strain range of 0 to 12% (a), elastic modulus, stress at break and failure strain (b).....86

Figure 4.8 Storage modulus, Loss modulus and Tan Delta of PECs during heating (a-f), and cooling process (g-m) 88

Figure 4.9 Mechanical reinforcement (a) and elongation at break (b) of rGO as a function of concentration. Experimental and theoretical elastic moduli derived from the Halpin-Tsai model for PAA/G//PDAC-based composites with aligned and random dispersions (c).....90

Figure 4.10 The cross-section SEM images of PAA/$G_{0.17}$//PDAC (a) (f) (k), PAA/$G_{0.30}$//PDAC (b) (g) (m), PAA/$G_{0.37}$//PDAC (c) (h) (n), PAA/$G_{0.40}$//PDAC (d) (i) (o) and PAA/$G_{0.48}$//PDAC (e) (j) (p). The (f) (g) (h) (i) and (j) are the regions marked by yellow dotted boxes in (a) (b) (c) (d) and (e) respectively. 93

Figure 4.11 Moisture content (a) stress (b) and strain at break (c) of PECs under different relative humidity. The stress-strain curves of PECs saved in RH70% (d), the images of PAA/$G_{0.37}$//PDAC under stretching (e) and after stretching (f). 94

Figure 4.12 Comparison of stress at break (a), Elastic modulus (b) and strain at break (c) between healed PECs dried in RH 35% at room temperature and pristine PECs, the stress-strain curves (d) and corresponding recovery degree of healed PECs (e), the cut and healed PAA/G//PDAC film (f).....96

Figure 5.1 Schematic representation of the two different methods for fabricating rGO decorated PAA/PDAC.....101

Figure 5.2 rGO inclusion in PAA solution (used for PAA/G//PDAC-S, first row) and PAA/PDAC-S solution (used for (PAA/PDAC-S)/G, second row) 102

Figure 5.3 rGO dispersions of (PAA/PDAC-S)/G (left) and PAA/G//PDAC-S (right) after 3 months 103

Figure 5.4 TGA, ATR-FTIR and Raman results of samples PAA/G//PDAC-S and (PAA/PDAC-S)/G 105

Figure 5.5 The cross-section view of PAA/G//PDAC-S (a) (b) and (PAA/PDAC-S)/G (c-f). Yellow arrows and circles: rGO, white arrows: cracks.....108

Figure 5.6 Tensile results of PAA/G//PDAC-S, (PAA/PDAC-S)/G and PAA/PDAC-s.....109

Figure 5.7 Cross-section images of (PAA/PDAC-S)/G_s1 (a-c), (PAA/PDAC-S)/G_s3 (d-f) and (PAA/PDAC-S)/G_s4 (g-i). The tensile results of (PAA/PDAC-S)/G-based samples with different sonication time (j) and (k).....110

Figure 5.8 TGA results of (PAA/PDAC-S)/G_si (i =1, 2, 3 or 4) with 1 to 4 sonication cycles (a), corresponding samples after salt-removing treatment (b), the components percentage variation with sonication time (c), the ATR-FTIR spectra for (PAA/PDAC-S)/G_si (i =1, 2, 3 or 4) (c) 112

Figure 5.9 Raman spectra of PAA/G//PDAC-S and (PAA/PDAC-S)/G with different sonication time 113

Figure 5.10 SEM images of PAA/G2//PDAC-S in cross-section (a) and (b), white arrows are cracks, dashed ellipses are crumpled rGO, dotted ellipse is pull-out of rGO sheet, and yellow arrows are small rGO. TGA results of PAA/G2//PDAC-S and $(PAA/G2//PDAC\text{-}S)^{R}$ (c) Mechanical property of PAA/G2//PDAC-S and other PECs (d).....114

Figure 5.11 SEM images of cross section of PAA/PDAC-s (a-c), PAA/G//PDAC-S (d-f), (PAA/PDAC-S)/G (g-i) soaked in water for 2 weeks. 116

Figure 5.12 SEM images of cross section of (PAA/PDAC-S)/G_s4 (a-c) and PAA/G2//PDAC-S (d-f) soaked in water for 5 weeks.....117

Figure 5.13 SEM images of top-view of PAA/PDAC-s (a-c), PAA/G//PDAC-S (d-f), (PAA/PDAC-S)/G (g-m) soaked for 2 weeks. 118

Figure 5.14 Top-view images of (PAA/PDAC-S)/G_s4 (a-c) and PAA/G2//PDAC-S (d-f) soaked for 5 weeks. (c-1) and (f-1) are the enlargement of (a) and (f) respectively. 119

Figure 5.15 Thermal conductivity of PEC samples (a), comparison of thermal conductivity between our samples and polymer composites embedding GRMs in literatures [322-346]. 121

Figure 5.16 Electrical conductivity of PEC samples 122

List of Tables

Table 1.1 Typical physical properties of graphene, GO and rGO 4

Table 1.2 The surface tension and Hildebrand parameters δ_T of solvents and solubility of GO and rGO in range of solvents by bath sonication. Reprinted from [57], with permission from Elsevier. 8

Table 2.1 Polyelectrolytes used for rGO dispersions and PEC composites 40

Table 2.2 Detail information for PEC samples.....43

Table 2.3 Fabrication information for rGO-PECs with different rGO loadings....43

Table 3.1 Surface tension of polyelectrolyte solutions reported in literatures. 56

Table 3.2 Weight residual of PE/rGO after TG and the weight percentage of rGO and PE in PE/rGO films.....63

Table 3.3 The PDI values of PE/rGO samples before and after aging 4 weeks. ...65

Table 4.1 Peak assignments of pristine PAA and PAA at pH7. 76

Table 4.2 Peak assignments of PDAC observed in FTIR and ATR-FTIR 77

Table 4.3 Element atomic percentage in cross-section of PECs based on EDS result 81

Table 5.1 The electrical conductivity and percolation thresholds of rGO reinforced polymer composites with different rGO production method, matrix and preparation method. 123

Chapter 1

1 Literature review

1.1 Liquid phase dispersion of graphene and graphene related materials

1.1.1 Graphene and graphene related materials: definitions, properties and applications

Graphene is a single-atom thick layer composed of sp^2 hybridized carbon atoms with a honeycomb lattice. As a super thin 2D material, graphene has a very high surface area (2630 m^2/g) and short atomic distance (only 0.142 nm), can be used as a barrier material to prevent passage of small molecules or even atoms [2]. It also reveals extremely high electron mobility 350 000 $cm^2\ V^{-1}\ s^{-1}$ [3], thermal conductivity ~5000 $W\ m^{-1}\ K^{-1}$ [4] and electrical conductivity 6000 S/m. Besides, strong stiffness and high strength have been found because of the strong in-plane carbon-carbon bonds (σ bond) of graphene [5]. The antibacterial and anticancer activities of graphene [6] have raised its potential in biomedical and therapeutic applications. Some of graphene properties are recorded in Table 1.1. These remarkable and intriguing properties make it become one of the competitively used additives for different applications in sustainable energy production, environmentally sustainable development and healthcare fields. For many of applications, it is required to have a scalable production of the single or few layers of graphene. Generally, graphene could be produced via either top-down method or bottom-up technique. High quality of monolayer graphene can be constructed by

bottom-up method, such as chemical vapour deposition (CVD) and epitaxial growth on SiC [7]. These methods typically involve high temperature (i.e., 750-1200 °C for CVD and ~1300 °C for epitaxial growth), high costs, but limited yields or impurities getting into graphene monolayer [8]. Another choice is the top-down method that produces of graphene flakes from exfoliation of graphite precursors in liquid media or isolated as powder [9]. For instance, the liquid-phase exfoliation technique is used to produce colloidal graphene suspensions by exfoliation of graphite-based materials, resulting in a mixture of single to multilayer of graphene dispersed in solvents with or without dispersants [10]. The top-down approach shows advantages of scalability and versatility using only simple instruments, while the graphene materials obtained in this way usually are not single-layer sheets but a series of derivatives with different sizes, layers and defects. The main challenge during manufacturing and processing of graphene is the strong van der Waals force and π-π stacking between monolayers, which make it difficult for graphene to be completely peeled off from graphite, and maintain its monolayer state [11].

In fact, because of the limited-scale production for graphene, to use so-called graphene related materials (GRMs) is common, including graphite nanoparticles (GNP), graphene oxide or graphite oxide (GO), reduced graphene oxide or reduced graphite oxide (rGO), several-layer graphene (FLG) and multilayer graphene (MLG) [12]. They are diverse in the number of layers, lateral dimensions and/ or degree of oxidation C/O ratio [13], thereby performing differences in mechanical property, thermal property, electrical property, and dispersibility in aqueous solutions. For instance, GO is a highly oxidized and chemically modified form of graphene consisting single layer graphene with carboxylic acids, epoxides and hydroxyl groups on planes. These oxygen-containing functional groups facilitate GO to be hydrophilic and efficiently dispersed in water, but also generate high defect densities that degrade mechanical, electrical and thermal performances [5, 14]. The rGO can be obtained via reduction treatment of GO that would partially restore π-π conjugated structure by deoxygenation and dehydration, resulting in few times to few orders of magnitude increase in electrical conductivity [15]. The pristine GO with electrical conductivity of around 0.4 S/m increased the value to 0.8 S/m, 1.7×10^3 S/m and 2×10^4 S/m respectively via applying different steps of reduction (Figure 1.1) [14]. Several physical properties of GO and rGO reported in previous researchers are summarized and compared with graphene in Table 1.1. Due to the structure defects, limited surface areas, and/ or increased layers, most of properties of GO and rGO are significantly lower than for graphene that could also be found in the comparison between other GRMs and monolayer graphene. The

attractive aspect of those GRMs is that those defects on surface and edges endow them more favourable for homogeneous dispersion and easier fine interface control. They can be used to fabricate graphene-based composites with still considerable performances improvement. Besides, most of GRMs are easier to scale up production compared to single layer graphene. Considering these advantages, GRMs have been investigated together with ceramic, polymer or metal matrix to form composite materials, which makes great potential in structure reinforced materials, biosensors, interference shielding, energy conversion and energy storage [16-18].

For most of GRMs, the strong cohesive force of graphene layers brings difficulties to exfoliation and makes the dispersed sheets compact, clustered and even re-aggregate into irreversible matrices. Therefore, it is essential to limit aggregation of graphene sheets. In particular, many applications need graphene dispersions, thus a stable GRMs dispersion in liquid medium is required.

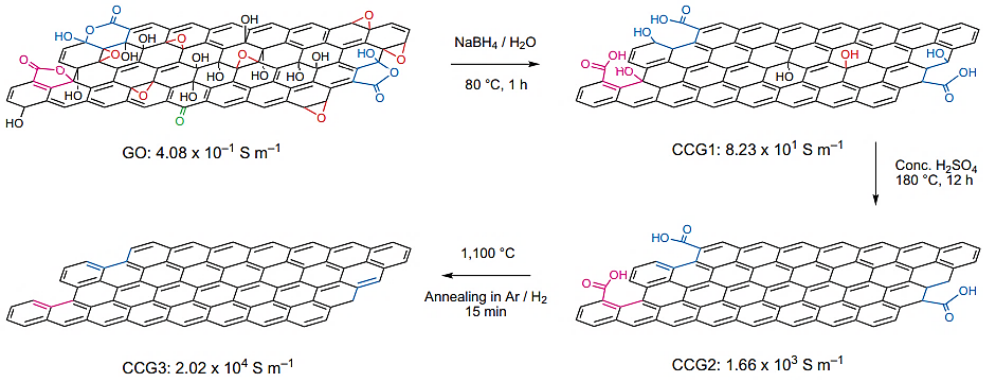

Figure 1.1 Schematic diagram of the GO reduction procedure and electrical characterization of the products. Reprinted by permission from Springer Nature Customer Service Centre GmbH: [Springer Nature] [Nature Chemistry] [14] Copyright 2009.

Table 1.1 Typical physical properties of graphene, GO and rGO

Property	Graphene	GO	rGO
Elastic modulus (GPa)	500 - 10^3 [19, 20]	208 ± 23 for monolayer GO [21], 32 for GO paper* [22]	250 ± 150 for monolayer rGO [23] 41.8 for rGO paper** [24]
Fracture strength (GPa)	130 [19]	0.015-0.13* [22]	0.293** [24]
Fracture toughness (MPa) √m	4 ± 0.6 [25]	-	-
Optical Transmittance	~ 97 % for monolayer [26, 27]	Not available (expected to be lower due to functional groups and defects)	60-90 depending on reduction agent and fabrication method [28]
Electron mobility at room temperature ($cm^2\ V^{-1}\ s^{-1}$)	3.5 ×10^5 [3]	0.05-200 [29]	17-2×10^3 [30]
Thermal conductivity (W $m^{-1}\ K^{-1}$)	~5 ×10^3 [4]	~18, ~770 [31]	30 - 250 [32] ~2×10^3 [31]
Electrical conductivities (S cm^{-1})	10^3-10^4 [33]	4 ×10^{-3} [14] 10^{-3} - 5 ×10^{-3} [34]	0.05-2 [34] 10^3 - 2.3 ×10^3 [35] 6.3 ×10^3 [36]
Specific surface area ($m^2\ g^{-1}$)	2630 [37]	2-10^3 [38, 39] ~2.4×10^3 [40]	~600-700 [41, 42] 320 [43]

* The paper-like material was made by flow-directed assembly of individual G sheets.
** The paper was fabricated by filtration of reduced graphene oxide dispersion, followed by annealing at 220 °C

1.1.2 What makes a good liquid dispersion of graphene and GRMs

A good dispersion of graphene materials requires at least 3 points: 1) the pristine GRMs can be dispersed/ exfoliated, the dispersion achieves a certain concentration,

2) a solvent/ dispersant appropriate to the application and 3) the dispersion is stable in a period. In order to obtain the good dispersion, it is important to overcome the van der Waals force and π-π stacking of graphene interlayers and maintain an energy barrier against aggregation or re-aggregation. Ultrasonication has been used to prepare graphene sheets in various solvents via exfoliation of the layered-graphitic materials, because the concentrated high-energy and shockwaves weaken van der Waals interaction between graphene sheets and caused increase of interlayer space [44]. It usually takes few days to obtain graphene sheets with single and few-layers. Sonication technique also allows the soft dispersion of GRMs, which only aims to simply separate aggregated graphitic materials. Even though dispersion or exfoliation of graphene could be achieved by sonication, the prolonged stabilization of graphene and GRMs depends on the surface charge density, selected solvent and the presence of dispersants, usually surfactants or polymers. It is well known that graphene was considered as a hydrophobic material that cannot be dispersed well within water [45]. Considering from the surface energy view, spontaneous wetting or spreading occurs when spreading coefficient, $S_{l/g}$ for solvent spreading on graphene is positive.

$$S_{l/g} = \gamma_g - \gamma_l - \gamma_{gl} > 0 \quad (1\text{-}1)$$

Where γ_g is the surface energy of graphene, γ_l is the surface tension of liquid, γ_{gl} is the interfacial energy of liquid/graphene interface. The surface tension of water γ_l at 25° C is about 72.8 mN/m, γ_g of graphene is 46.7 mN/m [46] and the interfacial energy is estimated as 77 mN/m from molecular dynamics studies [47]. The spreading coefficient far less than 0, therefore water does not spontaneously wet graphene surfaces. To achieve a favourable spreading coefficient, the surface tension of liquid phase γ_l and the interfacial energy γ_{gl} should be limited. It can be achieved by either solvent selection, or lowering the interfacial energy between aqueous solution and graphene by using surfactants or polymers to bind to the substrate [48].

Inspired from the dispersion and exfoliation of carbon nanotubes in solvents, the surface energy argumentation and solubility parameter modelling of graphene dispersion has been firstly studied with few organic solvents, for instance, N-methyl-pyrrolidone (NMP) [49] N, N-dimethylformamide (DMF) [50, 51], and Tetrahydrofuran (THF) [51]. Coleman et al. [52] prepared high-quality graphene exfoliated in NMP, which achieved concentration up to 1 mg/ml, and the yield scaled well with the square root of sonication time, $t^{1/2}$. Some other solvents were

also proved to be useful in dispersing graphene, such as dimethyl sulfoxide (DMSO) [53], and γ-butyrolactone [54]. Low surface tension is not the only important factor for choosing a suitable solvent, Hansen parameter and Hildebrand solubility parameter (HSP) [55] were also researched for understanding the dispersion mechanism of GRMs in solvents. The HSP (δ_T) can be expressed as equation (1-2)

$$\delta_T^2 = \delta_D^2 + \delta_P^2 + \delta_H^2 \tag{1-2}$$

$$\langle \delta_i \rangle = \frac{\sum_{solv} C\delta_{i,solv}}{\sum_{solv} C} \tag{1-3}$$

The square root of each of these components is a Hansen solubility parameter δi (i = *D*, *P*, *H*). δ_D, δ_P and δ_H are dispersion cohesion parameter, polarity cohesion parameter and hydrogen bonding cohesion parameter respectively. In theory, successful solvents are those where solvent and solute have similar values of HSP when solutes is nonpolar, or similar all three Hansen solubility parameters for solvent and the polar solute. However, graphene is not a molecular solute but a nanomaterial. Thus, the Hansen parameters of graphene is estimated by solvent screening, indeed, associating solubility parameters of solute with those of the most successful solvents [56]. The graphene Hansen parameters can be obtained by using equation (1-3), where *i* is *D*, *P*, or *H*. The *C* is the solubility of graphene in a given solvent and δi, is Hansen parameter in a given solvent [56]. Coleman et al. [56] measured dispersibility of graphene in 40 kinds of solvents and found that good solvents are characterized with Hildebrand solubility parameter close to graphene, with $\delta_T \sim 23$ MPa$^{1/2}$ and Hansen solubility parameters of $\delta_D \sim 18$ MPa$^{1/2}$, $\delta_P \sim 9.3$ MPa$^{1/2}$, and $\delta_H \sim 7.7$ MPa$^{1/2}$. The dispersibility of GO and rGO are compared in different solvents, taking into account of solvents polarity, surface tension, Hansen and Hildebrand solubility parameters [57]. Table 1.2 summarized solubility of GO and rGO under different solvents conditions [57]. The optimum concentrations of GO (8.7 μg/ml) and rGO (9.4 μg/ml) are both obtained in NMP with surface tension of 40.1 mN/m and δ_T of 23 MPa$^{1/2}$, which is consistent with the previous study in graphene. Except from surface tension and δ_T, the solubility of rGO is also affected via solvent polarity. By comparing dispersion of rGO in 1-Chloronaphthalene (CN) and Acetylaceton, both solvents have low surface tension and same value of δ_T but the solubility of rGO is very diverse. The good solvents to GO are NMP, ethylene glycol and water, while rGO has better solubility performance in solvents NMP, o-

Dichlorobenzene (o-DCB) and CN. However, the high boiling points of most effective organic solvents make solvents removal difficult, especially in polymer-GRMs hybrid systems. DMF, o-DCB, DMSO, ethylene glycol, NMP and CN display boiling points of 153°C, 174°C, 189°C, 195°C, 202 °C and 263 °C respectively [58]. The toxicity and health risks to human of certain organic solvents, such as NMP, ethylene glycol and DMF further limit their wide usages [58]. Additionally, the solubility and stability of GRMs dispersions could be improved by functionalization of graphene sheets, involving covalent and non-covalent functionalization. In case of covalent functionalization, small organic molecules or polymers are connected to graphene through a variety of chemical interactions occurring at the edges and defect sites of graphene [59]. Based on the characteristics of grafted molecules, the modified GRMs can be dispersed in specific solvents. More information will be provided in 1.1.4. Alternatively, another option is non-covalent functionalization, using dispersants to reduce surface tension of liquid phase and/ or reduce the interfacial energy by bonding to substrates, thus to obtain a stable graphene dispersion in water. The reduction amount of surface energy depends on the concentration and chemical structure of the stabilizer molecules [60]. The stability is controlled via electrostatic or steric repulsion, which induced formation of energy barrier to limits re-aggregation of graphene nanoplatelets [48]. The detail will be discussed in section 1.1.5.

Table 1.2 The surface tension and Hildebrand parameters δ_T of solvents and solubility of GO and rGO in range of solvents by bath sonication. Reprinted from [57], with permission from Elsevier.

	Dipole moment	Surface tension (mN/m)	δ_T (MPa $^{1/2}$)	GO solubility (μg/ml)	rGO solubility (μg/ml)
DI water	1.85	72.8	47.8	6.6	4.74
Acetone	2.88	25.2	19.9	0.8	0.9
Methanol	1.70	22.7	29.6	0.16	0.52
Ethanol	1.69	22.1	26.5	0.25	0.91
Propan-2-ol	1,66	21.66	23.6	1.82	1.2
Ethylene glycol	2.31	47.7	33	5.5	4.9
Tetrahydrofuran (THF)	1.75	26.4	19.5	2.15	1.44
N, N-dimethylformamide (DMF)	3.82	37.1	24.9	1.96	1.73
N-methyl-2-pyrrolidone (NMP)	3.75	40.1	23	8.7	9.4
n-Hexane	0.085	18.43	14.9	0.1	0.61
Dichloromethane (DCM)	1.60	26.5	20.2	0.21	1.16
Chloroform	1.02	27.5	18.9	1.3	4.6
Toluene	0.38	28.4	18.2	1.57	4.14
Chlorobenzene (CB)	1.72	33.6	19.6	1.62	3.4
o-Dichlorobenzene (o-DCB)	2.53	36.7	20.5	1.91	8.94
1-Chloronaphthalene (CN)	1.55	41.8	20.6	1.8	8.1
Acetylaceton	3.03	31.2	20.6	1.5	1.02
Diethyl ether	1.15	17	15.6	0.72	0.4

1.1.3 Types of GRMs used in liquid phase dispersions

GO

GO contains a large number of carboxylic acid, epoxide and hydroxyl groups on surface that not only reduce the interlayer forces, impart it strong hydrophilic

feature, but also provide an opportunity for surface modification with conjugate molecules and polymers. Depending on how strong the oxidation and delamination conditions are, single layer, multi-layer stack or several carbon layers can be obtained. These would properly be identified as single layer graphene oxide, multilayer graphene oxide or graphite oxide, respectively, but these are generally referred to as GO, also considering a range of different thicknesses are often obtained. The deprotonation of carboxylic groups of GO sheets dominates the colloidal stability and surface charge development, which can be modified by increasing pH [61]. The uncharged but polar epoxides and hydroxyls allow for weak interactions, hydrogen bonding and other surface reactions [28]. The solubility of GO in solvents and hydrophilicity/ lipophilicity can be changed by loading different molecules for functionalization. Besides, the unmodified areas of GO basal plane contain free surface π electrons, similar to hydrophobicity of graphene. In other words, GO is a kind of amphiphilic material, which allows different interactions with other molecules. The multi-layered GO could be produced by the rough oxidation of graphite in presence of oxidant reactants such as H_2SO_4, $KMnO_4$, H_2O_2, and then dispersed in aqueous media by sonication or other processes. Afterwards, repeated treatments, centrifugation and harsh environments produce monolayer GO [62, 63]. A highly purified monolayer GO aqueous dispersion has been prepared to concentration above 5 wt% [64]. Besides, the charges of carboxyl groups could be shield with addition of salts, such as KCl, NaCl and $MgCl_2$, consequentially, leading to an irreversible aggregation [65, 66], where divalent cations were found to aggregate GO sheets more efficiently than monovalent cations [66]. As the carboxyl groups are preferentially located at edges, smaller sheets are more charged than larger ones, which provides an alternative method (common method is centrifugation) to separate small sheets of GO from large ones by adjusting pH or ionic strength [10]. Based on the scale production and good dispersing ability of GO, it has been used widely in polymer composite materials. However, the electrical properties of GO are limited due to the break of long-range π-π conjugation structure. Based on the good performance in dispersion and the development of reduction technology, reduction of GO to obtain graphene dispersion has attracted much attention.

rGO

rGO is prepared via the reduction of graphene oxide or graphite oxide, which decreases the surface oxygen functional groups and mostly restores the sp^2 conjugation structure. However, rGO can be obtained by variously oxidized states,

which lead to the diversity of rGO in mechanical property, electrical property, thermal conductivities, and dispersion properties. Moreover, the rGO could also be different in layers: if it is monolayer or countable layer, it would be properly referred to as reduced graphene oxide, instead, if the layer are not countable or higher than 10, it should be referred to as reduced graphite oxide. However, this terminally has not been generally agreed and many autors just use rGO, regardless the thickness of the product, just the same as they call graphene particles that are in fact GNP. The reduction degree is decided by reduction approaches and conditions. The rGO could be obtained via different reduction approaches, involving thermal, chemical and UV reductions [51, 67, 68]. The rGO tends to agglomerate and precipitate in water since the reduction step increased hydrophobicity of sheets. One option is adopting a modest reduction process that reserves more oxygen content and reduces difficulties in the dispersion of rGO. The residual carboxylic acid groups of rGO sheets assist solubility and stability. Li et al. [62] prepared water-soluble rGO by using hydrazine monohydrate as reducing agent in ammonia solution at pH 10. However, the dispersed concentration and size of rGO are still limited in this way. To obtain a stable rGO dispersion with certain solubility, dispersants are typically used. Shi et al. [69] dispersed rGO in an aqueous solution by loading pyrenebutyrate (PB) towards rGO, as the large aromatic pyrene rings led PB molecules assembled on rGO via π-π stacking and the hydrophilic carboxyl groups induced repulsive interactions between rGO sheets. A frequently performed dispersion process is to disperse GO in solvent and then in situ reduce the exfoliated GO to generate a stable rGO dispersion. The used dispersant needs to be effective in separating graphite oxide into GO sheets and stabilizing the reduced counterparts. The reductants are also critical for forming final dispersions as the reduction process manipulates the amount of residual oxygen-containing groups and the quality of graphene sheets. Various reductants were used, including hydrazine [70], sodium borohydride and its derivatives [71, 72], hydrohalic acid [73], and sodium hydrosulfite [74, 75]. However, it was found commonly used reductants could be toxic to human beings and/ or environment. Some green reductants have been further studied, such as biomolecules, biomass waste biomass and plastic waste materials [76, 77].

Graphene

In addition, the liquid phase exfoliation of graphite has been studied for producing graphene flakes. Long-time sonication was applied in polar solvents for breaking apart graphite and exfoliating it into single and few-layer graphene sheets. The cavitation effects near graphite surface led to shockwaves caused by high-speed

liquid jets (up to hundreds of meters per second) that damaged graphene surface and weakened strong van der Waals interaction of adjacent layers [44]. The yield and layers of graphene sheets relay on sonication time and power. For instance, the graphene dispersion was presented with concentration of 0.3 mg/ml after sonication 400 h in aqueous solution with surfactant sodium cholate [78]. Furthermore, the concentration of exfoliated graphene reached to 1.2 mg/ml and the monolayers yields up to 4% when the process performed in solvent NMP with low-power sonication for 460 h [79].

Figure 1.2 provides a simplified structure of G, GO and rGO. The dispersibility of GRMs in water seems to be almost inversely proportional to its structural integrity, thus, the dispersion performance follows the trend of GO > rGO > graphene. It is difficult to improving dispersion of GRMs intensively without any negative impact to the structure. Selecting a suitable graphene-based material based on its end application is important because there is always a compromise between resultant physical and corresponding properties.

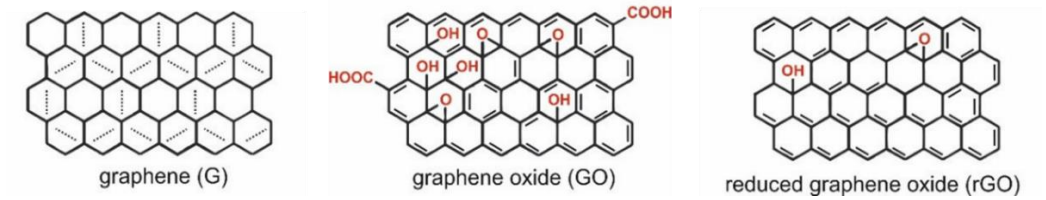

Figure 1.2 Structure of graphene (G), graphene oxide (GO) and reduced graphene oxide (rGO). Reprinted from Ref. [80]

1.1.4 Covalent functionalization for GRMs dispersions

The covalent functionalization of graphene is a useful modification method for improving liquid dispersion of GRMs as the interaction between graphene and molecules is strong and the loaded molecules impart changes in the hydrophobicity of GRMs flakes. GO is a commonly used starting material for covalent functionalization due to the sufficient functional groups for covalent grafting small organic molecules or polymers [59]. During covalent functionalization, different reactions occur between molecules and functional groups of GO, leading to differences in final graphene structures and properties. Figure 1.3 shows the fundamental information of covalent functionalization of GRMs, in respect of chemical reactions, functional groups involved in functionalization and the modifying agents [81].

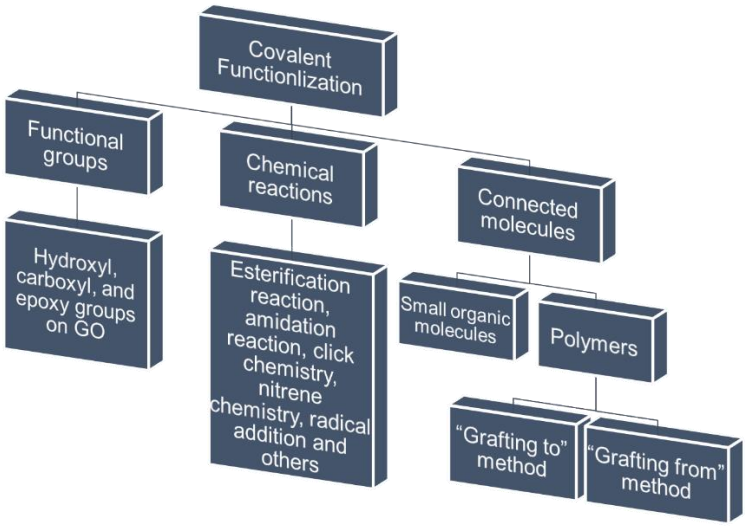

Figure 1.3 Main information of covalent functionalization of graphene sheets, including functional groups used in chemical reactions, grafting molecules and methods

Small organic molecules

In the early study, small organic molecules were used for covalent functionalization of graphene materials by combining small molecules with the oxygen-containing functional groups on GRMs. The attached new molecules with different structures induced interesting properties, in particularly, the improved dispersion performance in water and/or organic solvents. For instance, organophilic graphene was prepared via reacting of GO and octadecylamine (ODA) followed by reduction process [82, 83]. The amino of ODA covalent connected with carboxylic acid or epoxy of GO, and the long octadecyl chain transforms the hydrophilic GO to hydrophobic substance. The ODA functionalized graphene (ODA-G) dispersion reveals solubility in THF, cyclohexane, toluene, DMF, and ethanol [81]. Wang et al. [84] prepared hydrophilic GO sheets using allylamine at 90 °C for 0.5-2 h, which led to the improved solubility of GO in water from 0.69 mg/ml to 1.55 mg/ml. He [11] et al. prepared ethanol amine functionalized reduced graphene oxide (ETA-rGO), revealing dispersed nanosheets with maximum width of 1 μm and thickness of 0.8 nm in water. Functionalization of GO by imidazolium derivate has been reported by Yang [85] et al. that 1-(3-aminopropyl)-imidazolium bromide (IL-NH_2) was attached to the epoxy groups of GO nanoplatelets. The imidazolium-modified GO were stable for more than 3 months in water, DMF and DMSO due to improved solubility and electrostatic inter-sheet repulsion provided by IL-NH_2 units.

Polymers

With the research development of graphene functionalization, more and more polymers have been applied to the covalent functionalization procedure based on their apparent advantages. The polymer size could reduce significantly the cohesive interaction of graphene sheets and improve the stability of graphene-based dispersions. Besides, the presence of large number of functional groups in polymer chains increases the interfacial interaction between graphene filler and polymer matrix in graphene-polymer composites. Moreover, the structural parameters of polymers are tuneable, including monomer type, topological structure, molecular weight and electric property, which makes the covalent functionalization more feasible and effective [11]. Generally, highly soluble and processable graphene could be produced by grafting the synthetic polymers ("grafting-to" technique), or by grafting polymer monomer followed by in situ polymerization ("grafting-from" technique) [59]. The schematic diagram of grafting-from and grafting-to methods for covalent functionalization is presented in Figure 1.4 [8].

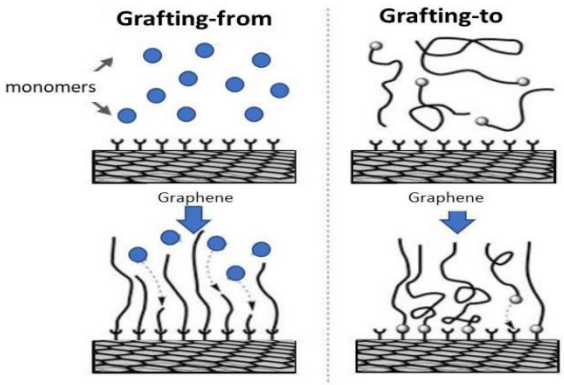

Figure 1.4 Schematic diagram of grafting-from and grafting-to methods to functionalized graphene with polymers. Reprinted from Ref [8].

Different reactions occur in the grafting-to methods. The functionalized GO was prepared through an esterification between carboxyl of GO and the hydroxyl of polyvinyl alcohol (PVA), and this functionalized GO was further reduced to produce a reduced graphene hybrid that is soluble in DMSO, or water in warm condition [86]. Rani et al. have modified GO by direct amidation with aniline, 2-aminothiazole, and 2-aminopyrimidine to synthesis the amide functionalized GO (AGO), which resulted in the solubility in water, DMSO and DMF for months stability [87]. In other cases, the former functionalization step of either graphene or polymers is required for fabrication conjugated polymer-functionalized graphene-based materials. For example, the GO was firstly acyl-chloride functionalized with

$SOCl_2$, then the esterification reaction occurs between functionalized GO and CH_2OH-terminated regioregular poly(3-hexylthiophene) (P3HT) [88]. Additionally, the nitrene chemistry is a simple and efficient strategy allowing various functional groups and polymers to covalently anchor on GO surface in one-step reaction [8]. The azido terminated poly(ethylene glycol) (PEG) and polystyrene (PS) chains were grafted on the graphene surface, and the PEG-functionalized graphene showed better dispersibility and exfoliation in water, while PS grafted graphene was dispersed better in chloroform, toluene and THF (Figure 1.5) [89]. Generally, the linkage reactions of polymers and graphene in grafting-to method are diverse, and the solubility of polymer-functionalized graphene can be adjusted from water-soluble to oil-soluble, from acidic to basic, and from polar to non-polar by choosing a suitable grafting polymer. However, the steric hindrance of polymer molecules influences their grafting density onto graphene. In addition, the attachment of the polymer to graphene usually requires a long reaction time due to the low diffusion constants of these macromolecules.

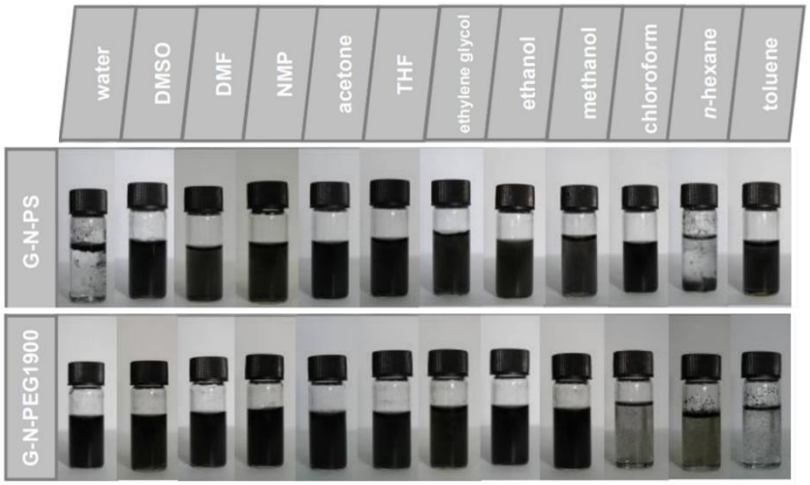

Figure 1.5 Photographs of polystyrene and poly(ethylene glycol) functionalized graphene nanosheets (G-N-PS and G-N-PEG1900) in various solvents. Reproduced with permission from [89]. Copyright 2010, American Chemical Society.

The grafting-from is a modification approach based on the anchoring of polymer-growth initiator on GRMs and followed by polymerization. This technique allows the polymers to grow directly on graphene surface, thus avoiding the slow reactivity during polymer grafting process. The length of the polymer chains and the graft density could be adjusted by varying the amount of graft initiator and its molar ratio to the polymer monomer [59]. Several grafting techniques are promoted, including atom transfer radical polymerization (ATRP) [90], reversible addition fragmentation chain transfer polymerization (RAFT) [91], polycondensation [92],

ring opening polymerization (ROP) [93], and Ziegler-Natta polymerization [94]. The poly(dimethyl aminoethyl methacrylate) (PDMA) was synthesized from GO surface via ATRP, which introducing amine group on GO firstly via amidation reaction between 1,3-diaminopropane and GO, subsequently grafting initiator via reaction of 2-bromo-2-methylpropionyl bromide with both the amine and hydroxyl groups of GO, finally forming the PDMA from GO surface after in-situ ATRP of monomer [95]. The final PDMA functionalized GO reveals significantly improved solubility in acidic aqueous solutions and in short chain alcohol. Due to the good control over the molecular weight, polymer composition and structure, the grafting-from method has shown great potential in covalently functionalizing graphene materials.

Yang et al. [96] compared the solubility of functionalized graphene sheets prepared by grafting-to method and grafting-from method respectively. The techniques of RAFT and click chemistry were used. Figure 1.6 displays the main reactions in two approaches[96]. The graphene was firstly decorated with alkyne groups using diazonium functionalization to form alkyne-functionalized graphene (alkyne-FG). In the grafting-to approach, various azide-capped polymers (polymer-N_3) were prepared by RAFT polymerization using azide-capped chain transfer agents (CTAs-N_3), then the formed polymers were grafted onto graphene sheets. In the grafting-from approach, the CTAs were introduced onto graphene by interaction of CTAs-N_3 and modified graphene at first step, which followed by RAFT polymerization to synthesis polymer chains on graphene. The grafting reaction, polymer chain length and graft density were further compared (in Figure 1.7) [96]. Due to the steric hindrance of grafted polymers, the graft density in both approaches were strongly associated with the polymer chain length, which is more obvious in grafting-to method. The solubility of functionalized graphene flakes prepared via grafting-from methods was much higher than that of samples from grafting-to because of the longer polymer chain length.

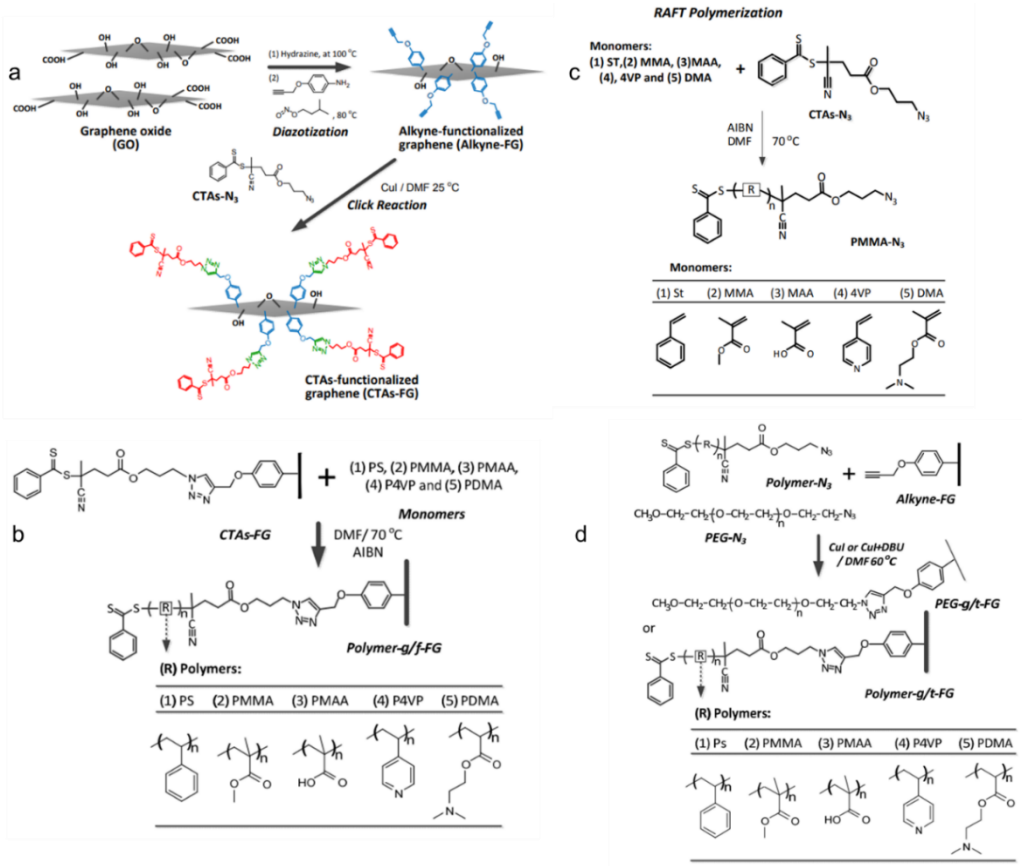

Figure 1.6 Synthesis of Alkyne-functionalized graphene (Alkyne-FG) and CTAs-functionalized graphene (CTAs-FG) (a), RAFT polymerization of vinyl monomers with CTAs-FG using 'Grafting from' method (b), RAFT polymerization of vinyl monomers with Azido-CTAs (CTAs-N3) (c), Click Reaction of polymer-N3 to Alkyne-FG using 'Grafting to' method (d). Reproduced with permission from [96]. Copyright 2010, American Chemical Society.

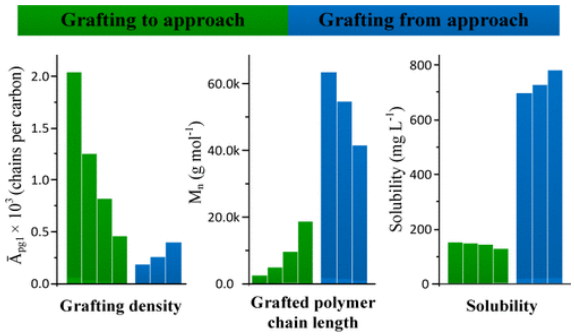

Figure 1.7 PMMA-g/t-FG samples (green) from left to right have molecular weight of PMMA-N_3 ~2 500, ~5 000, ~10 000 and ~20 000 g· mol^{-1}. PMMA-g/f-FG (blue) from left to right have weight ratios of the monomer MMA and initiator (2, 2′-azobis-(2-methylpropionitrile, AIBN) [M]/[I] 2700, 1350 and 650. Reproduced with permission from [96]. Copyright 2010, American Chemical Society.

Grafting-to and grafting-from approaches have different advantages and features in achieving covalent functionalization to graphene materials. Grafting-to method gives rise to well defined and controlled grafted polymer chains, which allows different grafting positions of polymers (at end, middle or branched chains). There are different kinds of interactions between polymers and graphene materials by taking use of different functional groups on GRMs. The major advantage of grafting-from technique is the limited effect of steric hindrance on polymer growth. The polymers typically connected on graphene via end of polymers in grafting-from approach. This method also requires fine control to reaction condition, concentration of initiator and substrate.

1.1.5 Non-covalent functionalization for GRMs dispersions

Compared to covalent functionalization, non-covalent functionalization of GRMs is considered a better choice in reducing impact on the graphene structure and, consequently, its properties [97, 98]. It depends mainly on the π-π interaction, van der Waals force, hydrogen bonding and ionic interaction. In recent years, numerous chemicals, involving surfactants and polymers (polyelectrolytes and biopolymers) have been investigated to produce GRMs dispersions in water [48, 99, 100]. These chemicals generally are bound to the graphene surface in purpose of minimizing the interfacial energy and assisting the stabilization of nanosheets dispersion.

Surfactants

GRMs can be dispersed in water by non-covalent functionalization using amphiphilic surfactants, which includes the commonly used traditional aliphatic surfactants (i. e. soaps) [101, 102] and the small polyaromatic dyes [63, 103, 104]. The polyaromatics, such as pyrene or perylene bearing polar groups, are indeed known to strongly interact with graphene via π-π stacking thanks to their aromatic structure, which provides sufficiently strong non-covalent bonding without compromising graphene properties [103, 105, 106]. The surfactants can also be classified as ionic or non-ionic surfactants based on their charges. Different surfactants interactions have been studied such as surface adsorption, micelle formation and/or π-π stacking [99, 107]. As a general principle, non-ionic surfactants exploit the hydrophobic domains to absorb to graphene surface, and the steric repulsion induced by hydrophilic heads spread into water to prevent re-aggregation. This behaviour was found in n-dodecyl β-D-maltoside (DBDM), perylenebisimide bolaamphiphile (PBI-Bola), different porphyrins and their derivatives. On the other hand, ionic surfactants impart effective charges to

graphene layers, leading to dispersions stability that can be altered via changing pH or adding salt [101, 107]. Sodium dodecylbenzen sulfonate (SDBS), the firstly investigated surfactant for graphite exfoliation, which possess an aromatic ionic molecule with a polar sulfonate group and hydrophobic dodecyl chain attached to benzene ring [102]. The suspensions with concentration of 0.002-0.05 mg/ml were obtained with ~3% monolayer and ~45% multilayer (< 5 layers) graphene sheets [102]. Nazari et al. [108] investigated graphene nanoplatelets aqueous dispersion in different types of surfactants solutions, including anionic sodium dodecylsulfate (SDS), anionic SDBS, cationic cetyltrimethylammonium bromide (CTAB) and non-ionic nonylphenolethoxylate (NPE), where CTAB-containing GNP dispersion showed the highest stability (it remained greater turbidity than other surfactants even after 200h) and lowest graphene flake size (mostly 0-10 μm). The molecular dynamic simulation demonstrated better coverage of planar surface of GNP by CTAB, while the SDS, SDBS were mainly absorbed on edge of GNP. Although it has been reported that non-ionic surfactants show better performance in dispersing GRMs than that of ionic surfactants, and the steric hindrance is more effective than electrostatic repulsion [101], the contrast results were also reported in other cases [105, 108]. The dispersion result depends on not only the type of ionic and non-ionic surfactants selected, but also the dispersing parameters, such as surfactant concentration, initial GRMs concentration, solution pH and solvents used. Theoretically, the non-ionic surfactants with larger size are more effective than smaller ones in increasing GRMs solubility in water (i.e. Brij30 vs. Brij700) due to better steric hindrance. In case of ionic surfactants, the molecules with higher electronegative functional groups are more competitive than others in driving adsorption of surfactants onto graphene sheets, while some other factors to dispersibility should also be considered, such as number and arrangement of functional groups in surfactants, and the distance between charged functional groups to their hydrophobic part. Recently, the mixed surfactants were studied for stabilizing graphene-based dispersions. The dispersion of graphene in pure surfactants of CTAB and SDS, as well as the mixture surfactants of cationic SDS/CTAB 10:90 and anionic SDS/CTAB 90: 10 were compared using UV-visible spectroscopy (UV-vis) in the study of M. Poorsargol et al., who discovered better solubility of graphene sheets (higher absorption intensity in UV-vis) in pure SDS and cationic SDS/CTAB 90:10 because the SDS's shorter alkyl chain than CTAB facilitates easier and stronger adsorption on graphene nanosheets [109].

Polymers

The non-covalent bonding can also be obtained between polymers and GRMs via different interactions. Similarly, the adhesion of polymer onto graphene and the anti-aggregation force are required for maintaining a stable dispersion when ionic or non-ionic polymers are used. Non-ionic polymer poly(vinylpyrrolidone) (PVP) has been investigated to directly exfoliated high quality graphene from graphite powder in aqueous solution, because it had a great affinity to graphite surface and the N-substituted pyrrolidone rings of PVP resembles structure of NMP [110]. L. Guardia et al. compared effect of a range of surfactants and polymers in producing graphene dispersion, where non-ionic polymer Pluronic®P-123 yielding the highest graphene concentration of 1.5mg/ ml after 5 h sonication [101]. Benefit from the π-π stacking, a number of pyrene-based polymers, such as pyrene-polyethylene glycol (Py-PEG_{2K} and Py-PEG_{5K}), pyrene-polycaprolactone (Py-PCL_{19} and Py-PCL_{48}) [111], poly(pyrenemethyl acrylate)-b-poly[(polyethylene glycol) acrylate] (polyPA-b-polyPEG-A) [112], pyrene-poly(2-N,N0 -(dimethyl amino ethyl acrylate) (Py-PDMAEA) and pyrene-poly(acrylic acid) (Py-PAA) [113] were also investigated to exfoliate graphite and fabricate stable dispersions. In addition, the hydrogen bonding was found between polyvinyl alcohol (PVA) and rGO in preparing nanocomposites as the residual carboxyl and hydroxyl groups on rGO surface interacted with hydroxyl of PVA [114, 115]. The hydrophobic interaction was also employed for adhesion polymers to graphene surface. For example, the biomolecule heparin consists of a relatively hydrophobic cellulose backbone, and a dense hydrophilic network of negatively charged carboxylates and sulfonate groups. The interaction of rGO and heparin is associated with the hydrophobic character of the heparin backbone and the rGO surface, while the repulsive forces between the charged surfaces of the composite keep it stable in aqueous biological media dispersion [116].

Compared with surfactant molecules, the polymers have the variable molecular weight and topological structure that make their dispersing ability to be tuneable, more important, the polymer assisted GRMs dispersions can be directly processed to fabricate composite materials.

Overall, a massive amount of research has been devoted to improving the liquid dispersion of graphene and GRMs by using different strategies. Among them, covalent functionalization provides strong and stable bonds between GRMs and other species, which allows dispersibility regulation in different solvents by taking use of functional groups of GRMs, typically GO. In contrast to the concept of "grafting" in covalent functionalization, non-covalent functionalization of GRMs

emphasizes the adsorption of molecules onto GRMs in a non-destructive way. It will not damage the conjugated basal network of graphene, thus providing better preservation of mechanical properties and inherent electronic properties.

1.2 Polyelectrolytes and polyelectrolyte functionalized GRMs dispersions

1.2.1 Polyelectrolytes

Polyelectrolytes (PEs) is a class of macromolecular materials that could be dissociated into highly charged polymeric chains when dissolved in a suitable solvent, generally in water [117]. PEs can be classified as cationic, anionic or zwitterionic type based on the group charges on the macromolecular chain. If the group is ionic (i.e. based on an ionic bond), dissociation should be complete, corresponding to a so-called strong PE whose charge is fixed. On the other hand, partial dissociation is usually obtained from polar covalent bonds, that may dissociate to produce ions, corresponding to a weak PE whose charge responds to the local electrostatic environment by the chemical equilibrium known as ionization [118-120]. Due to the partial or complete dissociation, the electrostatic intra- and intermolecular interactions raise and that result in dramatic deviations of PEs behaviours compared with an uncharged state.

Additionally, different stimuli were used to tune the PEs conformations and properties such as pH, ionic strength and polarity of solvent. The ionic strength can majorly alter PEs properties, like chain conformation, diffusion coefficients, solution viscosity, polarizability, miscibility and so on [117, 121, 122]. The conformation of PE chains depend on number of counterions strongly attached to the backbone of the PE, the higher the number of counterions, the smaller the chain size, which leads to the transition from extended to collapsed conformation [123]. . For the weak PEs, pH can influence the charge density and dispersing properties by changing the degree of dissociation [124]. The PEs are highly attractive in biomedicine, food and water treatment based on their sensitive to specific conditions. Due to the abundant of charges on polyelectrolytes, they are used for stabilizing, immobilizing or dispersing nanoparticles in liquid system. Many studies on complexation of biomolecules and polyelectrolytes have been performed out of interest in protein stabilization, immobilization and separation [121, 125].. Figure 1.8 shows a typical spherical polyelectrolyte brushes, consisting of polystyrene core and linear anionic polyelectrolyte grafted, polyacrylic acid (PAA) [126]. Comparing with free PAA with random coil conformation in solution, the

stretched-out conformation of PAA on colloidal particles provided enough space for immobilization of protein molecules. In addition, it is also reported that the PEs were useful for dispersing carbon nanotubes (CNTs), by attaching covalently to nanotubes surface [127] or via non-covalent modification [128, 129].

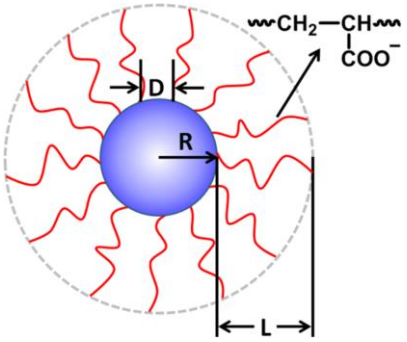

Figure 1.8 Structure of confined PAA on a nanoparticle surface. R is the radius of a polystyrene nanoparticle, D is the average distance between two PAA chains, and L is the thickness of PAA layer attached on the nanoparticle. Reprinted by permission from Springer Nature Customer Service Centre GmbH: [Springer Nature] [Colloid and Polymer Science] [126] Copyright 2019

1.2.2 PE-functionalized GRMs for aqueous dispersion

Similarly to un-charged polymers using for GRMs dispersion, the hydrophobic part or aromatic structure in PEs might also be considered for the preparation of GRMs water suspension, because PE is water soluble and its substantial amount of charges provide repulsive force to limit re-stacking of graphene sheets [97, 130]. For instance, poly(styrenesulfonate) (PSS) has been served for stabilizing graphene nanoplatelets suspension because its benzene rings offer the possibility for π-π stacking with graphene sheets, meanwhile the sulfophenyl groups allow rGO to be hydrophilic [131-133]. The stable graphene sheets dispersion in water was achieved via exfoliation/in-situ reduction of graphite oxide in presence of PSS [133]. With concentration lower than 0.1 mg/ml, the dispersion obtained after 30 min sonication could be stable for over one year, while a certain amount of precipitate appeared after several days in higher concentrated dispersions [133]. In the non-covalent modification, the high concentration of PSS is required for preventing aggregation of graphene sheets, usually 10 folds to rGO in weight ratio. In previous literature, PEs have been widely investigated in amount of empirical tests to facilitate the dispersion of GRMs by combining with other different auxiliary means, including the use or addition of organic solvents/surfactants [134, 135], in-situ reduction of GO to form covalent or non-covalent functionalization [136, 137], and modification

of polyelectrolytes, like pyrene-terminated polyacrylic acid (py-PAA) [111, 113]. In order to achieve aqueous dispersions of GRMs, the combined use of PEs and other dispersants was recently investigated. The hexadecyltrimethylammonium (CTAB)-exfoliated graphite followed by branched poly(ethylenimine) (BPEI) modification [134] was reported to produce a stable graphene dispersion with maximum concentration of 0.55 mg/ml, which was even more stable when using BPEI with higher molecular weight. In addition, the exfoliation and reduction of GO in presence/assistance of PEs were investigated. They are to exploit the strong ionic and/or hydrogen-bond interaction occurring between GO and PEs by performing the GO reduction in presence of the PE of selected [115, 138, 139] or GO reduction followed by in situ living free radical polymerization [140]. During the radical polymerization of PAA, the charged polymer is wrapped onto the graphene sheets because the radical initiators can activate graphene sheet to open π-bonds and allow graphene to participate in polymerization process[141]. It was reported that hydrogen-bond interaction occurring between carboxymethyl cellulose (CMC) and rGO by performing the GO reduction and then ultrasonication with CMC [139]. Interestingly, few PEs can yield synergistic reduction effects while exerting their main stabilizing function. For instance, Poly(diallyldimethylammonium chloride) (PDAC) not only induces the reduction process but also improves the stability of the resulting PDAC modified rGO (PDAC-rGO) dispersions due to electrostatic repulsion [142-144]. Chitosan (CS) was used as both a reductant and a stabilizing agent to prepare stable RGO suspensions [145]. Although the literature background has clearly highlighted the potentialities of different PEs in producing rGO dispersions, there are only few research works focused on the direct stabilization graphene sheets with only assistance of PEs. Viinikanoja et al. [146] compared some ionic molecules including six ionic surfactants and two PEs, in which the best colloidal stability, based on zeta potential of graphene flakes were obtained with PSS and BPEI. Lu et al. [147] studied stability of aqueous suspensions of exfoliated graphite nanoplatelets (GNP) with few polyelectrolytes, namely PDAC, PSS, BPEI or PAA, showing that approximately half of the initial GNP was retained after 48 h in PSS and BPEI dispersions.

As mentioned before, the morphology and properties of PEs responds to the local electrostatic environment, thus that could further influence the dispersion of GRMs when pH, ionic strength changed. The stability of BPEI dispersed graphene suspension increased at lower pH due to the increasing of electrostatic repulsion between graphene sheets by adsorption of PEI molecules, while aggregation of graphene sheets could be induced at high salt concentration [134]. The pH

responsive behaviour of the chitosan dispersed rGO suspension was also observed as the alterations of molecular conformation and charging state of chitosan [136]. These environmental parameters sensitive stability performance makes the dispersion system highly desirable and to be potential in biological and medical applications.

Numerous studies have been carried out on PE covalently or non-covalently functionalized GRMs and their dispersions, which connects the GRMs dispersion with polymers, providing a shortcut for the preparation of graphene/polymer composites. For the aqueous PEs dispersed GRMs, the step of solvent removal is eliminated which is a critical step when using organic solvent and other ionic molecules for GRMs stabilization. Nevertheless, how to improve the adsorption capacity and adsorption strength of molecules to GRM surface, and improve the higher stabilization efficiency still need to be further explored.

1.3 Polyelectrolyte complexes

1.3.1 Polyelectrolytes complexes and polyelectrolyte multilayers

A major characteristic of polyelectrolytes is the tendency to complex with oppositely charged one(s), forming polyelectrolyte complexes (PECs) or polyelectrolyte multilayers (PEMs). The electrostatic interaction accounts for the main effect for polymer chains bonding, other interactions, like hydrogen bonding, ionic dipole forces and hydrophobic interactions could also be included in some PECs [148].

Based on the thermodynamic contributions, the formation of PEC benefits from the entropy gained by releasing counterions [149-151]. PE molecules in aqueous solution are surrounded by the electrical double layer, which limit the motion of counterions closing to the ionic sites of PE chains. When the ionic groups of the opposite charged PEs interacted during complexation, the double layer is destroyed to a certain extent and these counterions are released. The fundamental interaction in a PEC is represented in equilibrium (1-4) [152]:

$$Pol^{+}A^{-}_{aq} + Pol^{-}C^{+}_{aq} \rightleftharpoons Pol^{+}Pol^{-}_{s} + A^{-}_{aq} + C^{+}_{aq} \tag{1-4}$$

Where Pol^{-} and Pol^{+} are respective polyanion and polycation repeat units, A^{-} and C^{+} are counteranion and countercation respectively. The subscript *s* represents PEC phase and *aq* refers to a solution phase. Therefore, the formation of PEC is favourable as the counterions release increases entropy and decreases the free

energy in system. The complexes formation also leads to the loss of freedom degree of PE chains that contributes to the entropy change, however, this loss is small compared with the entropy gain origin from counterions release [153]. The PEMs are established by self-assembly of polycations and polyanions from diluted solution onto a charged substrate, the widely used technique is called layer-by-layer electrostatic self-assembly (LbL) [154]. The thermodynamic contribution for the PEMs formation is similar to PEC, the entropy increases due to the release of counterions. Most of PEMs have been found to contain a very small numbers of counterions because they are removed during deposition and subsequent rinsing steps. Another entropy contribution to free energy change in LbL assembly is the release of solvent molecules from the hydration shell [148]. Thus, enhancing the electrostatic interaction during complexation is benefit to both of the PEC formation and PEM build-up because of the dropped free energy.

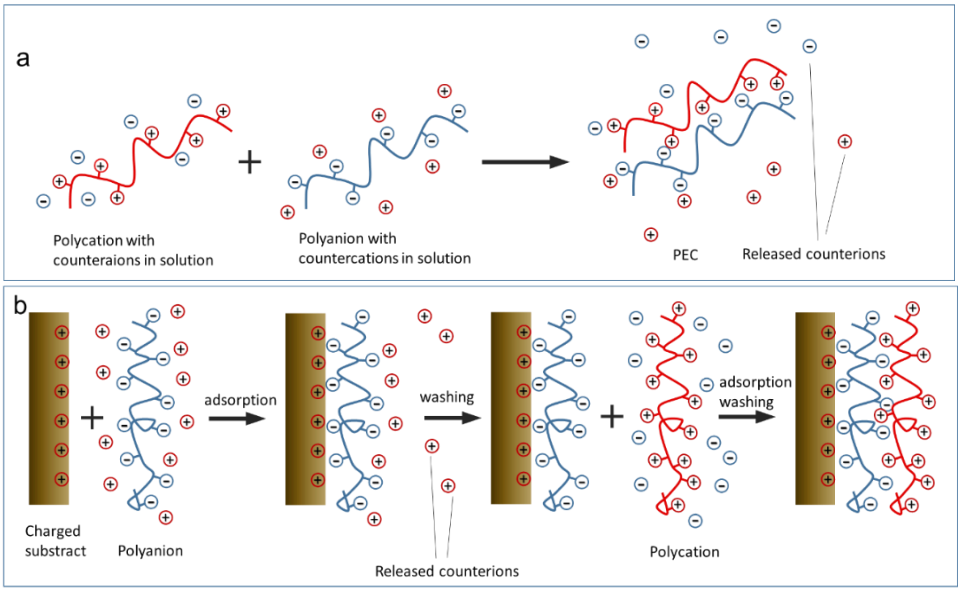

Figure 1.9 The formation of PEC in solution with counterions release (a) and PEM fabrication via LbL (b).

The complexation process of PEC can be usually divided into three steps, primary complex formation, intracomplex and intercomplex/ aggregation process [121, 148]. In the step one, the primary complexes formed immediately via electrostatic interaction after mixing oppositely charged PEs solutions. Then, new electrostatic bonds form and chains rearrangement occurs in 1-2 h that forms the PEC particles. At last, the intermediate complexes further aggregate to larger structures through hydrophobic interactions. The aggregation process can be accelerated via stirring. Similar to the formation of PEC, the deposition of PEM

shows two steps: a fast adsorption followed by a slow rearrangement. The PE molecules move to surface in few seconds as the electrostatic attraction, and then they move within layers and change conformation in few hours. The formation in PEC and PEM is affected by both polymer structure and complexation conditions.

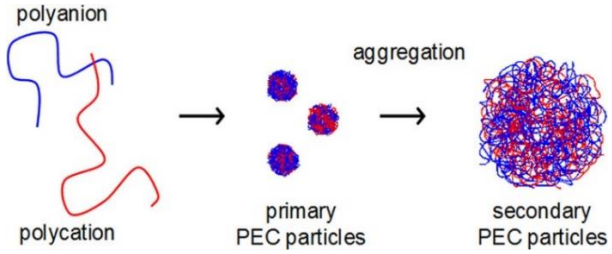

Figure 1.10 The processes occurring during mixing of PE solutions and formation of PEC particles [155]. Copyright 2012, American Chemical Society.

On a macroscopic level, the complexation process results in aggregated polymers and phase separation from a solution state into a highly diluted supernatant phase and a dense polymer-rich phase. The resulted dense phase could be solid-like precipitate or liquid-like coacervate (the loosely associated PEs with more liquid-like properties) depending on the interaction strength between PEs chains. The coacervate is a reversible and equilibrium phase near charge neutrality, which can be considered as a semidilute solution mediated by dynamic rearranging ion pairs between many distinct polymer chains [156, 157]. The coacervates have been studied as potential biopolymers with applications in cosmetic, food, pharmaceutical and biomedicine industry. Nevertheless, the formation of solid precipitate is a kinetically controlled process via strong attractive interaction of PEs, which is irrespective of the mixing stoichiometry [157]. The precipitates show stiff or rubber-like properties and are opaque due to intrinsic inhomogeneity [158]. The solid PECs are generally assumed to be a kinetically arrested glassy state [156]. The morphology of PEC is controlled by the balance of water, polymers and salt ions within the complexes. When the "doping" salt (counterions) concentration is increased, the intrinsic charge compensation (Pol^+ Pol^-) transfers into extrinsic charge compensation (Pol^- M^+, Pol^+ A^-) and eventually resulting in the dissociated PE chains, therefore the morphologies of PECs can be altered from dense precipitates to polyelectrolyte coacervates, or even a PEs solution[120, 159]. The intrinsic and extrinsic ionic pairs has been proposed [160] and shown in Figure 1.11. The transition of solid complex to coacervate leads to a dramatic decrease of viscosity and storage modulus as the physical cross-link of PE chains is contribute only by intrinsic interaction [156]. In addition, the ion-pairing strength and complex morphology (precipitates or coacervates) could be influenced by hydrophobicity of

PEs, where the more hydrophilic PECs tend to be weakly associated with each other and form coacervates , small primary amines bind strongly, carboxylates bind weakly, and aromatic sulfonates interact more strongly than aliphatic ones [161].

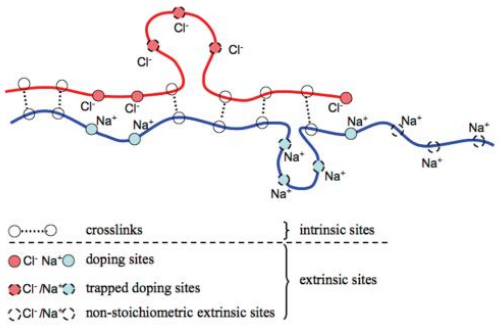

Figure 1.11 Representation of intrinsic and extrinsic compensation in PEC [160]

As there is abound of water in the dense polymer-rich phase, the PEC is usually densified by ultracentrifugation [160], extrusion [152], hot-pressing (compression moulding) [162] or sedimentation/evaporation [163]. The obtained dense solids are called compacted polyelectrolyte complexes (CoPECs). During compaction, much of water is removed and the aggregated structures are forced together. Centrifugation is a commonly used method to separate PEC and water via centrifugal force, but the CoPECs still contains pores and voids after drying [160]. Unlike the macroporous CoPEC prepared by centrifugation, extrusion process eliminates most of water and porous, resulting in a dense material that is less deformable [152]. Salt has been found to be useful in plasticizing PEC and blending the PEs under strong shear force during extrusion process [152]. It is notable to maintain sort of water in starting PEC for extrusion and hot-pressing as the dry PEC is brittle and impossible to be processed. The hot-pressing is a method applied to fabricate CoPEC films with desired shape and thickness [162, 164].

On the other hand, the PEMs are fabricated by repeatedly assembling oppositely charged PEs because the overcompensation of charges on deposited layer makes sure the adsorption of subsequently opposite charged PE chains and the formation of stable multilayer [165]. The deposition amount and multilayer thickness follow either linear or exponential growth mechanism [166-168]. In linear growth of PEMs, the charge inversion during each deposition is independent from deposited layer number, thus the increased mass for each layer is also constant that is typically found for PEs with high charge density. The PEMs fabricated with linear growth exhibit more controlled film structure and composition. In general, these films show low swelling and low solution transport due to the high degree of ionic crosslinking. However, the PEs with low charge density, low molecular

weight, high flexibility of the polymer chains and better hydrophilicity are favourable for the exponential growth of PEMs [148]. In the exponential growth, the incoming PE molecules acting as free polyions that not only interact with outer surface, but also enter multilayer structure. These polyions move to the surface to increase the surface net charges and then complex with opposite charged polymer chains during rinsing. Thus, more and more PE chains can diffuse in and out during LbL assembly, and the mass increment is varied with layer number increasing. These obtained PEMs can be considered similar to coacervate in PECs since they both have the loosely associated PEs and more liquid like properties. The permeable property of exponential growth films makes them to be effective in exchange process. Moreover, it should be noted that the growth mechanism in some of PEMs could be tuned with modifying LbL condition. For instance, in the alternating adsorption of poly(allyl amine hydrochloride) (PAH) and poly(acrylic acid) (PAA), different growth laws and properties were found depending to the pH value during deposition [168]. The identity of PEs and the interaction between PEs determine the thickness, roughness and wettability of PEMS. PEMs are recognized as materials with the potential for biomedical and environmental applications [169].

1.3.2 Parameters affecting the formation and properties of PEC

The formation and properties of PECs can be controlled by varying certain parameters including the structure parameters (like charge density and molecular size), media parameters (PE concentration, pH, ionic strength of react medium and salt concentration) and preparation parameters (mixing order, temperature, mixing ratio and so on).

The salt concentration is a significant parameter to control the cross-linking density and PECs' properties as the salt can transfer the intrinsic sites between polymer/polymer ion pairs into extrinsic sites of polymer/counterion pairs. The salt interacts with PEs based on the following equilibrium (1-5). M^+ and A^- are salt cations and salt anions respectively. The doping equilibrium is summarized by equation (1-6) [149], in which the salt doping level φ is defined as the ratio of extrinsic ion pairs to total ion pairs in PECs, and $(1-\varphi)$ is therefore the fraction of intrinsic ion pairs. With salt concentration increased, the association and cross-link of polymer chains became looser, until the number of the intrinsic ion pairs is not sufficient to maintain a polymer-dense phase and PEC dissociates, the salt concentration at this transform point is called critical salt concentration [170]. The doping level varies from 0 where no extrinsic charge compensation exists, to 1 where no intrinsic charge compensation exists. Besides, salt ions were found to

partition preferentially in supernatant phase compared to polymer-rich coacervate or precipitate phase due to the excluded volume effects [171, 172]. Since salt ions provide additional free volume for polymer chain motion and weaken ion pairing of Pol^+ and Pol^-, which leads to the weakness in mechanical properties and decrease in glass transition temperature (Tg). The Tg of PDAC/PSS with 24 wt% water decreased from 70 °C to 32 °C when the salt concentration increased from 0 to 1.5 M [173]. Additionally, the room temperature mending and self-healing process of PAA/PAH were faster and more complete with increasing salt concentration, which caused the fast inter-diffusion of polymer chains at the incision [174]. The self-healing ability of BPEI/PAA was improved after being exposed to NaCl solution, while it became more rigid after exposure in transition metal ion containing salt ($CuCl_2$) [164]. Not only salt concentration, but also salt type affects the complexation in polyanion and polycation [175, 176]. Dautzenberg et al. [175] studied the response of different PECs, PSS/PDAC poly(methacrylate) (PMA)/PDAC, to addition of various chloride salts, including LiCl, NaCl, KCl, $CaCl_2$, $MgCl_2$, $AlCl_3$, and $FeCl_3$, in which the ion radius of monovalent cations had essentially no effects on the response of PECs, but the multivalent cation brought about rapid flocculation of complexes, especially in the case of polyanion-excess complexes. Considering the strong power of salt to PEC fabrication, stability and physic-mechanical properties, interaction of salt and PEs, salt and PECs have been widely investigated in recent years.

$$Pol^+Pol^-_\varphi + \varphi M^+_{aq} + \varphi A^-_{aq} \rightleftharpoons Pol^+A^-_\varphi + Pol^-M^+_\varphi \tag{1-5}$$

$$K_{dop} = \frac{\varphi^2}{(1-\varphi)[MA]^2} \tag{1-6}$$

For the weak PE involved PECs and PEMs, the formation process and the properties could be strongly influenced by pH. During the fabrication of PAA/PAH multilayers, the layer thickness is depends greatly on the pH of PAA and PAH [177]. Larson et al. studied the effects of pH and concentration on the complexation behaviour of PAA- poly(N,N-dimethylaminoethyl methacrylate) (PDMAEMA) - KCl and PAA-PDAC-KCl , where the critical salt concentration for phase separation increased with increasing of PE ionization degree [178]. Rydzek et al. prepared poly-(methacrylic acid) (PMAA)/PAH CoPEC by mixing two polymers in an equimolar concentration at pH 7 and investigated the response of fabricated (PMAA)/PAH complexes to pH changes, including composition, charge balance,

microstructure, water content and cross-link points [179]. They found that the most of reticulations points of PMAA and PAA were reserved from pH 7 to 4.5, while at PH 3 and pH 9, the extrinsic charge compensation was predominant, indicating the breakage of PMAA/PAH bonds and increased doping rate of carboxylate groups. These structure variations of PMAA/PAA indicates the differences in composite's mechanical property and porosity, in brief, stiffer and more porous PEC was obtained owing to poor solubility of PMMA at low pH, and ductile softer PEC with modest porosity was formed at high pH resulting from the intake of counterions. In addition, the PE condition (concentration and PE molecular weight) and mixing condition (mixing ration and order) could directly affect the PEC products in structure, morphology and/ or stability. In general, the size of the formed PEC particles increases with increasing polymer concentration, while the complexes dispersion, polydispersity index could be constant or unstable with variation of concentration [148, 180]. During the titration process of poly(acrylate) (PA) with PAH, or in opposite direction, no phase separation was observed at low PE concentration ($C_{\text{titrand}} \leq 1\times10^{-3}$ mol L^{-1}) and no electrolyte present. In contrast, the coalescence with smaller primary complexes resulting in flocculation occurs near the equivalence by increasing PE concentration [181]. In the early study of polyelectrolyte complexation, it was reported that the constant binding between two oppositely charged PEs is associated with the number of contact point, which could be determined by molecular weight of PEs. The association of PEs has shown a preference to the components with higher molecular weight, the range of phase separation (flocculation and/or coacervation) enlarged by increasing molecular weight of molecules [182]. Monte Carlo simulations suggested that when the applied PEs have same length and the amount of both PEs are nearly equal, the tendency to form large clusters of PECs reached a maximum, however, when one of PEs is shorter, the propensity to form large clusters decreased and the fluctuations in cluster charge increased [183]. In the complexes system of PAA/PDAC, the PAA with lower molecular weight didn't show a pH-responsive conformational change, but the different electron spin resonance (ESR) spectroscopy was found in bigger-sized PAA at different pH, which could lead to the different complexation behaviour of PAA and other molecules [184]. On the other hand, using longer PAA chains (38k Da) to mix with PDAC at extremely low mixing ratio (molar ratio of PAA/PDAC=0.01), the PEC nanoparticles formed with radius 300 nm, while the soluble complexes were formed using short PAA chains (2k Da) at the same mixing condition [185].

The relative ratio of components determines the morphology, structure and stability of PECs. Stoichiometric mixing of PEs with comparable molecular weight

usually forms highly aggregated and insoluble complexes, however, a non-stoichiometric ratios could result in smaller complexes [153]. A complex having extremely low/high content of polycation (or polyanion) is colloidal stable as the hairy shell of excess charges covered hydrophobic core, while the neutral condensed coacervate droplets formed when the mixing ratio of polycation and polyanion is close to 1, which leads to the instability of complexes in liquid phase [148, 157, 183, 185]. The transition boundary of nano-sized stable complexes and insoluble unstable aggregates could be changed by salt: with increasing salt concentration ,the nanoparticles incline to flocculate and further dissociate [186]. Additionally, the highest ionic crosslink density of compact PAH/PAA was obtained at a stoichiometric ratio (1:1) of PAA to PAH, thus causing the highest storage modulus and loss modulus and the lowest water content [187]. On the other hand, the mixing order could also influence the formation of complexes. A two-step behaviour in thermodynamic titration of PDAC and sodium polyacrylate (PANa) (addition of PDAC to PANa or vice-versa) was observed: the primary process was the formation of highly charged complexes in size of 100 nm, then these charged complexes transformed towards coacervate droplet at around charge stoichiometry, which was referred as the second process. The results indicated that 1) the complexes formation was endothermic for both mixing orders, with small positive enthalpies (+(3.4-5.0) kJ mol^{-1}) and large positive entropies (+(83-98) J mol^{-1} K^{-1}); 2) the coacervate transition was exothermic for the addition of PDAC in PANa (-(2.1-3.0) kJ mol^{-1}), and endothermic for versa order (+(2.5-7.0) kJ mol^{-1}), while their entropies were both positive with number of (+(60-90) J mol^{-1} K^{-1} and +(90-110) J mol^{-1} K^{-1}, which indicates the entropically driven in PEC formation [188].

1.4 Incorporation of organic and in-organic particles into PECs

In the last decades, the incorporation of particles or molecules into PEMs and PECs has attracted great interest as potential composite materials in pharmaceutical and biomedical fields. The loaded active substances include drugs, proteins, peptides and other bioactive molecules. With the developments particles loading and releasing in PECs, other incorporated molecules have been explored into PEMs and PECs for extending applications, such as polyoxometalates (POMs), single- or multi-walled carbon nanotubes, GRMs, and other inorganic nanoparticles. In general, there are four different ways for the incorporation of active substances in PEMs or PECs [121]:

1) Entrapment of active substances in solution during complexation,

2) Adsorption of active substances by PEC with special structures, like porous materials or gels with sponge-like properties,

3) Chemical bonding between active components and PEs,

4) Employment of the active compounds as a partner of PEC formation.

The incorporation is affected by size, shape, charge and concentration of particles, as well as external parameters like ionic strength, pH and temperature.

1.4.1 Incorporation of proteins, drugs and bioactive molecules

A large number of bioactive substances, involving drugs, enzymes, proteins and liposomes, have been incorporated into PEMs and PECs for drug-releasing [189, 190]. The incorporation of bioactive molecules with PEs could be achieved either by encapsulating drugs or other bioactive components within a shell made of alternating anionic and cationic PEs, or by the adsorption within PEM nanofilms. Different strategies were applied to the loading and release of bioactive particles according to their structure and properties. The small charged drugs could directly participate in the PECs or PEMs fabrication, for example, cefazolin and gentamicin incorporated into poly-l-lysine/ poly-l-glutamic acid (PLL/PLGA) multilayer based on the electrostatic interaction [191]. The drug binding-sites within the PECs can be tuned simply by changing pH of solutions when the weak PEs were applied, which provided an effective method to control drug adsorption/ release. In the case of small, uncharged, hydrophobic molecules, the integration of amphiphilic block copolymer micelles was used, which provide a hydrophobic core to isolate drugs and a charged hydrophilic part to interact with the oppositely charged PE [192-194]. In addition, building microporous and/ or nanoporous structure is benefits to improve molecules adsorption. The microporous structure of PEI/PAA multilayers fabricated by freeze drying technique was used to load high content of hydrophobic drug, and these porous were healed via exposure to saturated humidity [195]. This healable porous PEI/PAA is favourable for the long-term sustained release of drugs. Proteins are long chain of polypeptides with particular sequences that are folded into globular structures by secondary intermolecular interactions, containing both positively and negatively charged amino acids as well as other amino acids [196]. Thus, the protein can complex with oppositely charged homo or block PEs to form bulk or micellar complexes. Generally, proteins are weakly charged macromolecules with low charge density but in a mon-uniform distribution. To enable their surface properties to be standardized, in recent studies the protein was complexed with PE to obtain protein-polyelectrolyte complex (PPC), which can be assembled via LbL assembly with another oppositely charged PE [197, 198].

1.4.2 Incorporation of metal nanoparticles

The tantalizing potential of PECs as sorbents or ion-exchange materials inspired investigators' interest in the incorporation of metal ions in macromolecule assemblies. The adsorption of metal ions from solutions is a useful method to embedded metal ions into PEMs, these multilayers could be further applied as precursors for polymer-metal nanoparticles fabrication. For instance, the Ag nanoparticles enriched nanocomposite films with improved catalytic and electrical properties were prepared by reducing PEC multilayer film containing Ag^+ (PAA-(PEI_1-Ag^+/$PAA_{0.45}$)) [199]. The metal ions in PECs or PEMs could be reduced into metal nanoparticles via chemical reduction or radiation reduction. The chemical reducer includes aluminium hydrides, borohydride, hypophosphites, formaldehyde and others [200-202]. Highly connected PEs capped Pt nanoparticles were fabricated by alternately soaking electrodes in PSS and Pt-PDAC nanoparticles dispersions, where the Pt nanoparticles were reduced from $PtCl_6^{2-}$ ions using reducer $NaBH_4$ in presence of PDAC [203]. Besides, PDAC has been proved to be considered as stabilizer for Au nanoparticles [142], or the reducer and encapsulate to Au particles [204]. On the other hand, the X-ray irradiation induced preparation of metal particles (copper, silver and gold) in coatings of PEI-PSS and PEI-PAA complexes, revealing an improved antibacterial activity [205]. The preparation of metal-polymer composite with a variable size of metal nanoparticles has driven the development in catalytic, antibacterial and magnetic materials.

1.4.3 Incorporation with silica, carbon nanotubes, GRMs and other inorganic particles

In the previous literature, the fabrication of organic/inorganic nanocomposites has been widely studied as the incorporation of inorganic fillers in a polymer matrix usually increases the strength and stiffness, as well as other properties. Beside of metal-based nanoparticles, a number of inorganic compounds with different shapes and sizes have been investigated for doping PECs and PEMs. PEC-silica hybrid colloidal particles have been synthesized by using negatively charged PEC micelles, nonstoichiometric complexation of polycation poly(L-lysine) (PLL) and PLGA, PSS, or PAA, as colloidal templates for silica mineralization [206]. The amino groups of PLL interacted with orthosilicic acid/ silicate oligomers, leading to the aggregation of silicate precursor near amino groups and polycondensation of orthosilicic acid. As reported in Figure 1.12, the polycation induced silica mineralization, the excess negative charges of PEC endowed the hybrid particles

with good colloidal stability. The size, charges of PEC-silica particles and the chain conformation of complex were determined by mixing ratio of polyanion and polycation, and the molecular weight of polymers. In addition, SiO_2 nanoparticles were finely dispersed in PEC nanohybrid membranes due to the pre-dispersion of SiO_2 nanoparticles in low viscosity anionic PE solutions and the in situ incorporation with polycations during complexation [207].

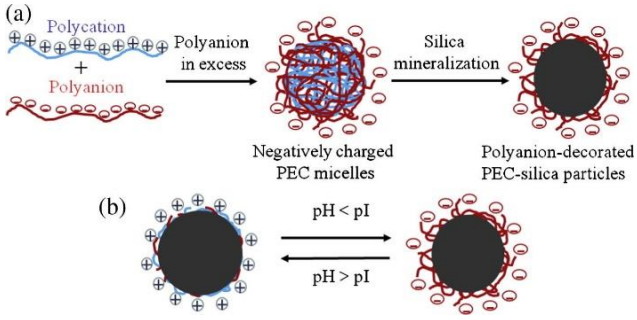

Figure 1.12 Schematic diagram of formation of polyanion-decorated PEC-silica particles (a) and the charge change on particles with varying pH (b). Reprinted from [206], Copyright (2015), with permission from Elsevier.

Nanocalys are nanosized phyllosilicate minerals with layered structure units, which bear a net surface charge resulting from isomorphic substitutions [208]. The nanoclay particles are very fine, and the charges between particles induce their stability in dispersions. The cationic PEs have been used in coagulation-flocculation processes of clays as the adsorption of polymer chains on particles resulted in the surface charge neutralization. The clay could also be used for improving mechanical, impermeability and flame retardancy properties of PECs. It was found that the montmorillonite (MMT) clay increased the degree of swelling, mechanical resistance, improved thermal stability of hydrogel PEC based on pectin, chitosan and MMT [209]. The kaolinite clay decorated PAA/PEI coacervate was prepared and deposited onto poly(ethylene terephthalate) (PET) film showing a high oxygen barrier [210].

Carbon nanotubes (CNTs) are one-dimensional tubular forms of sp^2 carbon, which possess unique electronic, mechanical and thermal properties and have wide applications in transistors, sensor technology, and biomedical material [211]. The incorporation of CNTs into PEMs and PECs requires a good miscibility of the components, especially for composites emphasizing CNTs reinforcement. Therefore, to overcome the high attraction between individual CNTs and achieve a solubility in organic or aqueous media, different strategies including covalent functionalization, oxidative cutting of the tubes, and noncovalent surfactant adsorption have been applied [212]. Unmodified CNTs are electrically neutral,

while oxidatively shorten CNTs can electrostatically interact with polycations as oxidation induced the formation of anionic groups (carboxylates) at open tube ends and side walls [213]. Thus, the combination of carboxylated CNTs and PEs has been studied, such as PDAC/multiwall carbon nanotube (MWNT) multilayers [214], nanocomposite of PDAC@CNTs-CMCNa bulk PEC [215]. For the noncovalent method, pyrene derivatives were used as the bridge of CNTs and PEs, indeed, they connected with CNTs via π–π stacking and simultaneously endowed surface charges to CNTs for further complexation with PEs, which is revealed in Figure 1.13 [212, 216]. This method not only retains the desired structure and properties of CNTs, but also allows fabrication of CNTs-based films with arbitrary composition and architecture as it enabled CNTs electrostatically connect with cationic PEs, anionic PEs, or even only oppositely charged CNTs.

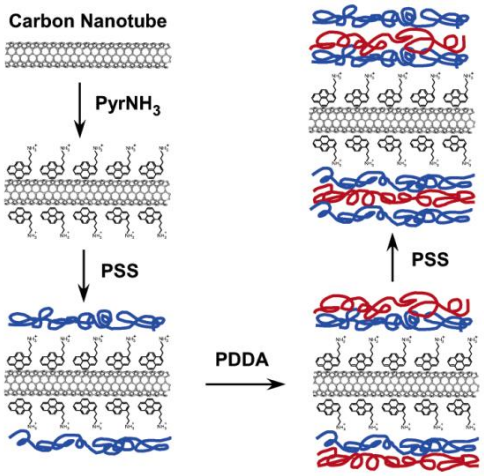

Figure 1.13 Schematic diagram of the carbon nanotube noncovalent modification in LbL electrostatic self-assembly. Reproduced with permission from [216]. Copyright 2012, American Chemical Society.

As an important two-dimensional carbon material with extremely good performance in mechanical strength, thermal conductivity, electrical conductivity and light transmittance, graphene and GRMs are considered as useful fillers to improve physico-chemical properties of PECs. Similar to CNTs, the unmodified graphene sheets are inclined to stack together to form multi-layered aggregates or even graphite, therefore, insolubility in common solvents, this has been fully discussed in 1.1. Inspired from the study of CNTs, oxidation of graphene/ using GO is a commonly reported solution to improve the compatibility with PECs. The presence of oxygen-containing functional groups allows GO to be easily exfoliated and to be dispersed in range of solvents. Considering the favourable structure feature of GO, various types of GO-containing PEM films and PEC scaffolds have

been developed. Zhang et al. [217] successfully fabricated GO decorated PEI/PAA dye-removing membrane by sequentially assembling of PEI-modified GO and PAA onto supporting substance, shown in Figure 1.14. Besides, the GO incorporated PEC membranes could also be obtained via solution casting of GO-PEC nanoparticles dispersions [218, 219]. The bulk materials of GO decorated PECs were fabricated via one-pot solution precipitation process, for instance, the BPEI/GO/PAA composites was fabricated by mixing GO/PAA dispersion and BPEI solution at a specific pH, in which GO (0 -12.6 wt%) restrained the viscous flow of complex and further improved the mechanical strength [220]. The electrostatic interaction was commonly used in assembly of the GO and PEs, while other interactions could also be observed in GO decorated PECs and PEMs. For instance, GO was dispersed homogeneously in poly (4- styrenesulfonic acid) (PSSA)/polyvinyl alcohol (PVA) blend matrix by colloidal processing and effectively reinforced the dielectric constant, which benefits from the strong interfacial interaction of hydrogen bonding between PSSA, PVA and GO [218].

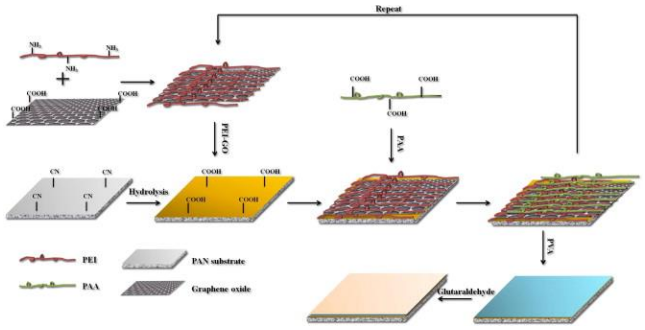

Figure 1.14 Fabrication of GO incorporated PEI/PAA nanohybrid membranes. Reprinted from [217], Copyright (2012), with permission from Elsevier.

Compared to GO, rGO was studied for incorporation into PEC due to its mostly recovered sp^2 conjugation structure and better electrical properties. Different strategies have been explored to improve the dispersibility and compatibility of rGO and PEC matrix. The rGO decorated PECs are usually fabricated via three steps of GO dispersion, reduction of GO in presence of PEs, and complexation of oppositely charged PEs with rGO [221-224]. During dispersion process, the GO sheets could be dispersed in at least one kind of PEs, polycation and/or polyanion. The carboxylic group of GO was firstly conjugated to BPEI and then be reduced with hydrazine monohydrate, thus the formed BPEI-rGO was further complexed with polyethylene glycol (PEG) through 1,1'-carbonyldiimidazole (CDI) coupling, this obtained nanocomposite showed improved colloidal stability and photothermal response [221]. In another case, GO dispersion was slowly dropped into PDAC and PSSNa solutions followed by sonication and chemical reduction to obtain

homogeneous dispersions of PDAC-rGO and PSSNa-rGO using for building antibacterial PEMs [222, 223]. These rGO-PSS/PDAC multilayers killed more than 90% of airborne bacteria within minutes of solar irradiation, since the rGO acts as a near-infrared photothermal converter to produce rapid localized heating [223]. Except for common chemical reducing agents hydrazine, sodium borohydride, and hydrogen sulphide, other environmentally friendly materials, such as amino acid and polyphenols [225, 226], or different reduction method, like electrochemical reduction [227] have been developed to produce rGO during fabrication of PEMs and PECs. The reduction was done with fenugreek seed extract, then the obtained rGO could be dispersed in xanthan gum (XG) solution and further complexed with chitosan (CS) in the presence of δ-galactone (GDL) as an acidifying agent [228]. The GDL created acidic condition for dissociation of CS as the amino groups of D-glucosamine residues turned to cationic ammonium ions at a pH lower than 6. This developed rGO decorated XG/CS PEC hydrogel shows potential in specific would dressing applications due to high antibacterial activity [228]. In addition, the excellent robustness and highly efficient healing property have been achieved by LbL assembly of PAA with complexes of BPEI grafted with ferrocene (BPEI-Fc) and rGO nanosheets modified with β-cyclodextrin (GO-CD) [229].

Another strategy to obtain rGO-containing PECs is in-situ polymerization of PE in presence of GRMs. Ma and co-workers [140] prepared the stable graphene sheets dispersion via an exfoliation/in situ reduction of GO followed by in situ polymerization of PAA, which was further used to build the PAA-rGO/PDAC-Prussian Blue (PB) multilayer by LbL technique. The polymerization was applied in both PAA and PAM during preparing rGO grafted polyacrylic acid/ polyacrylamide composite (rGO-g-PAA/PAM), in which the PAA grafted rGO (PAA-g-rGO) was synthesized from in-situ polymerization of monomer AA in presence of GO and followed by reduction process [230]. The PAA induced the uniform dispersion of graphene sheets and improved interfacial interaction of rGO and matrix.

Considering different requirements of functionalized materials, multiple incorporations of GRM-organic molecules, GRM-metals, and GRM-inorganic particles have been further studied, such as GO/CNT reinforced sodium carboxymethyl cellulose/poly(2-methacryloyloxy ethyl trimethylammonium chloride) CMC/PDMC composite [231], polyacrylamide-sodium carboxymethyl cellulose (PMC) hydrogels reinforced with GO and/or cellulose nanocrystals (CNCs) [232], and the spiky noble metal particles wrapped within rGO-PEI/PAA multilayers for biomedical applications [233]. The hybrid composites show a wide

range of applications based on the choice and combination of PEs as well as the doping molecules.

Generally, the property improvement and property stability of GRM-PECs require a certain number of GRMs fillers well dispersed in PEC matrix. For the rGO-reinforced PECs, whether using rGO directly or using GO dispersion followed by reduction, the good compatibility, solubility, and dispersion of rGO in selected PEs is the base for further fabrication of rGO-PECs composites with good dispersion of fillers in matrixes. The adsorption of PE on rGO involves different interactions, such as covalent bonding, hydrophobic interaction, hydrogen bonding, electrostatic attraction and van der Waals interaction [234]. Strong interfacial interactions based on covalent interaction or hydrogen bonding between rGO flakes and polymer matrix facilitate the load transfer from the polymer matrix to nanofillers, thus allowing improved mechanical properties. Moreover, the PE type and interaction between PEs could influence the properties of composites. The weak PE conformations (extended or collapsed conformation) is easily tuneable during complexation by changing pH, thus the complex morphology can be controlled in weak-weak PEs combination and weak-strong PEs combination. The different ion pairing strength, functional groups and charge density of PEs could also change the matrix properties, thus influence the final composites properties. For example, due to the strong interactions between polyanion and polycation, the high affinity of PAA for water appears to be inactivated in PAH/PAA, instead, the PDAC allows PAA to form more H-bonding with water, which is even competitive PAA-PDAC intrinsic interaction [235]. It is expected the rGO-PEC composite composing of PAA and PDAC could be sensitive to water, leading to a significant swelling.

1.5 Aim of research

The critical challenges in the preparation and development of rGO-PECs are the aggregation of graphene sheets and the limits of doping content. Usually the synthesis of rGO-PEC relies on the dispersion of GO and the reduction process in PE solution. In this thesis, we aimed at the achievement a high concentration of rGO incorporated in PEC with direct ultrasonic dispersion and self-assembly complexation.

Three main research objectives of this thesis are:

(1) To advance the knowledge and complete characterization of polyelectrolyte stabilized rGO dispersions in aqueous solution, in particular the interaction between

graphene sheets and different PEs, as well as the dispersion behaviour of rGO in PEs.

(2) The fabrication of self-assembled composites composed of strong-weak PEs and rGO, for the development of rGO reinforced PEC healing materials.

(3) Exploring the high loading of rGO in PECs based on monodisperse-complexation and multidisperse-complexation approaches, eventually obtaining composites with improved thermal and electrical conductivity, as well as stability in a high humidity environment.

The first objective is the basis for the other two objectives in this work. The study concerning the stability of rGO in different PE solutions is to determine appropriate polymer and conditions and further develop stable graphene-PE assembles. To better understand the effect of charge density of PEs on rGO dispersion, the rGO dispersed in weak PEs with different pH was also explored. In addition, the effect of molecular weight, chain structure and positive/negative charges was also investigated.

The second objective is to explore the application of rGO in the hybrid assembly of PECs. Considering the dispersion of rGO in the PE solutions and the tunability of PEC, we chose a strong-weak PEs combination. The quality of the composite films as well as the thermal stability, mechanical properties, and healing ability were regulated by ionic strength and/or graphene sheets.

Pristine PAA/PDAC has features of low thermal conductivity, low electrical conductivity, and unstable in high moisture environments. GRMs materials could help PEC composites to overcome these issues. However, another problem we faced is the limited content of rGO introduced in PEC matrix. Thus, the third objective of this thesis is to explore different methods to prepare high-content graphene-incorporated PECs, using either a PAA-based monodispersed-complexation approach or a PAA/PDAC-S-based multiple molecular dispersed-complexation approach. The former method has advantages of good affinity of PAA to rGO, and dispersion performance. In the second method, the hybrid system was designed to increase directly the proportion of rGO without the further addition of opposite PE, and transformation from dispersion to complexation is very fast and convenient.

Chapter 2

2 Materials and Methods

2.1 Materials and sample preparation

Avanzare Innovacion Tecnologica S.L. (Spain) provided the rGO. As reported previously [236], the synthesis procedure included the obtained by oxidation of graphite, ultra-sonication and then thermal reduction of GO. The surface area BET is 196 m^2/g, the oxygen percentage, atomic by XPS is 2 %. Figure 2.1a shows the X-ray diffraction (XRD) pattern and of pristine rGO measured in a range of 2θ from 5° to 80°. The XRD pattern of pristine rGO reveals a broad peak at 2θ=26.36, indicating a d-spacing of (002) plane of 0.337 nm. Meanwhile, the widely known characteristic peak of GO at around 9-12° [237, 238] is undetectable. These confirm the reduction to GO. Based on the SEM images of Figure 2.1b and Figure 2.1c, the rGO used in this study appears to be large (tens of μm) and very thin layers thicknesses, as indicated by the transparency in FESEM observation of Figure 2.1c.

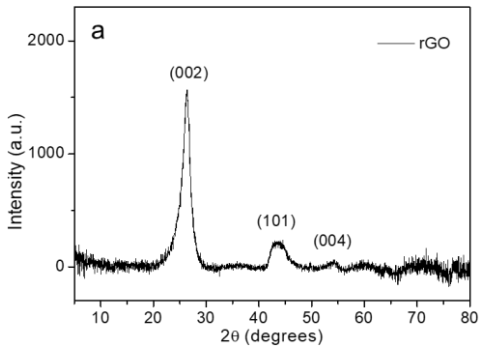

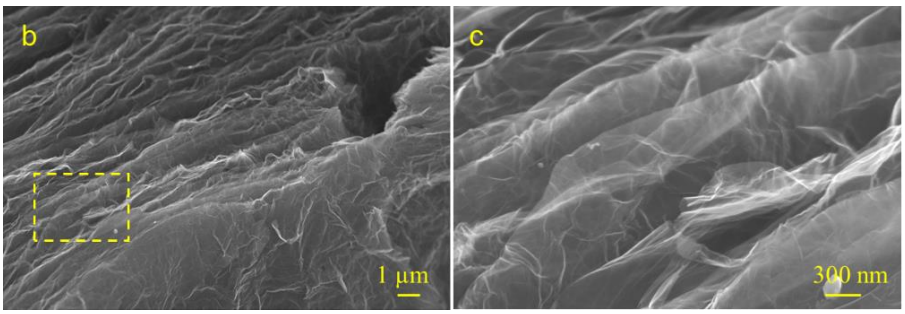

Figure 2.1 XRD pattern recorded (a) and SEM images (b) (c) for pristine rGO.

All polyelectrolytes involved in the building of dispersions and PECs are mentioned in Table 2.1. Sodium chloride (NaCl) was purchased from Sigma-Aldrich. All solutions and dispersions were prepared using deionized water (Direct-Q® 3 UV Millipore System, Milano, Italy).

Table 2.1 Polyelectrolytes used for rGO dispersions and PEC composites

Polyelectrolyte	Structure Formular	Molecular Mass Mw (Da)	pKa	Supplier
poly(acrylic acid sodium salt) (PAA)	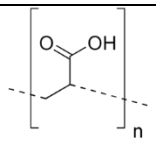	100 000, 250 000	4.5	Sigma-Aldrich
Branched Poly(ethyleneimine) (BPEI)	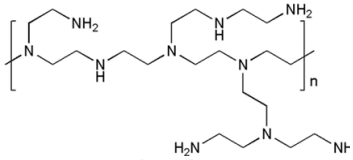	25 000, 270 000	4.5, 6.7, 11.6	Sigma-Aldrich
poly(sodium 4-styrenesulfonic acid) (PSS)	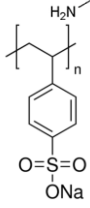	70 000, 200 000	-	Sigma-Aldrich
sodium carboxymethyl cellulose (CMC)	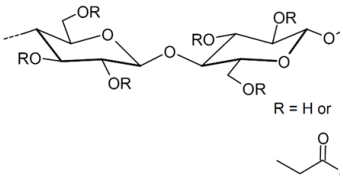	90 000, 250 000	-	Sigma-Aldrich
Poly(diallyldimethyl ammonium chloride) (PDAC)	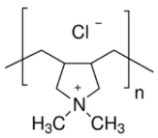	400 000-500 000	-	Sigma-Aldrich

2.1.1 Preparation of polyelectrolyte/rGO dispersions

The selected PEs (PAA, BPEI, PSS and CMC) were used for dispersing rGO in aqueous solution following the preparation process schematized in Figure 2.2. Each PE was dissolved at a concentration of 0.1 wt%, then 25mg rGO was added to the PE solution (100 ml) and sonicated for 30 min, using a probe sonicator VC-505 (Sonics & Materials, Newtown, CT, USA) with 15 s ON / 15 s OFF pulses cycles, 20 kHz frequency and 30% amplitude. The measured amount of energy for unit volume in 30 min sonication is ~344 J/ml. In this step, the standard sonic probe with threaded end and replaceable tip (model 630-0210, Sonics & Materials, Newtown, CT, USA) was immersed into solution and the distance of the top of probe to the bottom of beaker was set to 10 mm. The so-obtained suspension was allowed to settle overnight. Then, the PE/rGO dispersions were centrifuged for 15 min twice at 3300 rpm (Eppendorf centrifuge 5702, Milano, Italy) and the black or grey supernatant was collected. PAA and BPEI are weak PEs in water with a pH-dependent charge density. The pH of PAA and BPEI were adjusted from 2 or 4 to 12 with use of HCl or NaOH in 1 M. Thin films of PE/rGO were obtained by gravimetric filtration of the supernatants using polycarbonate membrane with 0.2 um pore size and then dried in oven at 60 °C for 24 h. The employed PE solutions are herein referred to with codes containing the PE name followed by the mass in kDa. For example, the PAA with M_w 100000 Da is coded as PAA100. Similarly, the dispersion stabilized with PAA100 is referred to as PAA100/rGO, and the same coding format was applied to the other dispersions.

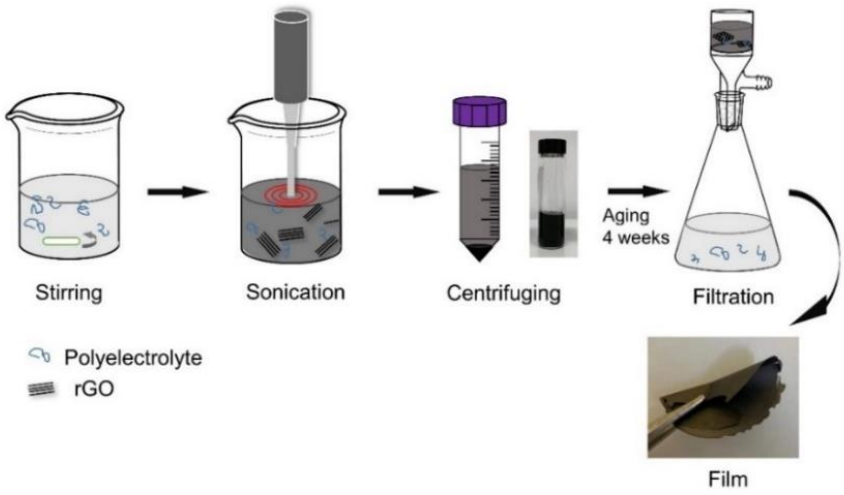

Figure 2.2 Illustration of fabrication process

2.1.2 Preparation of rGO and/or salt incorporated PAA/PDAC composite

The fabrication process of PAA/G//PDAC is provided in Figure 2.3. Firstly, 225 mg rGO were added into 0.125 M 100 ml PAA solution (input mass ratio PAA: rGO= 4: 1), and subsequently sonicated for 30 min with pulse 15 s (15 s ON and 15 s OFF). The resulting mixture was settled overnight. Afterwards, the dispersion was centrifuged at 3300 r/min for 30 min and the upper suspension of PAA/G was collected and saved. Mixing same volume of PAA/G dispersion and PDAC solution with monomer concentration 0.125 M at pH 7, the rGO incorporated PEC complex, PAA/G//PDAC aggregated and separated from liquid phase under stirring. After stirring for 1 h and setting overnight, the separated dense phases were dried at ambient conditions and then were compressed at 85 °C with 100 MPa hydraulic pressure. Since salt plays an important role in the properties of PEC, salt-addition and salt-removing treatments are also applied to PEC samples. For PAA/G//PDAC-s (complex of PAA/G//PDAC with salt), NaCl was added until 0.25M for each PE solution before mixing. PAA/PDAC and PAA/PDAC-s complexes were also prepared for comparison. Additionally, all these samples were soaked and rinsed in deionized water for four days to remove salt. The salted PEC samples are referred to as __-s, whereas rinsed samples are referred to as (_)^{R}. The detailed information of PEC samples are list in Table 2.2.

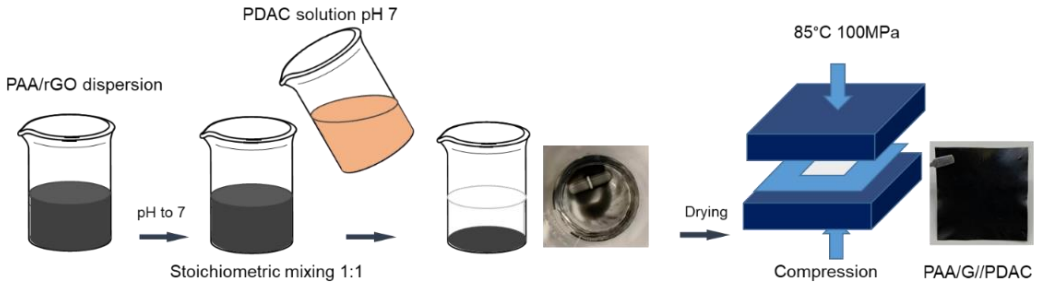

Figure 2.3 Schematic representation of the fabrication process used to create PAA/G//PDAC films

Table 2.2 Detail information for PEC samples

	Input PAA: PDAC	Input PAA: rGO	Input salt: PAA	Washing and soaking
PAA/PDAC	1: 1	--	--	no
PAA/G//PDAC	1: 1	4: 1	--	no
PAA/PDAC-s	1: 1	--	4:1	no
PAA/G//PDAC-s	1: 1	4: 1	4:1	no
$(PAA/PDAC)^{R}$	1: 1	--	--	yes
$(PAA/G//PDAC)^{R}$	1: 1	4: 1	--	yes
$(PAA/PDAC\text{-}s)^{R}$	1: 1	--	4:1	yes
$(PAA/G//PDAC\text{-}s)^{R}$	1: 1	4: 1	4:1	yes

To explore PAA/G//PDAC with higher rGO contents, indeed, higher concentrations of dispersed rGO, a few techniques were applied, for example enhancing feed rGO and/ or increasing the sonication time. In addition, the re-dispersion method was used by filtrating 2 PAA/G suspensions and then re-dispersing the deposited material into a new PAA/G suspension (80 ml). The prepared PAA/rGO dispersions were stoichiometric mixing with PDAC solution at pH 7, same process as before, sample details are list in Table 2.3.

Table 2.3 Fabrication information for rGO-PECs with different rGO loadings

	PAA/G//PDAC	$PAA/G_{0.17}$//PDAC	$PAA/G_{0.28}$ //PDAC	$PAA/G_{0.37}$ //PDAC	$PAA/G_{0.40}$ //PDAC	$PAA/G_{0.48}$ //PDAC*
Input PAA: rGO	4: 1	4: 1.5	4: 1	4: 1.5	4: 1	4: 1
Sonication time (min)**	30	30	60	60	30	30
Dispersions	1	1	1	1	3	3
rGO concentration in dispersions (mg/ml)	0.18	0.17	0.28	0.37	0.40	0.48
rGO concentration in dispersions (wt%)	0.02	0.02	0.03	0.04	0.04	0.05

** Sonication time for every dispersion

* PAA in $PAA/G_{0.48}$//PDAC has molecular weight 250 000 Da

2.1.3 Preparation of PAA/PDAC composites incorporating high rGO concentration

Two methods were applied in preparing high content of rGO decorated PAA/PDAC samples; synthesis processes are represented in Figure 2.4. In Type 1 method, 225 mg rGO was sonicated in 0.125 M 100 ml PAA solution where weight ratio of PAA to rGO is 4:1. Sonication time is 60 min with pulse circles of 15 s ON and 15 s OFF. Afterwards, the neutralized PAA/G dispersion was mixed with PDAC solution at pH 7, where the salt concentration was set as 0.25 M. The monomer ratio of PAA: PDAC =1:1.The formed rGO-containing complexes of PAA and PDAC in this way is named as PAA/G//PDAC-S (which is different to the PAA/G//PDAC-s defined in 2.1.2). Alternatively, the dispersion of Type 2 was prepared in hybrid solution of PAA, PDAC and salt, where the polymer concentrations, the molar ratio of PAA to PDAC were set same as Type 1. 0.5 M NaCl was used to keep liquid PEs solution instead of phase separation (dense polymer-rich phase and salt-rich supernatant). After pulse sonication with rGO 225 mg for 1 h, same volume of water to dispersion was input into system under stirring, thus the salt concentration in system dropped to 0.25 M. The formed composite is (PAA/PDAC-S)/G.

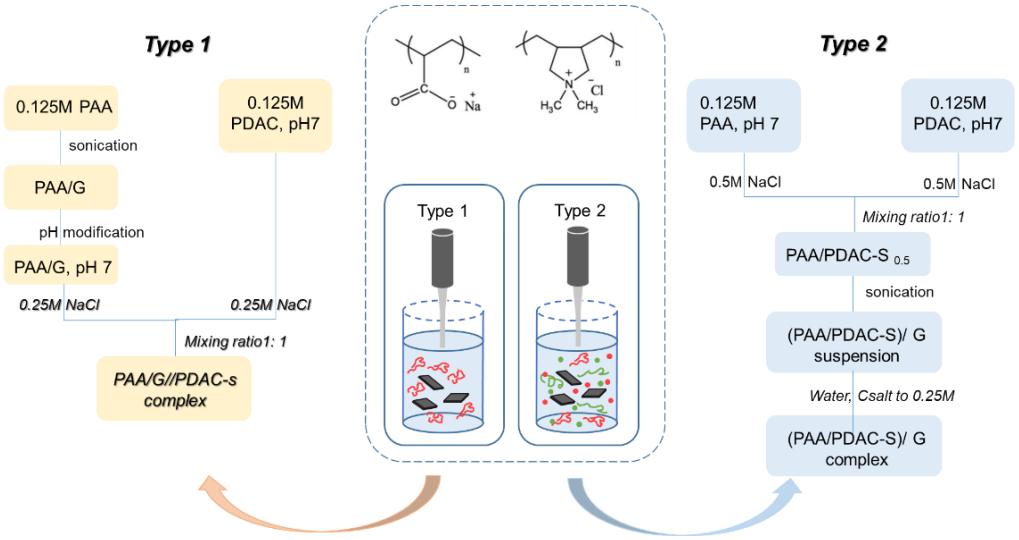

Figure 2.4 Schematic representation of the two different methods for fabricating rGO decorated PAA/PDAC

2.2 Characterization methods

2.2.1 X-ray diffraction

The rGO was determined by XRD using a Philips PW 1830 powder diffractometer by employing a scanning rate of 0.1 deg/s in a 2θ range from 5° to 80° with with CuKα radiation (λ¼1.542 Å)

2.2.2 Contact angle of polyelectrolyte on rGO film

The contact angle was qualitatively measured by dropping PE solution on rGO film. rGO (30mg) was loaded in 100ml deionized water (within 250ml beaker), and subsequently sonicated for 30min with 15 s ON/ 15 s OFF pulses cycles. At least 200 ml supernatant solution was filtrated by polycarbonate membrane with 0.1 μm pore size. Water or 0.1 wt% PE solution with 10 μl was placed on the resulting films by microsyringe, and the images of the liquid droplet were obtained instantaneously using camera. The contact angle of solid and liquid interface was obtained by measuring the angle between the tangent lines to the droplets and baseline. Five measurements for each solution were taken at different area of rGO film.

2.2.3 Dispersion stability and rGO concentration from Ultraviolet-visible spectroscopy

Ultraviolet-visible (UV-vis) spectra were recorded at wavelength range of 200-700 nm (Shimadzu 2600 UV-vis Spectrophotometer, Kyoto, Japan), using quartz cuvette from Exacta-Optech® with path length of 10 mm and a volume of 3.5 ml. The characterization of the stability of the polyelectrolyte/rGO dispersions was based on the fraction of rGO remaining for every dispersion after aging, which can be calculated from the ratio of absorption intensity $A_G/A_{G,i}$ of the rGO dispersed after aging (A_G) to that before aging ($A_{G,i}$), where the absorbance value was monitored at 600 nm.

Additionally, the dispersed concentration of rGO was obtained according to UV-vis spectroscopy and Beer-Lambert law ($A = \alpha cL$ where α is absorption coefficient, c is concentration and L is path length) [10, 79]. The first measurement of c used for determine α was obtained by filtration, drying and weight measure on a high sensitivity and resolution balance. The known volume of suspension was filtered through a pre-weighted polycarbonate filter membrane with pore size 0.2

μm, then the deposited mass was measured after drying the membrane for 24 h at 60 ºC. Weight fraction of rGO on filter membrane was determined by Thermogravimetric analysis (TGA) result. Thus, the concentration of rGO is calculated from equation (2-1):

$$c = \left((m_1 - m_0) * w_G\right)/V \tag{2-1}$$

$$w_G = \frac{M - M_{PE}}{M_G - M_{PE}} \times 100\% \tag{2-2}$$

Where m_1 and m_0 are the mass of filter membrane combined with deposited material, and the mass of pristine filter membrane respectively. V is the volume of dispersion for filtration. w_G is the mass proportion of RGO in deposited PE/rGO on filter membrane, which could be measured via equation (2-2), where M, M_{PE} and M_G represent the residual weight of PE/rGO, pure PE and rGO, respectively. TGA was performed with a Q500 thermobalance (TA Instruments, Newcastle USA) under nitrogen. The deposited samples after filtration were held isothermally at 100 °C for 30 min to remove weakly adsorbed water, followed by a heating rate of 10 °C/min from 100 °C to 800 °C.

The coefficients for each samples are reported in Figure 2.5. The coefficient α varied among different PE/rGO samples, but for the same type of PE with different molecular weight, the deviation of α was small. Taking corresponding α and A for each dispersion, the concentration after 4 weeks was obtained. Four samples were analysed for each dispersion to provide average values and experimental deviations.

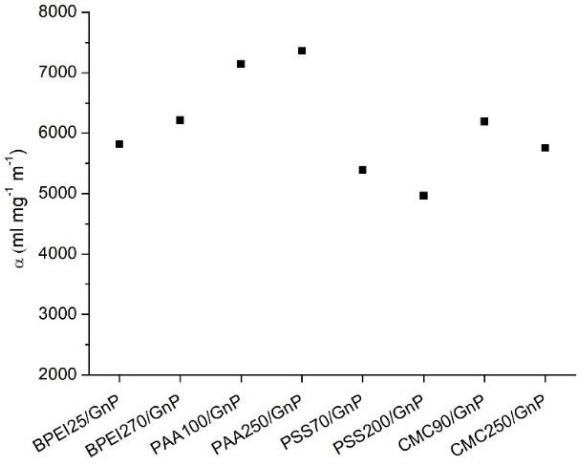

Figure 2.5 Absorption coefficient (α) of RGO dispersions with different PEs.

2.2.4 Size measurement by dynamic light scattering

Dynamic light scattering (DLS) measurement was evaluated by Malvern Zetasizer Nano ZS90 (Malvern Instruments, Malvern, UK) at 25 °C with a refractive index of solvent (water) 1.33. Every sample was tested three times and the results were averaged.

2.2.5 Raman spectroscopy

Raman spectra of filtrate polyelectrolyte/rGO thin films, PAA/G suspensions (0.125 M PAA) and (PAA/PDAC-S)/G suspensions (0.5M salt) were performed on a Renishaw Invia Raman microscope system (Renishaw, Wotton-under-Edge, UK) equipped with 532 nm laser. 20× objective lens was used for measurements. Raman spectra were collected at 5 random points for each sample, and the average spectrum was used for characterization.

2.2.6 Phase quantification and thermal properties of PECs

Quantification of rGO in PECs

The rGO content in PEC films was determined by TGA in temperature range 100-700°C, at a heating rate 10°C/min, under N_2 atmosphere. All samples were isothermal at 100°C for 30 min to remove water. Direct comparison the TGA results of rinsed PECs ($PECs^R$) with or without rGO addition allows the determination of the rGO content in composites, in formula (2-3).

$$W_G = \frac{M_{G@P/P^R} - M_{P/P^R}}{M_G - M_{P/P^R}} \quad (2\text{-}3)$$

Where W_G is the weight fraction of rGO in PEC^R composites, $M_{G@P/P^R}$, M_{P/P^R}, and M_G represent the residual weight (%) of rGO-containing PEC^R, $(PAA/PDAC)^R$ and pure rGO respectively. This calculation considers the PAA/PDAC as an independent phase and assumes that there is no interaction between components during decomposition. To be clear that the value is about rGO content in polymer/rGO matrix without consider of salt, and it might be inaccurate if the G content is quite low.

rGO concentration from direct method

The rGO concentration has been calculated via UV-vis spectroscopy method in the first part study about PE/rGO dispersions due to the simple and low dispersion

consuming advantages. However, the presence of large aggregates may result in significant scattering in addition to absorbance when high concentration of rGO was achieved, which precluding the application of UV-vis method, and the rGO dispersion (in chapter 4 and 5) was determined in a direct method via isolating and weighting dispersed graphene sheets. A known volume of PAA/G suspension was dried in an oven, and the deposited material was performed with TG test. The mass proportion of rGO in dried deposited mixture (w'_G) was calculated by mass residual of neat components and dried composite based on equation (2-4). The rGO concentration (c') was measured via formula (2-5).

$$w'_G = \frac{M_{PAA@G} - M_{PAA}}{M_G - M_{PAA}} \times 100\% \quad (2\text{-}4)$$

$$c' = (m * w'_G)/V' \quad (2\text{-}5)$$

Where m and V' are weight of dried composite and volume of dispersion respectively.

Quantification of salt content in PECs

The salt content was measured by applying PEC samples in TGA under air atmosphere, within temperature of 100-700°C. Polymers and rGO have been degraded, thus the residual weight was used to roughly consult salt content in PEC. This can also be used to check the residual salt of of PECs^R.

In chapter 5, the salt content was measured according to the residual weight of pure salt, PEC and PEC^R, where polymers and rGO in PEC was considered as an individual phase with residual mass percentage same to PEC^R.

$$W_{salt} = \frac{M_{PEC} - M_{PEC^R}}{M_{salt} - M_{PEC^R}} \times 100\% \quad (2\text{-}6)$$

W_{salt} is the weight fraction of salt in PECs, M_{PEC}, M_{PEC^R}, and M_{salt} represent the residual weight (%) of PEC, the salt-removed PEC^R and pure salt respectively.

Thermal stability

The thermal stability of PECs was compared with TGA curves of pristine PAA/PDAC, and decomposition temperature was obtained from the degradation speed curve (DTG). Samples were isothermally held at 100 °C for 30 min, and heated in temperature region of 100-600°C, at a heating rate 10°C/min, under N_2.

2.2.7 Fourier transformed infrared-Attenuated total reflection spectroscopy

To analyse the complexation of PAA and PDAC in PECs, a Frontier spectrometer (PerkinElmer Frontier, Waltam, USA) was applied to measure the Fourier transformed infrared (FTIR) and attenuated total reflection-Fourier transformed infrared (ATR-FTIR) spectra of neat components (PAA, PAA at pH 7 and PDAC) and the ATR-FTIR spectra of composites PECs in a range of 4000-400 nm.

2.2.8 Scanning electron micrographs and energy dispersive X-ray spectroscopy

The morphology characterization of PECs were evaluated by high-resolution field emission scanning electron micrographs (FESEM, Zeiss Merlin 4248, Jena, Germany; beam voltage: 5 kV), on the cross-section of films, obtained by cryo-fracturing after dipping films in liquid N_2. Samples were fixed on supports and surfaces were sputtered coated with gold-palladium before SEM observation. Energy dispersive X-ray spectroscopy (EDS) allows for targeted analysis of elements content and distribution of Na and Cl on cross-section surfaces.

2.2.9 Mechanical properties

Tensile test

Stress-strain measurements were conducted using a 5966 dynamometer (Instron, USA) at room temperature with initial strain rate of 1 mm/min during strain below 1%, then the speed increase up to 10 mm/min until films ruptured. The elastic modulus was calculated as the slop of initial linear region with strain under 1%. The test stops when force dropped to 60% of maximum force. The initial distance of clamps was 30 mm.The PECs with a thickness of around 150 μm after hot-pressing were cut in size of 15mm × 60mm. At least 6 specimens for each investigated PEC films were tested, and the results were averaged. All composite films were saved in relative humidity (RH) constant condition1 week before testing. In order to understand the relationship of tensile result of PECs and RH, different RH (50% and 70%) storage were applied to specimens before tensile measuring.

Dynamic Mechanical Thermal Analysis

Mechanical properties of composite films were measured by dynamic mechanical thermal analysis (DMTA) using a TA instrument Model Q800 (New

Castle, USA). Samples in size of 6mm width × 30mm height × 0.15mm thickness were used. All samples were saved in ambient condition (relative humidity 50% and 23 °C) for one week before tests. A heating/cooling rate of 3 °C min^{-1} was employed in temperature ramp under nitrogen environment, including heating from -100 °C to 160°C, isothermal for 20min and then cooling back to -100 °C. The test was carried out with a tension clamp, in a multi- frequency strain mode with frequency 1Hz and a strain of 0.05%.

2.2.10 Healing properties

To figure out the mechanical recovery ability of materials, the cut and healed specimens (films) were characterized via tensile test and compared with corresponding original samples. The cross-cutting wounds (4×6mm) at the central of tensile specimens were healed by add 2 µl water to the incisions. The healed samples were saved in RH 35% at room temperature for removing water.

2.2.11 Electrical conductivity

The electrical conductivity σ and electrical resistivity ρ are inversely to each other. The electrical conductivity can be calculated through measuring material electrical resistance and sample size according to formula (2-7) and (2-8).

$$\sigma = \frac{1}{\rho} \tag{2-7}$$

$$\rho = \frac{R \cdot S}{l} \tag{2-8}$$

Where R is resistance, S is the surface (thickness and wideness of sample) and l is the distance between the electrodes. The resistance was measured by connected devices, containing a direct current regulated power supplier (Tektronix PWS4323), a number table multimeter (HP 3458A) and two homemade brass electrodes, , which consisted of two parallel metal plates with 100 mm side and 3 mm thickness, and a plastic cuboid with 12.7 mm wide/height using for fixing the relative position of plates [239]. Every electrode has a hole for the connection and a wire furnished with a 4 mm banana plug. The system worked with the four-terminal measurement. Clamps were used in place of the usual "probe or test lead" to obtain more accurate results by limiting variability due to tip positioning and tilting on the sample [240]. Using strip shaped composites with 40 × 10× 0.15 mm^3. Each sample has been

measured three times in both sides, at least three parallel samples were set and tested.

2.2.12 Thermal conductivity

The thermal conductivity was measured by the slab method under hot disk AB (TPS 2500S, Göteborg, Sweden) equipped with a Kapton sensor (radius 3.189 mm). Samples were hot-pressed (110 °C) into disks with a thickness of 3 mm and diameter of 10mm, and saved in ambient condition for at least two days. The test was controlled at 23 ± 0.01°C by a silicon oil bath (Haake A40, Thermo Scientific Inc., Waltham, MA, USA) equipped with a temperature controller (Haake AC200, Thermo Scientific Inc., Waltham, MA, USA).

2.2.13 Stability in water

The composite stability in aqueous solution has been measured by immersing PEC films into water. After soaking 2 weeks or 5 weeks, samples were dried in vacuum freeze dryer (TOPT-10A, Toption Group Co. Limited, Xi'an, China) equipped with 4 layer of 200 mm trays and subsequently observed in top and cross-view using SEM.

Chapter 3

3 PE-enabled rGO water dispersions: effects of PE structure, molecular weight and charge density

3.1 Introduction

The surfactant and polymer are considered effective stabilizers for dispersing graphene and graphene related materials (GRMs) in an aqueous solution via non-covalent functionalization. As the central part of polymer-modified GRMs, dispersions of polyelectrolyte grafted graphene related materials (PE-GRMs) have been widely used in solution based processing of graphene, layer-by-layer fabrication of graphene based films [140, 241], and complexation to form GRM reinforced polyelectrolyte complexes (G-PECs) [220].

In general, the stability and dispersion of GRMs in PEs solutions could be influenced via PE features in solution, thus the molecular weight, chain structure, charges, and specific interactions of functional groups in molecules must be considered in the study of PE-GRMs dispersions. A comprehensive understanding of interaction mechanism of PE on graphene sheets in water is required and

essential to allow sustainable applications of graphene-based material. In previous studies, the dispersion-reduction method, the GO sonication/ exfoliation followed by reduction of GO in presence of PE molecules, has been usually used to prepare rGO dispersions. Considering that sort of PEs might affect the reduction process, for instance, PDAC and chitosan are favourable to the reduction of GO [145, 242]. This may interfere with the comparison of effect of PE on stability and dispersing performance of rGO, the rGO with higher reduction degree has higher dispersing resistance. Moreover, to avoid the influence of surfactants and organic solvents, the direct sonication dispersing with only PE molecules assistance was employed in this study. One thing should be noted that the nano-sized dispersion is not emphasized in this study, Lu [147] and co-workers studied the ability of several PEs to suspend exfoliated graphite nanoplatelets (xGnPs) with an average thickness of 1-10nm. However, the focus here is on dispersing efficiency from pristine large-sized reduced graphite oxide and the stability of separated graphene multilayers.

In this chapter, the effectiveness of PEs having different chemical structures for the production of a stable rGO dispersion in water was systematically investigated. The interactions occurred between rGO particles and weakly or strongly charged polyelectrolytes have been studied by combing a complete set of characterization techniques also considering different PE molecular weights. Moreover, the weakly charged PE-rGO interactions were further studied at different charge densities as a function of dispersion pH, since the dispersing ability and the assembly processing of weakly charged PE are tunable.

3.2 Result and discussion

3.2.1 Visual observation and surface tension

Polyelectrolyte/reduced graphite oxide (PE/rGO) dispersions were prepared by directly adding rGO in PE solutions and then sonicating in relatively mild conditions. It is interesting to note that within few seconds after rGO comes into contact with the liquid surface, the rGO powder rapidly produces a film at the water/air interface for PAA and BPEI solutions but not on water, PSS or CMC solutions, see in Figure 3.1.

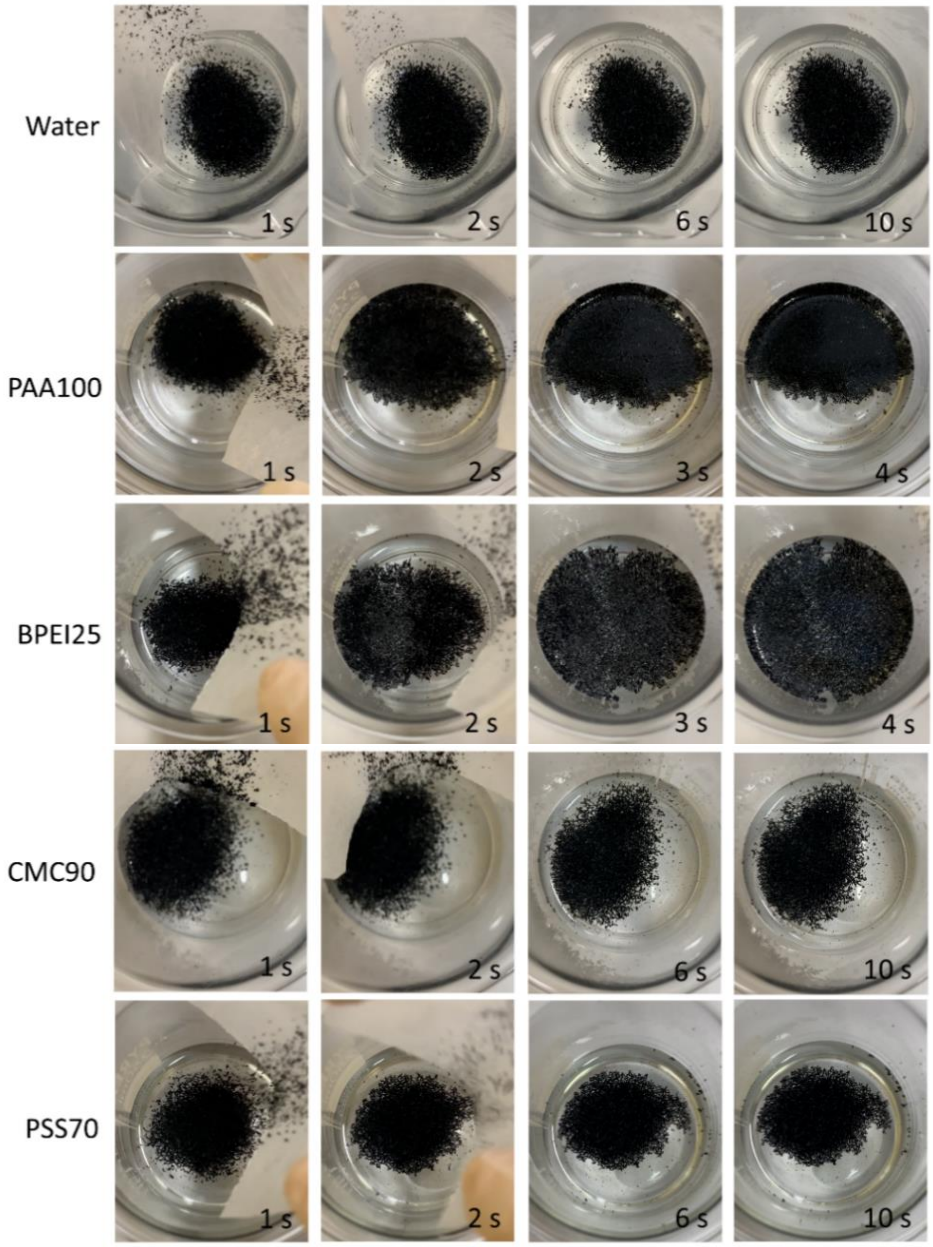

Figure 3.1 rGO inclusion in water and polyelectrolytes.

In addition, Figure 3.2 displays the condition of rGO entering into PE liquid phase without sonication over storage one night. It is easy to tell that more inclusion of rGO occurs in PAA-based solutions, subsequently, in the BPEI-based solutions. The PSS and CMC-based solutions show clear and transparent appearance, with hardly found rGO included. The observed, practical, behavior can be ascribed to change in surface energy of PE containing water-based solution.

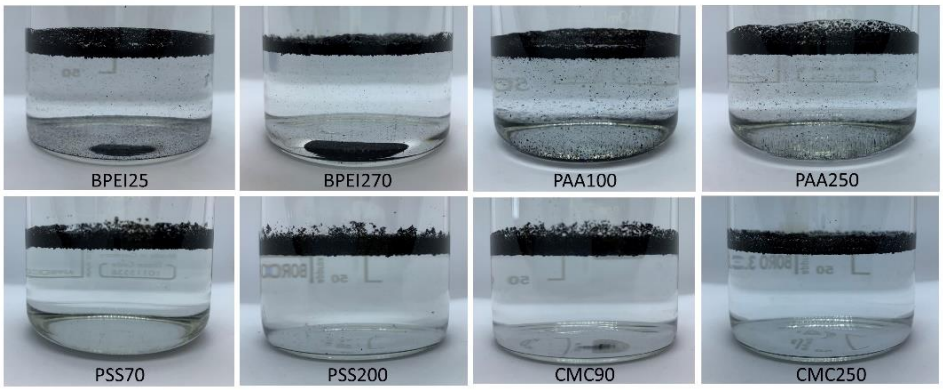

Figure 3.2 rGO inclusion in polyelectrolyte solutions over 1 night

It is indeed well-known from the literature that the type and concentration of the PE can affect surface energy value to different degrees. The values of surface energy of PEs aqueous solutions, extrapolated from the literature background, are summarized in Table 3.1. When the PE concentration is close to 0.1 wt% (the concentration employed in this work), the PSS, CMC and BPEI solutions show surface tensions similar to water (72.8 mJ m^{-2}), which is expected at such low concentrations. Conversely, PAA was reported to have a lower surface tension even at 0.1 wt%. This latter behavior is explained by the fact that PAA macromolecules consist of non-polar hydrocarbon backbones which tend to orient toward the surface of the solution to minimize the surface tension [243]. When rGO comes into touch with the surface of aqueous PE solution, the interplay of three interfacial tensions determine the wettability of the rGO, expressed as cosθ, following Young equation [244]:

$$r_{sg} = r_{sl} + r_{lg}\cos\theta \tag{3-1}$$

where γ_{sg}, γ_{sl} and γ_{lg} are the solid- air, solid-liquid and the liquid- air interfacial energy respectively. The solid surface free energy can be determined by several theoretical models or through direct contact angle measurements [245]. The surface energy of rGO has been estimated to be ~47mN/m by Neumann's method [46]. On the basis of state equation, contact angle is given as equation (3-2).

$$\cos\theta = -1 + 2\sqrt{\frac{\gamma_{sg}}{\gamma_{lg}}}e^{-\beta(\gamma_{sg}-\gamma_{lg})^2} \tag{3-2}$$

where β is the constant coefficient related to specific solid surface. γ_{sg} and γ_{lg} represent solid and liquid surface free energy respectively. By combining equation

(3-2) and the values reported in Table 3.1, it is immediately apparent that a lower γ_g would lead to smaller contact angle.

Table 3.1 Surface tension of polyelectrolyte solutions reported in literatures.

	Temperature (°C)	Concentration (w/v%)	Surface tension (mN/m)	Method
PAA	25	0.07	~ 59	Du Nouy ring method (Dickhaus et al. [246])
PAA	25	0.1	~ 63	Du Nouy ring method (Vasilieva et al [247])
BPEI	25	0.1	~ 71	Du Nouy ring method (Griffiths et al. [248])
BPEI	25	0.1	~ 72	Du Nouy ring method (Bellettini et al. [249])
CMC	20/ 25	0.1	~ 72	Wihelmy method/ axisymmetric drop shape analysis method (Guillot et al. [250])
CMC	25	0.5	~ 75 ~ 71 ~ 71	Du Nouy ring method, Harkins–Brown (HB) drop weight method, Lee–Chan–Pogaku (LCP) drop weight mrthod (Lee et al. [251])
CMC		0.25	~ 69	Du Nouy ring method (Weber et al.[252])
PSS	25	0.1	~ 72.5	Wihelmy method (Okubo et al.[253])

Therefore, PAA has a smaller contact angle when compared with water or other PE solutions in our study. This was confirmed by practically evaluating the wettability of rGO films as shown in Figure 3.3, which shows the variation of contact angle of PE droplet and rGO film with time. The contact angles of different PE solutions and water are similar within the first few seconds. Deionized water, BPEI25, PSS70 and CMC90 all formed spherical droplets with contact angles higher than 90 °. These droplets kept relatively stable angles on rGO in the first 4

min. However, PAA yielded smaller contact angles from 1 min, corresponding to a fast decrease in droplet height. After 10 min, all samples exhibit smaller contact angle than the corresponding initial shape, in which BPEI25, PAA100 and PSS70 have higher variation. This is related to the partial absorption of the solution. From the performed experiments, it seems that PAA has a better wettability to rGO when compared with water and other PEs. This could explain the inclusion of rGO clusters within the PAA solution without the need for external energy inputs. It is worth mentioning this fast rGO inclusion in the liquid was exclusively formed in PAA solutions at low pH values (namely within pH 2 and pristine pH 3.4), which suggests this being related to the low ionization degree of PAA at such pH conditions. Indeed, as reported by Dickhaus et al. [246], the surface tension of PAA solutions dramatically increase in the pH 4-7 range pH as the PAA is mostly ionized. Thus, rGO was not expected to incorporate into the liquid rapidly in PAA solution with pH above 5, which was consistent with the observation (Figure 3.4). On the other hand, BPEI also revealed ease of rGO inclusion into the liquid phase (Figure 3.2), despite its high surface tension, which suggests possible electrostatic effect as driving interactions [236].

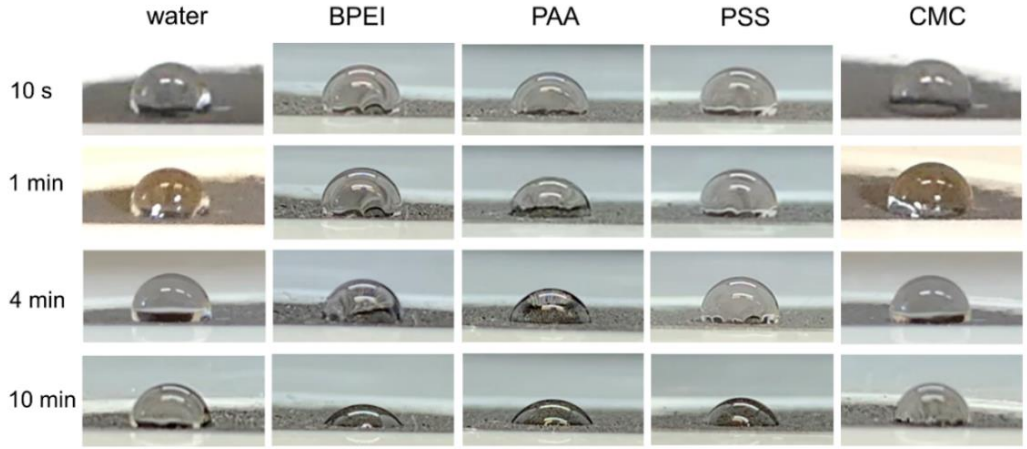

Figure 3.3 The liquid contact angel images of water, BPEI25, PAA100, PSS70 and CMC90 droplets on the surface of rGO with time

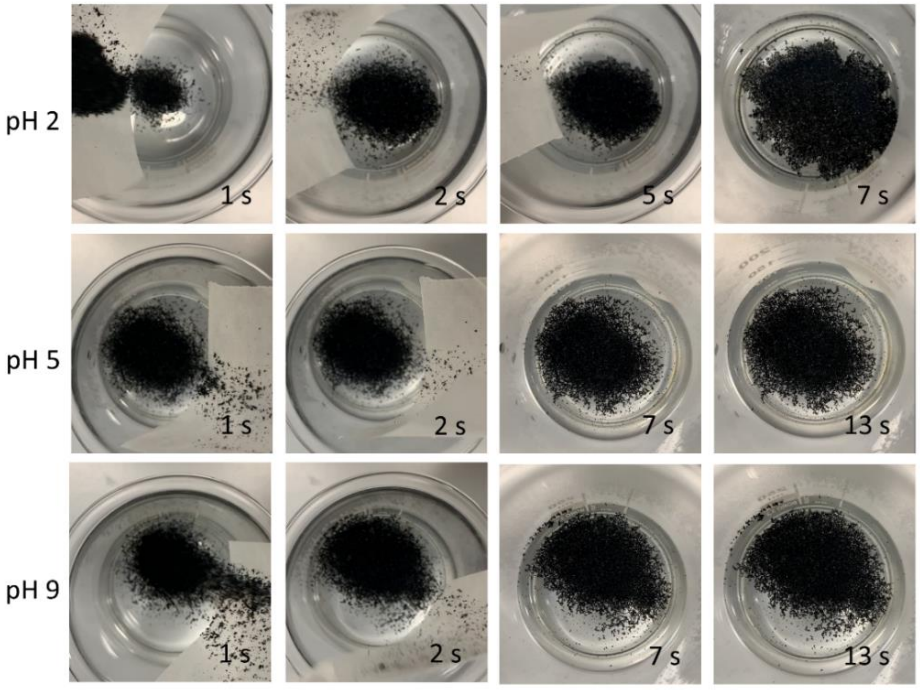

Figure 3.4 rGO inclusion in PAA solutions at different pH

Aiming at the separation of aggregated rGO flakes, rather than their extensive exfoliation, 30 min pulsed sonication was applied in this work, which is significantly shorter than conventionally employed in exfoliation procedures from graphite, where sonication times range from tens to hundreds of hours [78, 254]. The appearance of the dispersions obtained right after sonication can represent a first qualitative evaluation of the quality of the rGO dispersion. From an overall point of view, the darker the supernatant, the better is the dispersion, with a higher concentration of suspended rGO. However, the appearance of just-prepared dispersion is not representative of their long-term stability, which should be evaluated in time. Figure 3.5 shows the images of different PE-stabilized rGO dispersions before and after four-week storage in static conditions. Darkest rGO dispersions were obtained in PAA-based (both PAA100/rGO and PAA250/rGO) and BPEI-based dispersions (both BPEI25/rGO and BPEI270/rGO). Light grey supernatants were obtained for PSS-based (PSS70/rGO and PSS200/rGO) and CMC-based dispersions (CMC90/rGO and CMC250/rGO). This suggests that a higher content of rGO was dispersed in PAA-based and BPEI-based dispersions after preparation. After storing for 4 weeks, rGO in PSS-based dispersions was almost completely precipitated (Figure 3.5b). CMC-based dispersions also showed conspicuous sedimentation. On the other hand, the PAA-based and BPEI-based

dispersions remained qualitatively equivalent, suggesting for a good stability over 4 weeks.

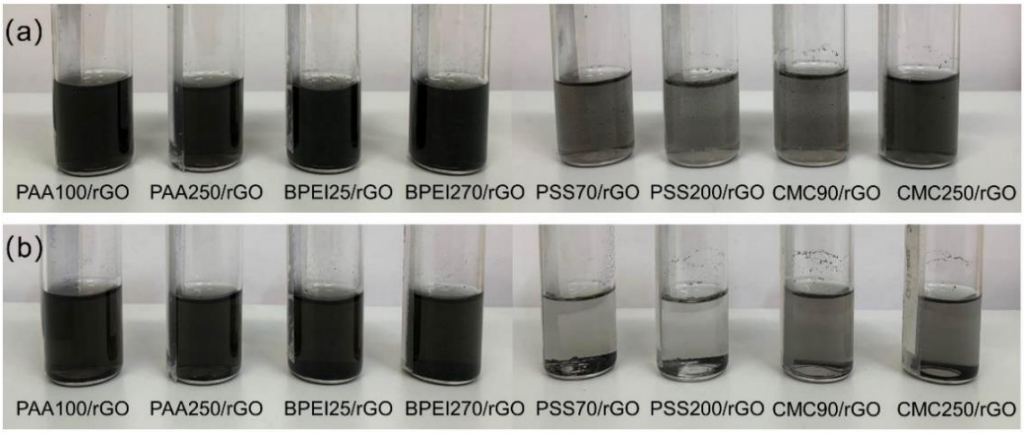

Figure 3.5 Photographs of rGO dispersed in different polyelectrolytes solutions before (a) and after four-week of aging in static conditions (b)

3.2.2 UV-vis analysis

UV-vis spectroscopy was used to investigate and quantify the rGO concentrations in the prepared PE solutions and their stability through time. Firstly, the UV-vis results of PE solutions (0.1 wt% PE) are presented in Figure 3.6a. The spectra of same type of PE with different average molecular weight (Mw) are quite similar. PAA displays an absorbance peak at 212 nm. PSS shows two characteristic shoulder peaks at 256 nm and 261 nm, partially overlapped to the main absorbance, which appears heavily saturated at this concentration. To resolve the position of the PSS main absorbance peak, a 0.01 wt% PSS solution was also analyzed (inset), exhibiting a peak at 222 nm. As for BPEI, a strong absorption is found below 250 nm, which saturates at 0.1 wt% concentration. Even at lower concentration (inset), the peak is not visible, which suggest this to occur at a wavelength lower than 200 nm. Finally, CMC only displays a weak absorbance below 225 nm. Figure 3.6b displays the UV-vis spectra of PE/rGO dispersions. Based on the PE solutions and PE/rGO results, the presence of rGO is related to the appearance of an additional signal at wavelength ~270 nm, ascribed to sp^2-conjugated graphene network [255]. Moreover, the addition of rGO increased the overall optical density of the dispersion within 200-700 nm, as a consequence the signal baseline shifted from the zero of neat PE solutions to variable values for PE/rGO dispersions. As the increased absorbance intensity is dominated by the concentration of graphene sheets [10, 100], the shift of the baseline can be related to the difference in the concentration of rGO dispersed in each PE. The selected different molecular

weights have little effects on the collected spectra of most samples as shown, for example, by comparing PAA100/rGO and PAA250/rGO. On the other hand, the absorption intensity of BPEI25/rGO was significantly higher than that of BPEI270/rGO, suggesting a better dispersing concentration of rGO for the former. The calculated concentrations of rGO for each prepared dispersion before (filled square) and after (filled round) 4 weeks are reported in Figure 3.6c. The initial dispersed concentration of rGO follows the trend: CMC90/rGO ≈ CMC250/rGO < PSS70/rGO < PSS200/rGO < PAA250/rGO < PAA100/rGO < BPEI270/rGO < BPEI25/rGO. This is in agreement with the qualitative considerations based on rGO wettability described at the beginning. The good dispersion of rGO in BPEI solutions is closely connected to its branched chains, electrostatic interaction and/or cation- π interaction with rGO [256, 257], which facilitates better entanglement and adsorption of BPEI molecules onto rGO flakes. The higher concentration of rGO in lower molecular weight BPEI25 could be associated with the polymer conformation in solution and interaction sites between rGO and polymer chains. As reported in the literature, the BPEI molecules in solution exhibit spherically symmetric compact molecules, and they are more compact with increasing molecules weight [258]. Lee et al. [259] found that the percentage of low molecular weight BPEI incorporated in to the rGO/PEI composites was higher than sample using high molecular weight BPEI, because the former had greater polymer chain flexibility and therefore the reactive nitrogen atoms of BPEI are more likely to interact with GO. Thus, the more flexible and loose conformation structure BPEI with lower molecular weight inclines to a better interaction with rGO. Moreover, the different molecular weight of BPEI indicates the significantly different number of branching and length of side chains that could also influence the adsorption of BPEI molecules on rGO. After 4 weeks the concentration remained almost unchanged only for PAA-based dispersion whereas decreases were observed for BPEI- and PSS-based dispersions (Figure 3.6c).

In addition, the UV-vis spectra were also employed to follow the stability of rGO dispersions as a function of time (i.e. 1, 2 and 4 weeks). The residual rGO fraction, expressed as % of the initial concentration, is plotted in Figure 3.6d. Most PEs clearly show that relatively large fractions of rGO had sedimented during the first week, after which limited reductions are observed. Interestingly, PAA-based dispersions yielded very low sediment fraction over the whole period (4 weeks). In addition, it is also possible to observe the effect of different molecular weights. Indeed, for both CMC and PSS lower molecular weight PEs led to relatively higher stability in time. On the other hand, the gaps between PAA100/rGO and

PAA250/rGO, BPEI25/rGO and BPEI270/rGO were narrow thus suggesting a limited effect of the molecular weight the on stability in time for these PEs. Interestingly, although the original absorbance of BPEI25/rGO was slightly higher than that of BPEI270/rGO (in Figure 3.6b), the two PEs absorbance decreased in time by equal proportions. In addition, although the BPEI-based samples show a quite drastic reduction in concentration during aging, the initial amount of dispersed rGO was so high that even after four weeks these dispersions still display the highest concentrations among all PEs. Combined with the results in Figure 3.6c and Figure 3.6d, it is concluded that, among the different PEs addressed, BPEI-based dispersions show the highest concentration of rGO, and the PAA-based dispersions exhibits the best stability over 4 weeks.

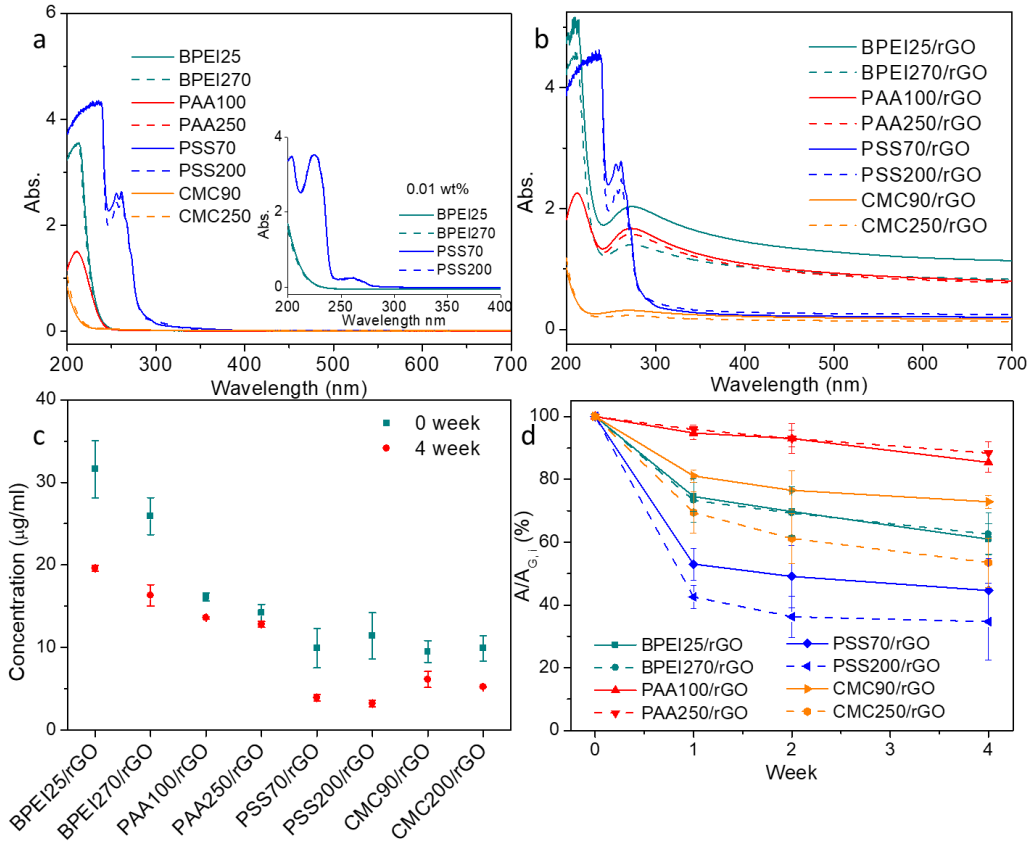

Figure 3.6 UV-vis spectra of of PEs with 0.1 wt%, inset: absorption spectra for BPEI25, BPEI270, PSS70 and PSS200 with 0.01wt% (a), PE/rGO dispersions (b), concentration of rGO in PE/rGO dispersions (c), the amount of remaining rGO in dispersions after 0 to 4 weeks, expressed as percentage of original absorptions (original concentration), $A/A_{G,i}$ (d).

3.2.3 Quantification of polyelectrolyte adsorbed to rGO

To further investigate the mechanism of stabilization of rGO dispersions, it is of importance to determine the amount of PE adsorbed on rGO in dispersion (PE: rGO) in time. To this aim, TGA was conducted for pristine rGO, PEs and PE/rGO films obtained after filtration, as shown Figure 3.7. Pristine rGO showed a mass loss of 4.9 % upon heating to 800 °C under nitrogen, indicated relatively small amount of oxygen-containing groups [260]. The selected PEs show a different weight loss behaviour. Indeed, BPEI start decomposing at 250 °C and above 650 °C it is completely volatilized [220]. PAA yielded two decomposition steps, the first assigned to the thermal decomposition of the carboxylic acid groups at around 280 °C and the second reflecting scission of the polymer backbone [261], eventually leading to a ~15 % residue. CMC exhibited a first main mass loss at 260 - 300 °C, assigned to the loss of CO_2 from decarboxylation coupled the pyrolytic decomposition of the main chain followed by further mass loss ascribed to aromatization, the final residues accounting for 35% (CMC250) and 27 % (CMC90). [262, 263] PSS shows a more complex and multi-step decomposition path with an onset temperature of mass loss of at approx. 400 °C and a final residual weight around 35% [264]. The TGA curve patterns of PE/rGO composite films were similar to their corresponding PEs, suggesting that the decomposition mechanism was not altered by the presence or rGO. The final residues fell within the values obtained for the neat film constituents thus allowing for the evaluation of the PE/rGO relative amounts Table 3.2 reports the weight residual of PE/rGO within the 100 - 800 °C temperature range, the weight percentage of rGO w_G and the corresponding fraction of PE in the PE/rGO composite (calculated as $1\text{-}w_G$). rGO accounted for more than 60wt% in all cases, with some differences between the different PEs. The ($1\text{-}w_G$) of PAA and BPEI are similar, whereas CMC shows the greatest ratio in PE/rGO composite and PSS gives the lowest value. Combined with previously measured concentrations, these results suggests that the fraction of PEs attached on the rGO basal plane was relatively low compared to the total in solution, leaving a significant excess of PEs solubilized in water.

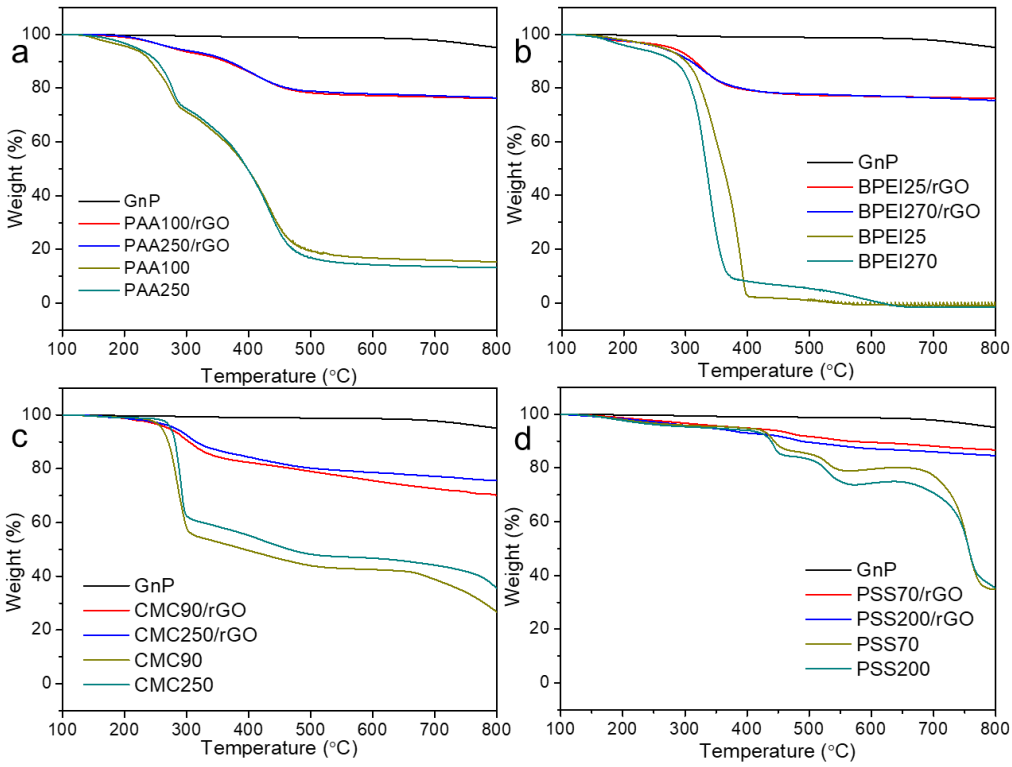

Figure 3.7 The TGA curves of PE/rGO after aging 4 weeks.

Table 3.2 Weight residual of PE/rGO after TG and the weight percentage of rGO and PE in PE/rGO films

Sample	Weight residual (%)	rGO weight percentage w_G (%)	PE weight percentage (1-w_G) (%)
BPEI25/rGO	76.1	80. 1	19.9
BPEI270/rGO	75.4	79.3	20.7
PAA100/rGO	76.3	76.4	23.6
PAA250/rGO	76.4	77.1	22.9
PSS70/rGO	86.7	86.0	14.0
PSS200/rGO	84.6	82.4	17.6
CMC90/rGO	70.2	63.5	36.5
CMC250/rGO	75.6	67.3	32.7

3.2.4 Size and defectiveness of suspended rGO

To investigate the evolution of suspended particles size vs. time, DLS measurements were carried out. DLS was used for measuring the size distribution of aqueous dispersion of GRMs in previous studies [146, 265]: however, it should be noted that this could only be considered as a semi quantitative analysis because of the complex shapes of GRMs, and is therefore taken as a purely comparative value between different dispersions. Z-average is the harmonic intensity average particle diameter, a measure of the average hydrodynamic diameter and corresponds to the radius of an equivalent hard sphere diffusing as the same rate as the particle under observation [266, 267]. Figure 3.8 displays the Z-average for the different PE/rGO dispersions during 4 weeks. PAA100/rGO and PAA250/rGO yielded the smallest initial Z-average, almost half of BPEI/rGO and PSS/rGO. The initial measurements for CMC90/rGO and CMC250/rGO were much higher than other samples. The average size of the suspended rGO generally decreased with time (Figure 3.8), suggesting the precipitation of larger size rGO. PSS-based and BPEI-based dispersions showed a significant Z-average size decrease within the first week, suggesting that most of the rGO precipitation occurs in this time-frame. CMC exhibited downward trend in overall period but still much higher in Z-average than other groups. PAA100/rGO and PAA250/rGO showed the most stable Z-average during the whole four weeks (PAA100/rGO changed from 644 ± 5 nm to 563 ± 4 nm, PAA250/rGO varied from 652 ± 3 nm to 575 ± 8 nm) thus confirming a better long-term stability of the prepared dispersion. Such result is consistent with UV-Vis measurements reported in Figure 3.6b. In addition, the light scatter analysis provides insight on the reasons behind the better stability obtained with PAA, which appears to be directly related to the reduced particle size dispersed, with respect to other PE systems. This suggests that PAA, compared to other PEs understudy, is more efficient in limiting the aggregation of rGO into larger and poorly suspended clusters. The polydispersity index (PDI) was also evaluated before and after aging (Table 3.3). PDI is a dimensionless parameter that indicates the width of the detected particle size distribution,) which is used to quantify the quality of the dispersion [268]. When PDI < 0.1, the sample is defined as monodisperse, values in the range of 0.1 < PDI < 0.2 indicate narrow particle size distributions and values between 0.2 < PDI < 0.5 are normally obtained for broad particle size distributions [268]. In PAA100/rGO and BPEI25/rGO, the smallest and greatest PDI values of 0.19 and 0.62 were obtained, respectively, highlighting a strong difference in the particle size distribution. Of all the tested PEs only PAA100 and PAA250 obtained

a PDI close to 0.2 thus suggesting their superior size distribution and better homogenous dispersion of rGO with respect to the other tested PEs. It is worth noting that the PDI decreased for almost all systems after aging likely due to the sedimentation of the big particle fractions.

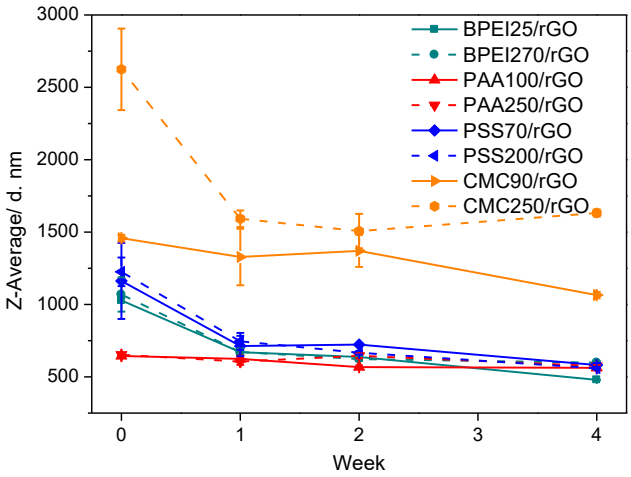

Figure 3.8 Average size of suspended rGO with different aging time

Table 3.3 The PDI values of PE/rGO samples before and after aging 4 weeks.

Sample	Storage time (week)	
	0 w	4 w
BPEI25/rGO	0.62	0.25
BPEI270/rGO	0.54	0.30
PAA100/rGO	0.19	0.24
PAA250/rGO	0.32	0.25
PSS70/rGO	0.60	0.50
PSS200/rGO	0.54	0.52
CMC90/rGO	0.57	0.43
CMC250/rGO	0.46	0.41

The structural quality of the dispersed rGO was further investigated by Raman spectroscopy. Figure 3.9 presents the spectra of PE/rGO composite film, pristine rGO as well as the sonicated rGO (rGO_s). The latter was treated in water with same process employed for PEs-based dispersion in order to evaluate the effects of sonication on the defectiveness of the pristine rGO. As shown in Figure 3.9, two

main sets of signals are observed in pristine rGO, rGO_s and other PE/rGO samples. The first-order of signal (1200-1700 cm^{-1}) is composed of D, G and D′ bands. The D band is related to the breathing modes of six-atom rings and it requires a defect for activation while the G band is ascribed to the in-plane stretching vibration mode of sp^2 carbon atoms [269, 270]. In the second-order, 2D band, D+ D′ band and DD′ band are observed. The 2D band and DD′ band are the overtone of D band and D+ D′ band, respectively [271, 272]. It is well established that the relative intensity of D band to G band (I_D/I_G) and full width at half maximum of G band (Γ_G) can be associated with the disorder of graphene material network [270]. The I_D/I_G ratio were found comparable at 1.41 ± 0.17 and 1.45 ± 0.06 for rGO and rGO_s, respectively. Meanwhile the Γ raised in D band and a very relevant increase is observed in Γ_G, indicating the formation of new edges or a slightly increase in defect content due to the sonication treatment [271, 273]. After being dispersed within the PEs, the calculated I_D/I_G values were similar to rGO_s and fell within the range of 1.40-1.45 except for BPEI25/rGO that reveals a lower ratio value of 1.26 ± 0.09. In addition, the slightly lower Γ_G and position of G band suggest a weak reduction effect by BPEI, that was previously reported in studies[274, 275]. Overall, the Raman results clearly point out a limited effect on the defectiveness of rGO, which is consistent with the non-covalent interaction between PE and rGO.

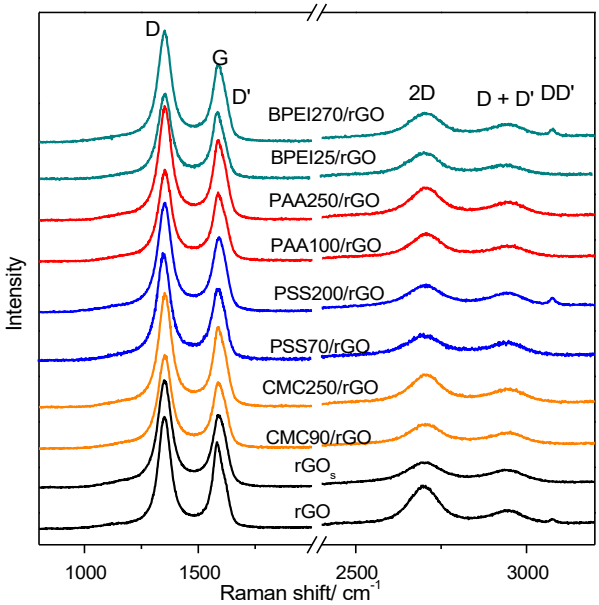

Figure 3.9 Raman spectra of rGO with PEs, pristine rGO and rGO_s after sonication in water.

3.2.5 Interaction between polyelectrolyte and rGO

Effect of charge density of PAA and BPEI to dispersibility of rGO

The above results clearly demonstrate the highest concentration of rGO in BPEI based dispersion and the remarkable stability for PAA/rGO dispersion. Considering both BPEI and PAA are weak PEs, their surface charge density is tunable with pH, which makes it possible to adjust the interaction between PE and rGO by reinforcing or weakening electrostatic interaction. Due to the similar dispersing and stability of PAA100 and PAA250 in above results, PAA100 was investigated. Conversely, BPEI25 was selected due to the obtained high concentration of rGO. rGO is well known to have weak negative charges in water mainly due to the ionization of residual functional groups of carboxylic[276]. Therefore, the pH modification changes the surface charges on rGO where the high pH leads to deprotonation of carboxyl groups into carboxylate groups thus the increase of negative charges. As the pristine PAA solution shows an acidic environment, the charge on rGO is weak. Thus, the adsorption of PAA to rGO surface is made possible by attractive hydrophobic interaction occurring between PAA backbone and rGO. The negatives charges ($-COO^-$) on PAA then provide effective repulsive force to prevent rGO sheets re-stacking [236]. The interaction between rGO and PAA as well as the surface tension of PAA solution are deeply related with the dissociation degree of PAA functional groups that can be modified by changing pH. Aiming at further investigating the nature of interaction between PAA and rGO, a series of PAA100/rGO with variable pH were prepared (Figure 3.10). The unmodified dispersion (pH 3.4) showed the highest intensity of absorbance in UV-vis spectra, corresponding to higher concentration of rGO, which can be qualitatively appreciated by visual inspection as it yields the darkest dispersion. The degree of ionization α can be calculated according to the Henderson–Hasselbalch equation (3-3) [277], where pKa is the dissociation constant. The α of PAA solution with pH 3.4 was calculated and it was around 0.12, which means that the functional groups were predominantly protonated and a limited fraction of the carboxyl groups were dissociated to $-COO^-$. At pH 2, α is 0.005, which results in limited repulsion interaction to counterbalance van der Waals and π-π driven rGO re-stacking. On the other hand, at pH 5, α strongly increases to 0.84, leading to a strong repulsion forces (due to the ionized $-COO^-$ from both PAA and rGO) that hinder the close contact between rGO and PAA. When pH reached 7 or above, α is further increased towards the full dissociation of PAA. At this point, it's extremely hard for PAA to adsorb on graphene. Therefore, the good dispersion performance of rGO in PAA appears to be the result of an optimum balance of both electrostatic repulsions and

hydrophobic interactions.

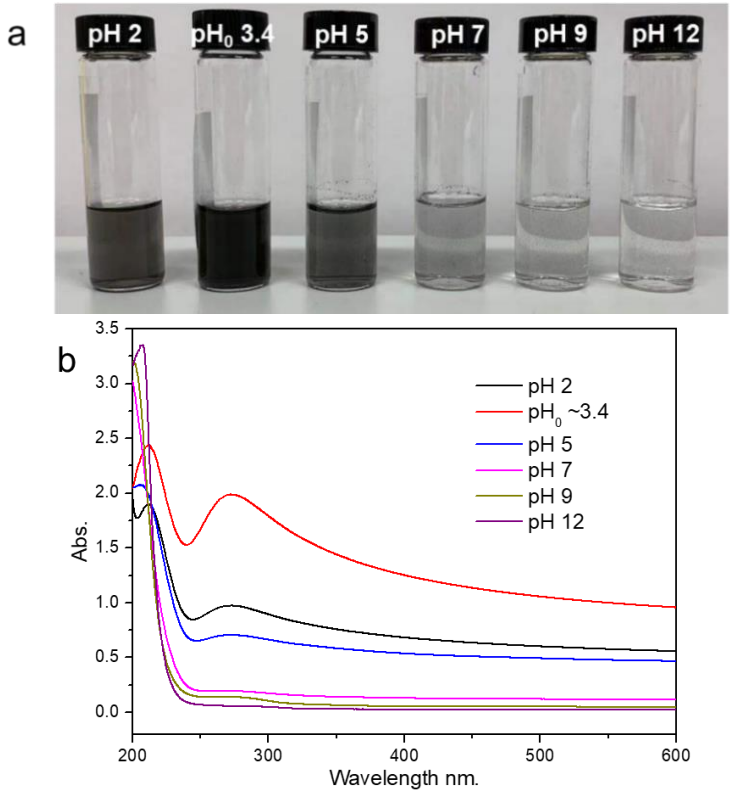

Figure 3.10 Photographs and UV-vis spectra of PAA100/rGO with different pH

$$pK_a = pH - \log\frac{\alpha}{1-\alpha} \tag{3-3}$$

Conversely, BPEI is a cationic hydrophilic PE bearing primary, secondary, tertiary amines, they easily coordinate with hydrogen to form positively charged functional groups of NH_3^+, NH_2^+ and NH^+ at a low pH condition. The protonation degree of BPEI increases gradually from 0 at pH 12 to 1 at pH 2, with three pKa calculated for primary, secondary and tertiary amines have been calculated as 4.5, 6.7 and 11.6, respectively [246, 278]. A strong electrostatic attraction is expected to form between BPEI and rGO at a suitable pH. In order to evaluate the adsorption behavior of BPEI to rGO, a series of BPEI25 solutions with different pH, from pH 4 to pH 12, are used to prepare BPEI/rGO dispersions (Figure 3.11). With decreasing degree of protonation, i.e. by increasing pH, it is possible to note that the concentration of rGO increases by moving from pH 4 to 10 and then drops in the 10 to 12 pH region. The uncharged BPEI solution (pH 12) reveals better rGO

dispersing performances with respect to that of solutions characterized by ionization degree α higher than 0.4 (pH ≤ 8).

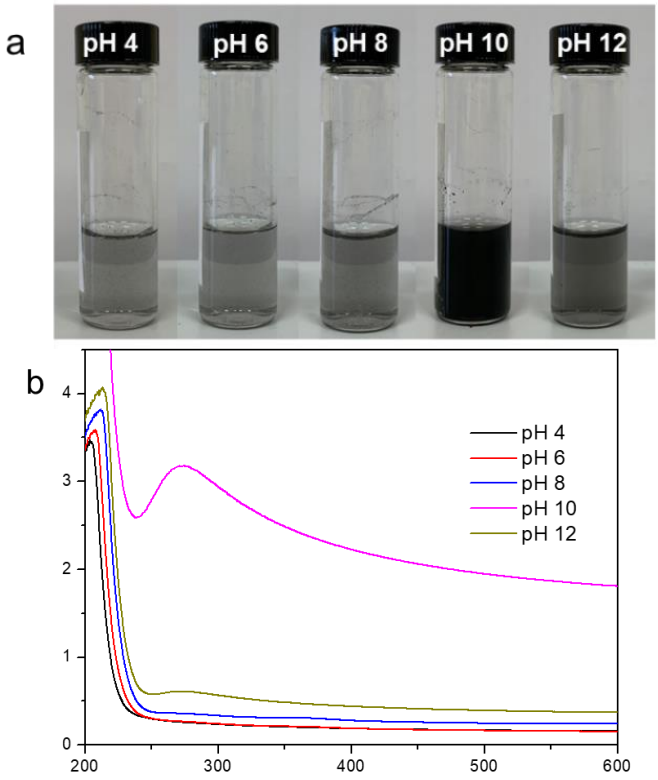

Figure 3.11 Photographs and UV-vis spectra of BPEI25/rGO with different pH

These results are in agreement with a previous study describing the adsorption of BPEI on uncharged graphite [279]. Indeed, the adsorption process of BPEI onto graphite could be divided into three steps: diffusion toward the surface, adhesion to the surface, and rearrangement [279]. Step two plays an important role in dispersing and stabilizing rGO, and it is influenced by the intramolecular segment-segment repulsion in BPEI. At lower pH, BPEI is highly protonated and shows a strong repulsive interaction between charged segments. Even if positive to negative charge compensation occurs at the surface of rGO, the interaction is limited based on the huge difference in charge density between poorly charged rGO and strongly ionized BPEI. Thus, the adsorption of a high number of highly protonated BPEI chains is limited due to charge repulsion effects. With decreasing charge density (higher pH) the repulsive force is reduced, consequently the adsorbed amount increases until it reaches a maximum with uncharged molecules. However, as demonstrated in Figure 3.11, the best dispersion is obtained at pH 10, not at pH 12. This can be easily explained by considering that the driving force for adsorption is limited with

the charged rGO but non-protonated BPEI. Even with small amount of BPEI adsorbed, electrostatic repulsion is lacked in order to achieve a stable dispersion. Thus, obtaining a suitable degree of protonation represents a critical condition for dispersing and stabilizing rGO as it limits BPEI segment-segment repulsion while allowing for optimal attractive van der Waals interactions between rGO and BPEI.

Interaction of CMC and PSS with rGO

In principle, similar interactions (like PAA to rGO) may also occur in rGO dispersions containing other negatively charged PEs, like PSS and CMC. CMC consists of β-linked glucopyranose units with varying level of carboxymethyl ($-OCH_2COO^-$) substitution [280]. The degree of solubility (colloidal dispersion or full solubility in solution) is accepted to be function of the degree of substitution (DS) as the carboxymethyl groups are deemed responsible for solubility as cellulose is insoluble in water at room temperature and mild pH [281]. It was reported that CMC with lower DS preferentially adsorbs on graphite due to attractive hydrophobic interactions [282]. This is also verified in this work where, although the two CMC grades used differ for both molar mass and DS, a greater uptake of CMC on rGO was measured for CMC90 with DS value 0.7 with respect to CMC250 with DS 1.2.

On the other hand, PSS is an amphiphilic polymer in which the hydrophobic benzene ring may provide π – π interaction with aromatic structure of rGO sheets, meanwhile the sulfonate functional groups might in principle confer stability to the rGO dispersion by charge repulsion [115, 283]. However, the stability of rGO in PSS resulted to be limited in this work, leading to about 60 % reduction in the concentration of rGO in dispersions after 4 weeks. This could be explained by considering that, although the hydrophobicity of PSS is much higher than PAA due to the hydrophobic backbone and side chain groups, the steric hindrance exerted by the PSS functional group and the high charge density prevent the adsorption of PSS chains on the surface of rGO.

3.3 Conclusions

In this part of the work, aqueous rGO dispersions were prepared using polyacrylic acid, branched poly(ethylenimine), sodium carboxymethyl cellulose and poly(sodium 4-styrenesulfonic acid). The effect of polyelectrolyte type, molar mass and charge density on the quality and stability of the dispersion have been evaluated. Unlike high-energy exfoliated single or few-layer graphene sheets, this

work emphasizes the ability of polyelectrolyte molecules to separate and stabilize reduced graphite oxide under mild ultrasonic conditions, implying larger size, more layers of graphene layers and more difficulties in maintaining stability. Moreover, the rarely mentioned relationship between the surface energy of polyelectrolyte solutions and their graphene dispersing ability is discussed, while the surface energy theory is usually applied in organic solvent dispersion systems.

According to the results, the dispersing performance of anionic polyelectrolytes is strongly correlated with the solution surface tension, and polyacrylic acid-based dispersions with lower surface tension displayed the lowest average particle size, a narrow size distribution as well as negligible change in rGO concentration after four weeks. Conversely, sodium carboxymethyl cellulose and poly(sodium 4-styrenesulfonic acid) showed limited dispersion capability achieving the lowest rGO concentration. On the other hand, the dispersion effectiveness of cationic polyelectrolytes is not limited by high surface energy, as rGO dispersions containing branched poly(ethylenimine) exhibited the highest concentration of dispersed rGO compared with other PEs after four-week aging, while concentration has been found to be inversely proportional to the molar mass. For weak polyelectrolytes, the possibility to control charge density through pH has been evaluated as well. When employed at the boundaries of high and low charge densities (i.e. very high or very low protonation and deprotonation degrees), both weak polyelectrolytes understudy obtained poor rGO dispersions. Conversely, the optimal dispersing conditions have been found to be related to mild charge densities allowing for favorable interplay of electrostatic repulsion/attraction and hydrophobic interactions between the polyelectrolytes and rGO. The results presented here open up for the further development of polyelectrolyte/rGO dispersions in water-based assembly processes exploiting electrostatic interactions for the production of membranes and functional coatings.

Chapter 4

4 PAA/PDAC complexes incorporating rGO

4.1 Introduction

In chapter 3, it was reported that rGO disperses well in PAA solution at pH 3.4 after tip- sonication for 30 min. The PAA/rGO dispersion exhibits good stability, narrow size distribution, and relatively high rGO concentration, which relays on the mild charge density and relatively low surface tension of PE solution. Additionally, a complexation forms with two oppositely charged PEs mixing together, which creates the possible approach to achieve rGO incorporated polymer-based composites under room temperature and aqueous-based conditions. The complexation of PEs occurs with the types of strong-strong, strong-weak or weak-weak combination. The weak-weak combination usually requires two different pH for fully dissociate the positively and negatively charged PEs, indeed, it requires more stringent conditions for completely complexing. Apparently, the complexation is easier to control with the combination of PAA and strong Pol^+ (positively charged polyelectrolyte), because the pH changes only the dissociation of PAA but has no influence on strong Pol^+. The poly(diallyldimethylammonium chloride) (PDAC), a linear positively charged PE, has been found to be attractive to GRM functionalization; indeed, PDAC modified GO followed by reduction process was used to fabricate PDAC-rGO [142, 284]. The rGO was loaded on

surface of structural defined nano-metal-oxo-cluster compounds, $[Ni_4(Trz)_6(H_2O)_2][SiW_{12}O_{40}]\cdot 4H_2O$ via bridging agent of PDAC, which increases the peroxidase-like activity, conductivity and stability [144]. The interaction strength between Pol^+ and Pol^- reveals the ability of salt added to break polymer ion pairs. Generally, the strong ion pairs of polymers are more likely to result in glassy PEC with lower permeability to small molecules or ions, while weak ion pairs are more likely to produce coacervate, which allows the transport of small molecules and are more sensitive to salt, indeed, it requires less salt concentration to achieve complete dissociation [153, 161]. The relatively weak association of PAA and PDAC endows favourable condition to the coacervate formation and thus facilitates subsequent processing of composite materials.

The addition of inorganic nanofillers could influence the properties of PEC multilayer and bulk materials. For instance, the tensile strength and elastic modulus of graphene oxide decorated sodium carboxymethyl cellulose/ poly(diallyldimethylammonium chloride (GO-CMC/PDAC) membrane reached to 115 MPa and 3.5 GPa with loading of 1.5 v/v% GO into PEC membrane, which were 3 and 1.5 times higher than pristine CMC/PDAC [285]. It is expected that the rGO addition could also improve the mechanical robustness of PAA/PDAC in present study due to the stiffness of fillers and transfer of stress distribution. However, the presence of salt and/ or the water in PECs could significantly change the cross-linking density of polymers and thus influence their mechanical properties [149, 170, 286, 287]. Salt ions doped PEC of poly(styrene sulfonate)/ poly(diallyldimethyl ammonium) (PSS/PDAC) could soften materials into viscous fluid-like state [160]. The presence of water can partially break the electrostatic interaction and improve mobility of polymers. The PEC fiber of alginate/poly(diallyldimethylammonium chloride) (ALG/PDDA) revealed a sensitive humidity response, it was plastic with a modulus of $\sim 10^9$ Pa at environment humidity lower than 65 %, and transferred into rubbery with modulus of $\sim 10^6$ Pa at humidity above 65 % [286]. Moreover, the reversible electrostatic interaction between PEs with assistance of water makes them intrinsically healing. In general, improving the mechanical property of PECs will suppress the mobility of polymer chains and decrease their healing property. As a result, the mechanical property and healing property of composites PAA/PDAC is expected to be defined by the combined effects of salt, rGO and moisture. Based on this consideration, this chapter reports the preparation of rGO-reinforced PECs based on the rGO dispersion in PAA solution and complexation of PAA and PDAC molecules. The distribution and dispersion of rGO in PEC, mechanical properties and healing

properties of these composites are studied systematically. Besides, the effect of salt into pristine PAA/PDAC and rGO-PECs is also discussed.

4.2 Result and discussion

4.2.1 Selection of PAA/PDAC complexation conditions

The mixing pH and salt concentration were determined at first, as shown in Figure 4.1. Only when the pH reached 7, the complex of PAA and PDAC formed a coacervate instead of precipitation. The coacervate is a reversible and equilibrium phase near charge neutrality, which indicates the PAA was dissociated and the charges almost fully interacted with PDAC at pH 7. Even if the solid precipitate phase could be transformed into coacervate with addition of salt, the precipitate of PAA/PDAC at pH 3 and pH 5 didn't show the transition point even with salt concentration as high as 1.2 M. On the other hand, the coacervate PAA/PDAC at pH 7 seems more sensitive with ionic strength, the viscosity decreased with increasing salt concentration, and turned into a single liquid phase at 0.5 M NaCl. Thus, in order to obtain processable complexes and better rGO incorporation conditions, the mixing pH was set to 7. For the salted samples, NaCl concentration was set as middle of phase separation turning point, i.e. 0.25 M.

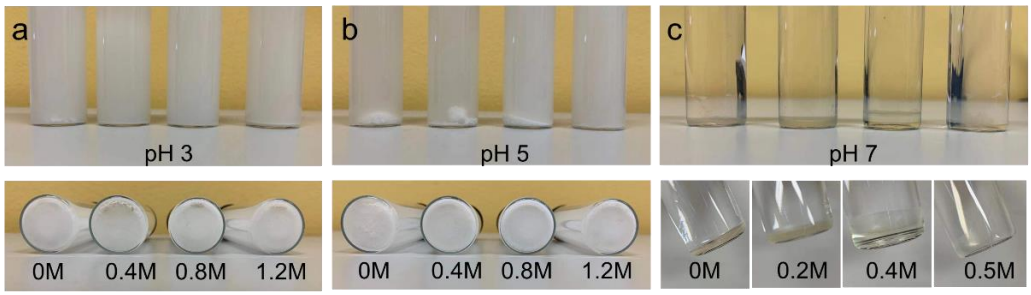

Figure 4.1 PAA and PDAC mixing at different pH and salt NaCl concentration

4.2.2 FTIR-ATR and components analysis

Before the discussion of PECs, the FTIR-ATR was applied to pure components PAA and PDAC. PAA, known as a weak PE, varies its degree of dissociation from COOH bond to ionized COO^- by increasing pH. The spectra of pristine PAA and PAA modified by NaOH to pH 7 are compared in Figure 4.2a and Figure 4.2b respectively. The main features of these spectra are summarized in Table 4.1. The FTIR spectrum of PAA shown in Figure 4.2a indicates that the broadband at 3445 cm^{-1} and the bands at 2960 cm^{-1} and 2657 cm^{-1} are assigned for the O-H stretching

in the presence of hydrogen bonding [288], overlapping with C-H stretching. The strong band at 1714 cm^{-1} indicates the C=O stretching vibration for the carboxylic acids. The weak bands at 1454 cm^{-1} with a shoulder band at 1416 cm^{-1} are due to the combination of -CH_2 stretching and symmetric –COO^-, the presence of latter indicates partially dissociation of PAA. The peaks with maximum at 1252 cm^{-1} and 930 cm^{-1} are associated with the occurrence of C-O stretching vibration. The band at 1176 cm^{-1} is due to –(C-O)H stretching mode [289]. The FTIR spectrum of PAA changes with pH modification because of the dissociation of COOH. The main difference is noticeable sharp bands at 1562 cm^{-1} corresponding to asymmetrical vibration of carboxylic anions COO^-, and the symmetrical vibrations of COO^- at 1411 cm^{-1} and 1330 cm^{-1}. Meanwhile, the disappearance of C=O (from COOH) at 1714 cm^{-1}, and the negligible –(C-O)H at 1170 cm^{-1} further confirm the deprotonation of PAA. Moreover, the narrowing of the O-H stretching band around 3400 cm^{-1} could be associated with limitation of intramolecular hydrogen bonding of hydroxyl groups due to the transformation of COOH to COO^-. Except from FTIR, the ATR-FTIR were also applied to solid (dried) PAA, and PAA at pH 7 for better comparison of the ATR-FTIR spectra with other PECs' results. Besides, the shift of wavenumbers and bands distortion may occur in ATR-FTIR measurement, the two kinds of measurements are also for better determination of characteristic bands. For instance, the C=O of PAA in ATR-FTIR is at 1690 cm^{-1}, which is lower than the well-known 1714 cm^{-1} in FTIR. A lower wavenumber of –(C-O)H at 1110 cm^{-1} is also observed in ATR-FTIR of PAA. The antisymmetric and symmetric COO^- in PAA at pH 7 are found in 1547 cm^{-1}, 1400 cm^{-1} and 1321 cm^{-1}.

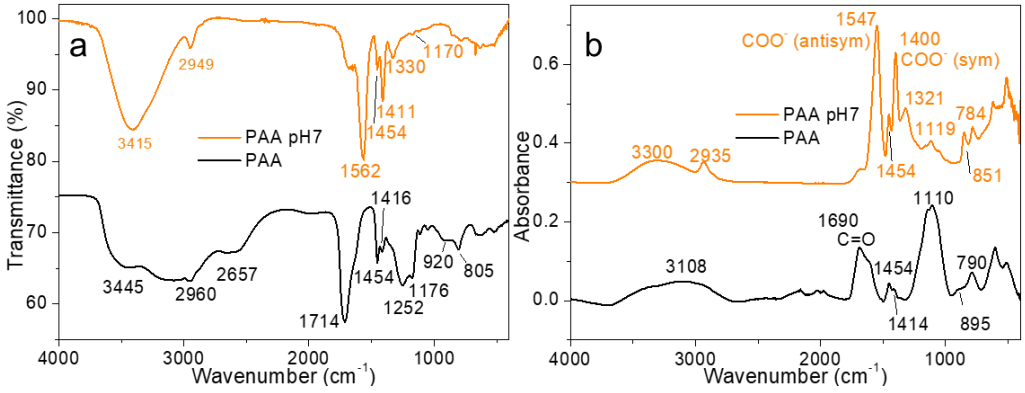

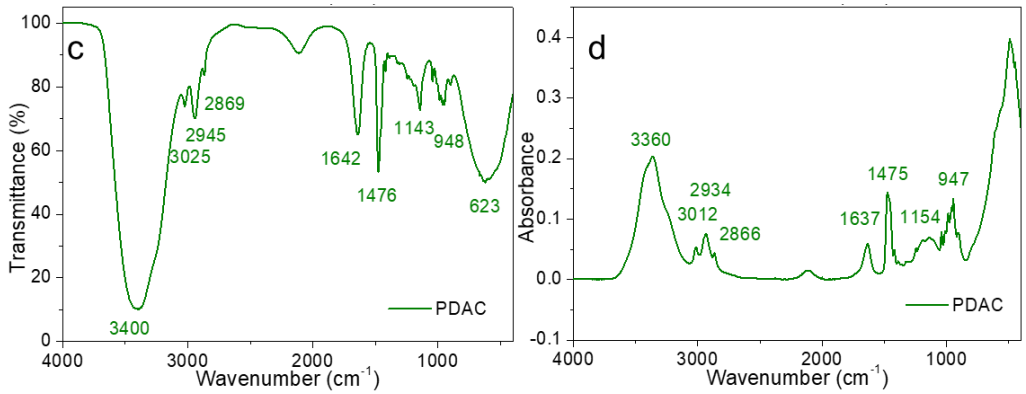

Figure 4.2 FTIR (a) and ATR-FTIR (b) spectra of pristine PAA and PAA at pH 7, FTIR (c) and ATR-FTIR spectra (d) of PDAC

Table 4.1 Peak assignments of pristine PAA and PAA at pH7.

Peak positions (cm^{-1})				Peak assignments	References
PAA bands in FTIR	PAA pH7 bands in FTIR	PAA bands in ATR-FTIR	PAA, pH 7 bands in ATR-FTIR		
3445	3415	3108	3300	O-H stretching	[288, 290]
2960	2949		2935	C-H stretching	
1714		1690		-C=O (free COOH)	[290, 291]
	1562		1547	$-COO^-$ (antisymmetric)	[291]
1454	1454	1454	1454	$-CH_2$	[289, 291, 292]
1416	1411	1414	1400	$-COO^-$ (symmetric)	[289, 291]
	1330		1321	$-COO^-$ (symmetric)	
1252				C-O stretching	[291, 293]
1176	1170	1110	1119	-(C-O)H stretching	[289, 290]
920		895		C-O stretching	[294]
805		790	784, 851	CH_2 rock	[289]

On the other hand, the FTIR and ATR-FTIR spectra of PDAC are shown in Figure 4.2c and Figure 4.2d, the band assignments are listed in **Error! Not a valid bookmark self-reference.**. In the FTIR of PDAC, O-H is found in broadband at 3400 cm^{-1}. The characteristic bands of C-H of -CH, $-CH_3$ and $-CH_2$ are located at 3025 cm^{-1}, 2945 cm^{-1}, 2869 cm^{-1} and 1476 cm^{-1} respectively. The C-N stretching band is observed in 1143 cm^{-1} and quaternary ammonium groups is confirmed at 948 cm^{-1}. Similar characteristic bands are observed in FTIR and ATR-FTIR spectra of PDAC.

Table 4.2 Peak assignments of PDAC observed in FTIR and ATR-FTIR

Peak positions (cm^{-1})		Peak assignments	References
Bands in FTIR	Bands in ATR-FTIR		
3400	3360	O-H stretch	[295]
3025	3012	C-H stretch of -CH	[295]
2945	2934	C-H stretch of $–CH_3$	[295]
2869	2866	C-H stretching of $–CH_2$	[295]
1476	1475	C-H bending of $–CH_2$	[295]
1143	1154	C-N stretching	[295, 296]
948	947	$-(CH_2)N^+(CH_3)_2(CH_2)-$ stretching	[295]

Figure 4.3 compares the ATR-FTIR spectra of initial PEs and the obtained PECs. The spectra of PECs contain spectral features of both starting polymers of PDAC and PAA at pH 7. In the spectra of PECs, Figure 4.3a displays the presence of characteristic bands related to symmetric and antisymmetric $–COO^–$ of PAA, as well as bands C-H, C-N and quaternary ammonium groups of PDAC, which proves the presence of both polymer components in PECs. Compared to pure components, the PAA/PDAC and PAA/G//PDAC show obvious band shifts, including symmetric $–COO^–$ bands shift from 1400 cm^{-1} to 1392 cm^{-1}, from 1321 cm^{-1} to 1314 cm^{-1}, and antisymmetric $–COO^–$ band shifts from 1547 cm^{-1} to 1555 cm^{-1} (in Figure 4.3b). The sign of peak shifting of $–COO^–$ indicates the interaction of carboxyl ion of PAA and $-(CH_2)N^+(CH_3)_2(CH_2)-$ of PDAC. The presence of rGO did not change the shape and position of absorption bands. Comparing to PAA at pH 7, the salt involved samples PAA/PDAC-s and PAA/G//PDAC-s reveal also a downwards shift for symmetric $–COO^–$ bands and an upwards shift for

antisymmetric –COO^- band, which confirms the interaction of PAA and PDAC. However, the –COO^- bands undergo weaker wavenumber shifts in salted PECs than that of PAA/PDAC (see in Figure 4.3b). It is because the conversion of polymeric ion pairs ($PDAC^+$ PAA^-) to extrinsic ion pairs ($PDAC^+$ Cl^-, PAA^- Na^+) in presence of salt. The polymer segments of (PAA^- Na^+) in PAA/PDAC-s and PAA/G//PDAC-s reveal similar features to individual PAA neutralized with NaOH. The absorption spectra of salt-removing $PECs^R$ are presented in Figure 4.3c and Figure 4.3d. They show similar features to each other, and the characteristic features in 1800-1200 cm^{-1} are similar to pristine PAA/PDAC, which suggests restoration of polymeric interaction after getting rid of salt ions.

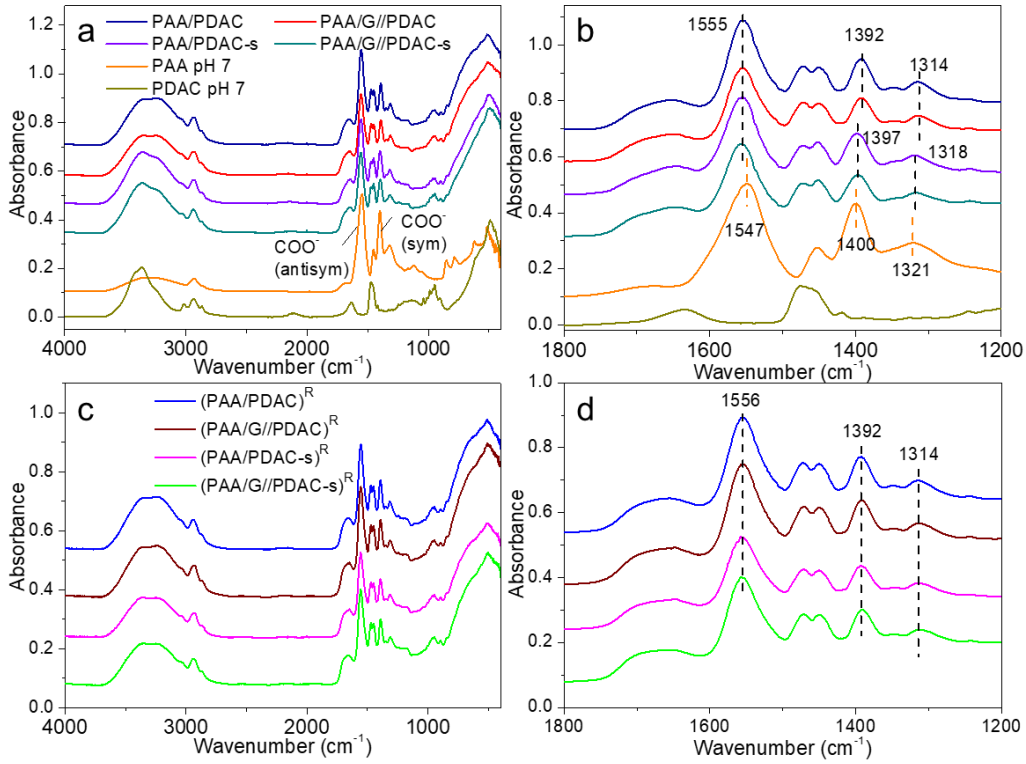

Figure 4.3 ATR-FTIR spectra of PAA, PDAC at pH 7 and the PECs, rinsed $PECs^R$ in wide range of 4000-400 cm^{-1} (a), (c) and specific range of 1800-1200 cm^{-1} (b), (d).

The concentration of G in PAA/G dispersion is around 0.18 mg/ml, which is obtained from the residual mass of individual components PAA, rGO and dried PAA/G in TGA and the volume of dispersion used. The rGO content in PAA/G//PDAC is around 0.6 - 0.7 wt%, where 0.6 wt% is rGO accounts on the sum of rGO, PAA and PDAC molecules in system, 0.7 wt% is based on the assumption of fully complexing of PAA and PDAC with release of small counterions. On the other hand, moisture content and salt content in different PECs are summarized in

Figure 4.4a, the moisture content is measured by weighing samples before and after drying in vacuum oven at 90 °C overnight and salt content is determined according to TG results in Figure 4.4b and Figure 4.4c.It should be noted that the mass percentage of salt and rGO in PECs exclude the moisture effect, and they are the wt% of net weight of samples. The moisture content of samples ranges from 14 to 18 wt%, where the rinsed samples PECs^{R} show slightly lower value (~15 wt%) than that of samples without salt-removing treatment (~18 wt%). However, the salt-rich samples PAA/PDAC-s and PAA/G//PDAC-s show comparable moisture content to that of PAA/PDAC and PAA/G//PDAC. Most of water in the coacervate is removed during drying at room temperature, transforming the materials from hydrogel to stiff solid. The water in PECs can be further removed during hot-pressing. As reported in literature [171, 297], water molecules exist in different microenvironments within PECs, including the bulk water independent from PE chains, and the water with tightly or loosely bound states near intrinsic and extrinsic ion pairs. The salt-removing treatment transfers ion pairs from extrinsic interaction (interaction of salt and PE) into intrinsic interaction of PEs, resulting in tighter packed assemblies of polymers. Moreover, the rGO-involved samples show slightly lower moisture content than rGO-free samples due to the hydrophobicity of rGO.

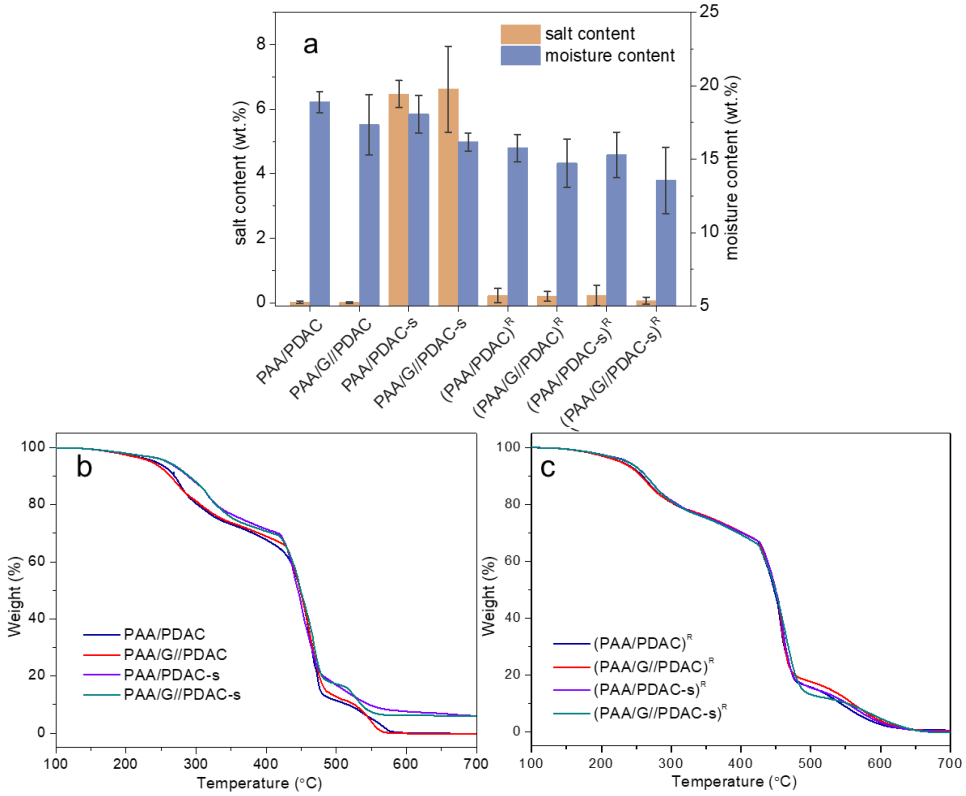

Figure 4.4 Salt and moisture contents in all samples (a), TGA curves of PECs (at air) (b) and PECs^{R} (c) for measuring salt content.

PAA/PDAC-s and PAA/G//PDAC-s show salt proportion at 6.5 ± 0.4 wt% and 6.6 ± 1.3 wt%, respectively (Figure 4.4a). Salt ions are distributed preferentially in the supernatant if comparing the input salt proportion of around 50 wt% to final salt reserved in complexes around 7 wt%, which is accordance with previous studies of exclusion of salt from the polymer-rich coacervate phase [298]. After rinsing and washing, salt in PAA/PDAC-s and PAA/G//PDAC-s are mostly removed, corresponding to approx. 0.2 wt% residual weight for their rinsed samples. It is worth mentioning that a small amount of salt was retained in PAA/PDAC and PAA/G//PDAC because Na^+ ions were introduced in the system when neutralized with NaOH, which could form NaCl together with the Cl^- ions. This is hard to be detected in TGA as the amount is comparable with the sensitivity of the TGA, but easy to confirm using EDS.

Element analysis in Table 4.3 shows the average percentage of Na and Cl in PECs. A small amount of Na and Cl have been found in PAA/PDAC as well as in PAA/G//PDAC, suggesting limited salt concentration in pristine samples. The concentration of Cl was significantly higher than Na in all cases, suggesting the excess Cl could be associated to incompletely complexed PDAC. After soaking and rinsing, Na was completely removed while there was residual Cl in corresponding $PECs^R$, while approx. 0.3% Cl remains. The complexed monomer ratio of PDAC and PAA ($n_{PDAC/PAA}$) can be calculated based on EDS results and euqation (4-1), where it is assumed that rGO in PECs would not consume the charges of PAA and PDAC, and the consumption of Cl is only because of complexation. Moreover, because the elements of Na and Cl in normal PECs could be influenced by salt, this calculation is only applied in $PECs^R$. The $N_{PEC}{}^R$ and N_{PDAC} are atomic percentage of nitrogen of PEC^R and PDAC respectively, and the $Cl_{PEC}{}^R$ and Cl_{PDAC} are atomic proportion of chlorine from PEC^R and PDAC respectively. The $n_{PDAC/PAA}$ of $(PAA/PDAC)^R$, $(PAA/G//PDAC)^R$, $(PAA/PDAC\text{-}s)^R$ and $(PAA/G//PDAC\text{-}s)^R$ are 1.04, 1.07, 1.03 and 1.07 respectively, indicating that the molar ratio of PDAC and PAA in complexes is close to 1.

Table 4.3 Element atomic percentage in cross-section of PECs based on EDS result

	Cl (%)	Na (%)	N(%)
PDAC	8.8 ± 0.5	---	8.9 ± 0.5
PAA/PDAC	1.0 ± 0.3	0.2 ± 0.1	6.6 ± 0.6
PAA/G//PDAC	0.9 ± 0.2	0.2 ± 0.1	6.8 ± 0.5
PAA/PDAC-s	2.6 ± 0.2	2.0 ± 0.1	5.6 ± 0.7
PAA/G//PDAC-s	2.6 ± 0.5	1.8 ± 0.1	5.9 ± 0.3
$(PAA/PDAC)^R$	0.3 ± 0.1	---	7.5 ± 0.7
$(PAA/G//PDAC)^R$	0.4 ± 0.1	---	6.6 ± 0.4
$(PAA/PDAC\text{-}s)^R$	0.2 ± 0.1	---	6.7 ± 0.6
$(PAA/G//PDAC\text{-}s)^R$	0.4 ± 0.04	---	6.3 ± 1.1

$$n_{PDAC/PAA} = \frac{{}^{N_{PEC^R}}/_{N_{PDAC}} \times Cl_{PDAC}}{{}^{N_{PEC^R}}/_{N_{PDAC}} \times Cl_{PDAC} - Cl_{PEC^R}} \quad (4\text{-}1)$$

4.2.3 Thermal stability and morphology

The thermal stability of PEC grafted with rGO and/or salt was further studied according to TGA results and mass loss rate of samples upon heating (DTG), in Figure 4.5. In order to evaporate water, all of the samples were heated at 100 °C for 30 min. Before discussing the thermal stability of PECs samples, the TGA results of pure components in Figure 4.5a are firstly studied. Both PAA and PDAC show two stages of degradations where the degradation of PAA takes place over two broad temperature ranges, corresponding to thermal decomposition of carboxylic acid group at 200-300 °C and decomposition of backbones at 350-500 °C. Instead, two decomposition stages of a wide range at 250-400 °C and a relatively narrow range at 400-485 °C are found in pure PDAC. The first thermal decomposition stage of PDAC was found to be related to the reaction similar to quaternary ammonium salts dissociate with the formation of alkyl halide, in reaction (4-12) [299]. Where Me is $–CH_3$. However, the pH modification may also change the degradation process of PEs since it influences the dissociation of weak PEs.

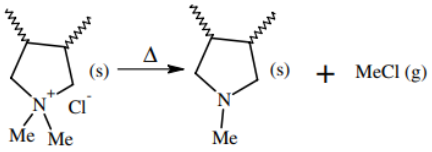

(4-2)

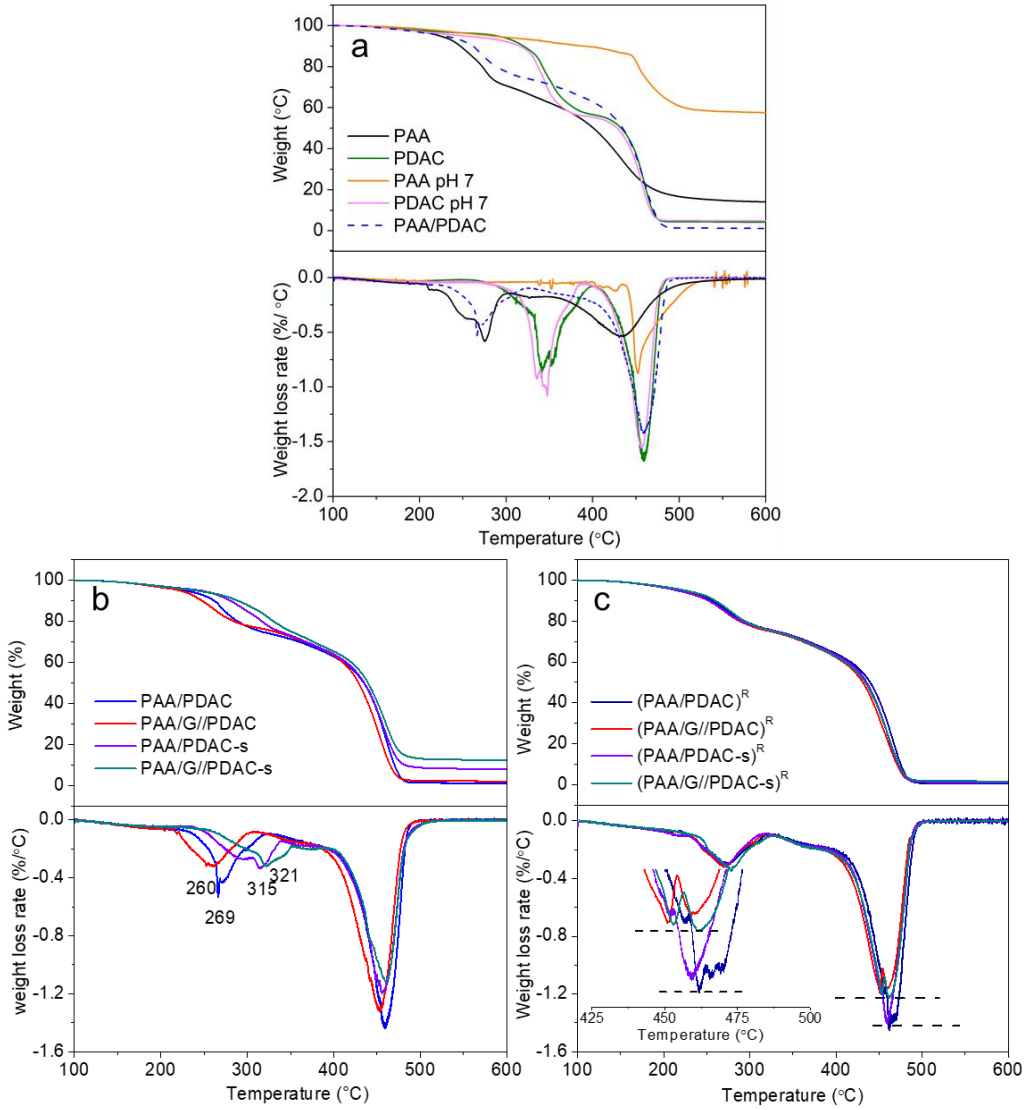

Figure 4.5 TGA and DTG of pure components (a), PECs (b) and PECs ^{R} (c) at N_2 atmosphere

As expected, the PDAC at pH 7 reveals similar results with pristine PDAC, while only one peak of DTG result is observed near 460 °C in PAA at pH 7. The PAA neutralized by NaOH can be considered as sodium polyacrylate (PANa). It shows a maximum weight loss at 440-500 °C and a substantial residual, around 60

% of the initial polymer weight, remaining at 600 °C, which consists mainly of sodium carbonate [300]. After complexation, it is interesting to note that the TGA curve for the first decomposition stage of PAA/PDAC (dash curve in Figure 4.5a, lower than 300°C) lies below that of individual pure PAA at pH 7 and PDAC at pH 7. The onset decomposition of PAA/PDAC starts at 230 °C (defined as 5 wt% weight loss), which is close to that of pure PAA (223 °C). Moreover, PAA/PDAC has no peak of DTG at 300-400 °C, suggesting that the conversion of PDAC to alkyl halides was limited by ionic bonding with PAA. Besides, the decomposition of PAA/PDAC approaches to decomposition curve of PDAC at high temperature, especially above 430 °C, where the PAA has been mostly decomposed and the degradation is dominated by the PDAC. At 500 °C the PAA/PDAC is completely decomposed, leaving negligible char residual. The mass residual is even lower than the individual pure components due to the amount of salt excluded in the complexation process.

Two decomposition steps are found as well in other kinds of PECs from according to TGA results in Figure 4.5b and Figure 4.5c. The decomposition of pristine PAA/PDAC gives the first DTG peak value of weight loss rate at about 270 °C, then a rapid weight loss with a maximum rate is observed at about 460 °C. The onset decomposition temperature of salt containing samples (PAA/PDAC-s and PAA/G//PDAC-s) increases to ~245 °C and the maximum weight loss rate in the first decomposition region drastically shifts to ~320 °C. The existence of salt partially replaced the interaction of polymers (Pol^+ Pol^-) into interaction of polymer and salt ions (Pol^+ Cl^- or Na^+ Pol^-). Therefore, the thermal decomposition of salted PECs is the sum of segments of different types ($PDAC^+$ PAA^-, $PDAC^+$ Cl^- and Na^+ PAA^-). The temperature increase corresponding to the first DTG peak (from ~270 °C to ~320 °C) in the salted samples (appears to be associated with the polymer segments of PDAC. Additionally, the maximum rate of weight loss (at ~460 °C) of saline samples decreased compared with PAA/PDAC due to the thermal stability of salt and lower polymer fraction. On the other hand, rGO in PAA/G//PDAC shows a minor influence to onset decomposition temperature (less than 10 °C deviation to PAA/PDAC), but its maximum weight-loss rate at ~460 °C is similar to PAA/PDAC-s that suggests a role of rGO in decreasing rate of volatilization, possibly by reduction of diffusivity for the decomposition products and/or adsobance of the volatiles onto the rGO surface.

Thus, PAA/G//PDAC-s displays the highest onset decomposition temperature and the lowest maximum weight-loss rate due to the effects of both rGO and NaCl. Besides, PAA/G//PDAC-s displays obviously higher residual amount than

PAA/PDAC-s. The residual amount of PAA/G//PDAC-s corresponds to the sum of carbonaceous residue out of polymer decomposition in presence of salt, residual rGO and the salt itself. The deviation is assigned to retained salt within the formulation, assuming the presence of salt is not promoting charring of the PEC. TGA and DTG curves of PECs^{R} are compared in Figure 4.5c. The salt-removing treatment yields TG curves corresponding to that of PAA/PDAC, which reconfirmed the salt influence in raising onset decomposition temperature. Besides, the rGO-containing PECs^{R} reveal a smaller maximum weight loss rate during decomposition, confirming rGO effect in slowing down PEs volatilization.

SEM is carried out to characterize cross-sectional surface of PEC films, shown in Figure 4.6. In Figure 4.6a and Figure 4.6b, cross-section of un-pressed PAA/G//PDAC exhibit surface with pores, micro cracks and the randomly oriented G (with size in the range of 0.6-2 μm), which is different with pressed films, where the defects are negligible (Figure 4.6c-f), meanwhile rGO distribute in parallel, orienting perpendicular to pressing direction. The comparison between nanocomposite PECs prepared with or without added salt is also informative. Indeed, PAA/G//PDAC-s displays a surface with less evident rGO flakes, suggesting the highly salted PEC to be softer even at low temperature during fracture, producing a less defined fracture surface embedding rGO.

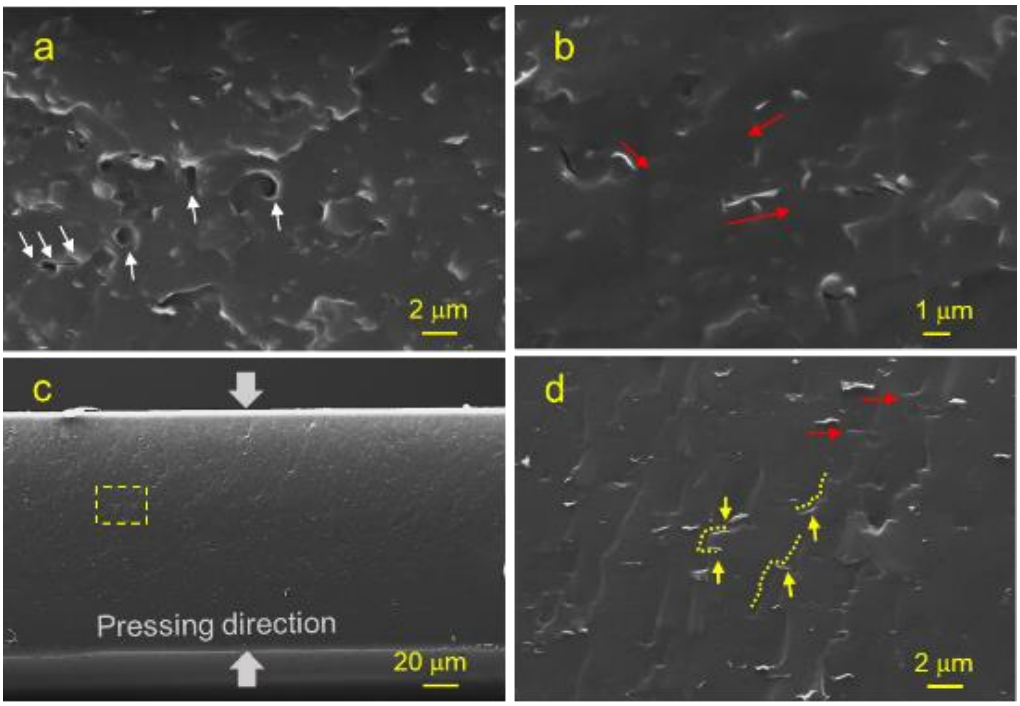

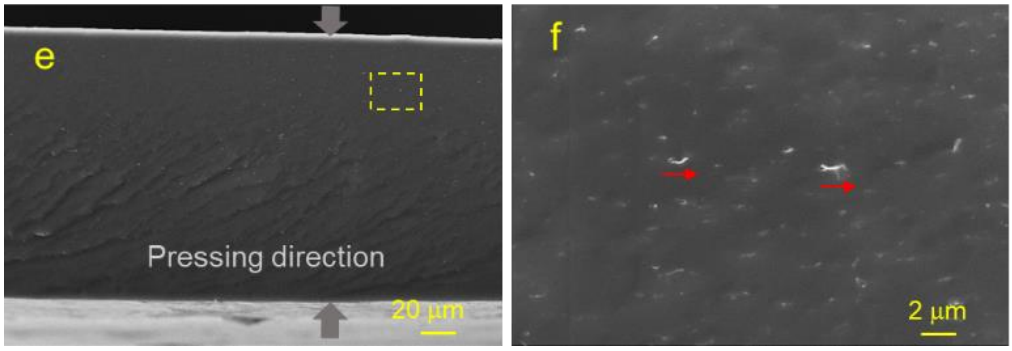

Figure 4.6 Cross-section images of un-pressed PAA/G//PDAC (a) and (b), PAA/G//PDAC (c), and (d), PAA/G//PDAC-s (e) and (f). The (d) and (f) are the regions marked by yellow dotted boxes in (c) and (e) respectively. White arrows: defects in un-pressed PAA/G//PDAC, red arrows: the direction of G, yellow arrows: the G at fracture boundary, dashed curve, the fracture boundary

4.2.4 Mechanical properties

The mechanical properties of PECs were measured via tensile test, as presented in Figure 4.7. The pristine PAA/PDAC shows brittle characteristics with ultimate stress and elastic modulus of 31.5 ± 2.4 MPa and 1114 ± 85 MPa respectively, while its deformation is only 7.7 ± 2.2 %. The presence of salt in PAA/PDAC-s transfers PAA/PDAC from brittle to ductile, leading to a much higher elongation at break (295 ± 90 %), as well as the decreased stress at break (1.6 ± 0.3 MPa) and elastic modulus (166 ± 43 MPa). The ion pairs of Pol^+ and Pol^- in PECs can be viewed as dynamic physical crosslinks, some of which break and reorganize during strain. According to the classical theories of rubber elasticity, the modulus is related to the cross-link density [170]. The salt doping to PECs has been previously shown to reduce the crosslink density, thereby decreasing the modulus and enhancing strain [152, 301]. This trend usually becomes more obvious with salt concentration increasing. The residual water in samples (Figure 4.4) also accounts for the softening of PECs, in particular, in the salted samples, the doping and water molecules make them significantly softer.

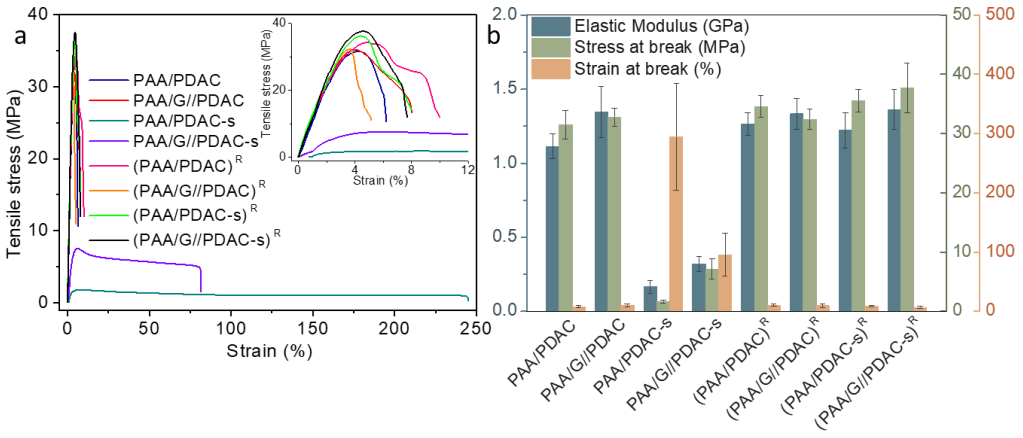

Figure 4.7 The stress-strain curve of PECs with the inset of enlargement at strain range of 0 to 12% (a), elastic modulus, stress at break and failure strain (b)

On the other hand, the increase of stress at break and elastic modulus are obtained (32.7 ± 1.6 MPa and 1346 ± 172 MPa respectively) in PAA/G//PDAC with rGO content of 0.7 wt%. The addition of rGO strongly improved the mechanical properties to salted samples; PAA/G//PDAC-s showed elastic modulus of 320 ± 51 MPa and stress at break of 7.13 ± 1.68 MPa, corresponding to the respective 1.9 and 4.4 times to those of PAA/PDAC-s. The improvements of rGO on elastic modulus and tensile strength in salted samples are accompanied by sacrifice of elongation at break. The reinforcement of rGO in PECs with and without of salt depends on the soft and rigid polymer matrix. The mechanical property of GRMs reinforced polymer composites is affected by the fillers size [302], number of layers [303], distribution and orientation [304, 305], interfacial adhesion [306, 307], and fillers loading [308]. For the hard polymeric composite, elastic modulus and mechanical strength are sensitive to fillers loading since the fillers support applied loads, therefore an increase in loading results in a stronger composite [308]. However, in GRMs reinforced polymers with low-modulus polymeric matrices, elastic modulus can be dramatically improved, depending on the aspect ratio, orientation and interfacial strength of the nanosheets [309].

With the removal of salt, the PECs turn to salt-free samples PECs^{R}, which bumps up the elastic modulus (1200 -1400 MPa) and tensile strength (35-38 MPa), slightly higher than that of pristine PAA/PDAC. A slight decrease in moisture content was found after the desalination treatment in Figure 4.4, which also facilitated the formation of a rigid polymer matrix. These results reveal that the mechanical properties of these PECs are reversible by controlling salt content, and the reinforcement of rGO in composites is strongly associated with the PEC matrix conditions.

DMTA was also carried out to measure the viscoelastic properties of PECs as a function of temperature. Figure 4.8 shows the storage modulus (E'), loss modulus (E'') and loss factor of PECs during heating and subsequently cooling process, those representing the dynamic mechanical property of moist and dried PEC films respectively. Indeed, on heating process the samples containing equilibrium moisture are measured, thus reflecting the viscoelastic properties of the moist samples. Heating in dry atmosphere results in a progressive moisture reduction, with consequent evolution of dynamo-mechanical properties as reported in Figure 4.8a-f. Pristine PAA/PDAC exhibits a progressive decrease in storage modulus until approx. 75 °C, followed by a subsequent increase in E', likely related to water loss and possible reorganization of the complex. PAA/G/PDAC exhibits a qualitatively similar trend, with higher E' value over the whole temperature range, in agreement with the stiffening previously observed in tensile tests, indicating the ability of rGO to restrict segmental motion in PEC. The inclusion of added salt in PECs resulted in much lower storage modulus compared to their salt-less counterparts, confirming the softening effect attributed to weaker interaction of polymer chains after salt ions substitute PAA and PDAC intrinsic ion pairs. Similar trend of significantly decrease followed by the increase in E' is also observed in heating of PAA/PDAC-s and PAA/G//PDAC-s (Figure 4.8d), but the turning point shifts to lower temperature of approx. 25 °C. The abrupt decrease in E' corresponds to peaks in the curves of loss modulus E'' (Figure 4.8b and Figure 4.8e) and loss factor (Figure 4.8c and Figure 4.8f), thus suggesting a reorganization of the PEC structure. Considering the dynamic variation of both temperature and moisture of PEC samples during heating, the E' and E'' curves can be considered as a segment combination of modulus curves of PEC with different water content at different temperature which is close to the real-life condition when materials are heated.

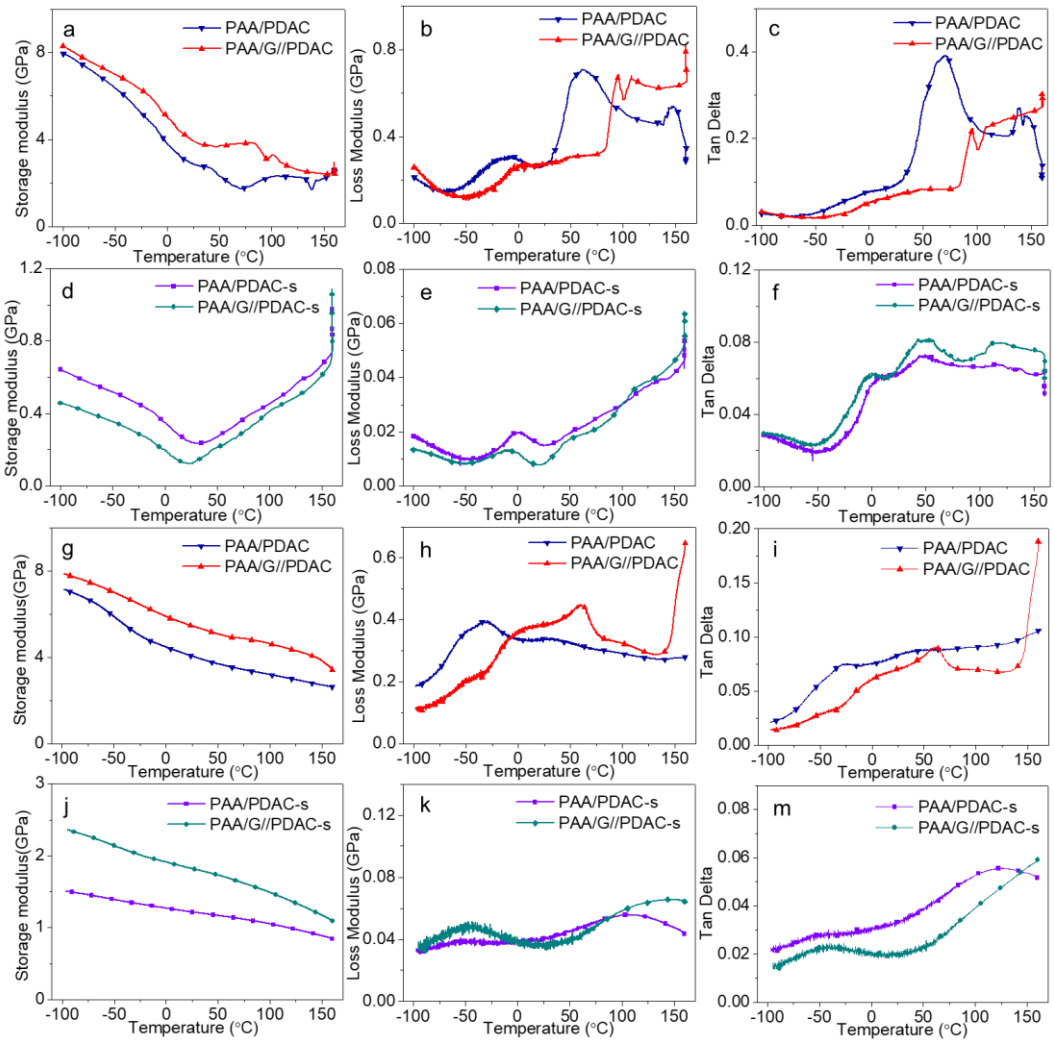

Figure 4.8 Storage modulus, Loss modulus and Tan Delta of PECs during heating (a-f), and cooling process (g-m)

After the isothermal at 160 °C for 20 min, almost of all the water is removed. Taking one sample heated in TGA for 20 min at 160 °C, the lost water weight was calculated to be around 23 wt%. Even though the TGA heating process is not exactly same as DMTA, which has a heating process of cooling from room temperature to -100 °C, and then healing to 160 °C isothermally for 20 min, it still reflects the water removal condition. Dynamic-mechanical properties measured on cooling in dry atmosphere are representative of the molecular relaxation of dried PECs with temperature, presented Figure 4.8g-m. PAA/PDAC expectedly shows a regular increase in stiffness with decreasing temperature, with a room temperature value of 4 GPa and a broad peak in E'' with maximum at -30 °C. PAA/G//PDAC shows a similar trend, with confirmed higher stiffness compared to PAA/PDAC

over the whole temperature range and further broadened E'' with maximum at significantly higher temperature. This confirms relaxation of PEC in dry state is strongly affected by the presence of rGO, despite the very low content of nanoflakes.

Salt-added PECs confirmed much lower E' than PAA/G//PDAC and PAA/PDAC as well as a stiffening effect brought by the presence of rGO. Indeed, E' of PAA/G//PDAC-s is significantly higher than that of PAA/PDAC-s during cooling process, and the difference increases with decreasing temperature. On the other hand, E'' plots of PAA/PDAC-s and PAA/G//PDAC-s are similar with a broad peak at approx. -50 °C, which illustrates the plasticizing effect of salt that shifts the relaxation of dried PEC-s to lower temperature. However, there is another broad peak at higher temperatures of E'' plots, corresponding to the maximum at approx. 140 °C in PAA/G//PDAC-s and 100 °C in PAA/PDAC-s. The E'' peak in salted samples at high temperatures (above 100 °C) appears to be related to the main relaxation of the complex. Based on previous study [310], as determined by differential scanning calorimetry (DSC), the glass transition temperature (Tg) of PAA/PDAC weakened and shifted toward higher temperature with the ionic complexation degree (ICD) increase, and finally became undetectable when ICD was above 0.16 (Tg was 123 °C when ICD = 0.16). The ICD was defined as the ratio of the number of ionized carboxylic acid groups interacting with PDAC to the total number of carboxylic acid. The undetectable Tg could be because ionic complexation between PAA and PDAC restricted the mobility of polymer chains, which could also be found in other PECs, such as PDAC/PSS and PAH/PAA [171, 311]. Therefore, with the ICD around 1 in this study, it is expected that the Tg of PAA/PDAC could be high and hard to be detected. Since the thermo-mechanical analysis, DMTA is more sensitive, and the Tg from DMTA is close to that of DSC, it is expected that the high-temperature transition in salted PECs could be associated with glass transition, as the salt doping reduced ionic interactions of PAA and PDAC. However, further confirmation requires a deep investigation with DMTA that is out of our aims of viscoelastic response of PECs with temperature.

4.2.5 Effect of rGO concentration in PECs

The reinforcement of rGO to PECs has been found in previous discussions, however, a further understanding of effect of rGO concentration in PECs to mechanical improvement and nanofiller distribution is lacking. Figure 4.9 compares mechanical reinforcement in composites under different rGO loadings, as well as the nonlinear curve fittings in stress at break and elastic modulus

improvement factor (E/E_0, E_0 is the elastic modulus of PAA/G//PDAC). A nearly linear increase in stress at break with rGO filler loading is found, while the reduction in reinforcing efficiency of elastic modulus, corresponding to a gradually decreased slope in fitting curve. In addition, the small value of failure strainis observed in PECs, which slightly decreases with rGO concentration (Figure 4.9b). Those results confirm the brittle features and mechanical reinforcement of rGO increases with rGO concentration.

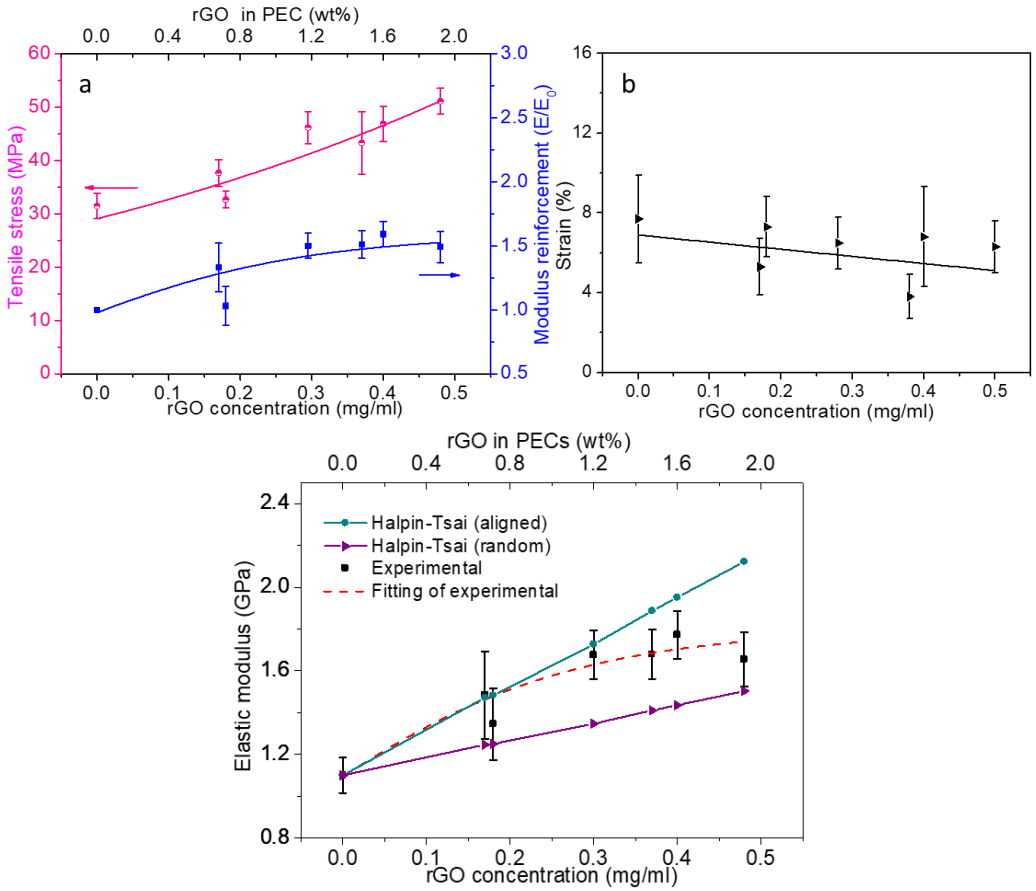

Figure 4.9 Mechanical reinforcement (a) and elongation at break (b) of rGO as a function of concentration. Experimental and theoretical elastic moduli derived from the Halpin-Tsai model for PAA/G//PDAC-based composites with aligned and random dispersions (c).

The elastic moduli of composites under unidirectional and random distributions were simulated and compared with the actual mechanical results. Halpin-Tsai equation was previously validated for predicting modulus of unidirectional or randomly distributed filler-reinforced nanocomposites, for instance, the GO reinforced PVA composite [312], GO-PAH/PSS nanomembrane [313], and

polyethyleneimine reduced graphene oxide incorporated methylcellulose (PEI-rGO/MC) composite[224]. The elastic moduli of rGO-PECs composites with randomly oriented and aligned parallel rGO, E_r and E_a, are given as follows:

$$E_r = E_m\left[\frac{3}{8}\frac{1+(2l_G/3t_G)\eta_L V_c}{1-\eta_L V_c}+\frac{5}{8}\frac{1+2\eta_T V_c}{1-\eta_T V_c}\right] \quad (4\text{-}3)$$

$$E_a = E_m\left[\frac{1+(2l_G/3t_G)\eta_L V_c}{1-\eta_L V_c}\right] \quad (4\text{-}4)$$

$$\eta_L = \frac{(E_G/E_m)-1}{(E_G/E_m)+(2l_G/3t_G)} \quad (4\text{-}5)$$

$$\eta_T = \frac{(E_G/E_m)-1}{(E_G/E_m)+2} \quad (4\text{-}6)$$

where E_G and E_m are elastic modulus of rGO and matrix respectively. E_G was assumed 0.25 TPa according with a previous study [224], while E_m =1.1 GPa is taken from result in 4.2.4while. This calculation considers the matrix modulus is basically constant with rGO loading. l_G, t_G are V_c are length, thickness and volume fraction of rGO flakes. The aspect ratio of l_G/t_G is estimated to 250, based on the FESEM images. The volume fraction of rGO V_c can be obtained from weight fraction of rGO (w) based on equation (4-7).

$$V_C = \frac{w\rho_P}{w\rho_p+(1-w)\rho_G} \quad (4\text{-}7)$$

Where ρ_p and ρ_G and density of matrix and rGO respectively, using as 1.1 g/cm^3 and 2.2 g/cm^3. Figure 4.9c displays the modulus based on Halpin-Tsai model and the measured modulus of rGO-PECs and its curve fitting. The experimental modulus is found closer to the theoretical plots of aligned rGO-PEC, especially at lower rGO loadings, in greement with the SEM experiemntal observation showing the distribution of rGO tends to be aligned. However, the stiffness for higher rGO concentration is lower than predicted by aligned Halpin-Tsai model. When the rGO loading reaches to 1.92 wt% (0.97 vol.%), the experimental data approachs to plots of random dispersion, suggesting the degree of orientation to depend on the concentration of rGO flakes.

The rGO distribution in cross-section of PECs with different rGO loadings is presented in Figure 4.10 **a-e, and the corresponding SEM images with higher magnification are displayed in** Figure 4.10 **f-p. Good dispersion and distribution of rGO in matrix have been observed**

in PECs when the rGO concertation ranged from 0.17 mg/ml to 0.48 mg/ml, corresponding to the rGO content in PECs ranging from ~ 0.6 wt% to ~2.0 wt%. Compared to the PAA/G//PDAC in Figure 4.6

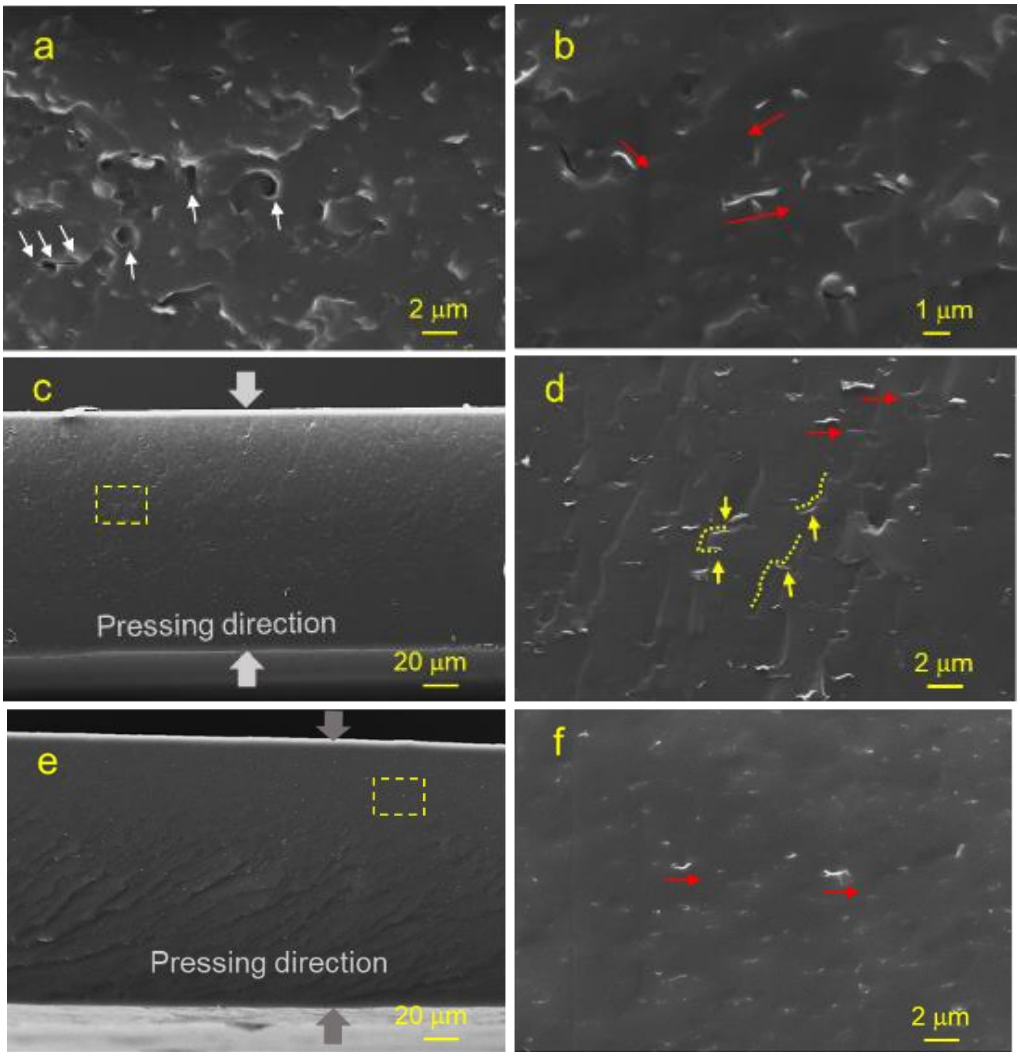

Figure 4.6c, the distribution density of rGO increases slightly in PEC prepared by increasing feed rGO amount (Figure 4.10a, f, and k), however, it increases obviously in other samples. They are PECs prepared using longer sonication time (Figure 4.10b, g, m and Figure 4.10c, h, n) or by filtration followed by re-dispersing method (Figure 4.10d, i, o and Figure 4.10e, j, p). Based on SEM with higher magnification, the rGO size ranges from 0.3 to 2 µm in PECs, however, it is easier to find rGO with size over 1 µm in samples prepared using 0.5 h sonication time at Figure 4.10 k , o and p. On the other hands, most of rGO are oriented perpendicular to pressing orientation (rGO oriented along with the top surface of pressed specimens) in PECs. Moreover, the preferential orientation of rGO flakes are easily found at lower rGO loadings, while the oriented rGO in PAA/$G_{0.40}$//PDAC is not as

clear as PAA/$G_{0.17}$//PDAC. This result is in accordance with the prediction of random/aligned rGO dispersion in Figure 4.9.

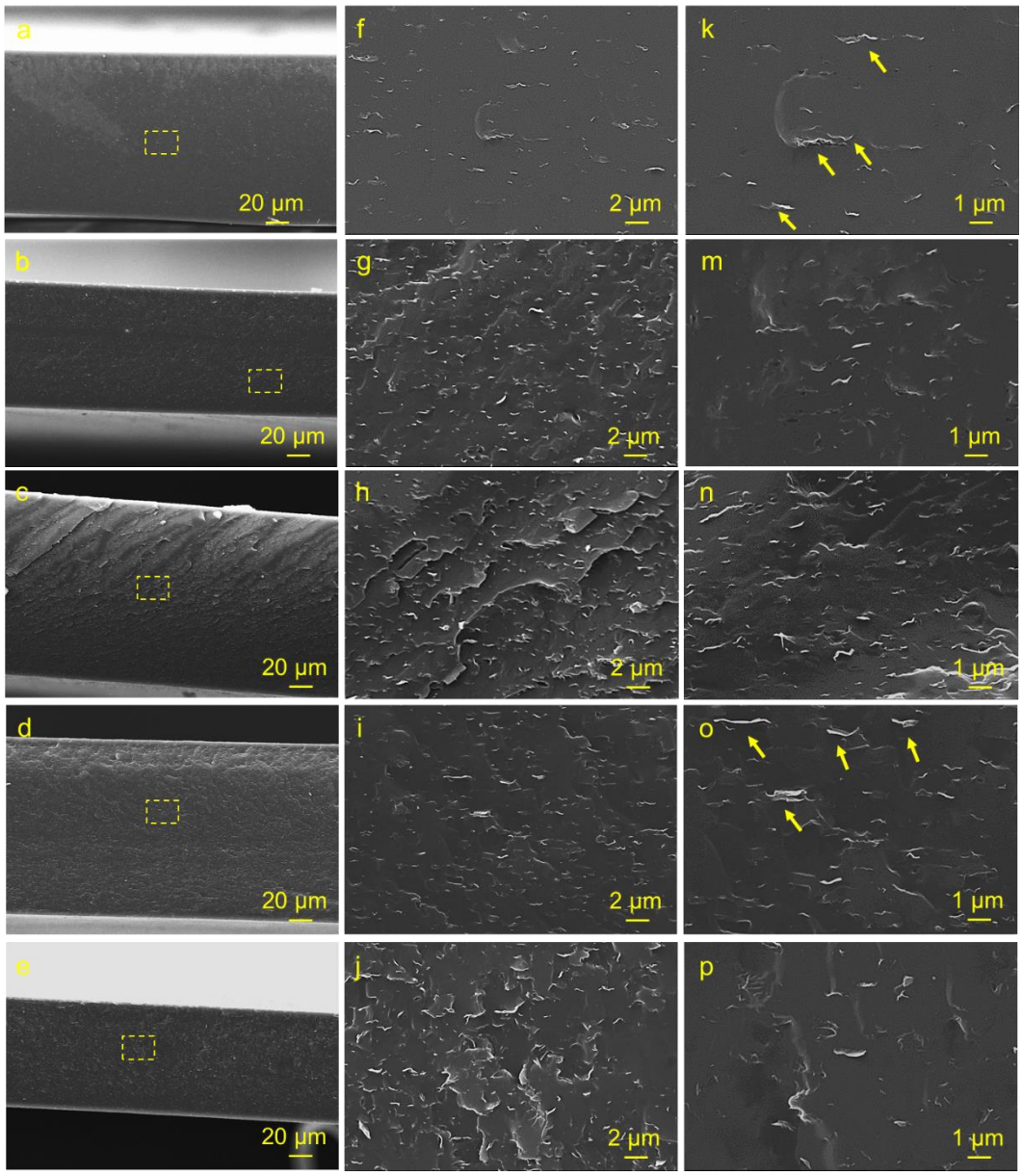

Figure 4.10 The cross-section SEM images of PAA/G $_{0.17}$//PDAC (a) (f) (k), PAA/G $_{0.30}$//PDAC (b) (g) (m), PAA/G $_{0.37}$//PDAC (c) (h) (n), PAA/$G_{0.40}$//PDAC (d) (i) (o) and PAA/$G_{0.48}$//PDAC (e) (j) (p). The (f) (g) (h) (i) and (j) are the regions marked by yellow dotted boxes in (a) (b) (c) (d) and (e) respectively.

4.2.6 Humidity influence on mechanical behavior

Mechanical reinforcement of rGO was demonstrated with a small concentration of rGO, as discussed in 4.2.4. These samples were pre-conditioned in ambient condition (23 °C 50% RH) for 1 week before mechanical measurement. Here, the effect of rGO and/or salt on mechanical properties of PECs after conditioning of higher relative humidity (RH 70%) is addressed. The moisture contents in PECs were firstly measured and summarized in Figure 4.11a. As expected, the PECs saved in RH 70% display higher moisture content (27-30 wt%) than samples saved in RH 50% (15-19 wt%). Besides, the desalted PECs^{R} conditioned at both RH 50% and RH 70% show lower water contents than other samples, indicating improved water resistance after restoring intrinsic interactions. The tight bonding of intrinsic interaction limits the space of adsorbed water molecules between polymer chains. The presence of rGO with contents of 0.7-1.5 wt% slightly reduced the moisture content in PECs, corresponding to the moisture contents lower than PAA/PDAC but higher than PECs^{R}. The higher the rGO, the lower in moisture.

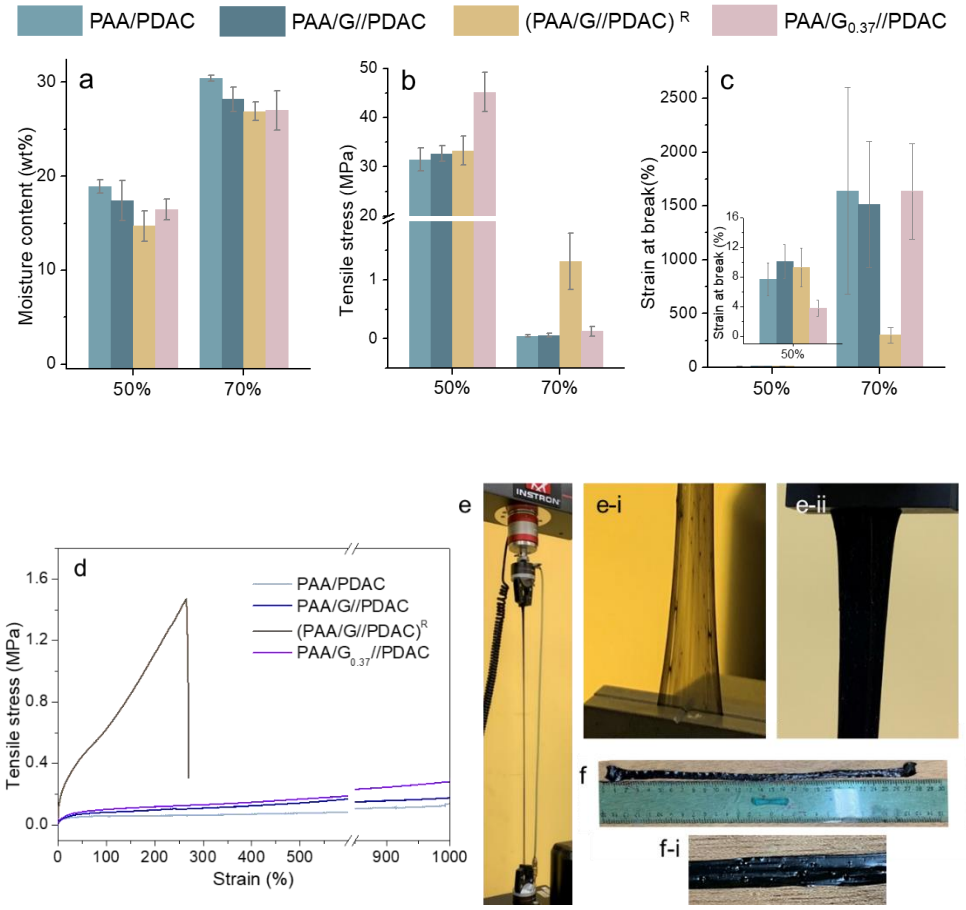

Figure 4.11 Moisture content (a) stress (b) and strain at break (c) of PECs under different relative humidity. The stress-strain curves of PECs saved in RH 70% (d), the images of PAA/$G_{0.37}$//PDAC under stretching (e) and after stretching (f).

The tensile test for PECs saved in RH 70% is carried out, and the results are summarized in Figure 4.11b-e. The stress-strain curves of PECs saved in RH 70% are presented in Figure 4.11d, the corresponding tensile strength and strain at break comparison between samples saved in RH 70% and RH 50% are shown in Figure 4.11b and Figure 4.11c. A high deformation over 1000 % and a low tensile strength can be observed in most of cases except $(PAA/G//PDAC)^R$. Based on the comparison results, it is obvious that PECs in RH 70% reveal much lower tensile strength and higher deformation than that of samples in RH 50%. It indicates that the higher moisture environment transferred PECs from brittle to ductile. The polymer matrix of PAA/PDAC was extremely soft and ductile at high moisture condition due to the plasticization of water molecules, which strongly weaken the intrinsic ion pairs and made space for facilitating the sliding motion and relaxation of PEs within the assembly [173, 287]. In the condition with RH 70%, $(PAA/G//PDAC)^R$ exhibits the highest strength of 1.3 ± 0.5 MPa that emphasizes the importance of salt removal, instead, the reinforcement of rGO is not obvious even with an increase of rGO amount, showing similar values (below 0.2 MPa) in PAA/G//PDAC and PAA/$G_{0.37}$//PDAC. Similarly, the elastic modulus of ~1.4 MPa for $(PAA/G//PDAC)^R$ is higher than other samples with only 0.1-0.4 MPa. The elongation at break results in Figure 4.11c show superior mechanical flexibility and higher stretchability for PAA/PDAC, PAA/G//PDAC and PAA/$G_{0.37}$//PDAC, but limited deformation ~300% for $(PAA/G//PDAC)^R$.

Figure 4.11e shows the images of PAA/$G_{0.37}$//PDAC during stretching with around 2000% deformation and after stretching. The deformation tends to start from one or a few regions usually near the clamps, and gradually develops to other places. The stretched regions with high deformation turn out to be semi-transparent with light grey appearance decorated with a few visible rGO aggregates (Figure 4.11e-i). The region with lower deformation still maintains black, Figure 4.11e-ii. After release of stretching force, the PEC could partially recover from 630 mm to around 260 mm, which indicates the partial recovery of sample length. The after-stretched PEC displays a rough surface due to the rGO fillers, shown Figure 4.11f.

Combined with the moisture result in Figure 4.11a, the mechanical enhancement of $(PAA/G//PDAC)^R$ is attributed to the limitations to salt plasticization and water plasticization, indeed, recovering intrinsic interaction of polymers and limiting polymer chain mobility. However, in RH 50%, the highest

stress at break and the smallest deformation are found in PAA/$G_{0.37}$//PDAC. Thus, the mechanical reinforcement at RH 50% is dominated by the rGO content in PECs, which is because the tight bond between the rGO filler and the polymer matrix allowing transferring the applied load to GO through interfaces. Owing to the limited moisture content (15-19 wt%), the small amount of extrinsic interaction between salt ions and polymer chains brings narrow influences to the sliding and relaxation of PEs, thus the results of PAA/G//PDAC and $(PAA/G//PDAC)^R$ are similar. These results further confirm the mechanical property of our specimens are controlled by the combination of three parameters, namely rGO concentration, salt concentration and equilibrium moisture.

4.2.7 Water triggered self-healing property

The healing capacity of PECs films was examined by adding water after cutting wounds. Adding 2 μl of water to cutting wounds then covering with plastic film for better contact between water and cuts. After exposing samples in 23 °C and RH 35% for 1-2 days, remove cover films and keep samples at the same condition for 1 week. Saving healed PECs in a relatively lower RH environment induced a shorter time for achieve a constant mass, where the healed PECs saved in RH 35% reached a relatively stable mass after 5 days, but the mass of PECs in RH 50% could not achieve equilibrium even after 2 weeks. It could be related to the high affinity of PAA to water [235], which hinder moisture removal at room temperature and/ or high RH environment. Figure 4.12 displays the mechanical results of healed PECs (Figure 4.12a-e) and the images of cut and healed PEC film (Figure 4.12f). The healed PECs were measured by tensile test and the mechanical recovery degree was calculated, which defined as the % to initial value. The comparison of stress at break, elastic modulus and strain values of pristine PECs and healed PECs are presented in Figure 4.12a, Figure 4.12b and Figure 4.12c. Figure 4.12d displays the stress-strain curves of healed PECs. Figure 4.12e shows the mechanical recovery degree, including stress at break recovery degree and elastic modulus recovery degree of healed PECs. During the calculation of stress/ modulus recovery, the average value is used in pristine and healed samples.

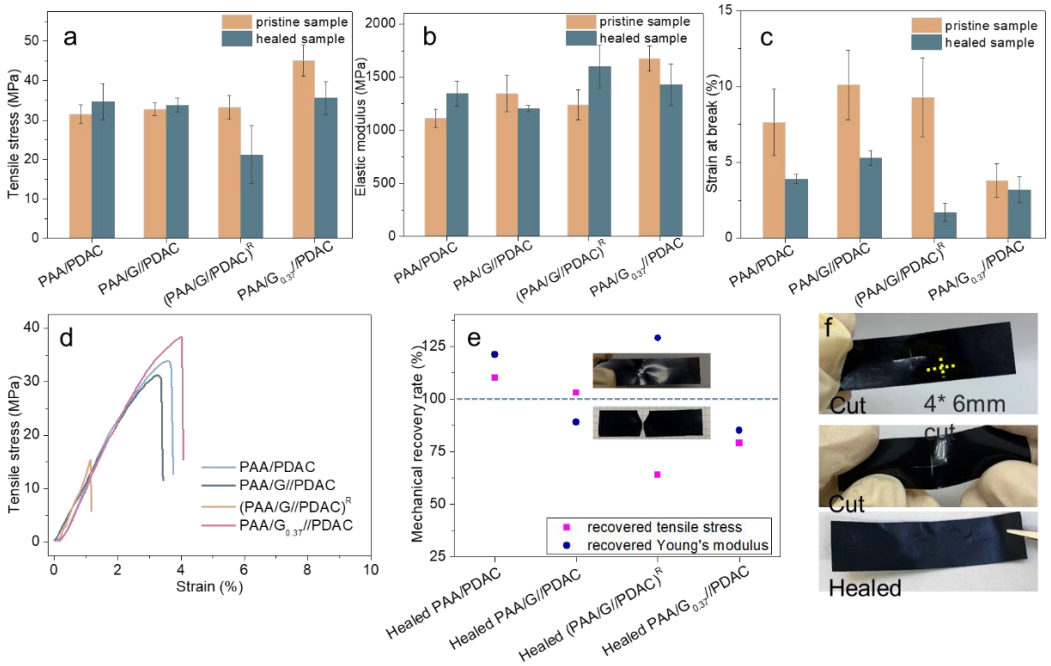

Figure 4.12 Comparison of stress at break (a), Elastic modulus (b) and strain at break (c) between healed PECs dried in RH 35% at room temperature and pristine PECs, the stress-strain curves (d) and corresponding recovery degree of healed PECs (e), the cut and healed PAA/G//PDAC film (f).

Based on the healed specimens of PAA/PDAC, PAA/G//PDAC and PAA/$G_{0.37}$//PDAC, the mechanical properties restored to a comparable level to pristine PECs, and the mechanical recovery degree decreases with increasing rGO content. The restored degrees of strength and elastic modulus in healed PAA/PDAC are even above 100%, which is possible due to the low RH (35%) during healing inducing more moisture removal in PECs. The healed PAA/G//PDAC shows ~90% and ~100% of elastic modulus and tensile strength of the pristine PAA/G//PDAC, and the corresponding values to healed PAA/$G_{0.37}$//PDAC are ~85% and ~80%, respectively. It should be noted that the stress at break of healed PEC_S reached similar levels of ~35 MPa (Figure 4.12a), but were different in the pristine PECs. On the other hand, the healed $(PAA/G//PDAC)^R$ is significantly different to other healed specimens, obvious increased elastic modulus but decreased tensile strength are found after healing, with restore degrees of ~130 % and ~64 %, respectively. Moreover, the healed samples exhibit obvious decreases in strain at break, where the healed $(PAA/G//PDAC)^R$ shows the smallest value at ~1.7 %. The break occurs at the healed position during stretching (insert of Figure 4.12c), confirming that the stress concentration at this area, owing to the presence of remaining defects after healing. During healing, the electrostatic interactions among PAA and PDAC at

fracture surface reformed accompanied by migration of the polymer across the damaged area and into intimate contact. Although the damaged area was restored in healed $(PAA/G//PDAC)^R$, there are a clear boundary of the water-wet region in the healed $(PAA/G//PDAC)^R$, where it could develop as stress concentration area. As a result, the factors of rGO content, salt and moisture not only influences the mechanical properties of PAA/PDAC based composites, but also bring different results in self-healing properties.

4.3 Conclusions

This chapter presents a simple and efficient approach to prepare homogeneously dispersed rGO-polymer composites at room temperature and in aqueous solution, which is different to traditional methods of melt mixing, or solution mixing under organic solvents, avoiding complex solvent removal process. The fabrication of rGO incorporated PAA/PDAC composite was demonstrated by complexing PAA dispersed rGO with PDAC solution followed by shape processing. The effect of rGO amount, salt and relative humidity on the mechanical properties of PEC composites have been studied. The rGO fakes have good dispersion and distribution in polymer matrix with this aqueous solution mixing method. The incorporation of rGO improved stress at break from 31 ± 2.4 MPa to 51 ± 2.4 MPa within around 2 wt% of rGO. The reinforcement of rGO in salted PEC is more obvious, with only around 0.6 wt% of rGO the tensile strength and elastic modulus of PAA/G//PDAC-s are 1.9 and 4.4 times to those of PAA/PDAC-s respectively. In contrast, the addition of salt endows materials ductility and higher deformation. Salt not only decreases the mechanical property in tensile test but also decreases strongly storage modulus of composites through transferring the intrinsic interaction from polyelectrolytes to extrinsic ion pairs between salt ions and PE charges. The mechanical properties of salted samples could back up to a similar level to pristine samples after soaking and rinsing to remove salt in composites. Despite from salt and rGO, the mechanical properties of rGO incorporated PAA/PDAC composites is strongly associated with environment moisture, and most samples reveal extremely high elongation (over 1000%) and low resistance at around RH70%. The reinforcement of rGO is restrict at this condition because of the mechanical mismatch of matrix and fillers rGO, while effect of salt plasticizing to ductile composites turns to important even if with only small amount of salt. The rGO-doped PAA/PDAC composites show potential in versatile applications as the good dispersion of rGO and tuneable strength and ductility, as well as moisture-triggered healing properties.

Chapter 5

5 PAA/PDAC complexes incorporating high rGO concentrations

5.1 Introduction

According to chapter 4, rGO can be introduced to PAA/PDAC complexes via dispersion into PAA solution and consequently further complexing with PDAC polymer chains at pH 7. The mechanical properties of rGO-PAA/PDAC composite can be controlled in terms of stiffness, resistance and deformation by rGO content, salt content and moisture. The addition of rGO is an effective way to reinforce PAA/PDAC matrix, especially in the salted PECs. However, the limited amount of rGO (less than 2 wt%) in the polymer matrix limits the performance improvement, not only in terms of mechanical properties but also for thermal and electrical conductivity. Moreover, pristine and rGO-containing PAA/PDAC samples failed to maintain a stable shape within a few minutes of immersion in water (100% RH) because of the strong swelling behaviour, although the salt-removing treatment could improve the stability in some degree (higher strength relative to samples with retained salt) at higher relative humidity (70%). In this chapter, a higher content of rGO in PEC is pursued for fabricating electrically and thermally conductive rGO-

PEC composites, with stability in water, which endows the PECs with potential in conductive devices and bio-sensing.

Generally, the synthesis of GRMs-filled PEC complexes contains two steps, GRM is dispersed in at least one of the PEs and then the PEs complexation. In our previous study, rGO can be well dispersed in PAA solution without pH modification. However, the PDAC solution is not suitable for rGO dispersing as significant precipitation was observed to occur after sonication which could be associated with its high surface tension. It has been found that the complexing of oppositely charged PEs leads to a decrease in surface tension compared to the individual PE solutions, which was observed in PEC composed of PAA and PDAC, PSS and PDAC [314]. The maximum decrease could be achieved with molar charge ratio equal to 1. On the other hand, in most cases, the complexation of PEs results in a coacervate or precipitation separated from liquid but the morphology could be further controlled by salt concentration. Using the critical salt concentration (0.5M) in PAA/PDAC, which has been studied in chapter 4, it is possible to transform a coacervate to a liquid. Therefore, the hybrid PEs system including PAA, PDAC and salt ions is designed to disperse rGO and build rGO-PAA/PDAC composites. The hybrid dispersing contains all the components during sonication and gives a high concentration of rGO in finally obtained composites, approx. double the sample prepared by the single PE-based dispersion. Moreover, adding water could simply trigger the complexation of PAA, PDAC, and rGO as the salt concentration drops below than critical salt concentration.

In this chapter, the preparation of electrical and thermally conductive rGO incorporated PAA/PDAC composites by using two different dispersion methods. The schematic representation for preparation methods and complexation processes are compared in Figure 5.1. Type 1 method prepared rGO-PAA/PDAC by adsorption of PAA molecules onto rGO followed by complexation triggered by the PDAC addition. Three steps were applied in Type 1 method, namely rGO dispersion in PAA solution, pH and salt concentration modifications in PE solutions, and the complexation by adding PDAC into PAA/G during stirring. The rGO decorated PAA/PDAC obtained in method one is named as PAA/G//PDAC-S. It is different with the PAA/G//PDAC-s in chapter 4, the dispersion of PAA/G in preparation of PAA/G//PDAC-S was not centrifuged. In the Type 2 method, the complexation of PEs was restricted by high salt concentration at first, then the PAA, PDAC and rGO intensively complexed with the trigger of water addition. The rGO was first dispersed in a mixture of PAA and PDAC solution with pH 7 and salt concentration of 0.5M, which is called PAA/PDAC-s. Secondly, the complexation

of PAA and PDAC was triggered via adding water that decreases salt concentration to 0.25M. The samples prepared in this way are referred to (PAA/PDAC-S)/G. The PEC composition, distribution of rGO and mechanical, thermal and electrical properties are investigated in rGO-PAA/PDAC composites fabricated via both methods. Besides, the stability of PEC composites in water is also compared. Both rGO content and distribution in PEC matrix influence these properties, thus the improved distribution of rGO and improved rGO content have been pursued as two methods to optimize their properties.

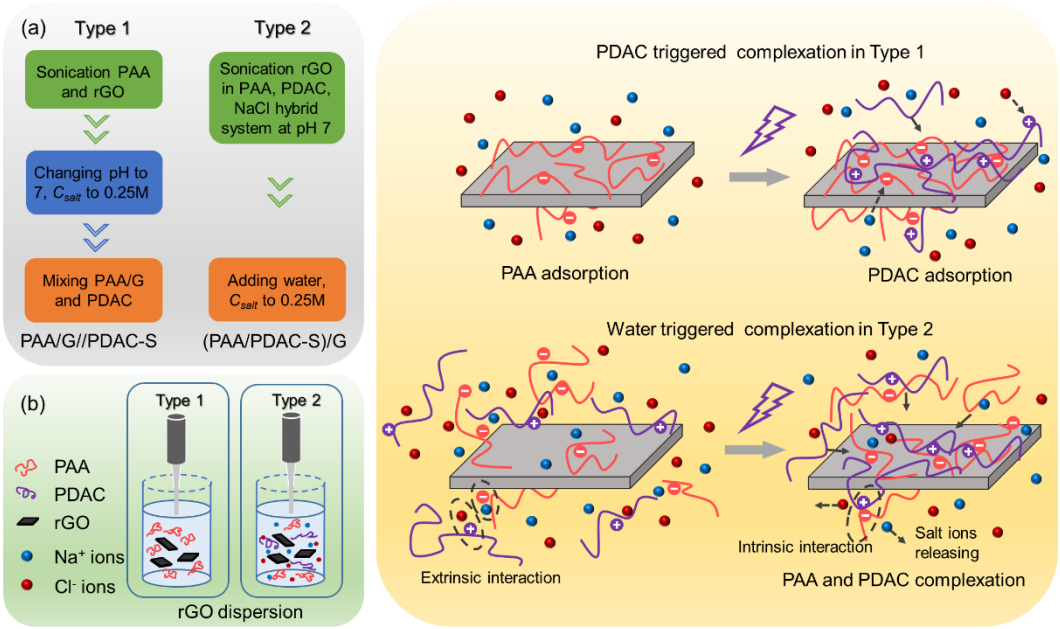

Figure 5.1 Schematic representation of the two different methods for fabricating rGO decorated PAA/PDAC

5.2 Result and discussion

5.2.1 Visual observation

Before sonication, the differences in the rGO inclusion into liquid phases were observed, as reported in Figure 5.2. The inclusion of rGO into PAA solution occurs immediately (in approx. ten seconds) when the rGO powder comes into contact with liquid surface, however it requires much longer time in PAA/PDAC-S solution. After 30 min in static conditions, there were still rGO on interface that were not wetted (Figure 5.2). As previously discussed in section 3.2, rGO can be included in PAA solution (0.1 wt%) in few seconds contact due to the relatively low surface tension of the solution. The surface tension of PAA solution is strongly

associated with the dissociation: the PAA would become a water soluble organic salt at high pH, corresponding to an increase in the surface tension of water at liquid/air interface, whereas the PAA acts as a water soluble organic compound at lower pH, which would facilitate the aqueous surface tension to level off at lower value [246]. As reported in literature, the surface tension of PAA solution decreased with increasing PAA concentrations. The surface tension was reported around 54 mN/m at PAA concentration of 0.11M without pH modification [247], which is close to the PAA concentration (0.125M) used here. The PAA concentration ranges from 0.1 wt% to 0.9 wt% (0.125M) inducing the solution pH to change from 3.4 to 2.8, corresponding to a dissociation degree decrease from 0.12 to 0.03. In contrast, most of the highly charged PEs are not hydrophobic enough to spontaneously adsorb at liquid-air interfaces at low concentrations owing to the hydrophilic and charged nature of polymer chains. The slower adsorption kinetics means that more time is needed to achieve equilibrium and the reduction of surface tension. In this regard, partially dissociated PAA appears more suitable than strongly charged PDAC in obtaining a lower surface tension at same concentration.

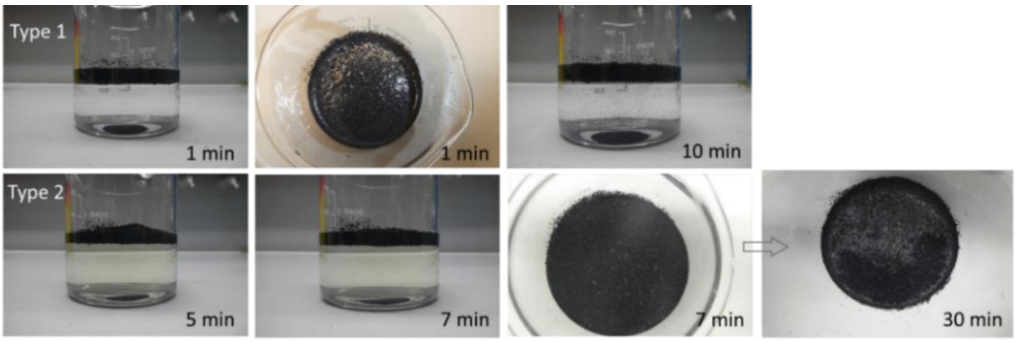

Figure 5.2 rGO inclusion in PAA solution (used for PAA/G//PDAC-S, first row) and PAA/PDAC-S solution (used for (PAA/PDAC-S)/G, second row)

The PDAC solution exhibits high surface tension similar to water at concentration below 3 wt% (we use PDAC solution here with 0.125M, around 2 wt%) [315]. This condition is improved in the presence of added electrolytes (salt), or at sufficiently high concentration, for example, PDAC reaches to 48 mN/m at 5 wt% [315]. The increased ionic strength via salt addition or achieve a sufficiently high PDAC concentration screens the electrostatic repulsions and leads to a decrease in surface tension. On the other hand, the mixture of oppositely charged PEs solutions would decrease the surface tension by the consumption of charges on polymer chains, which makes the assembly similar to a neutral polymer, particularly when mixing molar charge ratio close to 1: 1. Li et al. [314] found that the surface tension obtained with PECs are much lower than those found with PEs

alone at similar concentration, and mixing of PANa (full dissociated PAA modified by NaOH) and PDAC decreased the surface tension from 70 mN/m in PEs to 57 mN/m in PANa/PDAC suspension at PE solution 18.6mM, pH 10 and molar charge ratio 1: 1.

Predicting the surface tension of our mixing system of PAA/PDAC-S is complicated, because it involves both oppositely charged PEs and high ionic strength from the salt. The PAA/PDAC-S solution was prepared via mixing same volume of 0.125 M PAA and 0.125M PDAC at salt concentration 0.5 M, thus the polymer concentration (PAA and PDAC) and salt concentration in the hybrid system is 0.125M and 0.5 M respectively. The effects of salt addition on interfacial tension between coacervate and supernatant phases have been investigated systematically in previous studies. The coacervate/ supernatant interfacial tension (γ) decreases with salt concentration (C_s) increase, their relationship is in a law of $\gamma \sim (C_s^{cr} - C_s)^{3/2}$ [316, 317]. C_s^{cr} is critical salt concentration. The interfacial tension γ vanish at C_s^{cr}, corresponding to disappearance of phase separation. However, the surface tension (interfacial tension of liquid/air) of mixing PE solutions with salt concentration above to C_s^{cr} is unknown. The addition of salt could have two opposite effects. On the one hand, salt ions disrupt intrinsic interaction of polymers, loosening the tight bond between PAA and PDAC, and even make the polymer independent and free from complexes at a high enough salt concentrations. The fully charged polymers indicates a high surface tension. On the other hand, the high ionic strength inhibits the electrostatic barrier generated by the charged polymer chains. Even if the value of surface tensions of PAA/PDAC-S solution we used here is not known, the difference of rGO flakes wetted in PAA/PDA-S and pure PAA solution might suggest a lower surface tension in the latter. After sonication, both PAA/G and (PAA/PDAC-S)/G dispersions reveal dark appearance even after three months storage (Figure 5.3), suggesting a good stability of rGO in PAA solution and mixture of PAA, PDAC and salt.

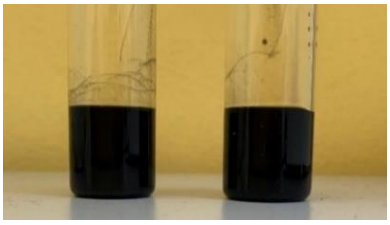

Figure 5.3 rGO dispersions of (PAA/PDAC-S)/G (left) and PAA/G//PDAC-S (right) after 3 months

5.2.2 General characterization

The rGO dispersions of PAA/G and (PAA/PDAC-S)/G were further used for rGO-PECs fabrication. Based on TGA results in Figure 5.4a and Figure 5.4b, rGO content in (PAA/PDAC-S)/G of 15.2 wt% is higher than PAA/G//PDAC-S of 8.4 wt% , which is expected because the initial polymer concentration and volume of dispersions are the same, but the further addition of PDAC solution during PAA/G//PDAC-S fabrication decreases rGO content. In PAA/G//PDAC-S, the complexation occurs with addition of PDAC solution into PAA/G dispersion, while reducing the salt concentration by water facilitates the complexation of PAA, PDAC and rGO in (PAA/PDAC-S)/G. For the salt content, both PAA/G//PDAC-S and (PAA/PDAC-S)/G reveal higher salt content (11.0-18.0 wt%) than that of sample PAA/PDAC-s (around 7.0 wt%), which was fabricated using same concentrations of salt and polymer to PAA/G//PDAC-S and (PAA/PDAC-S)/G during complexation. This difference of salt content is likely contributed by rGO inclusion. However, it is surprising that PAA/G//PDAC-S with lower rGO content reveals higher salt content of 17.0 wt%, which is higher than 11.5 wt% in (PAA/PDAC-S)/G.

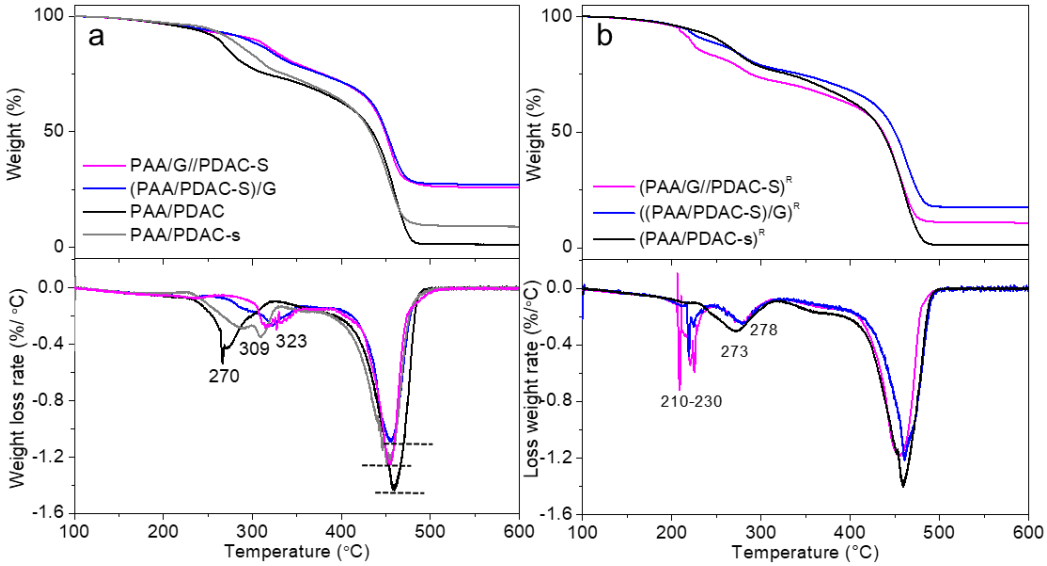

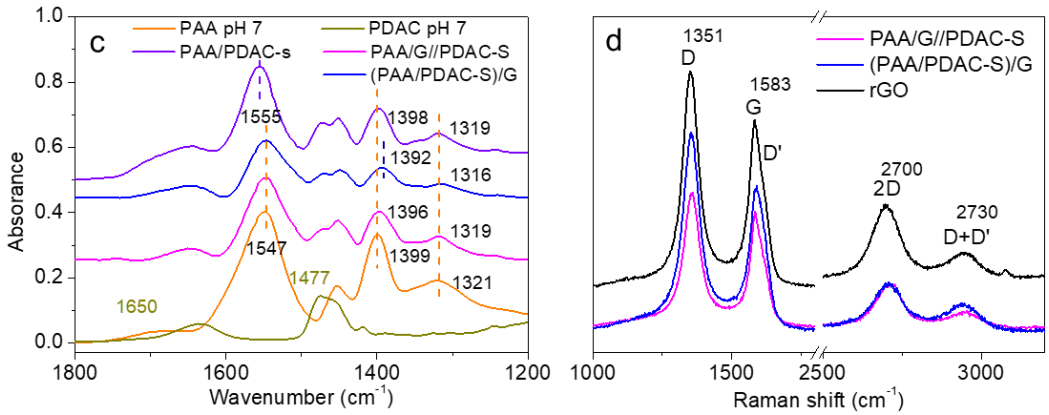

Figure 5.4 TGA, ATR-FTIR and Raman results of samples PAA/G//PDAC-S and (PAA/PDAC-S)/G

The rGO flakes help to trap more salt ions from supernatant during complexation, which could be affected not only by the content of rGO. One possible factor is the surface area of rGO flakes, which influenced by the rGO amount and the dispersion of rGO. The thermal stability was further analysed. In Figure 5.4a, the presence of salt and rGO shifts the onset decomposition to higher temperature. The first decomposition peak moves from 270 °C for PAA/PDAC to 309 °C for PAA/PDAC-s with salt content of approx. 7.0 wt%, whereas this decomposition peak shifts to a higher temperature at 323 °C for both PAA/G//PDAC-S and (PAA/PDAC-S)/G due to the presence of rGO and the higher salt concentration. Moreover, the maximum rate of weight loss at around 460 °C decreased the most in (PAA/PDAC-S)/G with effect of salt, rGO and lower fraction of polymer. As discussed in 4.2.3, the removal of salt in $(PAA/PDAC\text{-}s)^R$ makes the TGA curves like pristine PAA/PDAC. The salt in PECs is mostly removed after soaking and rinsing, and the variation of thermal stability of $(PAA/G//PDAC\text{-}S)^R$ and $((PAA/PDAC\text{-}S)/G)^R$ is mainly contributed by the rGO. The rinsing treatment applied to both cases not only shifts the onset decomposition peak to a lower temperature (around 278 °C), but also induces a dramatic change in loss weight loss at 210-230 °C (Figure 5.4b). The strong fluctuation of weight loss rate at around 210-230 °C is likely related to the intermittent elimination of bound water trapped in the structure, apparently related to the presence of rGO.

The ATR-FTIR result of PECs in Figure 5.4c shows bands derived from both PAA and PDAC, including antisymmetric $–COO^-$ at 1547-1555 cm^{-1}, $-CH_2$ at 1454 cm^{-1} and symmetric $–COO^-$ bands at 1392-1399 cm^{-1} and 1316-1321 cm^{-1} for PAA at pH 7, and C-H bending ($-CH_2$) at 1477 cm^{-1} and O-H at 1650 cm^{-1} for PDAC. As reported in 4.2.2, complexation of PAA and PDAC at pH 7 induced upwards

shift of antisymmetric and downwards shift of symmetric $–COO^-$, but the presence of salt in PEC caused a weaker shift in symmetric $–COO^-$ bands, indeed, the $–COO^-$ bands of PAA/PDAC-s is closer to PAA pH 7 than PAA/PDAC. For sample PAA/PDAC-s, the antisymmetric $–COO^-$ shifts from 1547 cm^{-1} to 1555 cm^{-1}, while the band positions of symmetric $–COO^-$ bands (1398 cm^{-1} and 1319 cm^{-1}) are close to PAA at pH 7 (1399 cm^{-1} and 1321 cm^{-1}). In spectra of PAA/G//PDAC-S and (PAA/PDAC-S)/G, the antisymmetric $–COO^-$ band is same to PAA pH 7 at 1547 cm^{-1}, however, slightly downwards shifts of symmetric $–COO^-$ bands occur, from 1399 cm^{-1} to 1392-1396 cm^{-1} and from 1321 cm^{-1} to 1319-1316 cm^{-1}, where the shifts in PAA/G//PDAC-S were smaller than that of (PAA/PDAC-S)/G because of the presence of higher salt content in former. Besides, no signals of rGO can be observed in PECs spectra.

The Raman spectra of PAA/G//PDAC-S and (PAA/PDAC-S)/G were measured using the rGO dispersion droplets (PAA/G and (PAA/PDAC-S)/G dispersions) dried on silicon wafer. The composite films PAA/G//PDAC-S and (PAA/PDAC-S)/G display the typical Raman spectra of carbon materials containing bands of D, G, 2D and D+D' for rGO. The D band (at around 1350 cm^{-1}) results from the presence of vacancies or dislocations in the graphene layer and at the edge of this layer [318]. The next band G peak is related to the in-plane vibration of sp^2 hybridized carbon atoms and is located at around 1580 cm^{-1} [270]. Based on the data obtained from Raman spectra, the intensity of D peak and G peak (I(D)/I(G)) is associated to the defects present in materials [319]. Pristine rGO, PAA/G//PDAC-S and (PAA/PDAC-S)/G show the I(D)/I(G) of 1.25 ± 0.20, 1.23 ± 0.09 and 1.22 ± 0.22 respectively, which indicates a limited influence to rGO quality obtained with 1 h sonication in different polyelectrolyte solutions. The smaller deviation of I(D)/I(G) in PAA/G//PDAC-S indicates the homogenous rGO quality. Besides, the full width at half maximum of G band ($FWHM_G$) always increases with disorder, which allows to indicate defects in graphene materials especially when the I(D)/I(G) values are close or same [270]. The $FWHM_G$ of rGO 55.5 ± 5.0 cm^{-1} is close to that of PAA/G//PDAC-S 53.1 ± 7.0 cm^{-1} but slightly smaller than 59.5 ± 7.3 cm^{-1} for (PAA/PDAC-S)/G, confirming the slight increase of disorder in latter one.

5.2.3 Morphology characterization

To determine the dispersion of rGO in PAA/G//PDAC-S and (PAA/PDAC-S)/G, SEM was employed and images of cross-sections are shown in Figure 5.5. The PAA/G//PDAC-S exhibits rugged fracture surfaces with randomly distributed rGO.

No obvious agglomeration of rGO was observed in SEM images of PAA/G//PDAC-S, and the crumpled thin sheets of rGO were found on cross-section surface as shown in Figure 5.5b. In addition, the microcracks generated at ahead of main cracks and mostly along rGO sheets, corresponding to the crack deflections near the rGO. This is explained by the mismatch between elastic modulus and Poisson's ratio of rGO and PAA/PDAC-s substrates, leading to stress concentration at interfaces. On the other hand, as expected that more rGO could be observed in (PAA/PDAC-S)/G. In Figure 5.5c the rGO aggregated with size over 100 μm, which could be related to the incomplete separation of rGO during sonication in the mixture of PAA, PDAC and salt, or the aggregation of rGO flakes during complexation. Indeed, higher content of rGO in (PAA/PDAC-S)/G during complexation may create more opportunities for the contact of rGO flakes. At higher magnification, a broad distribution of rGO size can be observed, ranging from a few microns (Figure 5.5f) to a few tens of microns (Figure 5.5e), the latter may in fact be a stack of several small individual flakes. All the input rGO were included in PAA liquid system before sonication and they were dispersed/ broken by the solvent cavitation during all the sonication duration, while in the case of rGO into PAA/PDAC-S solution, the gradually involving in liquid phase of rGO resulted in the difference the sonication effective time. (This is proved by the residual rGO on PAA/PDAC-S liquid surface after sonication 15min, 30min) This difference in affinity to the liquid phase could be the reason for the existence of big aggregates of rGO in (PAA/PDAC-S)/G.

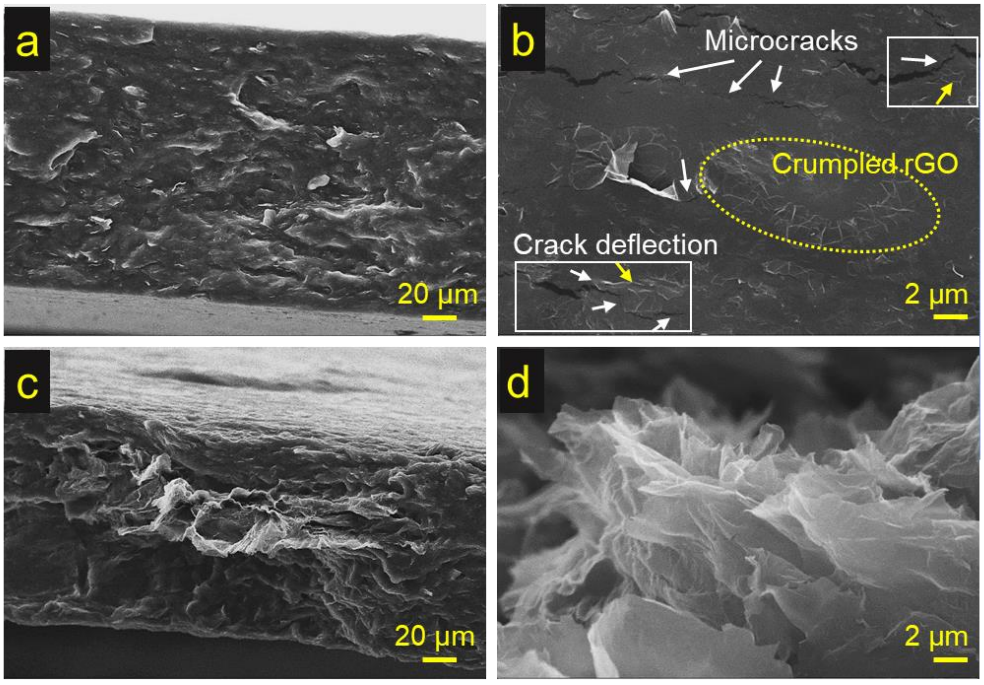

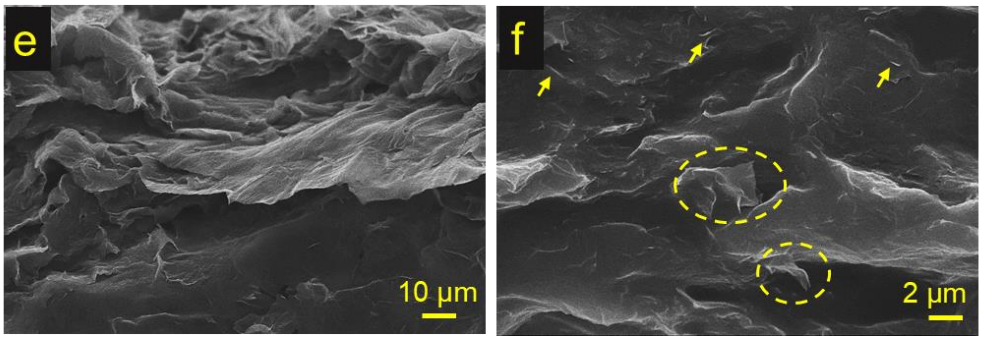

Figure 5.5 The cross-section view of PAA/G//PDAC-S (a) (b) and (PAA/PDAC-S)/G (c-f). Yellow arrows and circles: rGO, white arrows: cracks.

5.2.4 Mechanical properties

The mechanical properties of PECs were examined by performing tensile tests. The stress-strain curves of PAA/G//PDAC-S, (PAA/PDAC-S)/G and PAA/PDAC-s are shown in Figure 5.6. The stress at break of neat PAA/PDAC-s is 1.6 ± 0.3 MPa, whereas that of the PAA/G//PDAC-S is 7.0 ± 0.5 MPa and the (PAA/PDAC-S)/G is 8.5 ± 1.3 MPa, demonstrating the ultimate stress of PEC is improved by around 4 and 5 times in PAA/G//PDAC-S and (PAA/PDAC-S)/G respectively because of the addition of rGO. However, the expected higher strength doesn't show up in (PAA/PDAC-S)/G based on its composition with higher rGO content and less of salt content, due to the limitation of the incomplete dispersion of rGO in polymer matrix. The smaller elastic modulus is found in PAA/G//PDAC-S with 88 ± 11 MPa, compared to that of 283 ± 58 MPa in (PAA/PDAC-S)/G as the former has a higher amount of plasticizing component salt and a less reinforcing filler rGO. Compared to the high elongation in PAA/PDAC-s (over 300%), both PAA/G//PDAC-S and (PAA/PDAC-S)/G show much smaller deformation despite they have higher content in salt, evidencing an improvement in the rigidity of PAA/G//PDAC-S and (PAA/PDAC-S)/G with the restriction effect of rGO sheets. Meanwhile, the elongation at break increases from 3.8% for (PAA/PDAC-S)/G to 24% for PAA/G//PDAC-S, which confirms a better ductility for PAA/G//PDAC-S.

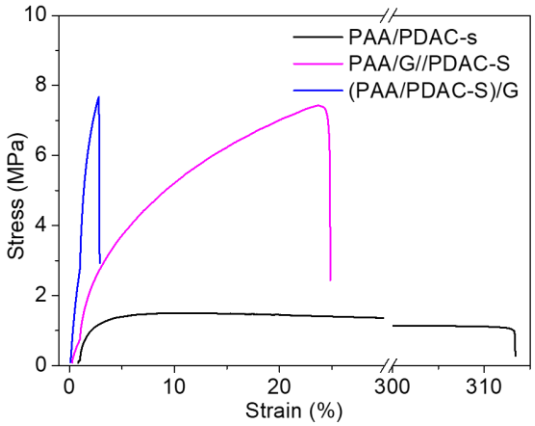

Figure 5.6 Tensile results of PAA/G//PDAC-S, (PAA/PDAC-S)/G and PAA/PDAC-s

5.2.5 Influence of sonication time on rGO distribution and mechanical behavior

Different sonication time was explored aiming for better dispersion of rGO in PAA/PDAC-S solution, eventually leading to the reduction of rGO agglomerates in the complexes. Every 0.5 h is set as a cycle, the (PAA/PDAC-S)/G-based samples were sonicated from 1 to 4 cycles, and in other words, from 0.5 h to 2 h. The (PAA/PDAC-S)/G-based samples fabricated with different sonication cycles are named as (PAA/PDAC-S)/G_s*i*, *i*=1, 2, 3 or 4, thus the (PAA/PDAC-S)/G used before (in sections 5.2.1-5.2.4) is also the (PAA/PDAC-S)/G_s2 here. Figure 5.7 displays the cross-section morphology and tensile result for samples with different sonication time. The sample in Figure 5.7a with a sonication time of 0.5 h shows a large aggregated rGO with length approx. 180 µm and thickness of approx. 30 µm embedded in the compact PEC matrix. In some other regions, like Figure 5.7b, the loose binding of matrix and fillers is found accompanied by many long cracks along the direction of PEC film. The micro-sized rGO in length of 5-10 µm distributed separately as observable from high magnification micrographs in Figure 5.7c. These suggest a poor dispersion of rGO in matrix and the scattered rGO size distribution in PAA/G//PDAC-S_s1. Increasing sonication time to 1.5 h changes the cross-view to a compact and relatively smooth surface with few of rGO aggregates (in size of 90×20 µm for the aggregate at Figure 5.7d). Besides, crumpled rGO, pull-out of rGO and the randomly distributed rGO flakes with size smaller than 4 µm can be observed in Figure 5.7f. After sonication 2 h, a rough and homogenous surface is obtained and no significant agglomeration can be observed. At higher magnification (Figure 5.7i), it is easy to find an increased number of rGO flakes pulled out with size of 5-10 µm, those are distributed close to each other but

not agglomerated into thick flakes or graphite. Smaller size rGO with length less than 4 µm can also be found.

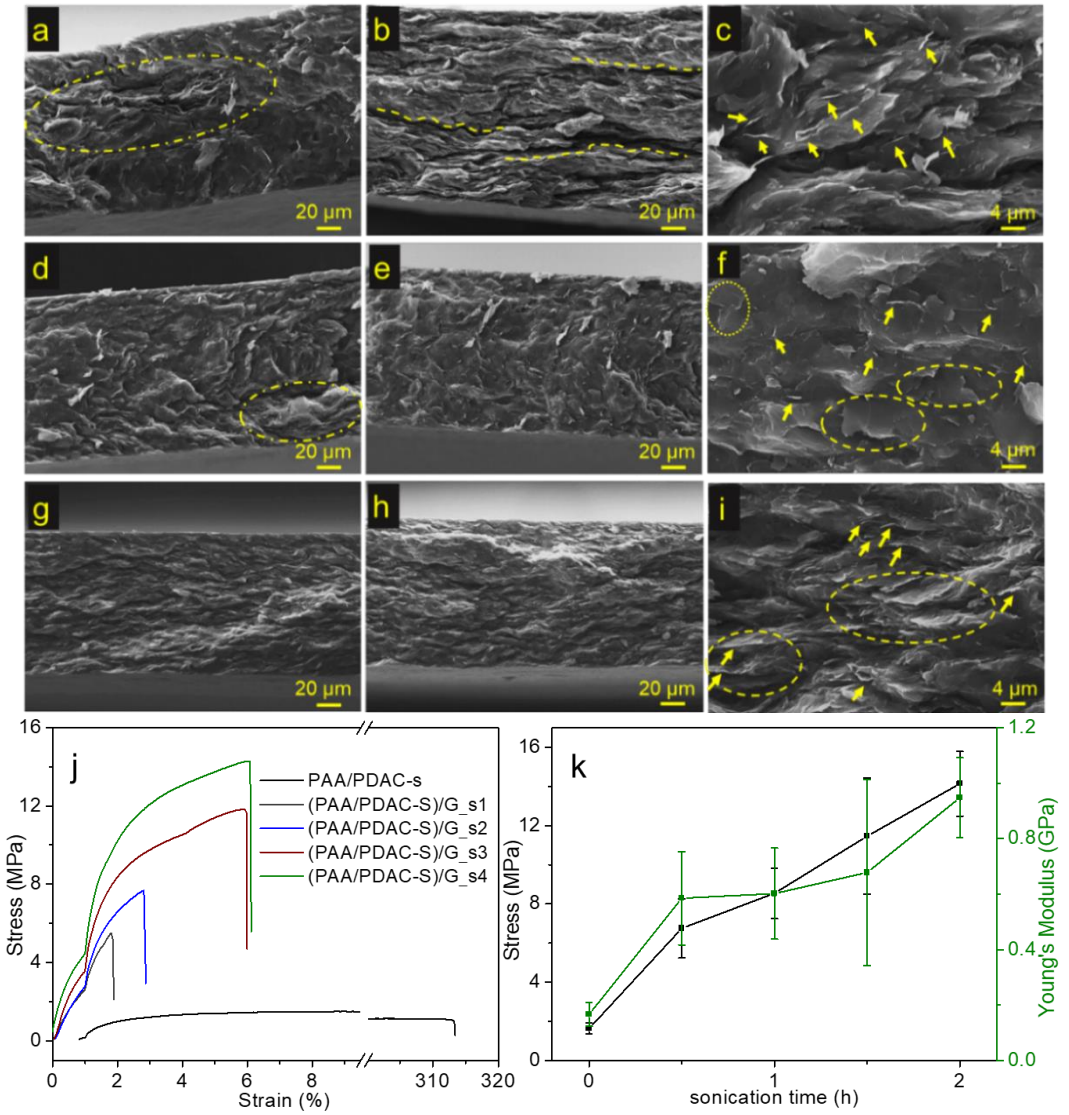

Figure 5.7 Cross-section images of (PAA/PDAC-S)/G_s1 (a-c), (PAA/PDAC-S)/G_s3 (d-f) and (PAA/PDAC-S)/G_s4 (g-i). The tensile results of (PAA/PDAC-S)/G-based samples with different sonication time (j) and (k)

The number and thickness of rGO aggregates decrease by increasing sonication time and they are basically eliminated with sonication 2 h, which is longer than the sonication time used in PAA/G//PDAC-S. Based on the differences in morphology of PECs, it is expected that the mechanical properties may change as well. Therefore, the tensile tests were applied to (PAA/PDAC-S)/G_s*i*, *i*=1, 2, 3 or 4, and the results are presented in Figure 5.7j and Figure 5.7k. Both strength and elastic modulus increase with sonication time. The tensile at break of sample

(PAA/PDAC-S)/G_s4 is 14.1 ± 1.7 MPa, around 9 times compared to PAA/PDAC-s and almost double compared to (PAA/PDAC-S)/G_s2. Meanwhile, the strain at break increases gradually with sonication time, from 2.2 ± 0.6% for 0.5 h sonication to 5.4 ± 0.8% for 2 h sonication. The increased area under stress-strain curves with sonication time indicates better toughness and fracture resistance. Combined with morphology of Figure 5.7a-i, the toughening mechanism could be associated with the pull-out of rGO sheets, those can initially bridge the crack-opening, then pull out from PEC matrix as the crack developing. The mechanical reinforcement of rGO to (PAA/PDAC-S)/G-based composites improved with limitation of rGO aggregation and improvement of rGO dispersion, which strongly depends on sonication time.

The effectiveness of rGO reinforcement and the efficiency of load transfer in rGO/PEC composites depends not only on the dispersion degree, orientation arrangement, shape factor of fillers, and interaction with the matrix, but is also dominated by the nature of the matrix. As we discussed in 4.2.3, salt-rich PEC matrices tend to form ductile materials with low strength. Therefore, it is necessary to compare the effects of different sonication times on the phase composition, especially in salt content. Similar TGA curves have been observed in samples with different sonication time, also similar TGA results were found in samples after soaking and rinsing, as shown in Figure 5.8a and Figure 5.8b. Based on the TGA results, the components formulation of salt, rGO and polymers was plotted in Figure 5.8c.

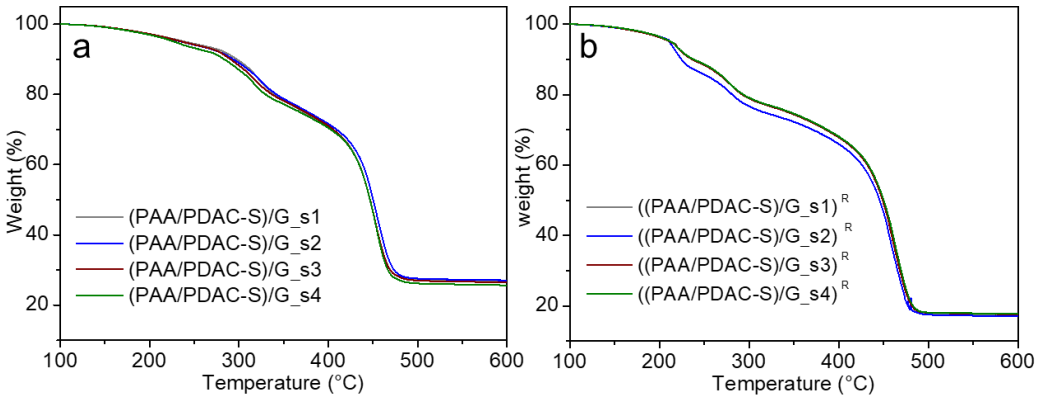

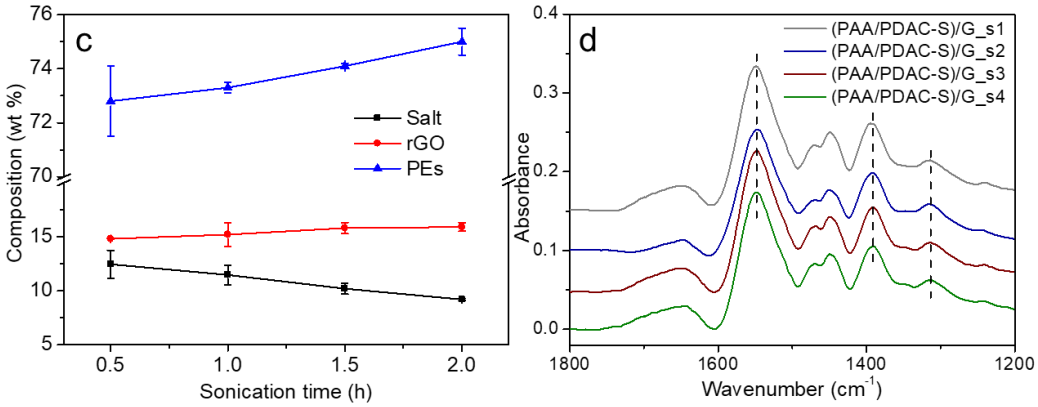

Figure 5.8 TGA results of (PAA/PDAC-S)/G_si (i =1, 2, 3 or 4) with 1 to 4 sonication cycles (a), corresponding samples after salt-removing treatment (b), the components percentage variation with sonication time (c), the ATR-FTIR spectra for (PAA/PDAC-S)/G_si (i =1, 2, 3 or 4) (c)

Salt content appears to slightly decrease with sonication time from 11.2-13.8 wt% for 0.5 h to around 9.2 wt% for 2 h sonicated sample, and the rGO was observed constant at around 15.0 -16.0 wt%. Polymer is the main component of PEC with weight a percentage over 70.0 wt%. The polymer amount in PECs changes in an opposite way to salt amount changes, which increase slightly with sonication time. The salt content in PECs was calculated by residual weight of pure NaCl, PEC^R and the corresponding PEC after TGA test, where the PAA, PDAC and rGO were consider as an individual phase and the salt has been completely removed during soaking and rinsing. One possible explanation for the slight decrease in salt content could be the evaporation of small amount of water during sonication, which makes the dispersion volume slightly lower than expected consequently the salt concentration was modified to a value slightly lower than 0.25 M in the following step, as the same volume of water was expected to be added. The effect of sonication time on salt amount could also contribute to the higher strength in sample with longer sonication time. Sonication time has no effect to the band shift of PECs ATR spectra, the consistent ATR results were observed in samples prepared with sonication time from 0.5 h to 2 h (Figure 5.8d).

On the other hand, the rGO quality in (PAA/PDAC-S)/G_s*i* (*i* =1, 2, 3 or 4) was monitored with Raman in Figure 5.9. All the samples show intense D peak and the shoulder peak of D', which indicates the presence of defects and/or new boundaries. With increasing of sonication time, the ratio of I(D)/I(G) gradually increases from 1.15 ± 0.22 for (PAA/PDAC-S)/G_s1 to 1.39 ± 0.02 for (PAA/PDAC-S)/G_s4, evidencing more of grain boundary defects formed under longer sonication process. The increased trend of $FWHM_G$ with sonication time

also confirms the increased defects in rGO flakes, it changes from 54.6 for (PAA/PDAC-S)/G_s1 to 62.4 for (PAA/PDAC-S)/G_s4. To be noted that I(D)/I(G) of (PAA/PDAC-S)/G_s1 shows a value slightly smaller than pristine rGO at 1.25 ± 0.2. On the one hand, with 0.5 h sonication, numerous of large-sized aggregated rGO are observed in PEC film in visual observation, the limited separation and dispersion of rGO leads to low increase in new boundaries, thus I(D)/I(G) increase is restricted. On the other hand, the PDAC has been described previously for assisting an in-situ reduction of graphene oxide, which may contribute to the slight decrease in I(D)/I(G) [242]. For each sample, the Raman spectra was measured in five points and the average and deviation of I(D)/I(G) were obtained. The deviation of I(D)/I(G) becomes narrower with sonication time ≥ 1.5 h indicating a more stable of rGO quality in (PAA/PDAC-S)/G- based samples after sufficient sonication. The PAA/G//PDAC-S reveals similar I(D)/I(G) value and deviation to that of (PAA/PDAC-S)/G_s3, meaning that the defectiveness of rGO is similar with 1 h sonication in PAA solution and 1.5 h sonication in PAA/PDAC-S solution. No shift of the D and G peaks was observed with increasing sonication time.

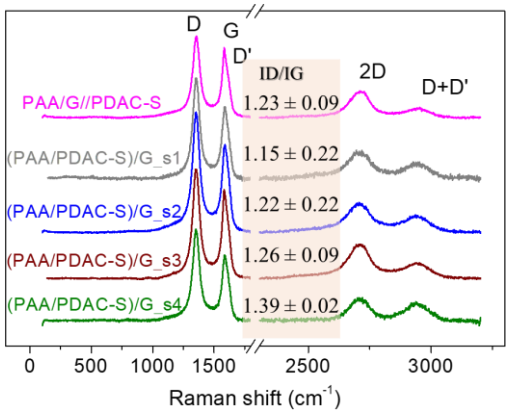

Figure 5.9 Raman spectra of PAA/G//PDAC-S and (PAA/PDAC-S)/G with different sonication time

5.2.6 PAA/G//PDAC-S with different PAA: rGO ratio

In order to achieve a comparable rGO content to (PAA/PDAC-S)/G-based samples, weight ratio of PAA: rGO changes from 4:1 to 2:1 during Type 1 fabrication approach. The new sample with double rGO is set as PAA/G2//PDAC-S. The higher concentration of rGO in sonication system was expected to bring more difficulties in good dispersion of rGO. In general, large amount of PE is required for dispersing and stabilizing GRMs in dispersions. Figure 5.10a and Figure 5.10b show the morphology of PAA/G2//PDAC-S in cross-section. A rough surface is observed due to the strong attachment of the PAA to rGO. rGO can be well

dispersed in matrix without obvious aggregation, and more crumpled rGO sheets (marked in yellow dashed circles) can be observed compared to PAA/G//PDAC-S in Figure 5.5. Besides, the cross-view image reveals the pull-out of rGO sheets and randomly-oriented rGO with size less than 2 µm. The good dispersion of rGO in PAA/G2//PDAC confirms the good dispersing ability of PAA to rGO even if under a relatively lower PE:rGO ratio. A few microcracks are found in cross-section. The rGO and salt contents in PAA/G2//PDAC-S were quantified by TGA (Figure 5.10c), showing as 14.2 wt% and 29.6 wt% respectively. As expected, the rGO content in PAA/G2//PDAC-S is increased: however, the salt in PAA/G2//PDAC-S is much higher than PAA/G//PDAC-S (17.0 wt%) and (PAA/PDAC-S)/G (11.5 wt%). The high amount of salt can also be evidenced via the white precipitation on PAA/G2//PDAC-S film after drying due to the super-saturation of NaCl. Obviously, the salt amount in rGO-PECs prepared via Type 1 is significantly affected by the input rGO amount. The mechanical strength and elastic modulus of PAA/G2//PDAC-S are lower than both PAA/G//PDAC-S and (PAA/PDAC-S)/G, and its deformation 13 ± 5 % is higher than that of (PAA/PDAC-S)/G, as reported in Figure 5.10d. This is obviously explained by the salt plasticizing effect of salt loosens ion-pairs of polymers and thus limits the mechanical properties.

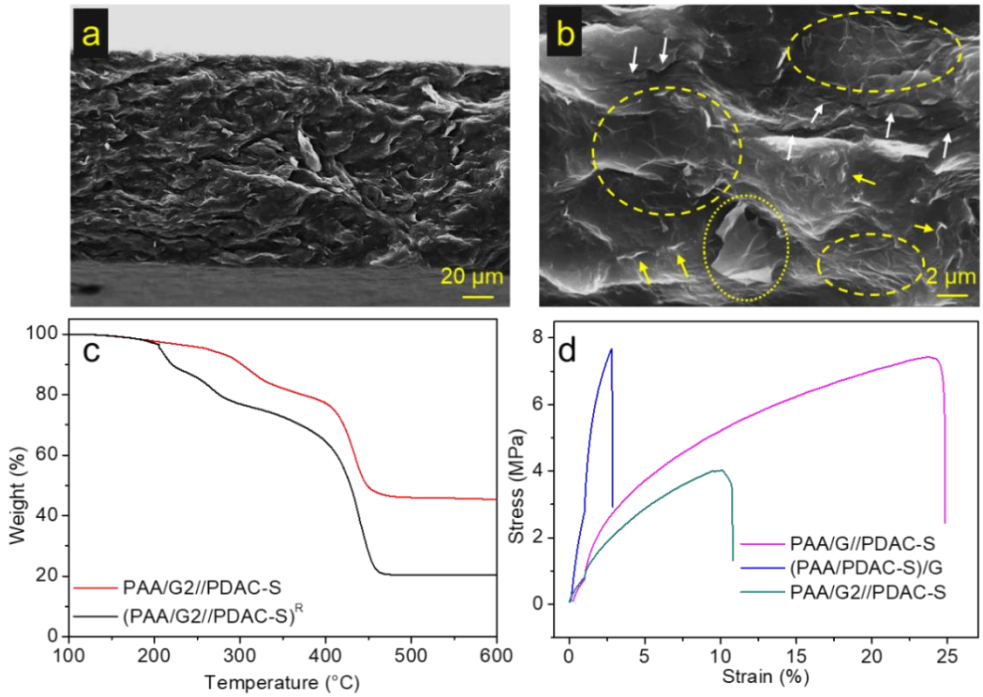

Figure 5.10 SEM images of PAA/G2//PDAC-S in cross-section (a) and (b), white arrows are cracks, dashed ellipses are crumpled rGO, dotted ellipse is pull-out of rGO sheet, and yellow arrows are small rGO. TGA results of PAA/G2//PDAC-S and $(PAA/G2//PDAC\text{-}S)^R$ (c) Mechanical property of PAA/G2//PDAC-S and other PECs (d).

5.2.7 Swelling and stability in water

The stability of PAA/PDAC-s, PAA/G//PDAC-S-based and the (PAA/PDAC-S)/G-based samples in water was investigated by immersing PECs films in water for a few weeks. All the immersed PECs were dried in a freeze dryer to keep their inner structure after swelling. The cross-section images of PECs after soaking 2 weeks are reported in Figure 5.11. PAA/PDAC-s reveals a cross-section with large numbers of non-connected pores in size of 10 to 200 um (Figure 5.11a). At inside walls of these pores, the much smaller micro-pores are observed in Figure 5.11b-c, arising from water absorption into PAA/PDAC-s. Besides, the soaked PAA/PDAC-s reveals the uneven thickness after inflation, from 300 um to 600 um. As discussed previously in literature [158], the short term water uptake is the result of hydration of PE ion pairs plus osmotic pressure exerted by the polymer network and counterions. The initial pores form quickly, and they keep expanding and fusing with continual osmotic stress and Laplace pressure (P), thus causing a flow or shape changes of PECs. P is generated depending on the interfacial tension of PEC and pore solution, and the curvature of the pores [320]. Besides, the salt releasing of PECs in pure water leads to a shrinkage where some of water is expelled into pores rather than bulk solution [321]. This could also happen at very early stage of immersion when PAA/PDAC-s releases salt ions rapidly into pure water and becomes more viscous with hydration of polymer ion pairs. With the increase of pore size and decrease of pressure, the inflation would gradually achieve equilibrium. However, for the long term immersion, the weak interaction of PEs generated at some region with the lots of charged ion pairs surrounding by shell of hydration, which makes it more like a coacervate and to be sensitive with small change in conditions, like local salt concentration or temperature [170]. This may be associated with the formation of micropores in Figure 5.11c. The immersed PAA/G//PDAC-S and (PAA/PDAC-S)/G are dramatically different to pristine PAA/PDAC-s. Firstly, they display stable film thickness after 2 weeks water soaking, evidencing a better stability within addition of rGO. Smaller pores and more uniform pores size are observed in (PAA/PDAC-S)/G due to the higher rGO content. The existence of hydrophobic rGO in PECs is beneficial to limitation of pores expansion and the flow of PECs, which is more obvious with higher rGO concentration in PECs. However, large cracks are also observed in (PAA/PDAC-S)/G, which could relate to the rGO aggregates and its limited compatibility with swollen PEC matrix. In Figure 5.11 f and Figure 5.11i, the micro-sized rGO flakes are found in both of PAA/G//PDAC-S and (PAA/PDAC-S)/G.

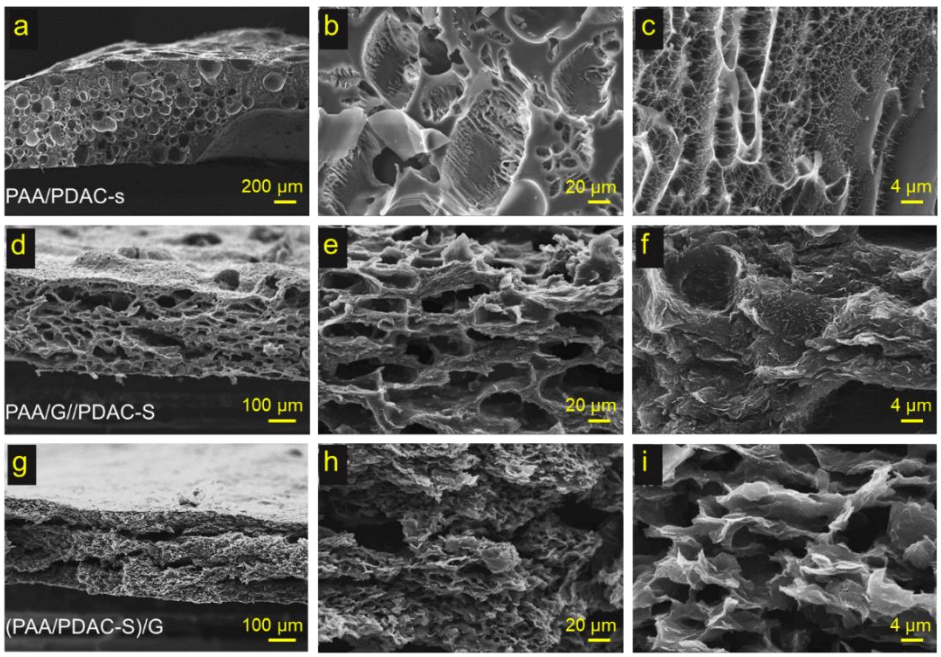

Figure 5.11 SEM images of cross section of PAA/PDAC-s (a-c), PAA/G//PDAC-S (d-f), (PAA/PDAC-S)/G (g-i) soaked in water for 2 weeks.

The improved samples (PAA/PDAC-S)/G_s4 and PAA/G2//PDAC-S were immersed in water for a longer time (5 weeks), because they have good dispersion of rGO at high rGO concentration in PECs. The cross-section results are shown in Figure 5.12. (PAA/PDAC-S)/G_s4 shows a stable thickness, small and homogenous pore size and pore distribution, indicating good stability in water. Besides, the micro-sized pores in (PAA/PDAC-S)/G_s4 are similar with those in (PAA/PDAC-S)/G (Figure 5.11h and Figure 5.11i) but in a smaller size, changing from approx. 10 µm to 4 µm, that indicates the increasing sonication time improves the PECs stability in water because of better dispersion of rGO in (PAA/PDAC-S)/G_s4. However, the PAA/G2//PDAC-S does not appear to be fully stable for a long time immersion based on the SEM results of uneven thickness and irregular pores after swelling. Compared with clear shape and boundaries of pores in PAA/G//PDAC-S (Figure 5.11e), the pores size and shape become irregular, and new pores formed at the thick wall or matrix regions. Moreover, PAA/G2//PDAC-S shows a looser structure in micro-sized observation than PAA/G//PDAC-S. The PAA/G2//PDAC-S has much higher salt (~29.6 wt%) than PAA/G//PDAC-S, which emphasizes the critical effect of salt into PECs stability in water, indeed, the improvement of PECs stability in water requires not only substantial rGO, but also the limitation of salt in matrix.

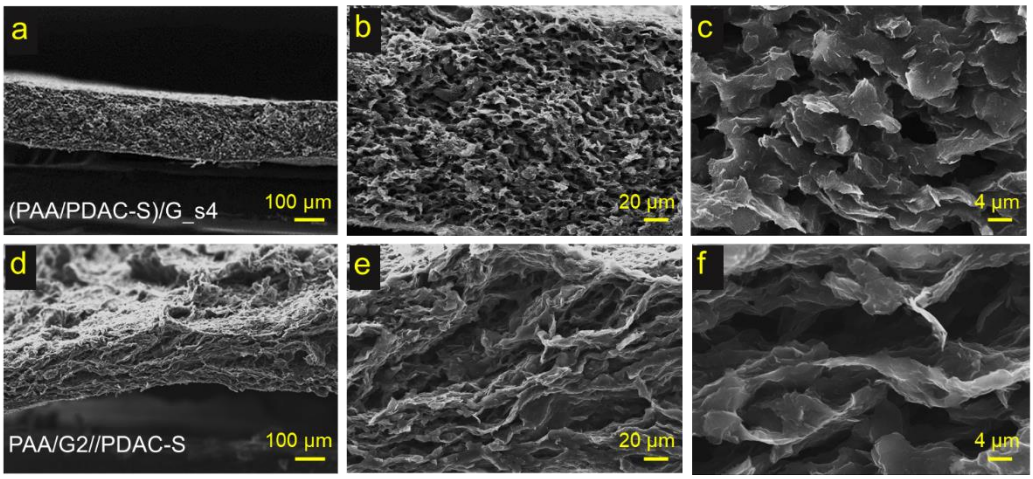

Figure 5.12 SEM images of cross section of (PAA/PDAC-S)/G_s4 (a-c) and PAA/G2//PDAC-S (d-f) soaked in water for 5 weeks

On the other hand, the top surface morphologies of soaked samples are also presented in Figure 5.13. PAA/PDAC-s shows similar morphology features to its cross-view, round pits almost fully covered the surface in size of 100-200 um. The similar micropores with size smaller than 4 µm are also observed at inside walls of expanded pits. While other rGO-PECs clearly show strong differences between top-view and cross-view topology after immersing in water for weeks. In overall, these rGO-PECs show better stability in top-view than in cross-section, the evidence for it is given in both PAA/G//PDAC-S and (PAA/PDAC-S)/G with strongly reduced pore sizes and numbers in top view images. The diverse performance could be related to the spatial orientation of rGO, the sheets distributed in parallel (or close to parallel) to top surface would provide more protection from water attacks. A few to hundred microns pores are found on top surface of PAA/G//PDAC-S. With the swelling continuous to inducing pores expanding, the crosslinks of polymers using for preventing swelling beyond a certain level cannot resist the inflation derived from osmotic pressure, thus the water-contained cavities keep expanding until they rupture. The rupture edges were observed in PAA/G//PDAC-S (Figure 5.13e). Sample (PAA/PDAC-S)/G reveals two different morphologies in Figure 5.13g-i and Figure 5.13j-m. The intact surface after soaking is attributed to the overlapping of rGO sheets which forms a good resistance to water permeation. However, some of cracks and pores are observed at the non-fully covered region (Figure 5.13m). Comparing the higher magnification of PAA/G//PDAC-S and (PAA/PDAC-S)/G (Figure 5.13i and Figure 5.13m), it is easily to tell overlapped larger-sized rGO flasks in (PAA/PDAC-S)/G and separated rGO with smaller size in

PAA/G//PDAC-S. This could because of the higher rGO content in (PAA/PDAC-S)/G samples.

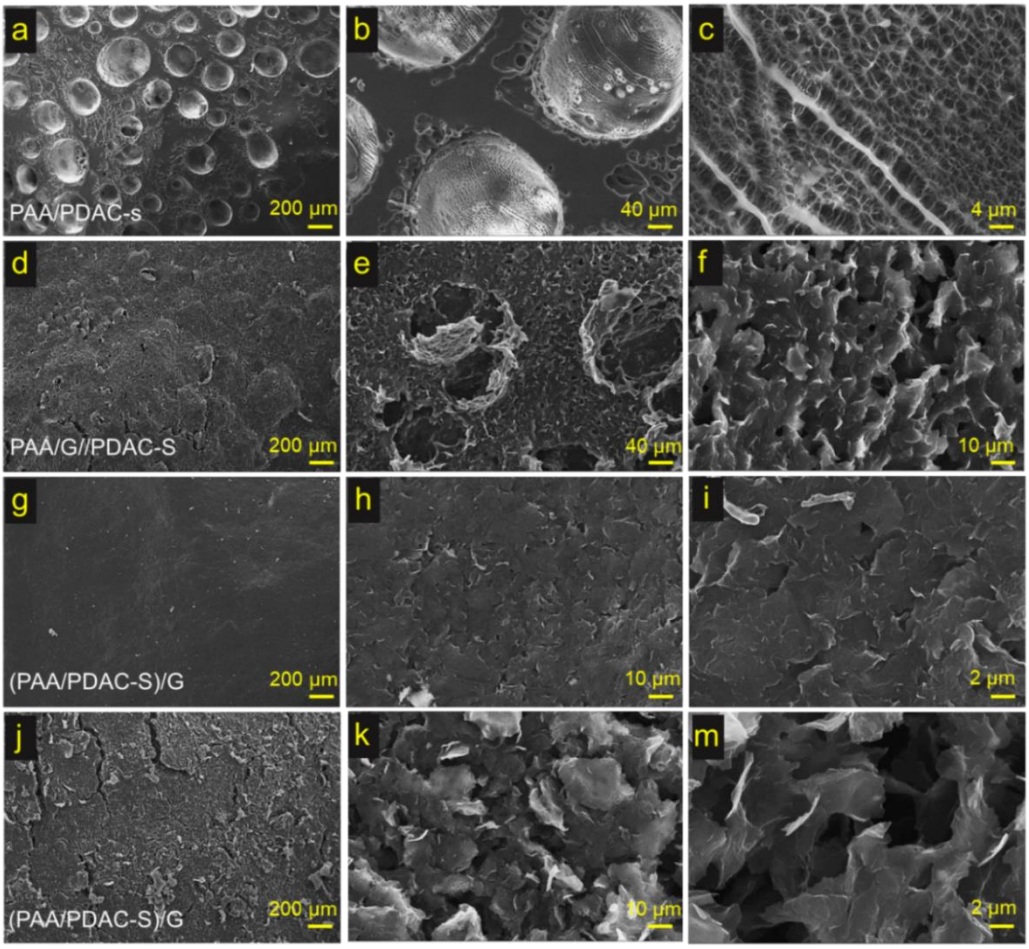

Figure 5.13 SEM images of top-view of PAA/PDAC-s (a-c), PAA/G//PDAC-S (d-f), (PAA/PDAC-S)/G (g-m) soaked for 2 weeks.

The (PAA/PDAC-S)/G_s4 (Figure 1.14a-c) display a homogenous and relatively flat surface with small sized voids (around 10-15µm) after 5 weeks soaking. Compared with top view of (PAA/PDAC-S)/G, the main difference is the increased uniformity, which indicates the better coverage of rGO on (PAA/PDAC-S)/G_s4 that is prepared with longer sonication time. PAA/G2//PDAC-S shows strong warping and peeling on top surface. The similar rupture edges are also observed but in a much higher density in PAA/G2//PDAC-S (Figure 5.14e) than PAA/G//PDAC-S (Figure 5.13e). Moreover, the looser structure can be observed at high magnification of PAA/G2//PDAC-S than that of PAA/G//PDAC-S (Figure 5.13f and Figure 5.14f). In addition, the comparison of (PAA/PDAC-S)/G_s4 and PAA/G2//PDAC-S confirms the better long-time stability of PECs with lower salt.

Based on the high magnification images of compact areas in (PAA/PDAC-S)/G_s4 and PAA/G2//PDAC-S (Figure 5.14c-1 and Figure 5.14f-1), the top surface of (PAA/PDAC-S)/G_s4 is found to be covered by crumpled thin rGO sheets (almost fully cover the region in c-1), while it is more likely to observe overlapping of rGO sheets in PAA/G2//PDAC-S. This indicates the water resistance effect of rGO could be achieved by covering with thin flakes or overlapping flakes. Based on the results above, the stability of PECs appears to be influenced by the combination of rGO and salt contents, as well as the distribution of rGO on the surface.

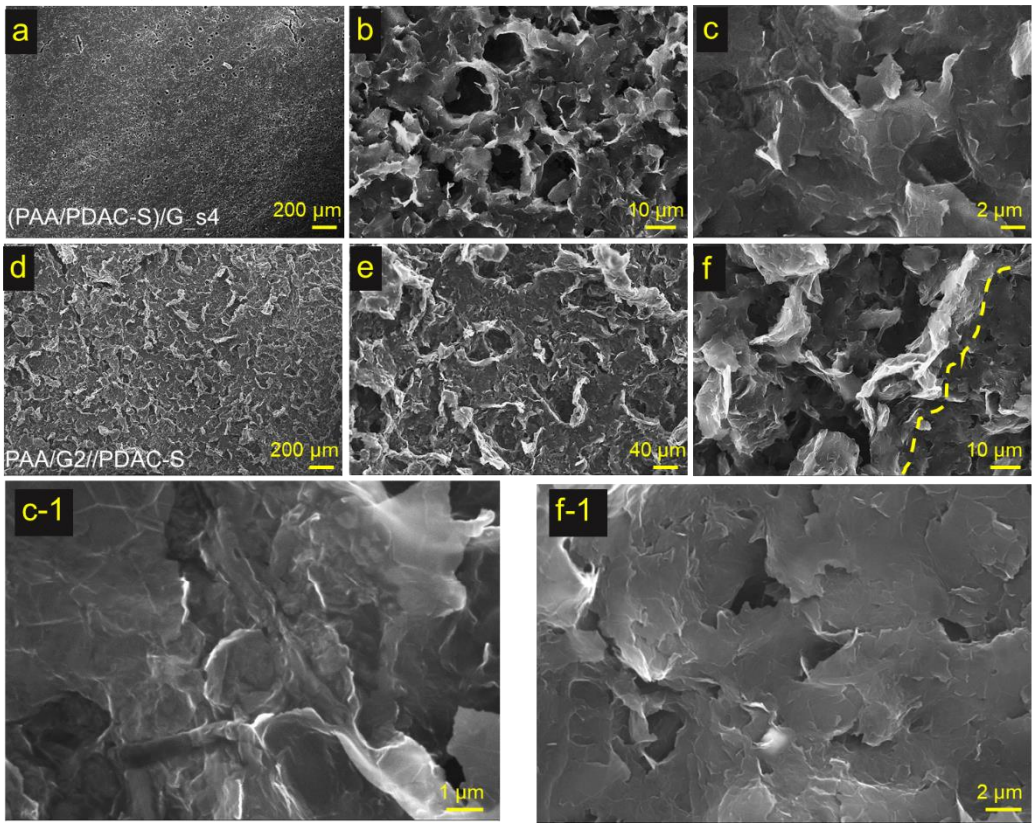

Figure 5.14 Top-view images of (PAA/PDAC-S)/G_s4 (a-c) and PAA/G2//PDAC-S (d-f) soaked for 5 weeks. (c-1) and (f-1) are the enlargement of (a) and (f) respectively.

5.2.8 Thermal conductivity and electrical conductivity

As shown in Figure 5.15a, there is a distinct contrast between thermal conductivity (TC) of pristine PAA/PDAC-s (0.40 ± 0.10 W/m·K) and rGO incorporated PECs. PAA/G//PDAC-S has TC of 1.11± 0.08 W/m·K with addition of rGO around 8.4 wt%, while PAA/G2//PDAC-S shows higher TC of 1.72 ± 0.04 W/m·K with 14.2 wt% rGO, confirming the obviously expected improvement of TC with increasing rGO content. Additionally, TC of polymer composites is also influenced by the

filler dispersion and GRM quality, such as size, number of layers and defects. Usually, the TC increases with increasing GRM content, improving distribution or increasing lateral size, while decreases with increasing defects density [322]. The TC of (PAA/PDAC-S)/G-based samples goes through an oscillating decline with sonication time elongation due to the combination of different effects, namely the improved dispersion, the size reduction and the increase in defectiveness. During the first 0.5 h of sonication, a high TC was observed with a number of 1.70 W/m·K. It's likely related to the connected large rGO aggregates (in length of around 0.2 mm, observed from SEM in 5.2.5) in PECs, which facilitates phonon transport along the rGO and thus results in a high TC. When the sonication time was 1-1.5 h, the change of defects was not obvious (based on Raman spectra in 5.2.5) and the amount of rGO aggregates decreased (SEM in 5.2.3 and 5.2.5). The rGO dispersion became the dominant factor affecting thermal conductivity, which increases with the improvement of rGO dispersion. With the sonication reaches to 2 h, the rGO dispersion in PECs has been improved significantly with aggregates disappearing, while the increase of I(D)/I(G) was observed in (PAA/PDAC-S)/G_s4 indicating the increase of defect density or new boundaries formed by smaller sized fillers. The reduction to rGO size or increase in defect density brings the decrease in TC, the (PAA/PDAC-S)/G_s4 shows TC of 1.33 W/m·K. Comparing PECs with different preparation methods, PAA/G2//PDAC-S displays better TC than (PAA/PDAC-S)/G_s2 due to the better dispersion of rGO, but similar to (PAA/PDAC-S)/G_s3.

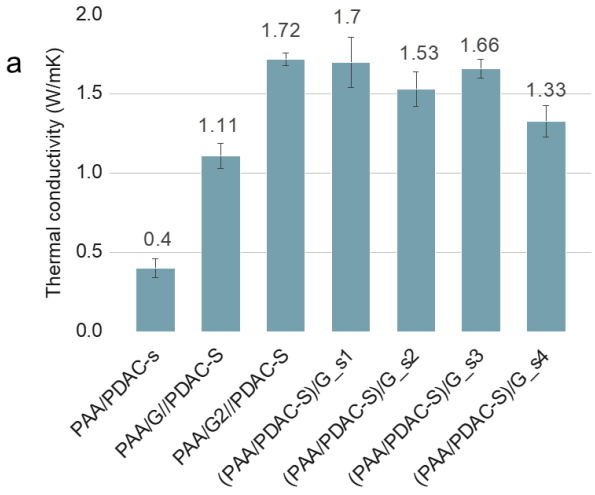

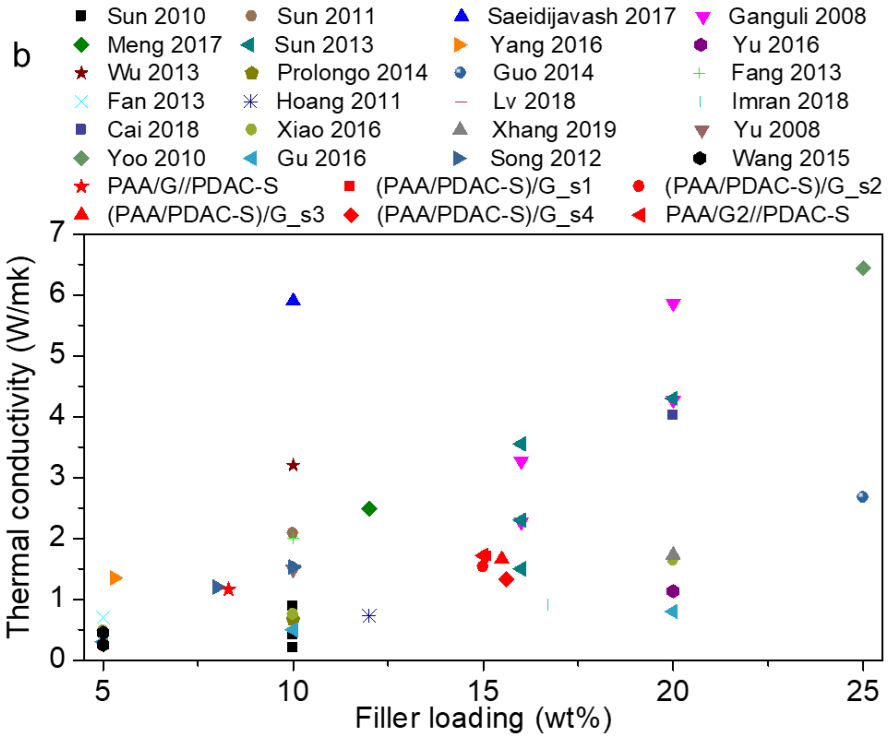

Figure 5.15 Thermal conductivity of PEC samples (a), comparison of thermal conductivity between our samples and polymer composites embedding GRMs in literatures [322-346].

Figure 5.15b summarizes the thermal conductivity of polymeric nanocomposites with different GRMs content. The TC of GRMs-based polymer nanocomposite in Figure 5.15b is highly scattered, due to the un-defined GRMs (including size, number of layers, defectiveness and oxidation, etc.), the polymer types, and the fabrication methods to nanocomposites [347]. These factors would influence the composites TC in different degrees. Besides, for the composites with same type of polymer and GRMs, the TC could also be influenced by interface issues between matrix and fillers, dispersion and distribution of GRMs, and morphology of GRMs [322]. Nevertheless, The TC comparison between our PECs and other GRM-based polymer composites at similar filler loadings is warranted. Based on our results and results in literatures, PAA/G//PDAC-S-based samples and (PAA/PDAC-S)/G-based samples show comparable TC with other GRMs-based polymer composites at similar filler loadings (~8 wt%, ~15 wt%). In particular, sample PAA/G//PDAC-S has comparable performance in TC when compared with other GRMs-based polymer composites at similar rGO loading.

The volume electrical conductivity (EC) of composites were also measured and reported in Figure 5.16. Considering the insulating properties of polymers, the

conductive polymer composite are commonly prepared via introducing conductive fillers. The EC of composites increases suddenly when the added fillers reaches to a specific loading, which is called percolation threshold (p_c) [348]. With increasing of the GRMs, the relationship of conductivity versus dosage shows a typical S-shape, showing three characteristic states: insulating, percolating and conducting [349]. The PAA/G//PDAC-S with rGO ~8.4 wt% shows a EC close to pristine PAA/PDAC-s, while a great improvement is obtained in PAA/G2//PDAC-S up to 126 S/m with rGO content of 15.2 wt%. The great improvement of EC from PAA/G//PDAC-S to PAA/G2//PDAC-S indicates overcoming of the percolation threshold at concentration between 8.4 wt% and 15.2 wt% rGO.

Table 5.1 summarizes the conductive properties of different rGO polymer nanocomposites in the literature. The p_c would be influenced by the structure characteristics of rGO (aspect ratio, defects, oxidation degree), preparation methods to composites (melt mixing, solution blending, in situ polymerization and etc.), rGO dispersion and distribution, and matrix types [348].

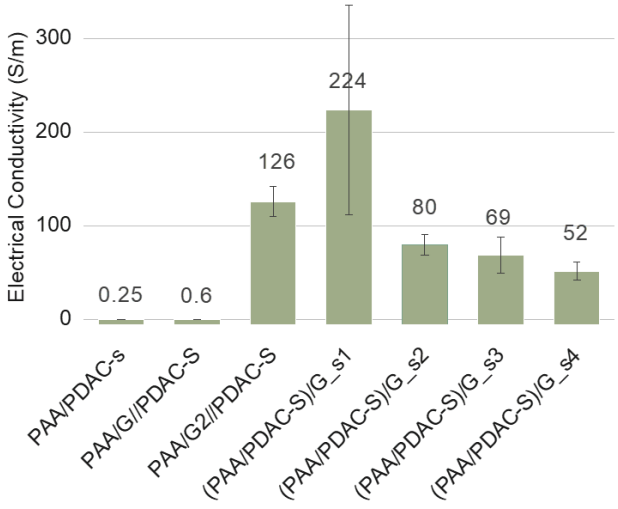

Figure 5.16 Electrical conductivity of PEC samples

Table 5.1 The electrical conductivity and percolation thresholds of rGO reinforced polymer composites with different rGO production method, matrix and preparation method.

Polymer matrix	Filler	Prepared method	Percolation threshold	Ultimate DC electrical conductivity (S/m)	Reference
PA6	TRGO*	Melt compounding	7.5 wt%	7.1×10^{-3}	[350]
PA12	TRGO	Melt compounding	2.5 wt%	8.9×10^{-2}	[351]
PC	TRGO	Melt compounding	2.5 wt%	0.1	[350]
PC	rGO	Solution blending/ in situ thermal reduction	0.21	0.1	[352]
POSS-PCL	rGO	Solution blending	2.5 vol%	0.1	[353]
PMMA	rGO	Solution blending	0.25 vol%	0.01	[354]
iPP	TRGO	Melt compounding	5 wt%	5.3×10^{-2}	[350]
PP	TRGO	Melt compounding	< 5 wt%	10^{-4}	[355]
PS	rGO	LbL assembly	0.2 vol.%	0.05	[356]
PU	f-TRGO	In situ polymerization	0.5 – 2 wt%	1.4×10^{-7}	[357]
PU	rGO	Solution blending	0.078 vol%	0.001	[358]
SAN	TRGO	Melt compounding	4 wt%	0.123	[350]
Epoxy	f-rGO	Solution blending	0.71 vol%	10^{-6}	[359]
Epoxy	CRGO**	In situ polymerization	0.12 vol.%	0.1	[360]
Epoxy	TRGO	Solvent free mixing method	1 wt%	2×10^{-6}	[361]
NR	CRGO	Coagulation method	3 wt%	10^{-4}	[362]
NR	rGO	Solution blending	0.21 vol%	0.23	[363]

The percolation threshold of PAA/G//PDAC-based samples is higher than the commonly studied rGO decorated polymer nanocomposites, but the ultimate bulk conductivity is also higher than most those composites,

Table 5.1. The latter could be ascribed to the different properties of matrix, our matrix of PAA/PDAC-s reveals EC around 0.25 S/m, which is higher than most of investigated insulating polymers. Besides, the EC and p_c. could also be influenced by the aspect ratio and dispersion of fillers. The EC of (PAA/PDAC-S)/G-based samples show a remarkable increase in EC comparing to pristine PAA/PDAC-s, from 0.2-0.3 S/m for PAA/PDAC-S to around 80.0 S/m for (PAA/PDAC-S)/G_s2. In (PAA/PDAC-S)/G-based samples, the decrease trend with sonication time is observed in EC, especially between (PAA/PDAC-S)/G_s1 and (PAA/PDAC-S)/G_s2. In most of previous studies, the EC could be improved due to more contacts of fillers forming a better connected network. However, the large size of rGO aggregates (approach to 200 μm) has to be considered in our samples prepared with short sonication time. This is because aggregated rGO with large sizes facilitates the formation of a network with fewer junctions than those with smaller rGO flakes, and fewer junctions reduces the total resistance of the network. Bao et al. [364] reported that the agglomeration of fillers may decrease *pc* and improve EC, which is less important at high loading of fillers. With sonication time increasing in range of 1-1.5 h, the rGO aggregates were limited in size and amount, the rGO concentration in other regions increased and dispersion of fillers improved, which brings two opposites effects onto EC. The obvious decrease of EC in range of 0.5-1 h indicates the dominant effect of decrease in agglomeration, whereas this decrease trend turns to be limited at 1-1.5h because of the better dispersion of rGO flakes and increased contacts. Moreover, the long-time sonication results in defects and smaller size of rGO, indeed, the quality and aspect ratio of rGO flakes decrease, which brings negative effect to EC. This could be the reason for the decrease EC at sonication 2h as higher defectiveness was found in (PAA/PDAC-S)/G_s4 from Raman result. Even with a downward trend, the (PAA/PDAC-S)/G_s4 sample with the smallest increment resulted in a conductivity 2 orders of magnitude higher that of the pristine PEC matrix.

It is worth mentioning that the discussion of the conductivity of polyelectrolytes and PE-based composites is more complicated than that of neutral polymer systems. PEs are macromolecules with many ionizable groups, which dissociate in aqueous solution and form counterions around the molecular chains, and they exhibits ion-conducting properties in solutions. Adding salt (ions) in solutions could further increase conductivity. However, the ionic conductivity of polyelectrolytes at low

humidity is very low due to the limited ion conduction in the absence of water molecules. It was reported that the ionic conductivity of PAH at low RH revealed six orders of magnitude lower than graphene quantum dots network [365]. Similarly, low conductivity was also observed in PECs, for example, PAA/PSS self-assembled multilayer was a good insulator with ionic conductivity of 3.5×10^{-11} S/m [366]. For hydrogel PECs, it is easier to obtain the improved conductivity especially in the system with added salt ions, the hydrogel of PAM/PAA chelating with Fe^{3+} and followed by loading NaCl reveals ionic conductivity of ~0.72 S/m [367]. The relatively high initial EC (0.25 S/m) in our sample of PAA/PDAC-s could because of the residual water and presence of salt ions.

EC of polyelectrolyte systems was improved by adding highly conductive nanofillers, such as metal particles or nanowires [368], carbon nanotubes [369] or GRMs. Rani et al. prepared the multilayer films of graphene-embedded PAH/PSS, displaying a EC of 20 S/m when the PE concentration was 0.2mg/ml, assembled layers were 6 bilayers and the film was annealed 2 h [370]. The EC and p_c of self-assembled rGO/PEI spray-coatings with different bilayers (n) and flakes lateral dimensions were studied in previous literature [371]. For rGO with a lateral size of 20 μm, the p_c was 0.2 vol % when n was 2, and p_c was 0.01 vol % when n was 10. For rGO with a lateral size of 100 μm, p_c was 0.1 vol % for n = 2, p_c was 0.01 vol % for n = 10. After percolation, the maximum conductivities (ultimate EC) of 19 S/m for 34 vol% of 20 μm-rGO, and 127 S/m for 39 vol% of 100 μm-rGO were obtained [371]. The *pc* of rGO/PEI with different lateral diameter and n was lower than that of PAA/G//PDAC-based samples, but the rGO/PEI with 100 μm-rGO and content of 39 vol% displayed a similar EC to PAA/G2//PDAC-s (14.2 wt% rGO). In a study of rGO-PEC system, EC of PAA grafted rGO/PAM at hydrated condition (water content ca. 80%) and it reached 1.26×10^{-3} S/m when the rGO grafted PAA was 0.6 wt% to acrylamide [230]. However, to the best of the candidate's knowledge, no studies concerning the electrical conductivity of compact rGO-PECs (not PEMs) with high rGO loadings (around and above 10 wt%) are reported at present, which is why the results obtained are compared to traditional polymer nanocomposites.

5.3 Conclusions

In this chapter, two dispersion-complexation methods are presented for the preparation of polyelectrolyte composites with high rGO content, and compared the rGO distribution in matrix, mechanical properties, electrical and thermal conductivity, as well as stability in water. The PAA/G//PDAC-S samples based on

PAA-based predispersion followed by complexation with PDAC exploit good compatibility of PAA molecules and rGO, yielding good dispersion of rGO in PAA/PDAC matrix within 1 h sonication. This approach allows to improve mechanical property (stress at break 7.0 ± 0.5 MPa) and thermal conductivity (~1.11 W/m·K) under a relative low rGO content (~8.4 wt%), but with minor improvement in electrical conductivity. Increasing rGO concentration using the same preparation procedure could transfer the composites from electronically insulating to conducting, with electrical conductivity in the range of 10^2 S/m. However, the PAA/G//PDAC-S-based samples were found to retain much higher amount of salt in composites. The salt content in PAA/G2//PDAC was 29.6 wt%, which strongly decreases the mechanical property (stress at break 3.9 ± 0.6 MPa). For the (PAA/PDAC-S)/G-based samples with multiple phases dispersion, the rGO content in composites was higher than PAA/G//PDAC-S as the rGO were dispersed in mixture system of PAA, PDAC and salt ions. The mechanical reinforcement, electrical and thermal improvement are obvious comparing to pristine PAA/PDAC-s. However, the optimum distribution of rGO in (PAA/PDAC-S)/G requires longer sonication time (2 h) than PAA/G//PDAC-S. Compared with (PAA/PDAC-S)/G_s2 (sonication 1 h), the (PAA/PDAC-S)/G_s4 (sonication 2 h) shows further increased ultimate stress of 14.1 ± 1.7 MPa, and slightly lower thermal (~1.33 W/m·K) and electrical conductivity (~52 S/m), which is due to better rGO dispersion but smaller and more defective rGO flakes. (PAA/PDAC-S)/G_s4 also reveals best stability in water even after immersing in water for 5 weeks, reflecting a higher resistance to PEC flow and internal pores expansion in water with assistance of rGO flakes. This part of the work contributed to the definition of methods for the simple and environmentally friendly synthesis of highly loaded rGO-doped polymer composites in aqueous phase at room temperature. Besides, the PEC composite materials with high rGO content could find potential applications in electronic packing materials, thermal interface materials and potentially conductive humidity sensors.

Chapter 6

6 General conclusions

The main goal of this dissertation is to study the aqueous dispersion of reduced graphite oxide (rGO) in polyelectrolytes (PEs) solutions and rGO-based polymer composites. While the work was oriented to fundamental research, composite polyelectrolyte complexes may find applications for electrical components and conductive humidity sensors, among others. To explore suitable PEs and conditions for rGO dispersion, the effects of polymer structure, molecular mass and charge density on stability of rGO in aqueous solutions were studied. The stable PE/rGO dispersions were then complexed with an oppositely charged PE to form rGO incorporated polyelectrolyte complexes (rGO-PECs). The effects of salt content, rGO content and humidity on composites mechanical properties were also explored. To obtain the conductive properties of rGO-PECs, high loadings of rGO were achieved via different fabrication approaches. The results of rGO distribution, composites mechanical properties, electrical conductivity, thermal conductivity and stability in water were compared systemically. The main findings and implications of each study are as follows:

The polyelectrolyte assisted aqueous dispersion of rGO: at the initial stage of this project, I evaluated the effect of different PEs (PAA, BPEI, CMC, and PSS) and dispersion conditions (charge densities) on dispersing and stabilizing rGO in water. Among them, PAA-based dispersions were shown to have obvious advantages in terms of rGO concentration, small size and narrow size distribution,

and dispersion stability over several weeks, as a result of the lower surface tension, and attractive/repulsive balance between rGO sheets attached with polymer chains under mild ionization. We found that the dispersion performance of rGO in anionic PEs was closely related to solution the surface tension, and the PE solutions with lower surface tension tend to have better rGO solubility and dispersion stability than PEs at high surface tension (e.g., PSS and CMC). In weak PEs dispersions (anionic PAA and cationic BPEI), the charge densities, and their interactions with rGO were effectively regulated by pH. The repulsion between PAA molecules and rGO flakes was strong at high charge density (at high pH), while for the BPEI molecules at high charge density (low pH), the strong repulsion within the segments of BPEI polymer chains also affected the adsorption of polymers onto rGO surface, resulting in a very limited dispersibility of rGO. Conversely, PEs with too low charge density couldn't maintain stability due to insufficient charges and limited repulsive forces, leading to a lower concentration of dispersed rGO. Both of PAA and BPEI-based dispersions revealed good dispersion performances of rGO under mild charge density. In addition, the dispersed concentration of rGO in BPEI solutions decreased with the use of higher molecular mass, which wasn't observed in other cases (PAA, CMC, and PSS). Before and after 4 weeks of storage, the BPEI-based dispersions showed the highest rGO concentrations than the other PEs, even though they had significant precipitation during the first week. This basic research is meaningful to the aqueous dispersion of GRMs with proper PEs and suitable fabrication conditions, which could be further used in water treatment and functional membranes.

Reduced graphite oxide and/or salt incorporate polyelectrolyte complexes (rGO-PECs): based on the good dispersion results of rGO in PAA solution and the complexation feature of oppositely charged PEs, I prepared rGO-reinforced PAA/PDAC composites and explored the effects of salt content, rGO content and moisture on the mechanical properties of composites. Notably, both ionic strength (salt) and hydration level influence the mechanical response of PECs as they are significant for facilitating PE motions. The salt addition (~ 7 wt%) or increase in moisture (RH from ~ 50% to ~ 70%) induced a significant decrease in stiffness and resistance, coupled with a much higher ductility, as a consequence of chain mobility increase. Salt ions could weaken or break the ion pairs from PEs (Pol^+ and Pol^-) and transfer the intrinsic interaction between polymers to extrinsic interaction between PE and counterions, while the water near PEC provided volume for PE chain motion and reduced the friction between them. The effect of rGO on PEC mechanical results is not only related to the incorporated amount of rGO but also depends on the mechanical property of matrix. The addition of a small amount of

rGO at ambient conditions resulted in a great improvement in tensile properties, especially for salt-rich PEC samples. With rGO incorporation of ~2 wt% in PAA/G//PDAC increased the tensile strength from 31 ± 2.4 MPa to 51 ± 2.4 MPa. The rGO reinforced salted sample PAA/G//PDAC-s with rGO around 0.6wt% showed around 1.9 and 4.4 times of elastic modulus and stress at break respectively to that of PAA/PDAC-s (salted but no rGO addition sample). Comparing the mechanical properties of the samples before and after desalting, salt-removing treatment bumped up the mechanical properties of salted samples (PAA/PDAC-s and PAA/G//PDAC-s) to a level similar to that of pristine complexes, but had limited effect on samples PAA/PDAC and PAA/G//PDAC with low initial salt content. This means that the stiffness improvement of the PECs under ambient conditions is controlled by the rGO content, while the plasticity of PECs is strongly dependent on the concentration of salt. Under a high humidity environment (RH 70%), all samples showed extremely high plasticity and low strength, and most of the deformation was above 1000%. The addition of rGO displayed limited improvement in mechanical property, as the PEC matrix was soft and very ductile, instead the salt-free state of composites is critical to the strength increase and deformation reduction. This part of study provided fundamental insight into the different conditions affecting the mechanical properties of rGO-doped PECs.

PAA/PDAC polyelectrolyte complex incorporating high concentration of rGO: the feasibility of incorporating rGO into PAA/PDAC substrates based on PEs complexation has been demonstrated in chapter 4. The thermal and electrical conductivities of rGO-PEC composites are dominated via rGO content, also influenced by factors of rGO dispersion, distribution, and orientation. In the last part of this research work, PECs with high loading of rGO have been manufactured using two different dispersing-complexing approaches, including PAA-based rGO dispersion followed by mixing with PDAC solution (PAA/G//PDAC-S), alternatively, water induced complexation after the dispersion of rGO in a mixed system consisting of PAA, PDAC and a high concentration of salt ((PAA/PDAC-S)/G). The former was applied due to the good compatibility of PAA and rGO, while the latter was designed because of the higher rGO content in composites. The rGO content, dispersion in matrix, and composites mechanical, thermal, and electrical properties have been studied based on these two methods. PAA/G//PDAC-S and (PAA/PDAC-S)/G showed rGO content at ~8 wt% and ~15 wt% respectively. Both of them increased significantly in mechanical (stress at break 7 ~ 9 MPa) and thermal conductivity (1.1~1.5 W/m·K) than pristine PAA/PDAC-s that with tensile at break 1.6 ± 0.3 MPa and thermal conductivity 0.4 ± 0.06 W/m·K. But their performances in electrical conductivity are quite different,

the electrical conductivity was improved from ~0.25 S/m in PAA/PDAC-s to ~80 S/m in (PAA/PDAC-S)/G, but narrow variation was observed in PAA/G//PDAC-S (~0.6 S/m). Considering these results, different strategies were applied in PAA/G//PDAC-S and (PAA/PDAC-S)/G to improve their mechanical property and electrical property respectively. Different sonication times were implemented for the (PAA/PDAC-S)/G-based samples, the significant improvements in rGO dispersion and the mechanical properties were observed with increasing sonication time, while the electrical and thermal conductivities slightly decreased accompanied by the separation of large aggregates of rGO and the formation of small-sized rGO/ development of defectiveness. After sonicated 2 h, sample (PAA/PDAC-S)/G_s4 revealed reinforced tensile strength (14.1 ± 1.7 MPa) and elastic modulus (948 ± 144 MPa), and the thermal conductivity and electrical conductivity were ~1.33 W/m· K and ~52 S/m respectively. On the other hand, increasing the input weight ratio of PAA to rGO in PAA/G//PDAC-S-based samples from 4:1 to 2:1 led to the increased rGO and salt contents in composites, which caused significantly improved electrical conductivity (~126 S/m) but a strong decrease in ultimate stress (~3 MPa).

Besides the physical properties of the complexes, their stability in water was addressed. Immersed rGO-PECs display different stability on different surfaces, the stability in the top view is better than that in the cross-section view. The optimum performance was observed in (PAA/PDAC-S)/G_s4, which has good rGO dispersion, high rGO concentration, and relatively lower salt concentration.

The GRMs-based polymer nanocomposites are often processed by melt-mixing, in-situ polymerization and solution mixing in terms of different fillers dispersion, effectiveness, cost and production scale. This work provides a simple and environmentally friendly method for fabricating rGO-PECs, which is a variant of the solvent-mixing method, but the process only involves pure components of composites and solvent water, indeed, there are less waste, low cost, and no issue of solvents removing (re-aggregation of GRMs flakes may occur during solvent evaporation). The good compatibility between rGO and PEs, such as PAA, is beneficial to improve the dissolution and dispersion of rGO in polymer solution, and create conditions for its good dispersion and distribution in PECs. Theoretically, this approach has a low limit on rGO content in composites; indeed, a large number of fillers can be embedded by complexation of PE chains in water. However, rGO-PECs with high concentration of rGO require higher salt concentration to maintain processability, but too much salt would be detrimental to the composites mechanical strength and stability in high moisture environments. In

this study, the Type 1 method prepared rGO-PECs composites in short sonication time and with good rGO dispersion, but increasing input pristine rGO greatly increased the salt content in final composites. Therefore, the salt content needs fine-tuning by modifying during PEs solution mixing or post-processing of soaking in designed salt solution. The type 2 exhibited a relatively lower salt content tendency, but it required longer sonication time to achieve better rGO dispersion. Considering the non-covalent interaction between rGO and PEs, and the presence of plasticizing phase salt, it is expected that the mechanical properties of rGO-PECs might be inferior to those prepared by methods using covalent interaction. Furthermore, it is always necessary to keep in mind the brittle nature of PECs in completely dry conditions as well as the intrinsic moisture affinity, causing a strong dependency on ambient humidity. While this could be a limit in structural applications, this dependency could be exploited for functional materials, including sensing applications.

References

[1] Jiang T, Maddalena L, Gomez J, Carosio F, Fina A. Polyelectrolytes Enabled Reduced Graphite Oxide Water Dispersions: Effects of the Structure, Molecular Weight, and Charge Density. Polymers (Basel) 2022;14.

[2] Berry V. Impermeability of graphene and its applications. Carbon 2013;62:1-10.

[3] Banszerus L, Schmitz M, Engels S, Dauber J, Oellers M, Haupt F, et al. Ultrahigh-mobility graphene devices from chemical vapor deposition on reusable copper. Science Advances 2015;1:1-6.

[4] Pop E, Varshney V, Roy AK. Thermal properties of graphene: Fundamentals and applications. MRS Bulletin 2012;37:1273-81.

[5] Zhu Y, Murali S, Cai W, Li X, Suk JW, Potts JR, et al. Graphene and graphene oxide: synthesis, properties, and applications. Advanced materials 2010;22:3906-24.

[6] Gurunathan S, Kim J-H. Synthesis, toxicity, biocompatibility, and biomedical applications of graphene and graphene-related materials. International Journal of Nanomedicine 2016:1927.

[7] Zhang Z, Fraser A, Ye S, Merle G, Barralet J. Top-down bottom-up graphene synthesis. Nano Futures 2019;3:042003.

[8] Diez-Pascual AM. Development of Graphene-Based Polymeric Nanocomposites: A Brief Overview. Polymers (Basel) 2021;13.

[9] Amiri A, Naraghi M, Ahmadi G, Soleymaniha M, Shanbedi M. A review on liquid-phase exfoliation for scalable production of pure graphene, wrinkled, crumpled and functionalized graphene and challenges. FlatChem 2018;8:40-71.

[10] David W. Johnson BPD, Karl S. Coleman A manufacturing perspective on graphene dispersions. Current Opinion in Colloid & Interface Science 2015;20:367-82.

[11] Liang A, Jiang X, Hong X, Jiang Y, Shao Z, Zhu D. Recent Developments Concerning the Dispersion Methods and Mechanisms of Graphene. Coatings 2018;8:33.

[12] Bianco A, Cheng H-M, Enoki T, Gogotsi Y, Hurt RH, Koratkar N, et al. All in the graphene family – A recommended nomenclature for two-dimensional carbon materials. Carbon 2013;65:1-6.

[13] Wick P, Louw-Gaume AE, Kucki M, Krug HF, Kostarelos K, Fadeel B, et al. Classification framework for graphene-based materials. Angewandte Chemie 2014;53:7714-8.

[14] Gao W, Alemany LB, Ci L, Ajayan PM. New insights into the structure and reduction of graphite oxide. Nature chemistry 2009;1:403-8.

[15] Bagri A, Mattevi C, Acik M, Chabal YJ, Chhowalla M, Shenoy VB. Structural evolution during the reduction of chemically derived graphene oxide. Nature chemistry 2010;2:581-7.

[16] Huang Y, Wan C. Controllable fabrication and multifunctional applications of graphene/ceramic composites. Journal of Advanced Ceramics 2020;9:271-91.

[17] Kumar HGP, Xavior MA. Graphene Reinforced Metal Matrix Composite (GRMMC): A Review. Procedia Engineering 2014;97:1033-40.

[18] Verma D, Gope PC, Shandilya A, Gupta A. Mechanical-Thermal-Electrical and Morphological Properties of Graphene Reinforced Polymer Composites: A Review. Transactions of the Indian Institute of Metals 2014;67:803-16.

[19] Lee C, Wei X, Kysar JW, Hone J. Measurement of the elastic properties and intrinsic strength of monolayer graphene. Science 2008;321:385-8.

[20] Soldano C, Mahmood A, Dujardin E. Production, properties and potential of graphene. Carbon 2010;48:2127-50.

[21] Suk JW, Piner RD, An J, Ruoff RS. Mechanical properties of monolayer graphene oxide. ACS Nano 2010;4:6557-64.

[22] Dikin DA, Stankovich S, Zimney EJ, Piner RD, Dommett GH, Evmenenko G, et al. Preparation and characterization of graphene oxide paper. Nature 2007;448:457-60.

[23] Gómez-Navarro C, Burghard M, Kern K. Elastic properties of chemically derived single graphene sheets. Nano letters 2008;8:2045–9.

[24] Chen H, Müller MB, Gilmore KJ, Wallace GG, Li D. Mechanically Strong, Electrically Conductive, and Biocompatible Graphene Paper. Advanced materials 2008;20:3557-61.

[25] Zhang P, Ma L, Fan F, Zeng Z, Peng C, Loya PE, et al. Fracture toughness of graphene. Nature communications 2014;5:3782.

[26] Zhu S-E, Yuan S, Janssen GCAM. Optical transmittance of multilayer graphene. EPL (Europhysics Letters) 2014;108:17007.

[27] Nair RR, Blake P, Grigorenko AN, Novoselov KS, Booth TJ, Stauber T, et al. Fine structure constant defines visual transparency of graphene. Science 2008;320:1308.

[28] Goenka S, Sant V, Sant S. Graphene-based nanomaterials for drug delivery and tissue engineering. Journal of controlled release : official journal of the Controlled Release Society 2014;173:75-88.

[29] Gupta S, Joshi P, Narayan J. Electron mobility modulation in graphene oxide by controlling carbon melt lifetime. Carbon 2020;170:327-37.

[30] Wang S, Ang PK, Wang Z, Tang AL, Thong JT, Loh KP. High mobility, printable, and solution-processed graphene electronics. Nano letters 2010;10:92-8.

[31] Mahanta NK, Abramson AR. Thermal Conductivity of Graphene and Graphene Oxide Nanoplatelets. 13th intersociety conference on thermal and thermomechanical phenomena in electronic systems, IEEE 2012:1-6.

[32] Kumar A, Sharma K, Dixit AR. A review of the mechanical and thermal properties of graphene and its hybrid polymer nanocomposites for structural applications. Journal of Materials Science 2018;54:5992-6026.

[33] Stankovich S, Dikin DA, Dommett GH, Kohlhaas KM, Zimney EJ, Stach EA, et al. Graphene-based composite materials. Nature 2006;442:282-6.

[34] Gómez-Navarro C, Weitz RT, Bittner AM, Scolari M, Alf Mews MB, Kern K. Electronic Transport Properties of Individual Chemically Reduced Graphene Oxide Sheets. Nano letters 2007;7:3499-503.

[35] Schniepp HC, Li J-L, McAllister MJ, Sai H, Herrera-Alonso M, Adamson DH, et al. Functionalized Single Graphene Sheets Derived from Splitting Graphite Oxide. The journal of physical chemistry B 2006;110:8535-9.

[36] Wang Y, Chen Y, Lacey SD, Xu L, Xie H, Li T, et al. Reduced Graphene Oxide Film with Record-High Conductivity and Mobility Materials Today 2018;21:186-92.

[37] Wei W, Qu X. Extraordinary physical properties of functionalized graphene. Small 2012;8:2138-51.

[38] Montes-Navajas P, Asenjo NG, Santamaria R, Menendez R, Corma A, Garcia H. Surface area measurement of graphene oxide in aqueous solutions. Langmuir : the ACS journal of surfaces and colloids 2013;29:13443-8.

[39] Esmaeili A, Entezari MH. Facile and fast synthesis of graphene oxide nanosheets via bath ultrasonic irradiation. Journal of colloid and interface science 2014;432:19-25.

[40] Zhang S, Wang H, Liu J, Bao C. Measuring the specific surface area of monolayer graphene oxide in water. Materials Letters 2020;261:127098.

[41] Jabari Seresht R, Jahanshahi M, Rashidi A, Ghoreyshi AA. Synthesize and characterization of graphene nanosheets with high surface area and nano-porous structure. Applied Surface Science 2013;276:672-81.

[42] Stoller MD, Park S, Zhu Y, An J, Ruoff RS. Graphene-based ultracapacitors. Nano letters 2008;8:3498-502.

[43] Wang Y, Shi Z, Huang Y, Ma Y, Wang C, Chen M, et al. Supercapacitor devices based on graphene materials. . The Journal of Physical Chemistry C 2009;113:13103-7.

[44] Muthoosamy K, Manickam S. State of the art and recent advances in the ultrasound-assisted synthesis, exfoliation and functionalization of graphene derivatives. Ultrasonics sonochemistry 2017;39:478-93.

[45] Parobek D, Liu H. Wettability of graphene. 2D Materials 2015;2:032001.

[46] Wang S, Zhang Y, Abidi N, Cabrales L. Wettability and surface free energy of graphene films. Langmuir : the ACS journal of surfaces and colloids 2009;25:11078-81.

[47] Shih CJ, Wang QH, Lin S, Park KC, Jin Z, Strano MS, et al. Breakdown in the wetting transparency of graphene. Physical review letters 2012;109:176101.

[48] Texter J. Graphene dispersions. Current Opinion in Colloid & Interface Science 2014;19:163-74.

[49] Hernandez Y, Nicolosi V, Lotya M, Blighe FM, Sun Z, De S, et al. High-yield production of graphene by liquid-phase exfoliation of graphite. Nature nanotechnology 2008;3:563-8.

[50] Vacacela Gomez C, Guevara M, Tene T, Villamagua L, Usca GT, Maldonado F, et al. The liquid exfoliation of graphene in polar solvents. Applied Surface Science 2021;546:149046.

[51] Park S, An J, Jung I, Piner RD, An SJ, Li X, et al. Colloidal suspensions of highly reduced graphene oxide in a wide variety of organic solvents. Nano letters 2009;9:1593–7.

[52] Coleman JN. Liquid Exfoliation of Defect-Free Graphene. Accounts of Chemical Research 2013;46:14-22.

[53] Fu C, Yang X. Molecular simulation of interfacial mechanics for solvent exfoliation of graphene from graphite. Carbon 2013;55:350-60.

[54] Shih C, Lin S, Strano MS, Blankschein D. Understanding the stabilization of liquid-phase-exfoliated graphene in polar solvents: molecular dynamics simulations and kinetic theory of colloid aggregation. Journal of the American Chemical Society 2010;132 14638-48.

[55] Hansen CM. Hansen solubility parameters: a user's handbook: CRC press; 2007.

[56] Hernandez Y, Lotya M, Rickard D, Bergin SD, Coleman JN. Measurement of multicomponent solubility parameters for graphene facilitates solvent discovery. Langmuir : the ACS journal of surfaces and colloids 2010;26:3208-13.

[57] Konios D, Stylianakis MM, Stratakis E, Kymakis E. Dispersion behaviour of graphene oxide and reduced graphene oxide. Journal of colloid and interface science 2014;430:108-12.

[58] Joshi DR, Adhikari N. An overview on common organic solvents and their toxicity. J Pharm Res Int 2019;28:1-18.

[59] Layek RK, Nandi AK. A review on synthesis and properties of polymer functionalized graphene. Polymer 2013;54:5087-103.

[60] Coleman JN. Liquid-Phase Exfoliation of Nanotubes and Graphene. Advanced Functional Materials 2009;19:3680-95.

[61] Shih CJ, Lin S, Sharma R, Strano MS, Blankschtein D. Understanding the pH-dependent behavior of graphene oxide aqueous solutions: a comparative experimental and molecular dynamics simulation study. Langmuir : the ACS journal of surfaces and colloids 2012;28:235-41.

[62] Li D, Muller MB, Gilje S, Kaner RB, Wallace GG. Processable aqueous dispersions of graphene nanosheets. Nature nanotechnology 2008;3:101-5.

[63] Backes C, Abdelkader AM, Alonso C, Andrieux-Ledier A, Arenal R, Azpeitia J, et al. Production and processing of graphene and related materials. 2D Materials 2020;7:022001.

[64] Narayan R, Kim JE, Kim JY, Lee KE, Kim SO. Graphene Oxide Liquid Crystals: Discovery, Evolution and Applications. Advanced materials 2016;28:3045-68.

[65] Wang M, Niu Y, Zhou J, Wen H, Zhang Z, Luo D, et al. The dispersion and aggregation of graphene oxide in aqueous media. Nanoscale 2016;8:14587-92.

[66] Wu L, Liu L, Gao B, Muñoz-Carpena R, Zhang M, Chen H, et al. Aggregation Kinetics of Graphene Oxides in Aqueous Solutions: Experiments, Mechanisms, and Modeling. Langmuir : the ACS journal of surfaces and colloids 2013;29:15174-81.

[67] Pei S, Cheng H-M. The reduction of graphene oxide. Carbon 2012;50:3210-28.

[68] Cote LJ, Cruz-Silva R, Huang J. Flash Reduction and Patterning of Graphite Oxide and Its Polymer Composite. J AM CHEM SOC 2009;131:11027–32.

[69] Xu Y, Bai H, Lu G, Li C, Shi G. Flexible Graphene Films via the Filtration of Water-Soluble Noncovalent Functionalized Graphene Sheets. Journal of the American Chemical Society 2008;130:5856-7.

[70] Park S, An J, Potts JR, Velamakanni A, Murali S, Ruoff RS. Hydrazine-reduction of graphite- and graphene oxide. Carbon 2011;49:3019-23.

[71] Shin HJ, Kim KK, Benayad A, Yoon SM, Park HK, Jung IS, et al. Efficient Reduction of Graphite Oxide by Sodium Borohydride and Its Effect on Electrical Conductance. Advanced Functional Materials 2009;19:1987-92.

[72] L. G. Guex, Sacchi B, K. F. Peuvot, R. L. Andersson, A. M. Pourrahimi, V. Strom, et al. Experimental review: chemical reduction of graphene oxide (GO) to reduced graphene oxide (rGO) by aqueous chemistry. Nanoscale 2017;9:9562-71.

[73] Pei S, Zhao J, Du J, Ren W, Cheng H-M. Direct reduction of graphene oxide films into highly conductive and flexible graphene films by hydrohalic acids. Carbon 2010;48:4466-74.

[74] Zhou T, Chen F, Liu K, Deng H, Zhang Q, Feng J, et al. A simple and efficient method to prepare graphene by reduction of graphite oxide with sodium hydrosulfite. Nanotechnology 2011;22:045704.

[75] Sun L, Yu H, Fugetsu B. Graphene oxide adsorption enhanced by in situ reduction with sodium hydrosulfite to remove acridine orange from aqueous solution. Journal of hazardous materials 2012;203-204:101-10.

[76] Xu C, Shi X, Ji A, Shi L, Zhou C, Cui Y. Fabrication and Characteristics of Reduced Graphene Oxide Produced with Different Green Reductants. PloS one 2015;10:e0144842.

[77] Kurian M. Recent progress in the chemical reduction of graphene oxide by green reductants–A Mini review. Carbon Trends 2021;5:100120.

[78] Lotya M, King PJ, Khan U, De S, Coleman JN. High-Concentration, Surfactant Stabilized Graphene Dispersions. CS Nano 2010;4:3155-62.

[79] Khan U, O'Neill A, Lotya M, De S, Coleman JN. High-concentration solvent exfoliation of graphene. Small 2010;6:864-71.

[80] Tadyszak K, Wychowaniec JK, Litowczenko J. Biomedical Applications of Graphene-Based Structures. Nanomaterials 2018;8.

[81] Kuila T, Bose S, Mishra AK, Khanra P, Kim NH, Lee JH. Chemical functionalization of graphene and its applications. Progress in Materials Science 2012;57:1061-105.

[82] Mungse HP, Kumar N, Khatri OP. Synthesis, dispersion and lubrication potential of basal plane functionalized alkylated graphene nanosheets. RSC Advances 2015;5:25565-71.

[83] Wang G, Shen X, Wang B, JaneYao, Park J. Synthesis and characterisation of hydrophilic and organophilic graphene nanosheets. Carbon 2009;47:1359-64.

[84] Wang G, Wang B, Park J, Yang J, Shen X, Yao J. Synthesis of enhanced hydrophilic and hydrophobic graphene oxide nanosheets by a solvothermal method. Carbon 2009;47:68-72.

[85] Yang H, Shan C, Li F, Han D, Zhang Q, Niu L. Covalent functionalization of polydisperse chemically-converted graphene sheets with amine-terminated ionic liquid. Chemical communications 2009:3880-2.

[86] Salavagione HJ, Gómez MA, Martínez G. Polymeric Modification of Graphene through Esterification of Graphite Oxide and Poly(vinyl alcohol). Macromolecules 2009;42:6331-4.

[87] Rani S, Kumar M, Kumar R, Kumar D, Sharma S, Singh G. Characterization and dispersibility of improved thermally stable amide functionalized graphene oxide. Materials Research Bulletin 2014;60:143-9.

[88] Yu D, Yang Y, Durstock§ M, Baek J-B, Dai L. Soluble P3HT-grafted graphene for efficient bilayer-heterojunction photovoltaic devices. ACS Nano 2010;4:5633–40.

[89] He H, Gao C. General approach to individually dispersed, highly soluble, and conductive graphene nanosheets functionalized by nitrene chemistry. Chem Mater 2010;22:5054-64.

[90] Lee SH, Dreyer DR, An J, Velamakanni A, Piner RD, Park S, et al. Polymer Brushes via Controlled, Surface-Initiated Atom Transfer Radical Polymerization (ATRP) from Graphene Oxide. Macromolecular rapid communications 2010;31:281-8.

[91] Moad G, Rizzardo E, Thang SH. Living Radical Polymerization by the RAFT Process – A Third Update. Australian Journal of Chemistry 2012;65:985.

[92] Chakraborty G, Gupta A, Pugazhenthi G, Katiyar V. Facile dispersion of exfoliated graphene/PLA nanocomposites viain situpolycondensation with a melt extrusion process and itsrheological studies. Journal of Applied Polymer Science 2018;135:46476.

[93] Zhang X, Fan X, Li H, Yan C. Facile preparation route for graphene oxide reinforced polyamide 6 composites via in situ anionic ring-opening polymerization. Journal of Materials Chemistry 2012;22:24081.

[94] Huang Y, Qin Y, Zhou Y, Niu H, Yu Z-Z, Dong J-Y. Polypropylene/Graphene Oxide Nanocomposites Prepared by In Situ Ziegler−Natta Polymerization. Chemistry of Materials 2010;22:4096-102.

[95] Yang Y, Wang J, Zhang J, Liu J, Yang X, Zhao H. Exfoliated graphite oxide decorated by PDMAEMA chains and polymer particles. Langmuir : the ACS journal of surfaces and colloids 2009;25:11808-14.

[96] Ye Y-S, Chen Y-N, Wang J-S, Rick J, Huang Y-J, Chang F-C, et al. Versatile Grafting Approaches to Functionalizing Individually Dispersed Graphene

Nanosheets Using RAFT Polymerization and Click Chemistry. Chemistry of Materials 2012;24:2987-97.

[97] Georgakilas V, Tiwari JN, Kemp KC, Perman JA, Bourlinos AB, Kim KS, et al. Noncovalent Functionalization of Graphene and Graphene Oxide for Energy Materials, Biosensing, Catalytic, and Biomedical Applications. Chemical reviews 2016;116:5464-519.

[98] Chortarea S, Kuru OC, Netkueakul W, Pelin M, Keshavan S, Song Z, et al. Hazard assessment of abraded thermoplastic composites reinforced with reduced graphene oxide. Journal of hazardous materials 2022;435:129053.

[99] Narayan R, Kim SO. Surfactant mediated liquid phase exfoliation of graphene. Nano convergence 2015;2:20.

[100] Feng B-B, Wang Z-H, Suo W-H, Wang Y, Wen J-C, Li Y-F, et al. Performance of graphene dispersion by using mixed surfactants. Materials Research Express 2020;7:095009.

[101] Guardia L, Fernández-Merino MJ, Paredes JI, Solís-Fernández P, Villar-Rodil S, Martínez-Alonso A, et al. High-throughput production of pristine graphene in an aqueous dispersion assisted by non-ionic surfactants. Carbon 2011;49:1653-62.

[102] Mustafa Lotya, Yenny Hernandez, Paul J. King RJS, Valeria Nicolosi LSK, Fiona M. Blighe SD, Zhiming Wang, et al. liquid phase production of Graphene by exfoliation of graphite in surfactant water. J AM CHEM SOC 2009;131:3611-20.

[103] Schlierf A, Yang H, Gebremedhn E, Treossi E, Ortolani L, Chen L, et al. Nanoscale insight into the exfoliation mechanism of graphene with organic dyes: effect of charge, dipole and molecular structure. Nanoscale 2013;5:4205-16.

[104] Englert JM, Röhrl J, Schmidt CD, Graupner R, Hundhausen M, Hauke F, et al. Soluble Graphene: Generation of Aqueous Graphene Solutions Aided by a Perylenebisimide-Based Bolaamphiphile. Advanced materials 2009;21:4265-9.

[105] Parviz D, Das S, Ahmed HST, Irin F, Bhattacharia S, Green MJ. Dispersions of Non-Covalently functionlized graphene with minimal stabilizer. Acs Nano 2012;6:8857–67.

[106] Cao M, Fu A, Wang Z, Liu J, Kong N, Zong X, et al. Electrochemical and Theoretical Study of π–π Stacking Interactions between Graphitic Surfaces and Pyrene Derivatives. The Journal of Physical Chemistry C 2014;118:2650-9.

[107] Mateos R, Vera S, Valiente M, Diez-Pascual AM, San Andres MP. Comparison of Anionic, Cationic and Nonionic Surfactants as Dispersing Agents for Graphene Based on the Fluorescence of Riboflavin. Nanomaterials 2017;7.

[108] Nazari B, Ranjbar Z, Hashjin RnR, Rezvani Moghaddam A, Momen G, Ranjbar B. Dispersing graphene in aqueous media: Investigating the effect of

different surfactants. Colloids and Surfaces A: Physicochemical and Engineering Aspects 2019;582:123870.

[109] Poorsargol M, Alimohammadian M, Sohrabi B, Dehestani M. Dispersion of graphene using surfactant mixtures: Experimental and molecular dynamics simulation studies. Applied Surface Science 2019;464:440-50.

[110] Bourlinos AB, Georgakilas V, Zboril R, Steriotis TA, Stubos AK, Trapalis C. Aqueous-phase exfoliation of graphite in the presence of polyvinylpyrrolidone for the production of water-soluble graphenes. Solid State Communications 2009;149:2172-6.

[111] Zheng X, Xu Q, Li J, Li L, Wei J. High-throughput, direct exfoliation of graphite to graphene via a cooperation of supercritical CO2 and pyrene-polymers. RSC Advances 2012;2:10632.

[112] Liu Z, Liu J, Cui L, Wang R, Luo X, Barrow CJ, et al. Preparation of graphene/polymer composites by direct exfoliation of graphite in functionalised block copolymer matrix. Carbon 2013;51:148-55.

[113] Liu J, Tao L, Yang W, Li D, Boyer C, Wuhrer R, et al. Synthesis, characterization, and multilayer assembly of pH sensitive graphene-polymer nanocomposites. Langmuir : the ACS journal of surfaces and colloids 2010;26:10068-75.

[114] Li Y, Sun J, Wang J, Qin C, Dai L. Preparation of well-dispersed reduced graphene oxide and its mechanical reinforcement in polyvinyl alcohol fibre. Polymer International 2016;65:1054-62.

[115] Wang X, Liu X, Yuan H, Liu H, Liu C, Li T, et al. Non-covalently functionalized graphene strengthened poly(vinyl alcohol). Materials & Design 2018;139:372-9.

[116] Lee DY, Khatun Z, Lee J, Lee Y, In I. Blood Compatible GrapheneHeparin Conjugate through Noncovalent Chemistry. Biomacromolecules 2011;12:336–41.

[117] Dakhara SL, Anajwala CC. Polyelectrolyte complex: A pharmaceutical review. Systematic Reviews in Pharmacy 2010;1.

[118] Xie AF, Granick SJM. Local electrostatics within a polyelectrolyte multilayer with embedded weak polyelectrolyte. 2002;35:1805-13.

[119] Glinel K, Moussa A, Jonas AM, Laschewsky AJL. Influence of polyelectrolyte charge density on the formation of multilayers of strong polyelectrolytes at low ionic strength. 2002;18:1408-12.

[120] Schlenoff JB, Ly H, Li MJJotACS. Charge and mass balance in polyelectrolyte multilayers. 1998;120:7626-34.

[121] Meka VS, Sing MKG, Pichika MR, Nali SR, Kolapalli VRM, Kesharwani P. A comprehensive review on polyelectrolyte complexes. Drug discovery today 2017;22:1697-706.

[122] Kujawa P, Audibert-Hayet A, Selb J, Candau FJM. Effect of ionic strength on the rheological properties of multisticker associative polyelectrolytes. 2006;39:384-92.

[123] Solis FJ, Cruz MOdl. Collapse of flexible polyelectrolytes in multivalent salt solutions. The Journal of Chemical Physics 2000;112.

[124] Longo GS, Olvera de La Cruz M, Szleifer IJM. Molecular theory of weak polyelectrolyte gels: the role of pH and salt concentration. 2011;44:147-58.

[125] Welsch N, Wittemann A. Enhanced Activity of Enzymes Immobilized in Thermoresponsive Core-Shell Microgels. J Phys Chem B 2009;113:16039-45.

[126] Chen K, Wang S, Guo X. Confinement effect on the aqueous behaviors of free poly(acrylic acid) and poly(acrylic acid) grafted on a nanoparticle surface. Colloid and Polymer Science 2019;297:1223-31.

[127] Han J, Kim H, Kim DY, Jo SM, Jang S-Y. Water-Soluble Polyelectrolyte-Grafted Multiwalled Carbon Nanotube Thin Films for Efficient Counter Electrode of Dye-Sensitized Solar Cells. Acs Nano, 4(6), 3503-3509 2000;4:3503-9.

[128] Moya SE, Ilie A, Bendall JS, Hernandez-Lopez JL, Ruiz-García J, Huck WTS. Assembly of Polyelectrolytes on CNTs by Van der Waals Interactions and Fabrication of LBL Polyelectrolyte/CNT Composites. Macromolecular Chemistry and Physics 2007;208:603-8.

[129] Manzetti S, Gabriel J-CP. Methods for dispersing carbon nanotubes for nanotechnology applications: liquid nanocrystals, suspensions, polyelectrolytes, colloids and organization control. International Nano Letters 2019;9:31-49.

[130] Zhao X, Xu Z, Xie Y, Zheng B, Kou L, Gao C. Polyelectrolyte-stabilized graphene oxide liquid crystals against salt, pH, and serum. Langmuir : the ACS journal of surfaces and colloids 2014;30:3715-22.

[131] Luo J, Chen Y, Ma Q, Liu R, Liu X. Layer-by-layer self-assembled hybrid multilayer films based on poly(sodium 4-styrenesulfonate) stabilized graphene with polyaniline and their electrochemical sensing properties. RSC Advances 2013;3:17866-73.

[132] Li X, Umar A, Chen Z, Tian T, Wang S, Wang Y. Supramolecular fabrication of polyelectrolyte-modified reduced graphene oxide for NO2 sensing applications. Ceramics International 2015;41:12130-6.

[133] Stankovich S, Piner RD, Chen X, Wu N, Nguyen ST, Ruoff RS. Stable aqueous dispersions of graphitic nanoplatelets via the reduction of exfoliated graphite oxide in the presence of poly(sodium 4-styrenesulfonate). J Mater Chem 2006;16:155-8.

[134] Griffith A, Notley SM. pH dependent stability of aqueous suspensions of graphene with adsorbed weakly ionisable cationic polyelectrolyte. Journal of colloid and interface science 2012;369:210-5.

[135] Sham AY, Notley SM. Graphene-polyelectrolyte multilayer film formation driven by hydrogen bonding. Journal of colloid and interface science 2015;456:32-41.

[136] Fang M, Long J, Zhao W, Wang L, Chen G. pH-Responsive chitosan-mediated graphene dispersions. Langmuir : the ACS journal of surfaces and colloids 2010;26:16771-4.

[137] Cai X, Lin M, Tan S, Mai W, Zhang Y, Liang Z, et al. The use of polyethyleneimine-modified reduced graphene oxide as a substrate for silver nanoparticles to produce a material with lower cytotoxicity and long-term antibacterial activity. Carbon 2012;50:3407-15.

[138] Peng D, Zhang J, Qin D, Chen J, Shan D, Lu X. An electrochemical sensor based on polyelectrolyte-functionalized graphene for detection of 4-nitrophenol. Journal of Electroanalytical Chemistry 2014;734:1-6.

[139] Priya T, Dhanalakshmi N, Thennarasu S, Thinakaran N. Ultra sensitive detection of Cd (II) using reduced graphene oxide/carboxymethyl cellulose/glutathione modified electrode. Carbohydrate polymers 2018;197:366-74.

[140] Ma J, Cai P, Qi W, Kong D, Wang H. The layer-by-layer assembly of polyelectrolyte functionalized graphene sheets: A potential tool for biosensing. Colloids and Surfaces A: Physicochemical and Engineering Aspects 2013;426:6-11.

[141] Shen J, Hu Y, Li C, Qin C, Shi M, Ye M. Layer-by-Layer Self-Assembly of Graphene Nanoplatelets. Langmuir : the ACS journal of surfaces and colloids 2009;25:6122-8.

[142] Li X, Zhong A, Wei S, Luo X, Liang Y, Zhu Q. Polyelectrolyte functionalized gold nanoparticles-reduced graphene oxide nanohybrid for electrochemical determination of aminophenol isomers. Electrochimica Acta 2015;164:203-10.

[143] Yan H, Wu Y, Luo X, Jiao L, Zhu C, Du D. Tuning polyelectrolyte-graphene interaction for enhanced electrochemical nonenzymatic hydrogen peroxide sensing. Analytica chimica acta 2019;1049:98-104.

[144] Tong Z, Xu M, Li Q, Liu C, Wang Y, Sha J. Polyelectrolyte-functionalized reduced graphene oxide wrapped helical POMOF nanocomposites for bioenzyme-free colorimetric biosensing. Talanta 2020;220:121373.

[145] Guo Y, Sun X, Liu Y, Wang W, Qiu H, Gao J. One pot preparation of reduced graphene oxide (RGO) or Au (Ag) nanoparticle-RGO hybrids using chitosan as a

reducing and stabilizing agent and their use in methanol electrooxidation. Carbon 2012;50:2513-23.

[146] Viinikanoja A, Kauppila J, Damlin P, Mäkilä E, Leiro J, Ääritalo T, et al. Interactions between graphene sheets and ionic molecules used for the shear-assisted exfoliation of natural graphite. Carbon 2014;68:195-209.

[147] Lu J, Do I, Fukushima H, Lee I, Drzal LT. Stable Aqueous Suspension and Self-Assembly of Graphite Nanoplatelets Coated with Various Polyelectrolytes. Journal of Nanomaterials 2010;2010:1-11.

[148] Das BP, Tsianou M. From polyelectrolyte complexes to polyelectrolyte multilayer: Electrostatic assembly, nanostructure, dynamics, and functional properties. Advances in colloid and interface science 2017;244:71-89.

[149] Schaaf P, Schlenoff JB. Saloplastics: processing compact polyelectrolyte complexes. Advanced materials 2015;27:2420-32.

[150] Schlenoff JB, Rmaile AH, Bucur CBJJotACS. Hydration contributions to association in polyelectrolyte multilayers and complexes: Visualizing hydrophobicity. 2008;130:13589-97.

[151] Wang Q, Schlenoff JBJM. The polyelectrolyte complex/coacervate continuum. 2014;47:3108-16.

[152] Shamoun RF, Reisch A, Schlenoff JB. Extruded Saloplastic Polyelectrolyte Complexes. Advanced Functional Materials 2012;22:1923-31.

[153] Gucht Jvd, Spruijt E, Lemmers M, Stuart MAC. Polyelectrolyte complexes: Bulk phases and colloidal systems. Journal of colloid and interface science 2011;361:407-22.

[154] Schönhoff M. Self-assembled polyelectrolyte multilayers. Current Opinion in Colloid & Interface Science 2003;8:86-95.

[155] Starchenko V, Muller M, Lebovka N. Sizing of PDADMAC/PSS complex aggregates by polyelectrolyte and salt concentration and PSS molecular weight. The journal of physical chemistry B 2012;116:14961-7.

[156] M. RA, E. JN, J. DPJ. Polyelectrolyte complex coacervates: Recent developments and new frontiers. Annu Rev Condens Matter Phys 2021;12:155-76.

[157] Liu X, Haddou M, Grillo I, Mana Z, Chapel JP, Schatz C. Early stage kinetics of polyelectrolyte complex coacervation monitored through stopped-flow light scattering. Soft Matter 2016;12:9030-8.

[158] Fares HM, Wang Q, Yang M, Schlenoff JB. Swelling and Inflation in Polyelectrolyte Complexes. Macromolecules 2018;52:610-9.

[159] Rumyantsev AM, Kramarenko EY, Borisov OVJM. Microphase separation in complex coacervate due to incompatibility between polyanion and polycation. 2018;51:6587-601.

[160] Porcel CH, Schlenoff JB. Compact Polyelectrolyte Complexes: “Saloplastic” Candidates for Biomaterials. Biomacromolecules 2009;10:2968-75.

[161] Fu J, Fares HM, Schlenof JB. Ion-Pairing Strength in Polyelectrolyte Complexes. Macromolecules 2017;50:1066-74.

[162] B AK, Lindhoud S, Vos WMd. Hot-pressed polyelectrolyte complexes as novel alkaline stablemonovalent-ion selective anion exchange membranes. Journal of colloid and interface science 2021;593:11-20.

[163] Costa RR, Costa AMS, Caridade SG, Mano JF. Compact Saloplastic Membranes of Natural Polysaccharides for Soft Tissue Engineering. Chemistry of Materials 2015;27:7490-502.

[164] Zhang H, Wang C, Zhu G, Zacharia NS. Self-Healing of Bulk Polyelectrolyte Complex Material as a Function of pH and Salt. Applied Materials & Interfaces 2016;8:26258-65.

[165] Vladimir A. Izumrudov, Binur Kh. Mussabayeva, Murzagulova KB. Polyelectrolyte multilayers preparation and applications. Russ Chem Rev 2018;87:192-200.

[166] Bütergerds D, Kateloe C, Cramer C, Schönhoff M. Influence of the degree of ionization on the growth mechanism of poly(diallyldimethylammonium)/poly(acrylic acid) multilayers. Journal of Polymer Science Part B: Polymer Physics 2017;55:425-34.

[167] Boulmedais F, Ball V, Schwinte P, Frisch B, Schaaf P, Voegel J. Buildup of exponentially growing multilayer polypeptide films with internal secondary structure. Langmuir : the ACS journal of surfaces and colloids 2003;19:440-5.

[168] Bieker P, Schönhoff M. Linear and Exponential Growth Regimes of Multilayers of Weak Polyelectrolytes in Dependence on pH. Macromolecules 2010;43:5052-9.

[169] Petrila LM, Bucatariu F, Mihai M, Teodosiu C. Polyelectrolyte Multilayers: An Overview on Fabrication, Properties, and Biomedical and Environmental Applications. Materials 2021;14.

[170] Wang Q, Schlenoff JB. The Polyelectrolyte Complex/Coacervate Continuum. Macromolecules 2014;47:3108-16.

[171] Lalwani SM, Eneh CI, Lutkenhaus JL. Emerging trends in the dynamics of polyelectrolyte complexes. Physical Chemistry Chemical Physics 2020;22:24157-77.

[172] Li L, Srivastava S, Andreev M, Marciel AB, de Pablo JJ, Tirrell MV. Phase Behavior and Salt Partitioning in Polyelectrolyte Complex Coacervates. Macromolecules 2018;51:2988-95.

[173] Zhang Y, Batys P, O'Neal JT, Li F, Sammalkorpi M, Lutkenhaus JL. Molecular Origin of the Glass Transition in Polyelectrolyte Assemblies. ACS Central Science 2018;4:638-44.

[174] Reisch A, Roger E, Phoeung T, Antheaume C, Orthlieb C, Boulmedais F, et al. On the benefits of rubbing salt in the cut: self-healing of saloplastic PAA/PAH compact polyelectrolyte complexes. Advanced materials 2014;26:2547-51.

[175] Dautzenberg H, Kriz J. Response of Polyelectrolyte Complexes to Subsequent Addition of Salts with Different Cations. Langmuir : the ACS journal of surfaces and colloids 2003;19:5204-11.

[176] Ghostine RA, Shamoun RF, Schlenoff JB. Doping and Diffusion in an Extruded Saloplastic Polyelectrolyte Complex. Macromolecules 2013;46:4089-94.

[177] Shiratori SS, Rubner MF. pH dependent thickness behavior of sequentially adsorbed layers of PAA PAH. Macromolecules 2000;33:4213-9.

[178] Jha P, Desai P, Li J, Larson R. pH and Salt Effects on the Associative Phase Separation of Oppositely Charged Polyelectrolytes. Polymers 2014;6:1414-36.

[179] Rydzek G, Pakdel A, Witecka A, Awang Shri DN, Gaudière F, Nicolosi V, et al. pH-Responsive Saloplastics Based on Weak Polyelectrolytes: From Molecular Processes to Material Scale Properties. Macromolecules 2018;51:4424-34.

[180] Buchhammer H-M, Mende M, Oelmann M. Formation of mono-sized polyelectrolyte complex dispersions: effects of polymer structure, concentration and mixing conditions. Colloids and Surfaces A: Physicochemical and Engineering Aspects 2003;218:151-9.

[181] Kremer T, Kovačević D, Salopek J, Požar J. Conditions Leading to Polyelectrolyte Complex Overcharging in Solution: Complexation of Poly(acrylate) Anion with Poly(allylammonium) Cation. Macromolecules 2016;49:8672-85.

[182] Koetz J, Kosmella S. Interactions between poly(diallyldimethylammonium chloride) and poly(acrylic acid) in dependence on polymer concentration. Il Nuovo Cimento D 1994;16:865-71.

[183] Hayashi Y, Ullner M, Linse P. Oppositely charged polyelectrolytes. Complex formation and effects of chain asymmetry. The Journal of Physical Chemistry B 2004;108:15266-77.

[184] Naveed K-U-R, Wang L, Yu H, Summe Ullah R, Nazir A, Fahad S, et al. Synthesis of spin-labelled poly(acrylic acid)s and their segmental motion study. Molecular Physics 2019;118:e1685690.

[185] Liu X, Chapel JP, Schatz C. Structure, thermodynamic and kinetic signatures of a synthetic polyelectrolyte coacervating system. Advances in colloid and interface science 2017;239:178-86.

[186] Zhang Y, Yildirim E, Antila HS, Sammalkorpi M, Valenzuela LD, Lutkenhaus JL. The influence of ionic strength and mixing ratio on the colloidal stability of PDAC/PSS polyelectrolyte complexes. Soft Matter 2015;11:7392-401.

[187] Reisch A, Tirado P, Roger E, Boulmedais F, Collin D, Voegel J-C, et al. Compact Saloplastic Poly(Acrylic Acid)/Poly(Allylamine) Complexes: Kinetic Control Over Composition, Microstructure, and Mechanical Properties. Advanced Functional Materials 2013;23:673-82.

[188] Vitorazi L, Ould-Moussa N, Sekar S, Fresnais J, Loh W, Chapel JP, et al. Evidence of a two-step process and pathway dependency in the thermodynamics of poly(diallyldimethylammonium chloride)/poly(sodium acrylate) complexation. Soft Matter 2014;10:9496-505.

[189] Izumrudov VA, Mussabayeva BK, Murzagulova KB. Polyelectrolyte multilayers: preparation and applications. Russian Chemical Reviews 2018;87:192-200.

[190] Jiang B, Barnett JB, Li B. Advances in polyelectrolyte multilayer nanofilms as tunable drug delivery systems. Nanotechnology, science and applications 2009;2:21-7.

[191] Jiang B, Li B. Tunable drug loading and release from polypeptide multilayer nanofilms. International journal of nanomedicine 2009;4:37-53.

[192] Addison T, Cayre OJ, Biggs S, Armes SP, York D. Incorporation of Block Copolymer Micelles into Multilayer Films for. Langmuir : the ACS journal of surfaces and colloids 2008;24:13328–33.

[193] Kim B-S, Park SW, Hammond PT. Hydrogen-Bonding Layer-by-Layer-Assembled Biodegradable Polymeric Micelles as Drug Delivery Vehicles from Surfaces. ACS Nano 2008;2:386–92.

[194] Schmidt DJ, Moskowitz JS, Hammond PT. Electrically Triggered Release of a Small Molecule Drug from a Polyelectrolyte Multilayer Coating. Chemistry of materials : a publication of the American Chemical Society 2010;22:6416-25.

[195] Chen X-C, Ren K-F, Zhang J-H, Li D-D, Zhao E, Zhao ZJ, et al. Humidity-Triggered Self-Healing of Microporous Polyelectrolyte Multilayer Coatings for Hydrophobic Drug Delivery. Advanced Functional Materials 2015;25:7470-7.

[196] Gao S, Holkar A, Srivastava S. Protein-Polyelectrolyte Complexes and Micellar Assemblies. Polymers (Basel) 2019;11.

[197] Straeten Av, Bratek-Skicki A, Germain L, D'Haese C, Eloy P, Fustin C-A, et al. Protein–polyelectrolyte complexes to improve the biological activity of proteins in laye. Nanoscale 2017;9:17186-92.

[198] Vander Straeten A, Lefevre D, Demoustier-Champagne S, Dupont-Gillain C. Protein-based polyelectrolyte multilayers. Advances in colloid and interface science 2020;280:102161.

[199] Rahim MA, Islam MS, Bae TS, Choi WS, Noh YY, Lee HJ. Metal ion-enriched polyelectrolyte complexes and their utilization in multilayer assembly and catalytic nanocomposite films. Langmuir : the ACS journal of surfaces and colloids 2012;28:8486-95.

[200] Dai J, Bruening ML. Catalytic nanoparticles formed by reduction of metal ions in multilayered polyelectrolyte films. Nano letters 2002;2:497-501.

[201] Demchenko V, Riabov S, Kobylinskyi S, Goncharenko L, Rybalchenko N, Kruk A, et al. Effect of the type of reducing agents of silver ions in interpolyelectrolyte-metal complexes on the structure, morphology and properties of silver-containing nanocomposites. Scientific reports 2020;10:7126.

[202] Pergushov DV, Zezin AA, Zezin AB, Müller AHE. Advanced Functional Structures Based on Interpolyelectrolyte Complexes. 2013;255:173-225.

[203] Fenoy GE, Maza E, Zelaya E, Marmisollé WA, OmarAzzaroni. Layer-by-Layer assemblies of highly connected polyelectrolyte capped-Pt nanoparticles for electrocatalysis of hydrogen evolution reaction. Applied Surface Science 2017;416:24-32.

[204] Ding N, Zhao H, Peng W, He Y, Zhou Y, Yuan L, et al. A simple colorimetric sensor based on anti-aggregation of gold nanoparticles for Hg2+ detection. Colloids and Surfaces A: Physicochemical and Engineering Aspects 2012;395:161-7.

[205] Klimov DI, Zezina EA, Lipik VC, Abramchuk SS, Yaroslavov AA, Feldman VI, et al. Radiation-induced preparation of metal nanostructures in coatings of interpolyelectrolyte complexes. Radiation Physics and Chemistry 2019;162:23-30.

[206] Hu JJ, Hsieh YH, Jan JS. Polyelectrolyte complex-silica hybrid colloidal particles decorated with different polyelectrolytes. Journal of colloid and interface science 2015;438:94-101.

[207] Zhao Q, Qian J, Zhu C, An Q, Xu T, Zheng Q, et al. A novel method for fabricating polyelectrolyte complex/inorganic nanohybrid membranes with high isopropanol dehydration performance. Journal of Membrane Science 2009;345:233-41.

[208] Shaikh SMR, Nasser MS, Hussein I, Benamor A, Onaizi SA, Qiblawey H. Influence of polyelectrolytes and other polymer complexes on the flocculation and rheological behaviors of clay minerals: A comprehensive review. Separation and Purification Technology 2017;187:137-61.

[209] Costa MPMd, Ferreira ILdM, Cruz MTdM. New polyelectrolyte complex from pectin/chitosan and montmorillonite clay. Carbohydrate polymers 2016;146:123-30.

[210] Chiang HC, Kolibaba TJ, Eberle B, Grunlan JC. Super Gas Barrier of a Polyelectrolyte/Clay Coacervate Thin Film. Macromolecular rapid communications 2021;42:e2000540.

[211] Popov V. Carbon nanotubes: properties and application. Materials Science and Engineering: R: Reports 2004;43:61-102.

[212] Hanna Paloniemi, Lukkarinen M, a¨ritalo TA, Areva S, Leiro J, Heinonen M, et al. Layer-by-layer electrostatic self-assembly of single-wall carbon nanotube polyelectrolytes. Langmuir : the ACS journal of surfaces and colloids 2006;22:74-83.

[213] Kim B, Park H, Sigmund WM. Electrostatic interactions between shortened multiwall carbon nanotubes and polyelectrolytes Langmuir : the ACS journal of surfaces and colloids 2003;19:2525-7.

[214] Meining Zhang, Yiming Yan, Kuanping Gong, Lanqun Mao, Zhixin Guo, Chen Y. Electrostatic layer-by-layer assembled carbon nanotube multilayer film and its electrocatalytic activity for O2 reduction. Langmuir : the ACS journal of surfaces and colloids 2004;20:8781-5.

[215] Zhao Q, Qian J, Zhu M, An Q. Facile fabrication of polyelectrolyte complex/carbon nanotube nanocomposites with improved mechanical properties and ultra-high separation performance. Journal of Materials Chemistry 2009;19:8732.

[216] Artyukhin AB, Bakajin O, Stroeve P, Noy A. Layer-by-layer electrostatic self-assembly of polyelectrolyte nanoshells on individual carbon nanotube templates. Langmuir : the ACS journal of surfaces and colloids 2004;20:1442-8.

[217] Naixin Wang SJ, Guojun Zhang, Jie Li, Lin Wang. Self-assembly of graphene oxide and polyelectrolyte complex nanohybrid membranes for nanofiltration and pervaporation. Chemical Engineering Journal 2012;213:318-29.

[218] Deshmukh K, Ahamed MB, Sadasivuni KK, Ponnamma D, AlMaadeed MA-A, Khadheer Pasha SK, et al. Graphene oxide reinforced poly (4-styrenesulfonic acid)/polyvinyl alcohol blend composites with enhanced dielectric properties for portable and flexible electronics. Materials Chemistry and Physics 2017;186:188-201.

[219] Wu J-K, Ye C-C, Zhang W-H, Wang N-X, Lee K-R, An Q-F. Construction of well-arranged graphene oxide/polyelectrolyte complex nanoparticles membranes for pervaporation ethylene glycol dehydration. Journal of Membrane Science 2019;577:104-12.

[220] Yipin Duan CW, Mengmeng Zhao, Bryan D Vogt, Nicole S Zacharia. Mechanical properties of bulk graphene oxide/poly(acrylic acid)/poly(ethylenimine) ternary polyelectrolyte complex. Soft matter 2018;14:4396-403.

[221] Kim H, Kim WJ. Photothermally controlled gene delivery by reduced graphene oxide-polyethylenimine nanocomposite. Small 2014;10:117-26.

[222] Li Y, Deng C, Yang M. Facilely prepared composites of polyelectrolytes and graphene as the sensing materials for the detection of very low humidity. Sensors and Actuators B: Chemical 2014;194:51-8.

[223] Hui L, Auletta JT, Huang Z, Chen X, Xia F, Yang S, et al. Surface Disinfection Enabled by a Layer-by-Layer Thin Film of Polyelectrolyte-Stabilized Reduced Graphene Oxide upon Solar Near-Infrared Irradiation. ACS applied materials & interfaces 2015;7:10511-7.

[224] Liu H, Liu C, Peng S, Pan B, Lu C. Effect of polyethyleneimine modified graphene on the mechanical and water vapor barrier properties of methyl cellulose composite films. Carbohydrate polymers 2018;182:52-60.

[225] Ma J, Wang X, Liu Y, Wu T, Liu Y, Guo Y, et al. Reduction of graphene oxide with l-lysine to prepare reduced graphene oxide stabilized with polysaccharide polyelectrolyte. J Mater Chem A 2013;1:2192-201.

[226] Thakur S, Karak N. Alternative methods and nature-based reagents for the reduction of graphene oxide: A review. Carbon 2015;94:224-42.

[227] Miyazaki CM, Adriano AM, Rubira RJG, Constantino CJL, Ferreira M. Combining electrochemically reduced graphene oxide and Layer-by-Layer films of magnetite nanoparticles for carbofuran detection. Journal of Environmental Chemical Engineering 2020;8:104294.

[228] Sudhakar K, Suneetha M, Rao KM, Han SS. Antibacterial reduced graphene oxide reinforces polyelectrolyte hydrogels with polysaccharides via a green method. Colloids and Surfaces A: Physicochemical and Engineering Aspects 2021;628:127340.

[229] Xiang Z, Zhang L, Li Y, Yuan T, Zhang W, Sun J. Reduced Graphene Oxide-Reinforced Polymeric Films with Excellent Mechanical Robustness and Rapid and Highly Efficient Healing Properties. ACS Nano 2017;11:7134-41.

[230] Li B, Wu C, Han Y, Ma X, Luo Z. Preparation of Poly(Acrylic Acid) Grafted Reduced Graphene Oxide/Polyacrylamide Composite Hydrogels with Good Electronic and Mechanical Properties by in-situ Polymerization. Journal of Macromolecular Science, Part B 2021;60:589-602.

[231] Wu J-K, Ye C-C, Liu T, An Q-F, Song Y-H, Lee K-R, et al. Synergistic effects of CNT and GO on enhancing mechanical properties and separation performance of polyelectrolyte complex membranes. Materials & Design 2017;119:38-46.

[232] Kumar A, Rao KM, Han SS. Mechanically viscoelastic nanoreinforced hybrid hydrogels composed of polyacrylamide, sodium carboxymethylcellulose, graphene oxide, and cellulose nanocrystals. Carbohydrate polymers 2018;193:228-38.

[233] Li X, Zhang Y, Wu Y, Duan Y, Luan X, Zhang Q, et al. Combined Photothermal and Surface-Enhanced Raman Spectroscopy Effect from Spiky Noble

Metal Nanoparticles Wrapped within Graphene-Polymer Layers: Using Layer-by-layer Modified Reduced Graphene Oxide as Reactive Precursors. ACS applied materials & interfaces 2015;7:19353-61.

[234] Sharma B, Shekhar S, Gautam S, Sarkar A, Jain P. Nanomechanical analysis of chemically reduced graphene oxide reinforced poly (vinyl alcohol) nanocomposite thin films. Polymer Testing 2018;70:458-66.

[235] Batys P, Kivisto S, Lalwani SM, Lutkenhaus JL, Sammalkorpi M. Comparing water-mediated hydrogen-bonding in different polyelectrolyte complexes. Soft Matter 2019;15:7823-31.

[236] Maddalena L, Benselfelt T, Gomez J, Hamedi MM, Fina A, Wagberg L, et al. Polyelectrolyte-Assisted Dispersions of Reduced Graphite Oxide Nanoplates in Water and Their Gas-Barrier Application. ACS applied materials & interfaces 2021;13:43301-13.

[237] Shalaby A, Nihtianova D, Markov P, Staneva AD, Iordanova RS, Dimitriev YB. Structural analysis of reduced graphene oxide by transmission electron microscopy. Bulgarian Chemical Communications 2015;47:291-5.

[238] Huang HH, De Silva KKH, Kumara GRA, Yoshimura M. Structural Evolution of Hydrothermally Derived Reduced Graphene Oxide. Scientific reports 2018;8:6849.

[239] Colonna S, Monticelli O, Gomez J, Saracco G, Fina A. Morphology and properties evolution upon ring-opening polymerization during extrusion of cyclic butylene terephthalate and graphene-related-materials into thermally conductive nanocomposites. European Polymer Journal 2017;89:57-66.

[240] Pošković E, Franchini F, Ferraris L, Carosio F, Actis Grande M. Rapid Characterization Method for SMC Materials for a Preliminary Selection. Applied Sciences 2021;11:12133.

[241] Liu H, Bandyopadhyay P, Kshetri T, Kim NH, Ku B-C, Moon B, et al. Layer-by-layer assembled polyelectrolyte-decorated graphene multilayer film for hydrogen gas barrier application. Composites Part B: Engineering 2017;114:339-47.

[242] Zhang S, Shao Y, Liao H, Engelhard MH, Yin G, Lin Y. Polyelectrolyte-Induced Reduction of Exfoliated Graphite Oxide: A Facile Route to Synthesis of Soluble Graphene Nanosheets. ACS Nano 2011;5:1785-91.

[243] Li L, Hsieh Y-L. Ultra-fine polyelectrolyte fibers from electrospinning of poly(acrylic acid). Polymer 2005;46:5133-9.

[244] Young T. An essay on the cohesion of fluids. Philosophical transactions of the royal society of London 1805;95:65-87.

[245] Perrozzi F, Croce S, Treossi E, Palermo V, Santucci S, Fioravanti G, et al. Reduction dependent wetting properties of graphene oxide. Carbon 2014;77:473-80.

[246] Dickhaus BN, Priefer R. Determination of polyelectrolyte pKa values using surface-to-air tension measurements. Colloids and Surfaces A: Physicochemical and Engineering Aspects 2016;488:15-9.

[247] Vasilieva E, Ibragimova A, Lukashenko S, Konovalov A, Zakharova L. Mixed self-assembly of polyacrylic acid and oppositely charged gemini surfactants differing in the structure of head group. Fluid Phase Equilibria 2014;376:172-80.

[248] Griffiths PC, Paul A, Fallis IA, Wellappili C, Murphy DM, Jenkins R, et al. Derivatizing weak polyelectrolytes--solution properties, self-aggregation, and association with anionic surfaces of hydrophobically modified poly(ethylene imine). Journal of colloid and interface science 2007;314:460-9.

[249] Bellettini IC, Nandi LG, Eising R, Domingos JB, Machado VG, Minatti E. Properties of aqueous solutions of hydrophobically modified polyethylene imines in the absence and presence of sodium dodecylsulfate. Journal of colloid and interface science 2012;370:94-101.

[250] Samuel Guillot, Michel Delsanti, De´sert S, Langevin D. Surfactant-Induced Collapse of Polymer Chains and Monodisperse Growth of Aggregates near the Precipitation Boundary in Carboxymethylcellulose−DTAB Aqueous Solutions. Langmuir : the ACS journal of surfaces and colloids 2003;19:230-7.

[251] Lee B-B, Chan E-S, Ravindra P, Khan TA. Surface tension of viscous biopolymer solutions measured using the du Nouy ring method and the drop weight methods. Polymer Bulletin 2012;69:471-89.

[252] Weber F E TSA, Stauffer K R. Functional characteristics of mustard mucilage. Journal of Food Science 1974;39:461-6.

[253] OKUBO T. Surface tension of synthetic polyelectrolyte solutions at the air-water interface. Journal of colloid and interface science 1988;125:386-98.

[254] Cai M, Thorpe D, Adamson DH, Schniepp HC. Methods of graphite exfoliation. Journal of Materials Chemistry 2012;22:24992.

[255] Chen D, Li L, Guo L. An environment-friendly preparation of reduced graphene oxide nanosheets via amino acid. Nanotechnology 2011;22:325601.

[256] Zhao G, Zhu H. Cation-pi Interactions in Graphene-Containing Systems for Water Treatment and Beyond. Advanced materials 2020;32:e1905756.

[257] Zhang C, Gao J, Hankett J, Varanasi P, Kerobo CO, Zhao S, et al. Interfacial Structure and Interfacial Tension in Model Carbon Fiber-Reinforced Polymers. Langmuir : the ACS journal of surfaces and colloids 2021;37:5311-20.

[258] Park IH, Choi E-J. Characterization of branched polyethyleneimine by laser light scattering and viscometry. Polymer 1996;37:313-9.

[259] Park WB, Bandyopadhyay P, Nguyen TT, Kuila T, Kim NH, Lee JH. Effect of high molecular weight polyethyleneimine functionalized graphene oxide coated polyethylene terephthalate film on the hydrogen gas barrier properties. Composites Part B: Engineering 2016;106:316-23.

[260] Shtein M, Pri-Bar I, Varenik M, Regev O. Characterization of graphene-nanoplatelets structure via thermogravimetry. Analytical chemistry 2015;87:4076-80.

[261] Zhong M, Yi-Tao Liu, Xu-Ming Xie. Self-healable, super tough graphene oxide/poly(acrylic acid) nanocomposite hydrogels facilitated by dual cross-linking effects through dynamic ionic interactions. Journal of Materials Chemistry B 2015;3:4001-8.

[262] Layek RK, Kundu A, Nandi AK. High-Performance Nanocomposites of Sodium Carboxymethylcellulose and Graphene Oxide. Macromolecular Materials and Engineering 2013;298:1166-75.

[263] Wang J, Feng M, Zhan H. Preparation, characterization, and nonlinear optical properties of graphene oxide-carboxymethyl cellulose composite films. Optics & Laser Technology 2014;57:84-9.

[264] Govindaiah P, Kim YS, Hong JK, Kim JH, Cheong IW. One-pot synthesis of grafted brush copolymers via a chain-growth radical/oxidative dual polymerization system. RSC Advances 2015;5:93717-23.

[265] Lotya M, Rakovich A, Donegan JF, Coleman JN. Measuring the lateral size of liquid-exfoliated nanosheets with dynamic light scattering. Nanotechnology 2013;24:265703.

[266] Eaton P, Quaresma P, Soares C, Neves C, de Almeida MP, Pereira E, et al. A direct comparison of experimental methods to measure dimensions of synthetic nanoparticles. Ultramicroscopy 2017;182:179-90.

[267] Amaro-Gahete J, Benitez A, Otero R, Esquivel D, Jimenez-Sanchidrian C, Morales J, et al. A Comparative Study of Particle Size Distribution of Graphene Nanosheets Synthesized by an Ultrasound-Assisted Method. Nanomaterials (Basel) 2019;9.

[268] G€oldel A, Marmur A, Kasaliwal GR, P€otschke P, Heinrich G. Shape-Dependent Localization of Carbon Nanotubes and Carbon Black in an Immiscible Polymer Blend during Melt Mixing. Macromolecules 2011;44:6094-102.

[269] Ferrari ACaR, J. Interpretation of Raman spectra of disordered and amorphous carbon. Phys Rev B 2000;61:14095--107.

[270] Ferrari AC, Basko DM. Raman spectroscopy as a versatile tool for studying the properties of graphene. Nature nanotechnology 2013;8:235-46.

[271] Muzyka R, Drewniak S, Pustelny T, Chrubasik M, Gryglewicz G. Characterization of Graphite Oxide and Reduced Graphene Oxide Obtained from Different Graphite Precursors and Oxidized by Different Methods Using Raman Spectroscopy. Materials 2018;11.

[272] Wu JB, Lin ML, Cong X, Liu HN, Tan PH. Raman spectroscopy of graphene-based materials and its applications in related devices. Chemical Society reviews 2018;47:1822-73.

[273] Chee SY, Poh HL, Chua CK, Sanek F, Sofer Z, Pumera M. Influence of parent graphite particle size on the electrochemistry of thermally reduced graphene oxide. Physical chemistry chemical physics : PCCP 2012;14:12794-9.

[274] Liu H, Kuila T, Kim NH, Ku B-C, Lee JH. In situ synthesis of the reduced graphene oxide–polyethyleneimine composite and its gas barrier properties. Journal of Materials Chemistry A 2013;1:3739.

[275] Jiang F, Zhao W, Wu Y, Wu Y, Liu G, Dong J, et al. A polyethyleneimine-grafted graphene oxide hybrid nanomaterial: Synthesis and anti-corrosion applications. Applied Surface Science 2019;479:963-73.

[276] Konkena B, Vasudevan S. Understanding Aqueous Dispersibility of Graphene Oxide and Reduced Graphene Oxide through pKa Measurements. The journal of physical chemistry letters 2012;3:867-72.

[277] Ullner M, Jönsson B, Widmark PO. Conformational properties and apparent dissociation constants of titrating polyelectrolytes: Monte Carlo simulation and scaling arguments. The Journal of Chemical Physics 1994;100:3365-6.

[278] Ong BC, Leong YK, Chen SB. Interparticle forces in spherical monodispersed silica dispersions: effects of branched polyethylenimine and molecular weight. Journal of colloid and interface science 2009;337:24-31.

[279] Marc Schneider MB, Helmuth Mohwald. Adsorption of Polyethylenimine on Graphite An Atomic Force. Macromolecules 2003;36:9510-8.

[280] C. Clasen W-MK. Determination of viscoelastic and rheo-optical material functions of water-soluble cellulose derivatives. Progress in Polymer Science 2001;26:1839-919.

[281] Lopez CG, Rogers SE, Colby RH, Graham P, Cabral JT. Structure of Sodium Carboxymethyl Cellulose Aqueous Solutions: A SANS and Rheology Study. Journal of polymer science Part B, Polymer physics 2015;53:492-501.

[282] Lee J-H, Paik U, Hackley VA, Choi Y-M. Effect of Carboxymethyl Cellulose on Aqueous Processing of Natural Graphite Negative Electrodes and their Electrochemical Performance for Lithium Batteries. Journal of The Electrochemical Society 2005;152:A1763.

[283] Liang Y, Qu C, Yang R, Qu L, Li J. Molecularly imprinted electrochemical sensor for daidzein recognition and detection based on poly(sodium 4-

styrenesulfonate) functionalized graphene. Sensors and Actuators B: Chemical 2017;251:542-50.

[284] Xue Y, Zhao H, Wu Z, Li X, He Y, Yuan Z. The comparison of different gold nanoparticles/graphene nanosheets hybrid nanocomposites in electrochemical performance and the construction of a sensitive uric acid electrochemical sensor with novel hybrid nanocomposites. Biosensors & bioelectronics 2011;29:102-8.

[285] Zhao Q, An Q-F, Liu T, Chen J-T, Chen F, Lee K-R, et al. Bio-inspired polyelectrolyte complex/graphene oxide nanocomposite membranes with enhanced tensile strength and ultra-low gas permeability. Polymer Chemistry 2013;4:4298.

[286] Huang W, Li J, Liu D, Tan S, Zhang P, Zhu L, et al. Polyelectrolyte Complex Fiber of Alginate and Poly(diallyldimethylammonium chloride): Humidity-Induced Shape Memory and Mechanical Transition. ACS Applied Polymer Materials 2020;2:2119-25.

[287] Chen Y, Yang M, Schlenoff JB. Glass Transitions in Hydrated Polyelectrolyte Complexes. Macromolecules 2021;54:3822-31.

[288] Santhiya D, Subramanian S, Natarajana KA, Malghan SG. Surface chemical studies on the competitive adsorption of poly (acrylic acid) and poly (vinyl alcohol) onto alumina. Journal of colloid and interface science 1999;216:143-53.

[289] Liew C-W, Ng HM, Numan A, Ramesh S. Poly (acrylic acid)–based hybrid inorganic–organic electrolytes membrane for electrical double layer capacitors application. Polymers 2016;8:179.

[290] Thi Hai Yen D, Pham TD, Yamashita Y, Adachi Y. Adsorption of Poly(acrylic acid) onto Negatively Charged Polystyrene Sulfate Latex Particles by Means of Particle Tracking of Brownian Motion, Electrophoretic Mobility and Fourier Transform Infrared Spectroscopy. Polymer Science, Series A 2020;62:321-9.

[291] Kirwan LJ, Fawell PD, Bronswijk Wv. In Situ FTIR-ATR Examination of Poly(acrylic acid) Adsorbed onto Hematite at Low pH. Langmuir : the ACS journal of surfaces and colloids 2003;19:5802-7.

[292] H. Hu JS, Garcia-Alejandre J, Castaiio VM. Fourier transform infrared spectroscopy studies of the reaction between polyacrylic acid and metal oxides. Materials Letters 1991;12:281-5.

[293] M'Bareck CO, Nguyen QT, Metayer M, Saiter JM, Garda MR. Poly (acrylic acid) and poly (sodium styrenesulfonate) compatibility by Fourier transform infrared and differential scanning calorimetry. Polymer 2004;45:4181-7.

[294] Cukrowicz S, Sitarz M, Kornaus K, Kaczmarska K, Bobrowski A, Gubernat A, et al. Organobentonites Modified with Poly(Acrylic Acid) and Its Sodium Salt for Foundry Applications. Materials 2021;14.

[295] Zhang L, Yi D, Hao J. Poly (diallyldimethylammonium) and polyphosphate polyelectrolyte complexes as an all‐in‐one flame retardant for polypropylene. Polymers for Advanced Technologies 2019;31:260-72.

[296] Jareansin S, Sukaam P, Kusuktham B. Preparation and characterization of modified cotton fabrics with responsive pH. Polymer Bulletin 2018;76:4507-20.

[297] Eneh CI, Bolen MJ, Suarez-Martinez PC, Bachmann AL, Zimudzi TJ, Hickner MA, et al. Fourier transform infrared spectroscopy investigation of water microenvironments in polyelectrolyte multilayers at varying temperatures. Soft Matter 2020;16:2291-300.

[298] Radhakrishna M, Basu K, Liu Y, Shamsi R, Perry SL, Sing CE. Molecular Connectivity and Correlation Effects on Polymer Coacervation. Macromolecules 2017;50:3030-7.

[299] Francis S, Varshney L, Sabharwal S. Thermal degradation behavior of radiation synthesized polydiallyldimethylammonium chloride. European Polymer Journal 2007;43:2525-31.

[300] McNeill IC, Sadeghi SMT. Thermal stability and degradation mechanisms of poly (acrylic acid) and its salts: Part 2—Sodium and potassium salts. Polymer degradation and stability 1990;30:213-30.

[301] Jaber JA, Schlenoff JB. Mechanical properties of reversibly cross-linked ultrathin polyelectrolyte complexes. J Am Chem Soc 2006;128:2940-7.

[302] Kim J, Kim J, Song S, Zhang S, Cha J, Kim K, et al. Strength dependence of epoxy composites on the average filler size of non-oxidized graphene flake. Carbon 2017;113:379-86.

[303] Gong L, Young RJ, Kinloch IA, Riaz I, Jalil R, Novoselov KS. Optimizing the reinforcement of polymer-based nanocomposites by graphene. ACS nano 2012;6:2086-95.

[304] Li Z, Young RJ, Wilson NR, Kinloch IA, Vallés C, Li Z. Effect of the orientation of graphene-based nanoplatelets upon the Young's modulus of nanocomposites. Composites Science and Technology 2016;123:125-33.

[305] Sun X, Huang C, Wang L, Liang L, Cheng Y, Fei W, et al. Recent Progress in Graphene/Polymer Nanocomposites. Advanced materials 2020;33:2001105.

[306] Liu S, Liu J, Xu Z, Liu Y, Li P, Guo F, et al. Artificial Bicontinuous Laminate Synergistically Reinforces and Toughens Dilute Graphene Composites. ACS Nano 2018;12:11236-43.

[307] Maity N, Mandal A, Nandi AK. Synergistic interfacial effect of polymer stabilized graphene via non-covalent functionalization in poly(vinylidene fluoride) matrix yielding superior mechanical and electronic properties. Polymer 2016;88:79-93.

[308] Alasvand Zarasvand K, Golestanian H. Investigating the effects of number and distribution of GNP layers on graphene reinforced polymer properties: Physical, numerical and micromechanical methods. Composites Science and Technology 2017;139:117-26.

[309] Young RJ, Liu M, Kinloch IA, Li S, Zhao X, Vallés C, et al. The mechanics of reinforcement of polymers by graphene nanoplatelets. Composites Science and Technology 2018;154:110-6.

[310] Qian QZ, An Q, Yang Q, Gui Z. Synthesis and characterization of solution-processable polyelectrolyte complexes and their homogeneous membranes. ACS applied materials & interfaces 2009;1:90-6.

[311] Vidyasagar A, Sung C, Gamble R, Lutkenhaus JL. Thermal transitions in dry and hydrated layer-by-layer assemblies exhibiting linear and exponential growth. Acs Nano 2012;6:6174-84.

[312] Liang J, Huang Y, Zhang L, Wang Y, Ma Y, Guo T, et al. Molecular-Level Dispersion of Graphene into Poly(vinyl alcohol) and Effective Reinforcement of their Nanocomposites. Advanced Functional Materials 2009;19:2297-302.

[313] Kulkarni DD, Choi I, Singamaneni SS, Tsukruk VV. Graphene Oxide-Polyelectrolyte Nanomembranes. ACS Nano 2010;4:4667–76.

[314] Li H, Fauquignon M, Haddou M, Schatz C, Chapel JP. Interfacial Behavior of Solid- and Liquid-like Polyelectrolyte Complexes as a Function of Charge Stoichiometry. Polymers (Basel) 2021;13.

[315] Noskov BA, Bilibin AY, Lezov AV, Loglio G, Filippov SK, Zorin IM, et al. Dynamic surface elasticity of polyelectrolyte solutions. Colloids and Surfaces A: Physicochemical and Engineering Aspects 2007;298:115-22.

[316] Spruijt E, Sprakel J, Cohen Stuart MA, van der Gucht J. Interfacial tension between a complex coacervate phase and its coexisting aqueous phase. Soft Matter 2010;6:172-8.

[317] Priftis D, Farina R, Tirrell M. Interfacial energy of polypeptide complex coacervates measured via capillary adhesion. Langmuir : the ACS journal of surfaces and colloids 2012;28:8721-9.

[318] Guo H-L, Wang X-F, Qian Q-Y, Wanga F-B, Xia X-H. A green approach to the synthesis of graphene nanosheets. ACS Nano 2009;3:2653–9.

[319] Gómez J, Villaro E, Navas A, Recio I. Testing the influence of the temperature, RH and filler type and content on the universal power law for new reduced graphene oxide TPU composites. Materials Research Express 2017;4:105020.

[320] Diez JA, Gratton R, Thomas LP, Marino B. Laplace pressure driven drop spreading. Physics of Fluids 1994;6:24-33.

[321] Sadman K, Delgado DE, Won Y, Wang Q, Gray KA, Shull KR. Versatile and High-Throughput Polyelectrolyte Complex Membranes via Phase Inversion. ACS applied materials & interfaces 2019;11:16018-26.

[322] Huang X, Zhi C, Lin Y, Bao H, Wu G, Jiang P, et al. Thermal conductivity of graphene-based polymer nanocomposites. Materials Science and Engineering: R: Reports 2020;142:100577.

[323] Sun X, Ramesh P, Itkis ME, Bekyarova E, Haddon RC. Dependence of the thermal conductivity of two-dimensional graphite nanoplatelet-based composites on the nanoparticle size distribution. J Phys: Condens Matter 2010;22:334216.

[324] Sun X, Yu A, Ramesh P, Bekyarova E, Itkis ME, Haddon RC. Oxidized Graphite Nanoplatelets as an Improved Filler for Thermally Conducting Epoxy-Matrix Composites. Journal of Electronic Packaging 2011;133.

[325] Saeidijavash M, Garg J, Grady B, Smith B, Li Z, Young RJ, et al. High thermal conductivity through simultaneously aligned polyethylene lamellae and graphene nanoplatelets. Nanoscale 2017;9:12867-73.

[326] Ganguli S, Roy AK, Anderson DP. Improved thermal conductivity for chemically functionalized exfoliated graphite/epoxy composites. Carbon 2008;46:806-17.

[327] Meng F, Huang F, Guo Y, Chen J, Chen X, Hui D, et al. In situ intercalation polymerization approach to polyamide-6/graphite nanoflakes for enhanced thermal conductivity. Composites Part B: Engineering 2017;117:165-73.

[328] Sun Z, Pöller S, Huang X, Guschin D, Taetz C, Ebbinghaus P, et al. High-yield exfoliation of graphite in acrylate polymers: A stable few-layer graphene nanofluid with enhanced thermal conductivity. Carbon 2013;64:288-94.

[329] Yang J, Zhang E, Li X, Zhang Y, Qu J, Yu Z-Z. Cellulose/graphene aerogel supported phase change composites with high thermal conductivity and good shape stability for thermal energy storage. Carbon 2016;98:50-7.

[330] Yu J, Choi HK, Kim HS, Kim SY. Synergistic effect of hybrid graphene nanoplatelet and multi-walled carbon nanotube fillers on the thermal conductivity of polymer composites and theoretical modeling of the synergistic effect. Composites Part A: Applied Science and Manufacturing 2016;88:79-85.

[331] Wu H, Drzal LT. High thermally conductive graphite nanoplatelet/polyetherimide composite by precoating: Effect of percolation and particle size. Polymer Composites 2013;34:2148-53.

[332] Prolongo SG, Moriche R, Jiménez-Suárez A, Sánchez M, Ureña A. Epoxy Adhesives Modified with Graphene for Thermal Interface Materials. The Journal of Adhesion 2014;90:835-47.

[333] Guo W, Chen G. Fabrication of graphene/epoxy resin composites with much enhanced thermal conductivity via ball milling technique. Journal of Applied Polymer Science 2014;131:n/a-n/a.

[334] Fang X, Fan L-W, Ding Q, Wang X, Yao X-L, Hou J-F, et al. Increased Thermal Conductivity of Eicosane-Based Composite Phase Change Materials in the Presence of Graphene Nanoplatelets. Energy & Fuels 2013;27:4041-7.

[335] Fan L-W, Fang X, Wang X, Zeng Y, Xiao Y-Q, Yu Z-T, et al. Effects of various carbon nanofillers on the thermal conductivity and energy storage properties of paraffin-based nanocomposite phase change materials. Applied Energy 2013;110:163-72.

[336] Tien DH, Park J, Han SA, Ahmad M, Seo Y, Shin K. Electrical and Thermal Conductivities of Stycast 1266 Epoxy/Graphite Composites. Journal of the Korean Physical Society 2011;59:2760-4.

[337] Lv J, Cai X, Ye Q, Zhang H, Ruan Z, Cai J. Significant improvement in the interface thermal conductivity of graphene-nanoplatelets/silicone composite. Materials Research Express 2018;5:055606.

[338] Imran KA, Lou J, Shivakumar KN. Enhancement of electrical and thermal conductivity of polypropylene by graphene nanoplatelets. Journal of Applied Polymer Science 2018;135:45833.

[339] Cai X, Jiang Z, Zhang X, Gao T, Yue K, Zhang X. Thermal property improvement of polytetrafluoroethylene nanocomposites with graphene nanoplatelets. RSC Adv 2018;8:11367-74.

[340] Xiao Y-j, Wang W-y, Lin T, Chen X-j, Zhang Y-t, Yang J-h, et al. Largely Enhanced Thermal Conductivity and High Dielectric Constant of Poly(vinylidene fluoride)/Boron Nitride Composites Achieved by Adding a Few Carbon Nanotubes. The Journal of Physical Chemistry C 2016;120:6344-55.

[341] Zhang Y, Park S-J. Imidazolium-optimized conductive interfaces in multilayer graphene nanoplatelet/epoxy composites for thermal management applications and electroactive devices. Polymer 2019;168:53-60.

[342] Yu A, Ramesh P, Sun X, Bekyarova E, Itkis ME, Haddon RC. Enhanced Thermal Conductivity in a Hybrid Graphite Nanoplatelet – Carbon Nanotube Filler for Epoxy Composites. Advanced materials 2008;20:4740-4.

[343] Yoo Y, Cui L, Yoon PJ, Paul DR. Morphology and Mechanical Properties of Rubber Toughened Amorphous Polyamide/MMT Nanocomposites. Macromolecules 2009;43:615-24.

[344] Gu J, Yang X, Lv Z, Li N, Liang C, Zhang Q. Functionalized graphite nanoplatelets/epoxy resin nanocomposites with high thermal conductivity. International Journal of Heat and Mass Transfer 2016;92:15-22.

[345] Song SH, Park KH, Kim BH, Choi YW, Jun GH, Lee DJ, et al. Enhanced thermal conductivity of epoxy-graphene composites by using non-oxidized graphene flakes with non-covalent functionalization. Advanced materials 2013;25:732-7.

[346] Wang M, Hu N, Zhou L, Yan C. Enhanced interfacial thermal transport across graphene–polymer interfaces by grafting polymer chains. Carbon 2015;85:414-21.

[347] Colonna S, Battegazzore D, Eleuteri M, Arrigo R, Fina A. Properties of Graphene-Related Materials Controlling the Thermal Conductivity of Their Polymer Nanocomposites. Nanomaterials 2020;10.

[348] Marsden AJ, Papageorgiou DG, Vallés C, Liscio A, Palermo V, Bissett MA, et al. Electrical percolation in graphene–polymer composites. 2D Materials 2018;5:032003.

[349] Zhang H-B, Zheng W-G, Yan Q, Yang Y, Wang J-W, Lu Z-H, et al. Electrically conductive polyethylene terephthalate/graphene nanocomposites prepared by melt compounding. Polymer 2010;51:1191-6.

[350] Steurer P, Wissert R, Thomann R, Mulhaupt R. Functionalized Graphenes and Thermoplastic Nanocomposites Based upon Expanded Graphite Oxide. Macromolecular rapid communications 2009;30:316-27.

[351] Hofmann D, Keinath M, Thomann R, Mülhaupt R. Thermoplastic Carbon/Polyamide 12 Composites Containing Functionalized Graphene, Expanded Graphite, and Carbon Nanofillers. Macromolecular Materials and Engineering 2014;299:1329-42.

[352] Xu C, Gao J, Xiu H, Li X, Zhang J, Luo F, et al. Can in situ thermal reduction be a green and efficient way in the fabrication of electrically conductive polymer/reduced graphene oxide nanocomposites? Composites Part A: Applied Science and Manufacturing 2013;53:24-33.

[353] Nezakati T, Tan A, Seifalian AM. Enhancing the electrical conductivity of a hybrid POSS-PCL/graphene nanocomposite polymer. Journal of colloid and interface science 2014;435:145-55.

[354] Zeng X, Yang J, Yuan W. Preparation of a poly(methyl methacrylate)-reduced graphene oxide composite with enhanced properties by a solution blending method. European Polymer Journal 2012;48:1674-82.

[355] Hofmann D, Wartig K-A, Thomann R, Dittrich B, Schartel B, Mülhaupt R. Functionalized Graphene and Carbon Materials as Additives for Melt-Extruded Flame Retardant Polypropylene. Macromolecular Materials and Engineering 2013;298:1322-34.

[356] Fan W, Zhang C, Tjiu WW, Liu T. Fabrication of electrically conductive graphene/polystyrene composites via a combination of latex and layer-by-layer assembly approaches. Journal of Materials Research 2013;28:611-9.

[357] Appel A-K, Thomann R, Mülhaupt R. Polyurethane nanocomposites prepared from solvent-free stable dispersions of functionalized graphene nanosheets in polyols. Polymer 2012;53:4931-9.

[358] Yousefi N, Gudarzi MM, Zheng Q, Aboutalebi SH, Sharif F, Kim J-K. Self-alignment and high electrical conductivity of ultralarge graphene oxide–polyurethane nanocomposites. Journal of Materials Chemistry 2012;22:12709.

[359] Li Y, Tang J, Huang L, Wang Y, Liu J, Ge X, et al. Facile preparation, characterization and performance of noncovalently functionalized graphene/epoxy nanocomposites with poly(sodium 4-styrenesulfonate). Composites Part A: Applied Science and Manufacturing 2015;68:1-9.

[360] Yousefi N, Lin X, Zheng Q, Shen X, Pothnis JR, Jia J, et al. Simultaneous in situ reduction, self-alignment and covalent bonding in graphene oxide/epoxy composites. Carbon 2013;59:406-17.

[361] Tschoppe K, Beckert F, Beckert M, Mülhaupt R. Thermally Reduced Graphite Oxide and Mechanochemically Functionalized Graphene as Functional Fillers for Epoxy Nanocomposites. Macromolecular Materials and Engineering 2015;300:140-52.

[362] Potts JR, Shankar O, Du L, Ruoff RS. Processing–Morphology–Property Relationships and Composite Theory Analysis of Reduced Graphene Oxide/Natural Rubber Nanocomposites. Macromolecules 2012;45:6045-55.

[363] Dong B, Wu S, Zhang L, Wu Y. High Performance Natural Rubber Composites with Well-Organized Interconnected Graphene Networks for Strain-Sensing Application. Industrial & Engineering Chemistry Research 2016;55:4919-29.

[364] Bao WS, Meguid SA, Zhu ZH, Pan Y, Weng GJ. A novel approach to predict the electrical conductivity of multifunctional nanocomposites. Mechanics of Materials 2012;46:129-38.

[365] Sreeprasad TS, Rodriguez AA, Colston J, Graham A, Shishkin E, Pallem V, et al. Electron-tunneling modulation in percolating network of graphene quantum dots: fabrication, phenomenological understanding, and humidity/pressure sensing applications. Nano letters 2013;13:1757-63.

[366] Nabok AV, Hassan AK, Ray AK. Optical and electrical characterisation of polyelectrolyte self-assembled thin films. Materials Science and Engineering: C 1999;8-9:505-8.

[367] Li S, Pan H, Wang Y, Sun J. Polyelectrolyte complex-based self-healing, fatigue-resistant and anti-freezing hydrogels as highly sensitive ionic skins. Journal of Materials Chemistry A 2020;8:3667-75.

[368] Li Y, Chen S, Wu M, Sun J. Polyelectrolyte multilayers impart healability to highly electrically conductive films. Advanced materials 2012;24:4578-82.

[369] Nakashima T, Zhu J, Qin M, Ho S, Kotov NA. Polyelectrolyte and carbon nanotube multilayers made from ionic liquid solutions. Nanoscale 2010;2:2084-90.

[370] Rani A, Oh KA, Koo H, Lee Hj, Park M. Multilayer films of cationic graphene-polyelectrolytes and anionic graphene-polyelectrolytes fabricated using layer-by-layer self-assembly. Applied Surface Science 2011;257:4982-9.

[371] Vallés C, Zhang X, Cao J, Lin F, Young RJ, Lombardo A, et al. Graphene/Polyelectrolyte Layer-by-Layer Coatings for Electromagnetic Interference Shielding. ACS Applied Nano Materials 2019;2:5272-81.